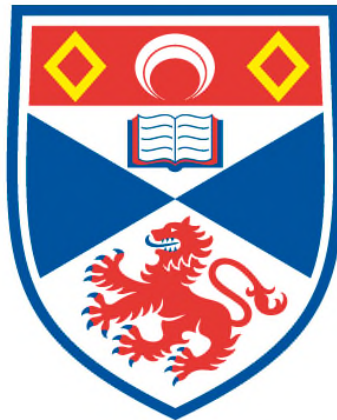


**THE APPLICATION OF SPONTANEOUS PARAMETRIC
DOWNCONVERSION TO DEVELOP TOOLS FOR VALIDATING
PHOTONIC QUANTUM INFORMATION TECHNOLOGIES**

Peter J. Thomas

**A Thesis Submitted for the Degree of DEng
at the
University of St Andrews**



2010

**Full metadata for this item is available in
St Andrews Research Repository
at:**

<http://research-repository.st-andrews.ac.uk/>

Please use this identifier to cite or link to this item:

<http://hdl.handle.net/10023/3050>

This item is protected by original copyright

**The application of spontaneous parametric downconversion
to develop tools for validating photonic quantum
information technologies**

Peter J. Thomas



University
of
St Andrews

Portfolio submitted for the degree of Engineering Doctorate

September 2010

Declarations

I, Peter J. Thomas, hereby certify that this portfolio, which is approximately 55,000 words in length, has been written by me, that it is the record of work carried out by me and that it has not been submitted in any previous application for a higher degree.

I was admitted as a research student in September, 2004 and as a candidate for the degree of Engineering Doctorate in September, 2004; the higher study for which this is a record was carried out at the National Physical Laboratory, Teddington and in the University of St Andrews between 2004 and 2010.

Peter J. Thomas

September 2010

I hereby certify that the candidate has fulfilled the conditions of the Resolution and Regulations appropriate for the degree of Engineering Doctorate in the University of St Andrews and that the candidate is qualified to submit this portfolio in application for that degree.

Professor Malcolm Dunn
(Academic supervisor)

September 2010

Dr Christopher Chunnillall
(Industrial supervisor)

September 2010

In submitting this portfolio to the University of St Andrews I understand that I am giving permission for it to be made available for use in accordance with the regulations of the University Library for the time being in force, subject to any copyright vested in the work not being affected thereby. I also understand that the title and the abstract will be published, and that a copy of the work may be made and supplied to any bona fide library or research worker, that my portfolio will be electronically accessible for personal or research use unless exempt by award of an embargo as requested below, and that the library has the right to migrate my portfolio into new electronic forms as required to ensure continued access to the portfolio. I have obtained any third-party copyright permissions that may be required in order to allow such access and migration, or have requested the appropriate embargo below.

The following is an agreed request by candidate and supervisors regarding the electronic publication of this portfolio:

Embargo on both all of printed copy and electronic copy for the same fixed period of one year on the following grounds: publication would be commercially damaging to the researcher, or to the supervisors, or the University.

Peter J. Thomas

September 2010

Professor Malcolm Dunn

September 2010

Dr Christopher Chunnillall

September 2010

Acknowledgments

I would like to thank my academic supervisor Professor Malcolm Dunn at the University of St. Andrews and my industrial supervisor Dr Christopher Chunnilall at the National Physical Laboratory for allowing me to undertake the EngD with them and for their consistently superb guidance and encouragement throughout.

Within the non-linear optics group at the University of St. Andrews I would like to thank Dr David Stothard, his impressive expertise in electronics was vital to the success of the experiments carried out there. Thanks are also owed to David Walsh for his assistance about the laboratory and for thoughtful technical discussions. I am grateful to Richard Tatham for useful discussions of theoretical concepts. I would also like to thank Caroline Thomson and Shona Matthew for helping to create a friendly and productive working environment.

At the National Physical laboratory I would like to thank all members of the former Optical Technologies and Scientific Computing Team for providing an interesting and educational working environment, particular thanks goes to Dr Jessica Cheung for her expertise about the laboratory and for her constant encouragement, also I thank Dr Richard Hubbard and Rainer Winkler for stimulating conversations.

I would like to give special thanks for the persistent support and encouragement I received from Randi-Helene and my family, without which I surely wouldn't have made it to this stage.

This work was co-funded from the National Measurement System (NMS) Physical and Pathfinder Programmes of the National Measurement Office (NMO), an Executive Agency of the Department for Business, Innovation and Skills. The work was also funded by the Engineering and Physical Sciences Research council (EPSRC).

Abstract

This portfolio of work contributes to the remit of the National Physical Laboratory (NPL) to develop the underpinning expertise and tools for validating nascent and future optical quantum technologies based on the discrete and quantum properties of photons. This requirement overlaps with the requirement to provide validation for devices operating in the photon-counting regime. A common theme running through the portfolio is photon pairs generated through spontaneous parametric downconversion (SPDC).

A Hong-Ou-Mandel (HOM) interferometer sourced with visible wavelength photon pairs from an SPDC process in beta-barium borate (BBO) was designed, built and characterised. The visibility of the HOM interference is dependent on the indistinguishability of the interfering photons, but is also influenced by imperfections of the interferometer; therefore an investigation was carried out to quantify the effects of the interferometer imperfections on the measured visibility so that the true photon indistinguishability could be measured with a quantified uncertainty.

A bright source of correlated pair photons in the telecoms band based upon a pump enhanced SPDC process in periodically-poled potassium titanyl phosphate (PPKTP) was designed, built and characterised. From the characterisation measurements the source brightness was estimated to be 6.2×10^4 pairs/ s/ mw pump. The photon pairs were further characterised through their incorporation as a source in a HOM interference experiment.

The developed correlated photon pair source was at the heart of a novel scheme for the generation of polarisation entangled photon pairs, for which the design, build and characterisation work is presented. The source was demonstrated to produce two of the four maximally entangled Bell states with quantum interference visibilities of around 0.95. The generated states were also shown to break a form of Bell's inequality by around six standard deviations. The polarisation entangled photon pair source was originally built at the University of St Andrews and was later transferred to the NPL where it will extend NPL's capabilities to this key spectral region.

Finally a study was carried out to investigate the possibility of a wavelength tuneable device for the absolute measurement of single photon detector quantum efficiencies based upon an established SPDC technique.

Knowledge transfer activities

- Peter Thomas, Jessica Cheung, Christopher Chunnillall and Malcolm Dunn “Metrology using Two Photon Interference” presented at Physics 2005 - A Century after Einstein, Warwick 2005 (Poster)
- Peter Thomas, Jessica Cheung, Christopher Chunnillall and Malcolm Dunn “Quantifiable measurements using two photon interference” presented at Photon06, Manchester 2006 (Poster)
- Peter Thomas, Jessica Cheung, Christopher Chunnillall and Malcolm Dunn “Towards entangled photon metrology with known uncertainty” presented at SPIE Optics and Photonics, San Diego 2006 (Poster)
- Peter Thomas, Jessica Cheung, Christopher Chunnillall and Malcolm Dunn “Few photon and quantum metrology” QNLO 2008 (Poster)
- Peter Thomas, Jessica Cheung, Christopher Chunnillall and Malcolm Dunn “The Hong-Ou-Mandel interferometer; A new procedure for alignment”, *Review of scientific instruments*, **80**, 036101-1-3, 2009
- Christopher Chunnillall, Peter Thomas and Malcolm Dunn, “ A source of entangled photons for the 1550 nm telecommunications window” Single Photon Workshop, NIST Boulder, 2009
- Peter Thomas, Jessica Cheung, Christopher Chunnillall and Malcolm Dunn, “The measurement of photon indistinguishability to a quantifiable uncertainty using a Hong-Ou-Mandel interferometer” *Applied Optics*, **49** (11), 2173-2182, (2010)

Contents

Declarations	I
Acknowledgments.....	III
Abstract	V
Knowledge transfer activities	VII
Contents	IX
1 Introduction.....	1
1.1 Quantum entanglement	1
1.2 Quantum entangled photons and Spontaneous Parametric Downconversion	2
1.3 This portfolio, in the context of quantum metrology at the National Physical Laboratory	3
2 Hong-Ou-Mandel interferometer design & build	7
2.1 Introduction.....	7
2.2 Hong-Ou-Mandel interferometer configurations	9
2.3 Photon pair generation	12
2.4 Single photon detection.....	16
2.5 Coincident photon detection	22
2.6 Alignment and path balancing of the HOM interferometer paths.....	26
2.7 Interferometer characteristics	36
2.8 Conclusions.....	44
3 Measurement of photon indistinguishability to a quantifiable accuracy.....	47
3.1 Introduction.....	47
3.2 Quantifying the visibility of the measured interferogram – V_{HOM} – with an associated uncertainty	48
3.3 Photon indistinguishability and its determination from V_{HOM}	60
3.4 Polarisation effects influencing the measured visibility - $f_{\Delta\phi_{int}}$	62
3.5 Beam splitter influence on the measured visibility - $f_{R,T}$	65
3.6 Influence of angular interferometer alignment on the measured visibility – f_{θ}	68
3.7 Influence of beam centre Interferometer alignment on the measured visibility – f_{ϵ}	76
3.8 Surface effects on the measured visibility - $f_{surface}$	80

3.9	Compiled uncertainty budget for photon distinguishability measurement and discussion.....	85
3.10	Conclusions.....	89
4	Pump enhanced source of correlated photons in the telecoms band.....	91
4.1	Introduction.....	91
4.2	Non-linear crystal choice.....	92
4.3	Waveguide and bulk pump-enhanced approaches to improved downconversion efficiencies.....	97
4.4	Pump enhancement cavity design.....	101
4.5	Experimental setup for pump enhanced pair generation scheme.....	111
4.6	Characterisation of pump enhanced pair photon source.....	122
4.7	Further source characterisation; Hong-Ou-Mandel interference.....	131
4.8	Conclusions.....	137
5	Pump enhanced source of polarisation entangled photon pairs in the telecoms band .	141
5.1	Introduction.....	141
5.2	Theory of source design.....	143
5.3	Experimental setup.....	148
5.4	Experimental results.....	158
5.5	Rebuild of experiment at the NPL.....	164
5.6	Conclusions.....	167
6	Design of a wavelength tuneable device for the absolute measurement of detector quantum efficiency.	169
6.1	Introduction.....	169
6.2	Modelling theory and calculation method.....	171
6.3	Modelling of FSQEM system based on noncollinear 351.1 nm (e) → 702.2 (o) +702.2 (o) process in BBO.....	177
6.4	Conclusions.....	195
7	Conclusions and forward look.....	199
	References.....	203
	Appendix 1: SPDC wavefunction.....	211
	Appendix 2: Correlation functions for SPDC and SPDC sourced 2-beam interferometers	215

1 Introduction

1.1 Quantum entanglement

In the thought experiment of Einstein, Podolsky and Rosen (EPR), [1] measurements are made on two physical systems that are quantum entangled with respect to an observable. The quantum entanglement is characterised by a strong correlation of the measurements between the two systems, which could be spaced an infinite distance apart, while each system individually shows a random outcome for each measurement. The individual measurement outcomes are effectively undetermined before the measurements, and therefore quantum entanglement conflicts with physical reality. In addition locality is violated by the notion that the measurement of an observable in one system instantaneously determines the state of the second system with respect to that observable, even if the two systems are infinitely separated. The incompatibility of quantum theory with local realism led Einstein to believe it to be an incomplete description. Bell developed this discussion into a experimental test of the quantum mechanical disagreement with local realism [2]. The test consists of a set of ‘Bell inequalities’ that must be satisfied for measurements on a system described by any local and realistic model, but the Bell inequalities are violated for measurements on a quantum entangled system. A Bell inequality violation due to measurements from an experimentally produced EPR type system was first demonstrated by Clauser and Shimony [3].

Quantum mechanics is now routinely used to describe phenomena across a wide range of physical disciplines such as condensed matter, molecular and subatomic physics. Quantum entanglement is central to the thriving research fields of quantum information and communication. Quantum cryptography, a technology derived from this research, has now reached commercial realisation.

1. Introduction

1.2 Quantum entangled photons and Spontaneous Parametric Downconversion

The first violations of Bell inequalities were reported for entangled systems based upon photon pairs [3-4], and photon pairs remain the most popular resource for Bell inequality tests and other experiments in quantum mechanics. However the atomic cascade method employed in early experiments for the production of photon pairs is associated with low production rates and collection efficiencies. Spontaneous Parametric Downconversion (SPDC) later became the method of choice for producing photon pairs in quantum optics due to relatively large photon pair production rates and narrow emission angles leading to higher collection efficiencies. SPDC is a second order non-linear process whereby a higher energy pump photon is split into two lower energy daughter (signal and idler) photons within a non-linear medium. SPDC was first studied theoretically in 1961 [5] and first experimentally observed in 1967 [6]. The wavelength tuneable nature of downconverted light meant that many of the first studies focussed on applications in spectroscopy [7]. However the majority of SPDC work in the past 25 years has been in the field of quantum optics. Perhaps the most notable quantum optics experiments incorporating SPDC sources include the first demonstration of a Hong-Ou-Mandel interferometer [8] (874 citations) and the first demonstration for the teleportation of entangled states [9] (1680 citations). In addition, proposals that were inspired by the increased availability of SPDC sources were those for quantum cryptography using entangled photon pairs [10] (862 citations) and for quantum lithography, which can beat the classical Rayleigh criterion for the diffraction limit [11] (366 citations). SPDC features heavily in the quantum optical investigations of this portfolio.

Entanglement is always with respect to an observable, one such observable for photons is the spatial information they possess. Spatially entangled states can be produced using a device such as an SPDC-sourced Hong-Ou-Mandel interferometer [8], studies of which are reported in chapters two and three of this portfolio.

Photon polarisation is another observable that is often chosen for entanglement; such experiments are popular because of their relatively simple implementation. Polarisation entangled states are readily produced from SPDC sources in combination with other simple optical elements [12-14], as studied in chapters four and five of this portfolio.

1. Introduction

Photons can also be entangled in time, so-called ‘time-bin’ entanglement schemes were suggested as an alternative to polarisation entanglement for quantum systems based upon optical fibre networks, because time-bin entangled states are not affected by the polarisation mode dispersion of the fibre [15]. Quantum cryptography systems based on time-bin encoding have been commercialized [16]. Time as an entanglement variable is not studied at length within this portfolio.

1.3 *This portfolio, in the context of quantum metrology at the National Physical Laboratory*

Over the past couple of decades, many have sought to develop devices based on quantum principles such as entanglement. The interest in quantum technology has been fuelled further by the rapid growth of the semiconductor industry, where the current-increasing levels of performance due to component down-sizing is certain to be stifled as quantum mechanical considerations start to grow in importance [17]. The research into quantum technology has resulted in the production of quantum states having specific purposes, and the progress of such work could eventually lead to the formation of a complete and general set of quantum tools; quantum control, quantum communication, and quantum computation. Two critical stumbling blocks in realising such tools stems from the lack of good deterministic single photon sources [18], and the lack of high quantum efficiency photon-counting-regime detectors [19], particularly at telecoms wavelengths where the technology is underdeveloped yet there exists the possibility to establish distributed quantum system based upon existing fibre networks (see Figure 1-1). It has been recognised at the National Physical Laboratory (NPL) that a key step in overcoming these stumbling blocks is through the development of validation techniques based upon Spontaneous Parametric Down conversion (SPDC). All of the work contained within in this portfolio has SPDC at the focus and can be linked to facilitating the validation of single photon sources or detectors.

Chapter two relates to the design and build of an SPDC sourced Hong-Ou-Mandel interferometer that produces spatially entangled states. The visibility of the HOM interference feature gives a measure of photon indistinguishability (a key metric in quantum information). However, the measured visibility is susceptible to interferometer imperfections and such effects need to be quantified in order to determine the ‘true’ photon indistinguishability and this is the focus of chapter three, where a procedure for photon indistinguishability

1. Introduction

measurement is developed. A similar procedure to the one presented could be applied to the characterisation of single photon sources, and therefore in the framework of Figure 1-1 the work of chapters two and three contributes to facilitating the validation of single photon sources.

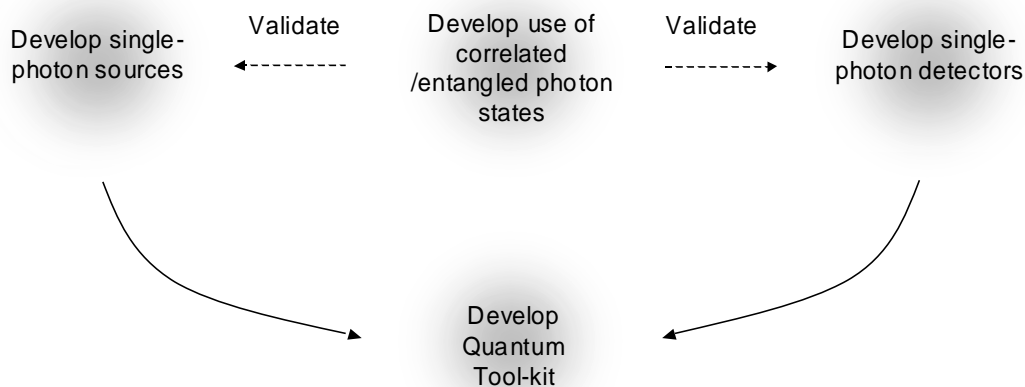


Figure 1-1 Dependencies of quantum information process development on research topics of interest at NPL.

Chapter four describes the design and build for a bright SPDC-based source of correlated photon pairs in the telecoms band. The mechanism for the additional brightness above that for a ‘single-pass’ SPDC process was achieved through enhancement of the pump beam within an optical cavity housing the downconversion medium. The developed correlated photon pair source was incorporated into the heart of a novel design for polarisation entangled photon pairs for which the design, build and characterisation is described in chapter five. This source is intended to be utilized for investigations into how to characterize optical states and processes which may be implemented at this wavelength using fibre or waveguide networks, as well as being available for the characterisation of novel single photon detectors and coupling with other quantum systems.

Chapter six presents a theoretical study of a wavelength tuneable system for the absolute measurement of single photon detector quantum efficiency, and as such the chapter also contributes to facilitating the validation of single photon sources.

When high performance single photon sources and detectors become a reality, the general quantum toolkit may also become a reality and large-scale information transfer will be possible using quantum processes. In parallel to negotiating the pathways towards the quantum toolkit, the NPL also seeks the realization of optical radiation scales based on

1. Introduction

numbers of photons, namely the quantum candela [20]; this topic will not be discussed at depth within this portfolio, although the studies described in chapter six may become relevant to this work.

2 *Hong-Ou-Mandel interferometer design & build*

2.1 *Introduction*

The Hong-Ou-Mandel (HOM) interferometer is a device that recombines individual photons at a beam splitter. Classically there are four outcomes to the recombination; two where the photons leave the beam splitter through different output ports and two where the photons emerge spatially superimposed. (Figure 2-1) Interpreting these outcomes as probability amplitudes, and assuming the incident photons are ‘indistinguishable’ in terms of their spatial, temporal, spectral and polarization modes, it can be shown that the classical possibilities of photons leaving separate ports of the beam splitter are forbidden, and the purely quantum phenomenon of photons always emerging paired from the recombiner occurs [8].

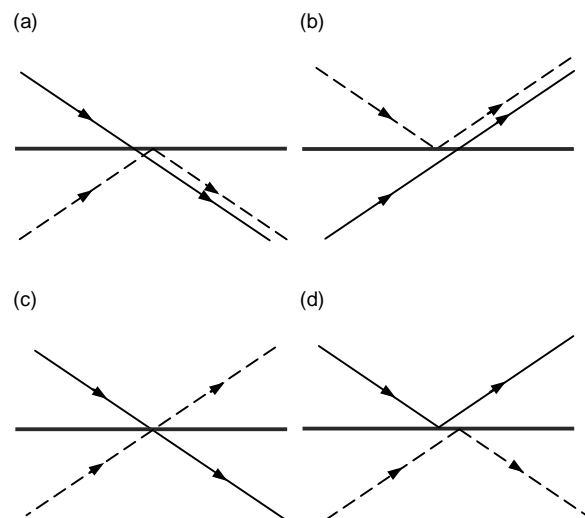


Figure 2-1 *Possible outcomes when two photons recombine from two separate input ports of a beamsplitter. The defining feature of HOM interference is when (c) and (d) cease to be possibilities and this occurs when the two photons are indistinguishable in all respects.*

Since the first HOM experiment, the interferometer has been used as a basis for further demonstrations of quantum mechanics [21-24] including Bell inequality tests, [12] and also Bell-state measurements for quantum teleportation and entanglement swapping [25]. In addition, the interferometer has become a useful tool in teaching laboratories [26]. The

2. Hong-Ou-Mandel interferometer design & build

sources of choice in the experiments are photon pair downconverters [27]. Such sources are widely available and suitable for quantum interference due to the high degree of simultaneity in creation of photon pairs, ensuring temporal indistinguishability.

The high simultaneity of photon production has meant that the parametric pair sourced HOM interferometer has found applications in time delay metrology. Studies have shown that by measuring the shift of the interference feature upon inserting an optical medium into one arm of the interferometer, it is possible to determine the medium polarisation mode dispersion with sub femtosecond precision [27]. A materials characterization technique known as Quantum Optical Coherence Tomography (QOCT) is also based on a pair-photon HOM interferometer. QOCT offers a method for material refractive index characterization and exhibits the favourable feature that the form of the interferogram is not influenced by wavelength dispersion of the material [28].

Perhaps the most pressing application for the HOM interferometer was revealed with the possibility to implement quantum computations using only linear optics, detectors and indistinguishable photons [29]. Subsequently there has been intense research to produce triggered sources of indistinguishable photons [30-35]. Since the HOM effect is dependent on photon indistinguishability, a HOM interferometer may be used to test the suitability of photon sources for application to these computation protocols [36-37].

This chapter describes the design and build of a two-photon interferometer sourced by pair photons from a parametric downconversion process. The interferometer was built to serve several purposes. The interferometer would give insight into the measurement process for the HOM interferogram and highlight the practical conditions that need to be fulfilled for optimal performance of the interferometer. In combination with a measurement equation formulated in chapter 3, measurements made on the built interferometer were used to develop a method for the quantification of photon indistinguishability with an estimated uncertainty. The framework of the interferometer was also a key component of two photon fluorescence experiments at NPL.

The chapter begins with an overview of the possible interferometer architectures and presents the arguments for the chosen configuration. The non-linear process and downconversion medium chosen for the interferometer source are discussed, together with the reasons for their selection over competing alternatives.

2. *Hong-Ou-Mandel interferometer design & build*

The single photon detection scheme for the interferometer is described and validated through estimation of the effective non-linear coefficient for the source interaction using a photon counting method presented in the literature [38]. The scheme used for coincident detection of photon pairs is also described, in addition to the methods used in order to optimize the pair collection efficiency.

The chapter also describes the procedure developed for assembling the interferometer. The two critical steps in the alignment procedure were: (i) the overlapping of the two interferometer optical paths at a beam cube and (ii) the balancing of the two interferometer optical paths. Finally the investigations serving to characterize the observed Hong-Ou-Mandel interference feature are discussed.

2.2 *Hong-Ou-Mandel interferometer configurations*

The Hong-Ou-Mandel interferometer has common properties with a Mach-Zehnder interferometer; i.e. the source light is split between two optical paths which are then recombined at a point that is spatially distant from the interferometer input. The separate paths enable properties such as time delay and relative polarization to be varied between the paths. The difference between the two interferometers lies in the source; for a classical Mach-Zehnder interferometer the source light is amplitude split radiation whereas in the HOM interferometer the source light are individual photons. Since the measurement of interest in HOM experiments is the rate at which photon pairs leave different output ports of the recombiner, a Michelson type configuration would not be practical.

SPDC sources are convenient for HOM interferometers because single photons are coupled into each arm of the interferometer simultaneously. SPDC sourced HOM interferometers can be distinguished in terms of whether the phase matching geometry of the source is collinear or non-collinear. For collinear source geometries orthogonally polarised (type II) photon pairs are normally chosen for HOM experiments, and there are two possible HOM configurations that allow for mapping of the complete interference feature with τ (τ is the time delay between photons), see Figure 2-2; for configuration (a) first the photons are separated at a polarising beam splitter in order that travelling mirrors can be used to advance or delay one photon, and then both photons are recombined at a beam splitter using beam steering mirrors (see section 4.7). For configuration (b), the collinearity of the pair is retained and a temporal delay is imposed by passing them through a polarisation dispersive material [27].

2. Hong-Ou-Mandel interferometer design & build

Configuration (a) is an advantageous because polarisation distinguishing information may be removed by positioning a half wave plate at 45° to the polarisation axis in one arm of the interferometer in configuration (b) polarisation analyzers need to be positioned in front of the detectors in order to remove the distinguishing information, resulting in signal loss.

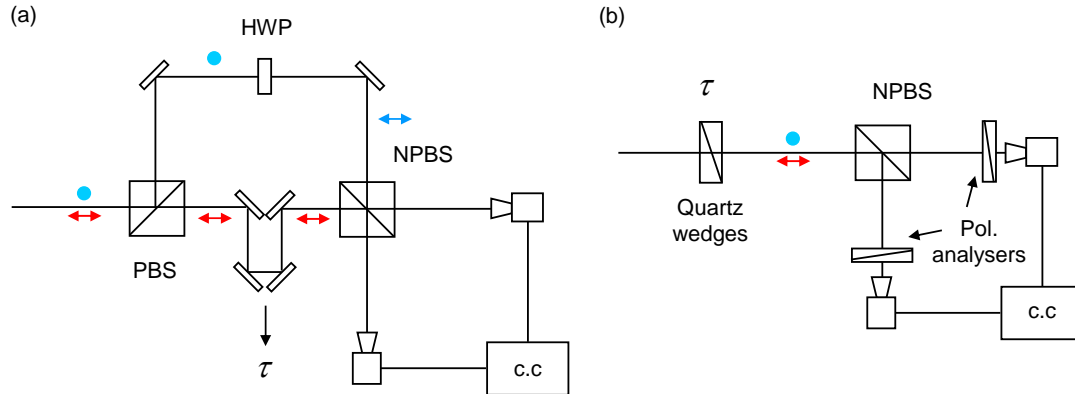


Figure 2-2 Configurations for HOM interferometers source by a type II parametric downconversion process. The τ -delay mechanisms are either a (a) travelling roof mirror or (b) polarisation dispersive medium. Polarisation distinguishing information is either removed by (a) half wave plate (HWP) in one arm of the interferometer or (b) polarisation analysers in front of each detector. Other symbols, NPBS/PBS- non/polarising beam splitter.

A collinearly phasematched source of parallel polarised (Type I) pair photons could also be used in a scheme similar to that shown in Figure 2-2 (a); first the pairs are split at a non-polarising beam splitter before imposing the temporal delay using travelling mirrors. However in this situation the photon pairs will only follow different paths after the beam splitter half of the time, resulting in the visibility of the HOM dip being limited to 0.5.

The experimental investigations of this chapter and of chapter 3 concern a HOM interferometer sourced with a non-collinearly phasematched downconverter. The non-collinear emission precludes the need of an additional beamsplitter to separate the photons and the temporal delay then may be applied directly to the different emission paths using travelling mirrors and subsequently combined with beam steering mirrors to the recombiner (see Figure 2-3). The interferometer source has type-I phasematching and therefore no additional polarizing optics are required to remove the polarisation information as in the type-II case. The relative simplicity associated with an interferometer employing a non-collinearly and type I phasematched source, coupled with the higher non-linear coefficients for type I processes were the motivations for choosing this interferometer/source configuration for the investigations.

2. Hong-Ou-Mandel interferometer design & build

In previous investigations of HOM interferometers sourced by type-I non-collinear parametric downconverters, designs have generally taken one of two architectures. The differences lie in the optical delay mechanisms; in the first HOM interferometer, a displacement of the beamsplitter in the perpendicular direction to the recombining surface increased one optical path of the interferometer while decreasing the other, see Figure 2-3(a) [8]. The architecture in Figure 2-3(a) has the advantage of minimizing the required optical components, but alignment of the beams is only maintained for $\tau \sim d$, where d is the beam diameter. In a later experiment [39] the relative optical path change between the two HOM arms was achieved by keeping one path fixed while varying the other through the slide of an optical trombone, see Figure 2-3 (b). Since the alignment of the interferometer holds for a much greater range of optical path changes for the second configuration, this was the basic design chosen for the interferometer build.

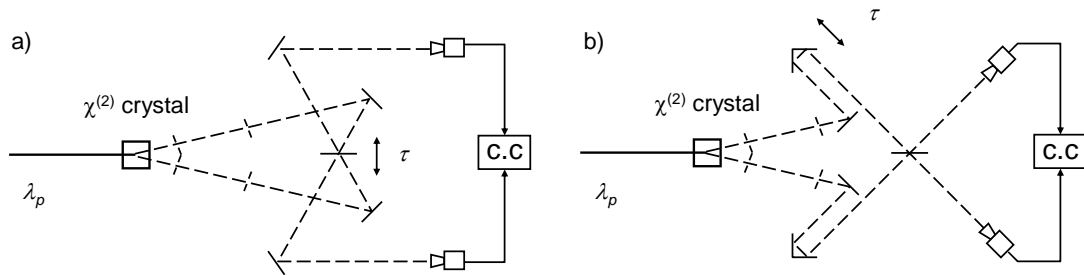


Figure 2-3 Configurations for non-collinearly sourced HOM interferometers (a) shows an arrangement where the optical delay is actuated through of the recombiner, and (b) shows an optical trombone arrangement for the delay.

The possibility of building an optical fibre HOM interferometer where the recombiner is a fused silica 2×2 coupler was ignored because although such a configuration would ensure good mode overlap of the photons (and therefore high visibility interference), this would be at the expense of signal loss due to non-unity coupling efficiency into the fibre. In addition it was felt that the characterisation measurements required when applying HOM framework as a tool for determining photon indistinguishability would be more straightforward in the case of a free-space interferometer, see chapter 3.

2.3 Photon pair generation

2.3.1 Parametric downconversion medium and phasematching

In the previous section, it was established that the interferometer source would be a parametric downconverter with non-collinear type-I phase matching. This section details the considerations and decisions that were taken in deciding the remaining details of the phase matching interaction, in particular the non-linear medium used, the photon wavelengths involved and the non-collinear emission angle.

It was desirable to have pair photons at visible wavelengths where photon counting technology is well developed and since the HOM effect requires indistinguishable photons the photon pairs created were required to be degenerate. The wavelength and degeneracy constraints precluded the use of the popular downconverters lithium niobate (LiNbO₃) [40] and potassium titanyl phosphate (KTP) [41] crystals since although they transmit visible wavelengths, their linear absorption coefficients are rather high in the near-UV wavelength region that would be required for the pump. Two widely available materials with high transparency across the visible spectrum and down to 350 nm are potassium dihydrogen phosphate (KDP) [8] and beta-barium borate (BBO) [42].

KDP and BBO are both negative uniaxial crystals and birefringent phase matched solutions for both crystal types were investigated for their suitability to the interferometer. The aim of the following analysis was to find the laboratory emission angles of the signal and idler photons from an incident pump photon, $\theta_{s,lab}$ and $\theta_{i,lab}$ respectively. The pump photon was chosen to be extra-ordinarily polarised since the wavevector length k_p for a given wavelength can be varied by changing the angle of the wavevector to the optic axis θ_{pm} therefore increasing the probability of finding a birefringent phasematching solution. Both downconverted photons were chosen to be ordinarily polarised serving to fulfil the indistinguishability requirement for HOM interference without additional polarization control optics. By considering momentum conservation in both horizontal and vertical planes:

$$k_p = k_s \cos \theta_s + k_i \cos \theta_i \quad (2.3.1)$$

$$k_s \sin \theta_s = -k_i \sin \theta_i \quad (2.3.2)$$

2. Hong-Ou-Mandel interferometer design & build

where k_p , k_s and k_i are the pump signal and idler crystal momenta magnitudes respectively. θ_s and θ_i are the angles of the signal and idler wavevectors respectively to the pump wave vector in the crystal. Squaring equation (2.3.2) and using $\sin^2 \theta = 1 - \cos^2 \theta$ gives:

$$k_s^2 \cos^2 \theta_s = k_i^2 (\cos^2 \theta_i - 1) + k_s^2 \quad (2.3.3)$$

Comparing equation (2.3.1) with the square of equation (2.3.3) then yields:

$$\theta_s = \cos^{-1} \left(\frac{k_p^2 - k_s^2 + k_i^2}{2k_p k_i} \right) \quad (2.3.4)$$

θ_i is then obtained through equation (2.3.2) and the application of Snell's law gives the emission angles in the laboratory space:

$$\sin \theta_{s,lab} = n_s \sin \theta_s, \quad \sin \theta_{i,lab} = n_i \sin \theta_i \quad (2.3.5)$$

Since k_s and k_i wavevectors for a given wavelength do not vary with direction in the crystal, the calculated $\theta_{s,lab}$ and $\theta_{i,lab}$ applies for all azimuthal angles of k_s and k_i about k_p and therefore defines a cone of emission about the pump beam.

Figure 2-4 show the semi cone angles corresponding to the phasematched signal emission from BBO and KDP when considering pump photons from the 351.1 nm line of an argon ion laser; similar solutions were obtained for the 363.8 nm line of the argon ion laser and also the 350.7 nm and 356.4 nm lines of a krypton ion laser. The Sellmeier coefficients given in references [43] and [44] were used to calculate the spectral variation of refractive index in BBO and KDP respectively.

From the calculated phasematching solutions, the following considerations were used to determine those most suitable for sourcing the interferometer; i) ideally the cone angle should not be too small since a smaller cone angle would require the interferometer to have longer optical paths and/or additional beam steering mirrors in order that the spatial separation of the photon pairs is sufficient to allow positioning of path defining apertures critical to the alignment procedure and ii) the angle spreading of wavelengths about degeneracy should be kept low in order that maximum photon fluxes can be input to the interferometer. By analysis

2. Hong-Ou-Mandel interferometer design & build

of Figure 2-4, it can be seen that there was a trade off between i) and ii). $\theta_{pm} \approx 35.0^\circ$ and $\theta_{pm} \approx 55.0^\circ$ appeared to be good compromise solutions for BBO and KDP respectively.

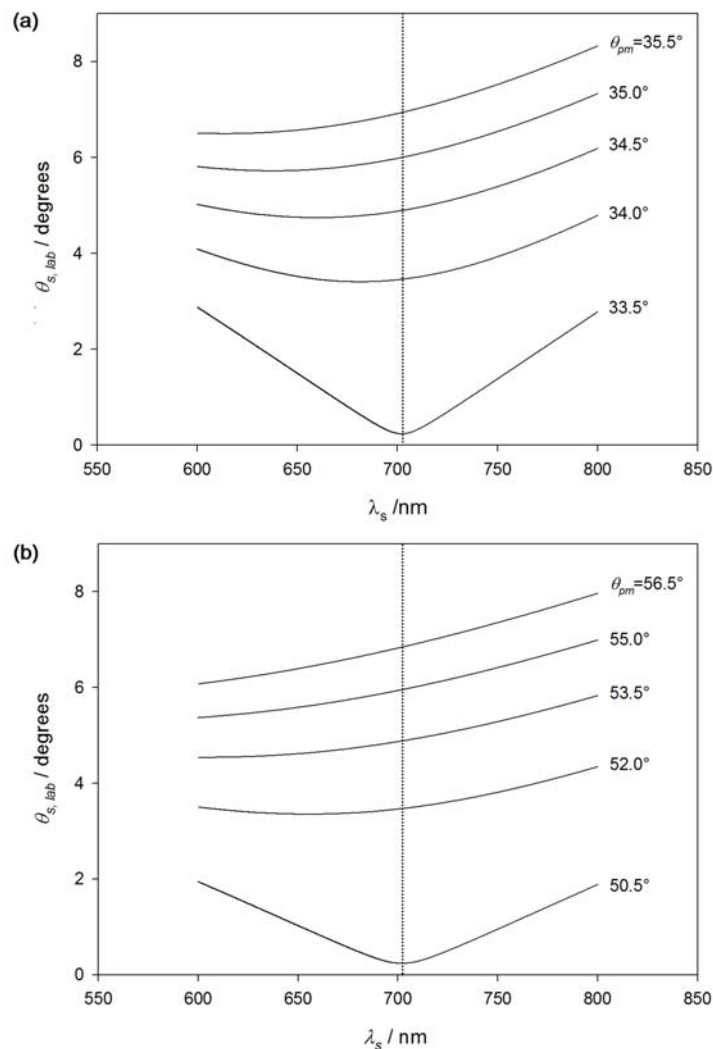


Figure 2-4 Half cone angles for the $e \rightarrow o + o$ downconversion in the laboratory frame with respect to the 351.1 nm pump beam for cuts of the crystal corresponding to different phase matching angles. (a) BBO (b) KDP.

Photon fluxes will be influenced by the effective non-linear optical coefficients for the $e \rightarrow o + o$ non-linear processes. BBO belongs to the point group $3m$ and therefore the effective non-linearity is given by equation (2.3.6) [42]. KDP, which belongs to the point group $\bar{4}2m$, has an effective non-linearity given by equation (2.3.7) [45].

$$d_{eff}(BBO) = d_{31} \sin \theta_{pm} - d_{11} \cos \theta \cos 3\phi_{pm} \quad (2.3.6)$$

$$d_{eff}(KDP) = d_{36} \sin \theta_{pm} \sin 2\phi_{pm} \quad (2.3.7)$$

2. *Hong-Ou-Mandel interferometer design & build*

ϕ_{pm} is the azimuthal angle of the pump beam about the crystal optic axis. KDP and BBO are both uniaxial crystals, hence the phasematching calculations were independent of ϕ_{pm} . Choosing $\theta_{pm}(\text{BBO})=35.0^\circ$, $\theta_{pm}(\text{KDP})=55.0^\circ$ such that $\theta_{s,lab}=5.9^\circ$ and choosing $\phi_{pm}(\text{BBO})=0^\circ$, $\phi_{pm}(\text{KDP})=45^\circ$ such that the magnitudes of (2.3.6) and (2.3.7) are optimised gives $d_{eff}(\text{BBO})=1.26$ pm/V and $d_{eff}(\text{KDP})=0.32$ pm/V. Photon fluxes are proportional to d_{eff}^2 (see section 2.4) and therefore BBO was chosen for the interferometer source.

The procured BBO crystal was 5 mm long with a 7 mm x 7 mm cross section. Both the input and output faces were anti-reflection coated to give $R < 0.5\%$ at both the pump and downconverted wavelengths.

2.3.2 *Pump photon source characteristics*

The pump was the 351.1 nm line of an argon ion laser (Coherent Innova-90). The pump was vertically polarised with a purity of 100:1.

The beam propagation characteristics were estimated by focusing the laser output through a 500 mm converging lens to a waist and then measuring the beam diameter at various points along a 400 mm distance about the waist. A beam profiler (Spiricon) was used for the diameter measurements. A non-linear least squares fitting procedure was used to fit a hyperbola to the data, (equation 4.4.9) which gave an M^2 value of 1.28 ± 0.05 . An ABCD matrix transformation (see section 4.4.2 for more detail) of the fitted profile back through the focussing lens implied a beam diameter of 1.80 mm at the laser aperture, and a beam waist of 1.66 mm at 1.01 m behind the aperture, which is consistent with the flat high reflector, long radius output coupler design of the laser.

Initially a narrowband interference filter was used to suppress fluorescence from the laser, but this was found to suffer optical damage when pump powers > 10 mw were used. Therefore the filter was replaced with an F2 flint glass wavelength dispersive prism positioned in the beam at the angle of minimum deviation.

2. Hong-Ou-Mandel interferometer design & build

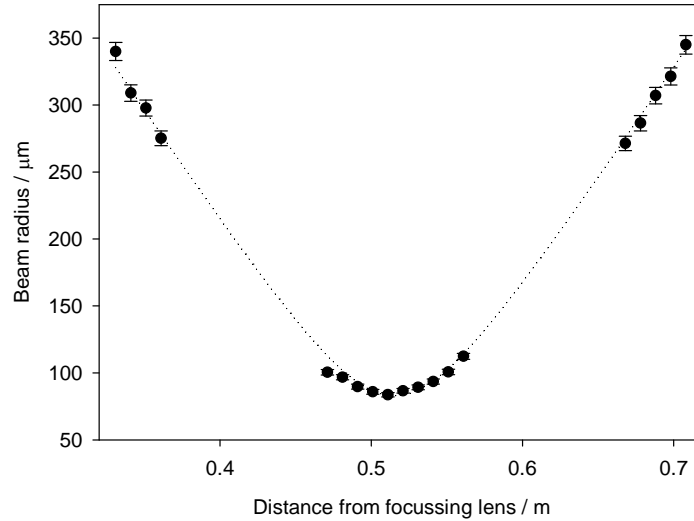


Figure 2-5 Measured profile of the argon pump beam radius with distance from a 500 mm focal length lens 0.6 m in front of the output aperture of the laser. The data points are the average beam radius of measurements in the horizontal and vertical plane. The fitted curve is based on equation 4.4.9.

A half wave plate was positioned before the crystal so that the pump polarisation could be rotated for optimisation or minimisation of phasematching for the $e \rightarrow o+o$ processes, and therefore served as an on-off switch for the downconversion process.

2.4 Single photon detection

2.4.1 Experimental setup

The setup required for detecting the photons from the downconversion process described in section 2.3 is shown in Figure 2-6.

The detectors used in this investigation were silicon avalanche photodiodes (PerkinElmer SPCM-AQR), with dark count rates of $\sim 100 \text{ s}^{-1}$. The detectors are continuously ready to receive photons until a photon is detected when the devices become ‘blind’ to further photons arriving during a 50 ns dead time, after which the detectors recover to their ready state. The detectors were placed 70 cm from the crystal along the 5.92° angle that defines the emission direction of the degenerate downconversion.

2. Hong-Ou-Mandel interferometer design & build

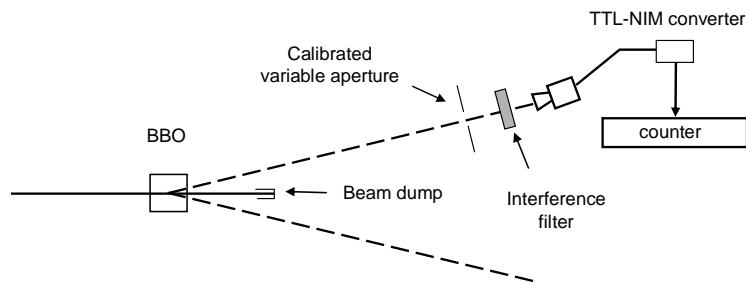


Figure 2-6 Setup for measuring and counting single photons emitted from BBO

The downconverted photons were imaged onto the 180 μm detector active area using a 30 mm focal length achromatic lens which was mounted to the detectors using mounts allowing 3 axis translation of the lens relative to the detector and 2 axes of tilt. The degenerate photons from the broadband emission were selected using a narrow band pass (3 nm) interference filter centred at 702.2 nm and optimising the observed count rate by adjusting the detector and lens positions.

Upon detection of a photon, the device gave a single TTL electrical pulse which was converted to a NIM pulse and sent to a single pulse counter (EG&G model 994).

2.4.2 Calculation of single photon count rates and the estimation of d_{eff}

The collection optics and electronics were validated by relating the observed single photon count rates to a value for the effective non-linear coefficient for the interaction d_{eff} . The power of the downconverted emission, δP_s emitted from a nonlinear crystal within a spectral bandwidth $\delta\lambda_s$ over all solid angles can be shown to be [46]:

$$\delta P_s = (2\pi)^4 \frac{2\hbar c d_{\text{eff}}^2}{\epsilon_0 n_p^2} \frac{\lambda_p}{\lambda_s^5 \lambda_i^2} \int_0^L P_p(l) dl \delta\lambda_s \quad (2.4.1)$$

Where λ_p , λ_s and λ_i are the pump signal and idler wavelengths respectively, n_p is the refractive index of the pump wavelength, ϵ_0 is the permittivity of free space, L is the crystal length, and $\hbar = h/2\pi$ where h is Planck's constant. The integral term takes into account the linear absorption of the material through Beer's law:

2. Hong-Ou-Mandel interferometer design & build

$$P_p(l) = P_p(0)e^{-\alpha l} \quad (2.4.2)$$

The absorption coefficient α for BBO at visible wavelengths is $\sim 100 \text{ m}^{-1}$. Because downconversion is spectrally broad, the total power is given by summing over $\delta\lambda$, and therefore summation limits need to be set. The aperture defines a collection angle $\Delta\theta_{collect}$, which can limit the collected range of λ_s in the absence of spectral filtering. The laboratory emission angle is related to λ_s through equations (2.3.4)-(2.3.5), and within $\Delta\theta_{collect}$ it is possible to associate all laboratory emission angles θ_{lab,λ_j} with a wavelength λ_j , see Figure 2-7(a). The resulting range of λ_j , $\Delta\lambda_{collect}$ can then be used for setting limits for $\delta\lambda_s$ summation in equation (2.4.1). However, as discussed in section 2.3.1, the θ_{λ_j} values in Figure 2-7(a) apply for all azimuthal angles about the pump beam and therefore equation (2.4.1) evaluated over $\Delta\lambda_{collect}$, gives the total downconversion power into a cone of thickness $\Delta\theta_{collect}$. Therefore equation (2.4.1) needs to be modified in order to account for the fact that the aperture selects only a small part of the emission cone, see Figure 2-7 (b). In addition, the measured singles count rate will be further reduced by transmittance losses along the optical path to the detector and by the non-unity quantum efficiency of the detector. Accounting for the $\Delta\lambda_{collect}$ limits, the aperturing of the emission cone and systems losses, equation (2.4.1) is re-written as [38]:

$$P_s = (2\pi)^4 \frac{2\hbar c d_{eff}^2 \lambda_p}{\epsilon_0 n_p^2} \sum_{\lambda_j \in \Delta\lambda_{collect}} \frac{T(\lambda_j) \eta_D \eta}{\lambda_j^5 \left(\frac{1}{\lambda_p} - \frac{1}{\lambda_j} \right)^{-2}} \frac{R \Delta\theta_{collect}}{2\pi R \sin(\theta_{lab,\lambda_j})} \delta\lambda_j \int_0^L P_p(l) dl \delta\lambda_s \quad (2.4.3)$$

Since $\delta N_s = \delta P_s \lambda_s / \hbar c$, P_s can be associated with a photon count rate N_s . Equation (2.4.3) assumes square apertures and that $R \Delta\theta_{collect} \ll R \sin(\theta_{lab,\lambda_j})$. $T(\lambda_j)$ is the interference filter transmittance function that was measured independently using a spectrophotometer (Cary 5E) and η_D is the quantum efficiency of the detector, taken from manufacturer specifications to be 0.65. The lens was AR coated such that the transmittance was > 0.995 , and therefore the associated loss was ignored. η represents other undetermined losses in the system that may reduce the overall collection efficiency.

2. Hong-Ou-Mandel interferometer design & build

η and d_{eff} are the only non-directly determined quantities. The product $\sqrt{\eta} d_{eff}$ for a given set of experimental parameters may be determined using a numerical approach whereby equation (2.4.3) is evaluated for a range of $\sqrt{\eta} d_{eff}$, the solution value of $\sqrt{\eta} d_{eff}$ corresponds to when the calculated N_s equals the measured count rate associated with the experimental parameters of the calculation.

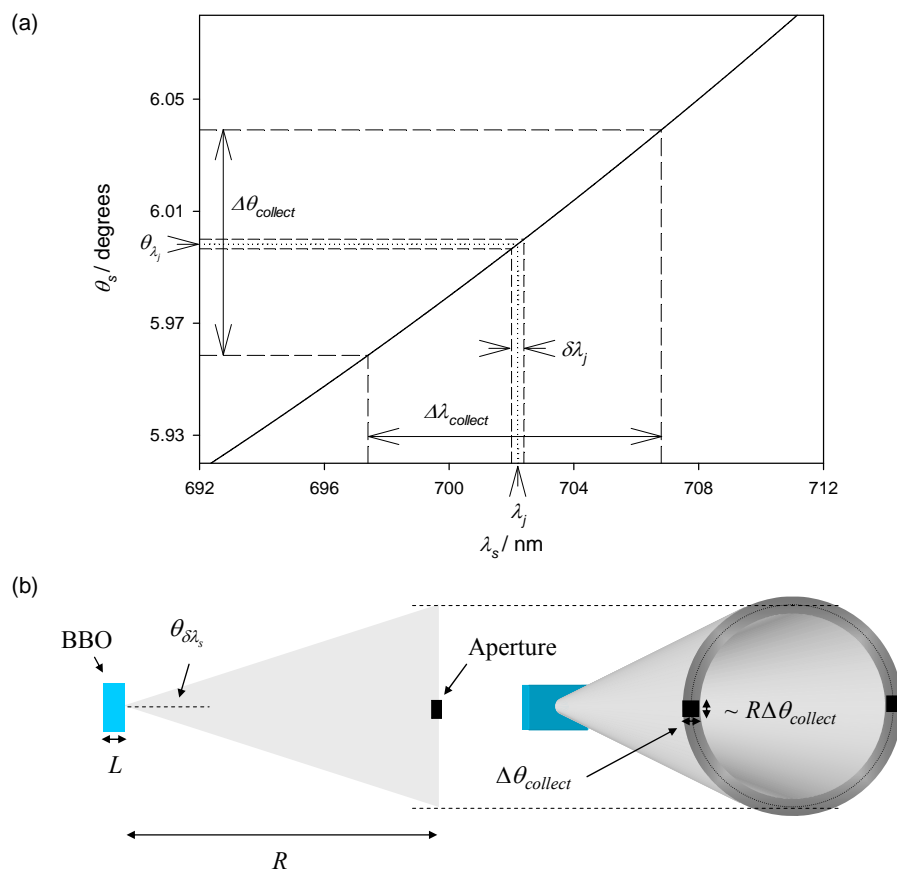


Figure 2-7 (a) Plot of laboratory emission angle versus wavelength in BBO ($\phi_{pm} = 35^\circ$) with 351.1 nm pump. $\Delta\theta_{collect}$ defines the range of λ_j used for the calculation of singles count rates using equation (2.4.3) (b) Side and 3D projection of the geometry of downconversion collection through square apertures. R is the crystal centre to aperture separation.

Figure 2-8 plots the measured singles count rate at the detector for various $\Delta\theta_{collect}$ that were defined by a calibrated aperture. The plotted values include a correction to the measured counts rates $N_{s,measured}$, due to the experimentally measured detector dark count rates $N_{DC,measured}$, and a correction due to detector dead time τ_d :

2. Hong-Ou-Mandel interferometer design & build

$$N_{s,corrected} = \frac{N_{s,measured}}{1 - (\tau_d N_{s,measured})} - N_{DC,measured} \quad (2.4.4)$$

By examination of the phase matching curve in Figure 2-7 (a), it was determined that for all collection angles represented by the data in Figure 2-8 the spectral bandwidth was filter limited, and therefore the contribution to N_s due to photons collected from the horizontal plane should remain constant with $\Delta\theta_{collect}$. Therefore the linear increase in N_s up to $\Delta\theta_{collect} \sim 8$ mrad must either be associated (i) the increasing vertical dimension of the aperture, allowing photons within the same spectral band but with different ϕ (azimuthal angle about pump) to pass, and/or (ii) due to an increase in proportion of the crystal length over which parametric photons are collected as $\Delta\theta_{collect}$ increases.

The first option would be consistent with the $\Delta\theta_{collect}$ term in equation (2.4.3). The second option implies some change in the loss factor η with $\Delta\theta_{collect}$, therefore $\sqrt{\eta} d_{eff}$ would also change since d_{eff} is a constant. The approximately constant solution value for $\sqrt{\eta} d_{eff}$ upto $\Delta\theta_{collect} \sim 8$ mrad suggests that there is no change with $\Delta\theta_{collect}$ of the crystal depth from which downconverted photons are collected, and η can be assumed constant. This is further justified by realising from geometry that the length along the pump beam within the crystal that is viewed by the detector is approximated by $L_{collect}$:

$$L_{collect} = R\Delta\theta_{collect} / \left[\tan(\theta_{\lambda_j}) \cos(\theta_{lab,\lambda_j}) \right] \quad (2.4.5)$$

θ_{λ_j} is the crystal emission angle corresponding to θ_{lab,λ_j} ; taking $\Delta\theta_{collect} = 1.4$ mrad (the smallest collection angle used) with the crystal and laboratory emission angles at 702.2 nm, $L_{collect} \sim 16.2$ mm which is much greater than the crystal length. Therefore the increase in N_s with $\Delta\theta_{collect}$ is likely the cause of explanation (i).

It is also informative to look at the spot size formed by the collected beam at the detector surface w_D ; by assuming $R \gg R\Delta\theta_{collect}$ w_D can be approximated by $\sim f/R \times R\Delta\theta_{collect}$, where f is the focal length of the detector mounted lenses. For $\Delta\theta_{collect} = 1.4$ mrad, $w_D \sim 40$ μm which is considerably smaller than the 175 μm diameter active area of the detector.

2. Hong-Ou-Mandel interferometer design & build

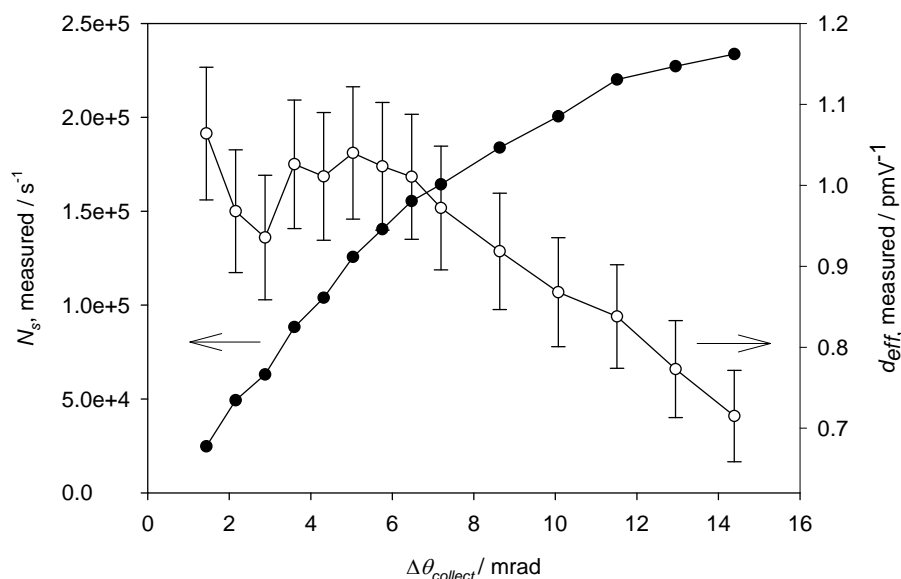


Figure 2-8 The filled circles show the measured singles counting rate for various aperture sizes in the downconversion beam path. The unfilled circles show the d_{eff} values calculated by matching the measured count rates with those calculated through equation (2.4.3). The quantity is actually the product $\sqrt{\eta} d_{\text{eff}}$ and it has been assumed that $\eta \rightarrow 1$ for all $\Delta\theta_{\text{collect}}$. The pump power was 21 mW.

The measured non-linear coefficient begins to drop away when the collection angle grows beyond 8 mrad where the spot size at the detector is estimated to be $\sim 190 \mu\text{m}$. Note that for the largest collection angle at which measurements were made $R\Delta\theta_{\text{collect}} \sim 0.07 \times R\sin(\theta_{\text{lab},\lambda_j})$ and therefore the assumption $R\Delta\theta_{\text{collect}} \ll R\sin(\theta_{\text{lab},\lambda_j})$ required for equation (2.4.3) still holds.

Considering the seven data points corresponding to the smallest aperture radii in Figure 2-1 gives an estimate for d_{eff} of $1.03 \pm 0.04 \text{ pm/V}$. This is slightly less than the value of 1.26 pm/V found in the literature [42], and the difference could be due to some unaccounted for loss factor in the experiment such as imperfect optical alignment, or due to some minor damage to the non-linear crystal that had occurred over time. Note that the exact value for η_D was not known, the value taken was an ‘optimistic’ estimate given by the typical peak value at 650 nm. If the actual quantum efficiency of the detector was lower, then the determined d_{eff} would have been higher.

2. Hong-Ou-Mandel interferometer design & build

2.5 Coincident photon detection

The setup required for measuring the coincident arrival of photons from the downconversion process described in section 2.3.1 is shown in Figure 2-9.

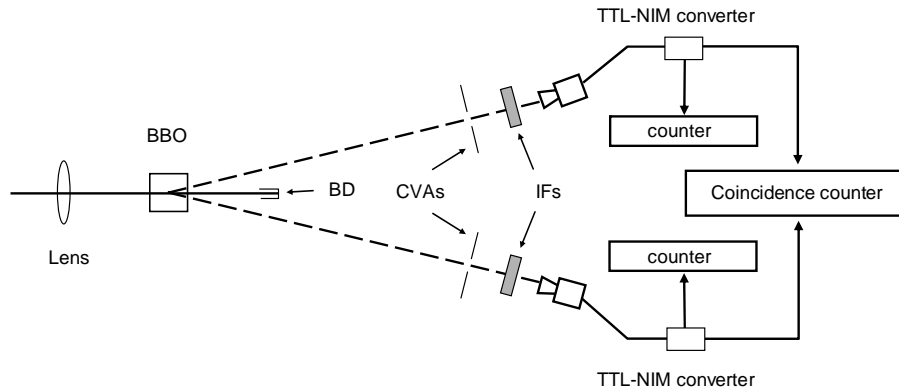


Figure 2-9 Setup for measuring coincident arrival of BBO generated pair photons at two detectors. BD stands for beam dump, CVAs; calibrated variable apertures and IF; interference filters.

The output pulse from each detector is split between the single event counter and one of two ports on a coincidence counter (EG&G model 9308). The coincidence counter distinguishes between the two detectors; one detector is designated ‘start’ and the second ‘stop’. The coincidence counter is unable to directly record a coincidence event due to the simultaneous arrival of pulses because it is rendered inactive during a ‘dead-time’ of ~ 50 ns after receiving one pulse. Therefore the ‘stop’ pulse is delayed relative to the ‘start’ pulse by 60 ns using a coaxial delay line. A coincidence is logged provided the ‘stop’ pulse is received within an 80 ns window after receiving the ‘start’ pulse. After the ‘stop’ pulse is received, or the expiration of the 80 ns time window, the coincident counter is readied to receive a ‘start’ pulse again. Depending on the exact time separation between when the counter receives the ‘start’ and ‘stop’ pulses, the coincidence event is assigned to one of 65536 time bins of equal size, in this way a histogram of coincidence events with time delay is built up for a set of start events, see Figure 2-10.

The coincidence histogram consists of a peak that occurs when the start and stop pulses are associated with correlated photons pairs, and this peak is superimposed upon an underlying level of ‘accidental’ coincidences. The accidental coincidences occur when one or both of the start and stop pulses are due to dark counts from the detectors, stray light, downconverted

2. Hong-Ou-Mandel interferometer design & build

photons created into different pairs, and secondary pulses from earlier detection events [47]. The number of accidentals was estimated by calculating the average bin population outside the coincidence peak (between 60-70ns and 80-140 ns), and then multiplying this figure by the total number of bins. The accidental-corrected coincidence measurement was the total number of coincidences in the histogram minus the estimated number of accidentals. Typically the estimated accidental coincidence events accounted for $\sim 1\%$ of the total number of measured events.

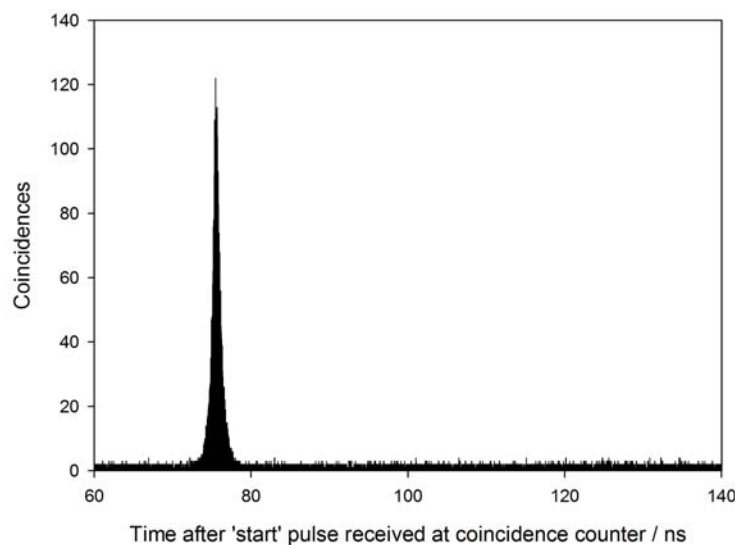


Figure 2-10 Coincidence histogram of photon arrivals from the system in Figure 2-9. The data was collected over one minute.

Maximisation of the singles count rates at the two detectors does not always correspond to a maximum in the coincidence counting rate. In order to maximize the coincidence counting rate, the two detectors are placed to collect photons from regions of the downconversion cone that are diametrically opposed and equally distant from the cone centre (since the required photons are degenerate). In practice this is achieved by positioning one detector for the optimum singles count rate and then making small positional adjustments of the second detector in order to optimise the coincidence counting rate while maintaining the overall single count rate at that detector. However even with perfect detector positioning, the efficiency at which photon pairs are detected is still less than unity, i.e. the observed singles count rate at the two detectors is greater than the observed coincidence counting rate. The pair detection efficiency is defined as:

$$\eta_{12} = \frac{R_{12}}{\sqrt{R_1 R_2}} \quad (2.5.1)$$

2. Hong-Ou-Mandel interferometer design & build

Where R_1 and R_2 are the dark count corrected single photon counting rates at detectors 1 and 2 respectively and R_{12} represent the accidental corrected coincidence rate between the two detectors.

For a Gaussian pump beam of radius w close to the detection plane and finite circular detector apertures of radius a , the pair detection efficiency may be shown to be given by [48]:

$$\eta_{12}(a) = \frac{B}{1 + \frac{w^2}{2a^2}} \left[1 - \frac{\sqrt{\pi} \operatorname{erf} \left(\sqrt{1 + \frac{2a^2}{w^2}} \right)}{2\sqrt{1 + \frac{2a^2}{w^2}}} \right] \quad (2.5.2)$$

Equation (2.5.2) shows that as $a \rightarrow 0$, $\eta_{12}(a) \rightarrow 0$. This is because those photons occupying a cross sectional area A_1 in one optical path between the crystal and detector have correlations with photons in the second path that occupy a cross sectional area $A_2 > A_1$, even though A_1 and A_2 may be equally distant from the point of generation. When the apertures are large, it is possible to collect all of the generated photons, and η_{12} is dominated by the constant B_η :

$$\eta_{12}(a)_{a \rightarrow \infty} = B_\eta = \sqrt{\eta_{start} \eta_{stop} \eta_{filter1} \eta_{filter2} \eta_{lens1} \eta_{lens2}} \quad (2.5.3)$$

Where η_{start} and η_{stop} are the quantum efficiencies of the start and stop detectors respectively, while $\eta_{filter1}$ (η_{lens1}) and $\eta_{filter2}$ (η_{lens2}) are the transmittances of the spectral filter (focussing lens) in front of the start and stop detectors respectively.

Significantly, equation (2.5.2) indicates that for fixed collection apertures η_{12} can be maximized by minimising w , i.e. by focusing of the pump beam to a waist at the detection plane.

For the system in Figure 2-9, (minus the lens before the BBO crystal) η_{12} was studied by mounting variable diameter calibrated apertures to the detectors, and then measuring R_1 , R_2 and R_{12} for various aperture radii while keeping the aperture radius in the two channels equal,

2. Hong-Ou-Mandel interferometer design & build

for these data there was no focussing of the pump beam. The measurements were then repeated after positioning a 1 m focal length converging lens before the crystal such that the optical path along the pump beam from the lens to the crystal in addition to the downconversion path from the crystal to the detector was ~ 1 m. As a result of the focusing the pump beam was focussed to a $656 \mu\text{m}$ diameter waist at the detection plane. A non-linear least squares fitting routine was used to fit expression (2.5.2) to the η_{12} measurements as a function of a , where A and w were the fitting parameters. The data and associated fits are shown in Figure 2-11.

It is clear from the data in Figure 2-11 that the deleterious effect on η_{12} of small aperture radii is reduced when the pump beam was focussed. This is because the focussed pump beam results in a focussing down of the correlation area A_2 occupied by photons in one optical path that are correlated to those photons occupying an area A_1 in the other optical path [49].

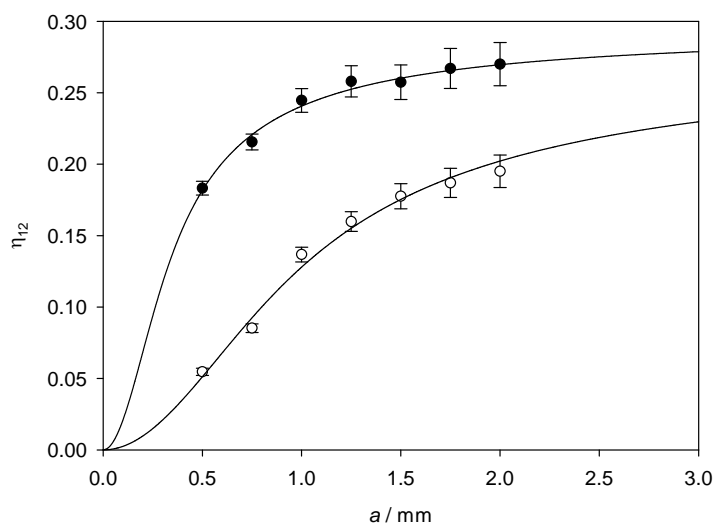


Figure 2-11 Measurements of the pair collection efficiency. The unfilled circles denote data where the pump beam was unfocussed whereas the filled circles describe data where the pump has been focussed as described in the text. The solid lines are fit to expression (2.5.2)

The system losses were estimated in order to determine value of B_η from equation (2.5.3). Using the phasematching arguments outlined in section 2.4.2 that relate an aperture-defined collection angle with the spectral bandwidth associated with the collected photons, it was determined that the bandwidth of the collected photons was filter limited. Therefore $\eta_{filter1}$ and $\eta_{filter2}$ were estimated by the average measured filter transmission across the entire 3 nm bandwidth (0.441 for both). η_{start} and η_{stop} were taken to be the typical peak values of the

2. *Hong-Ou-Mandel interferometer design & build*

detector spectral response curve as quoted by the manufacture (0.65). Since the lenses coupling the photons onto the detector were AR coated at 700 nm, $\eta_{lens1}, \eta_{lens2} \rightarrow 1$. Combining the estimated efficiencies through equation (2.5.3) gives $\eta_{12}(a)_{a \rightarrow \infty} = B_{\eta} = 0.284 \pm 0.031$. This value is in good agreement with the value $B_{no\ lens} = 0.280 \pm 0.013$ determined from the fit to the ‘no lens’ data in Figure 2-11, and also the value $B_{lens} = 0.296 \pm 0.009$ resulting from the fit to the ‘with lens’ data. The uncertainty on B_{η} was dominated by the estimated 0.05 uncertainty estimation on η_{start} and η_{stop} . The uncertainty on $B_{no\ lens}$ was greater than the uncertainty on B_{lens} because the ‘with lens’ data available to the fitting procedure covered a greater proportion of the slope than for the ‘without lens’ data.

From the least-squares fit procedure to the data in Figure 2-11, the values for w under non-focussed and focussed pump conditions were $751 \pm 33 \mu\text{m}$ and $258 \pm 19 \mu\text{m}$ respectively. This made reasonable correspondence with the directly measured pump beam radii near the detection plane ($844 \mu\text{m}$ and $328 \mu\text{m}$ without and with the lens respectively.)

2.6 *Alignment and path balancing of the HOM interferometer paths*

2.6.1 *The HOM interferometer layout and HOM interferogram measurement*

The basic HOM interferometer configuration is shown in Figure 2-12. The pump beam, downconversion medium, single photon and coincidence counting setups are those described in previous sections. The measurement of interest is the coincidence counting rate between the two detectors as a function of τ . Since HOM interference corresponds to when the photon pairs always emerge from recombiner (BS) through the same output, the interference feature is marked by a drop in the measured coincidence counting rate. The extent or visibility of the HOM interferogram is defined as:

$$V_{HOM} = \frac{N_{c,classical} - N_{c,min}}{N_{c,classical}} \quad (2.6.1)$$

2. Hong-Ou-Mandel interferometer design & build

Where $N_{c,classical}$ is the measured coincidence counting rate in the absence of HOM interference and $N_{c,min}$ is the minimum in the measured coincidence counting rate due to the HOM interference. In order to observe HOM interference the photon pairs must have some level of indistinguishability; this is discussed further in the following section.

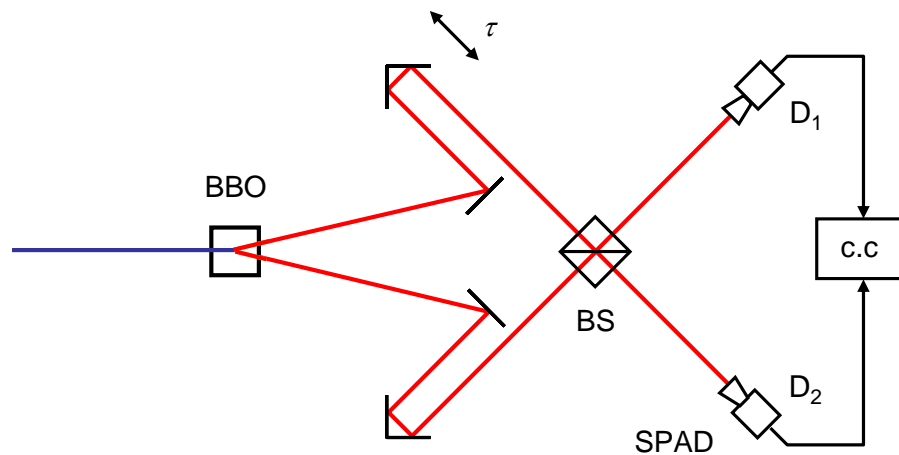


Figure 2-12 Schematic of built HOM interferometer. The blue line shows the pump beam path and the downconversion is shown by the red lines.

2.6.2 The removal of distinguishing information

HOM interference is an interference effect between the probability amplitudes of different but indistinguishable experimental outcomes as opposed to direct interference between the photon wavepackets at the beam splitter. This implies that under certain experimental conditions quantum interference could be observed in a HOM-like interferometer without the photons ever meeting at the recombiner [22].

For a ‘normal’ HOM interferometer, it transpires that in order for the indistinguishability requirement to be met for quantum interference, the photon wavepackets must arrive at the recombiner at the same point in space and time. This can be shown through Feynman-like diagrams shown in Figure 2-13. Each diagram is a representation of a probability amplitude associated with the HOM interferometer and corresponds to a coincidence detection event involving two indistinguishable photons A and B, i.e. when A and B are either both reflected (RR) or both transmitted (TT) at the recombiner. (a) and (b) in Figure 2-13 are two coincidence probability amplitudes that can occur when photon A and photon B arrive at the beam splitter at the same point in time and overlap spatially [(c) and (d) in Figure 2-1]; both

2. *Hong-Ou-Mandel interferometer design & build*

amplitudes lead to detectors D_1 and D_2 triggering with the same relative time separation (in Figure 2-13 (a)-(b) this time separation is shown to be zero). Therefore the two probability amplitudes described by (a) and (b) are spatially and temporally indistinguishable and will quantum-interfere provided they have no other property (e.g. wavelength, polarisation) that makes them distinguishable. (c) and (d) represent two coincidence probability amplitudes that occur when the photons paths overlap spatially at the beam splitter but due to a delay imposed on photon A, photon A arrives at the beam splitter after photon B; in this situation D_1 or D_2 is triggered first according to whether the two photons have been reflected (c) or transmitted (d) respectively. Therefore although spatially distinguishable, the amplitudes (c) and (d) are temporally distinguishable and will not quantum-interfere. It is also possible to imagine a configuration where the two photons travel the same optical distance from the source to the beam splitter but intersect the beam splitter at different points in space. Both the RR and TT amplitudes representing this situation are shown in (e); the two detectors fire at the same instant for both amplitudes and are therefore temporally indistinguishable, but the amplitudes are spatially distinguishable and therefore do not quantum-interfere. Poor path alignment and temporal control of the photons will result in an increased presence of (c)-, (d)- and (e)-like amplitudes in the output state of the interferometer, together with amplitudes where photons A and B are neither spatially nor temporally superimposed at the beam splitter. An output state consisting of such amplitudes is associated with poor quantum interference visibility, while high visibility interference is associated with an output state consisting of (a)- and (b)-like amplitudes only, occurring when optical alignment and temporal control is good. The above arguments illustrate the importance of robust procedures for beam overlap and optical path balancing in the Hong-Ou-Mandel interferometer build.

2. Hong-Ou-Mandel interferometer design & build

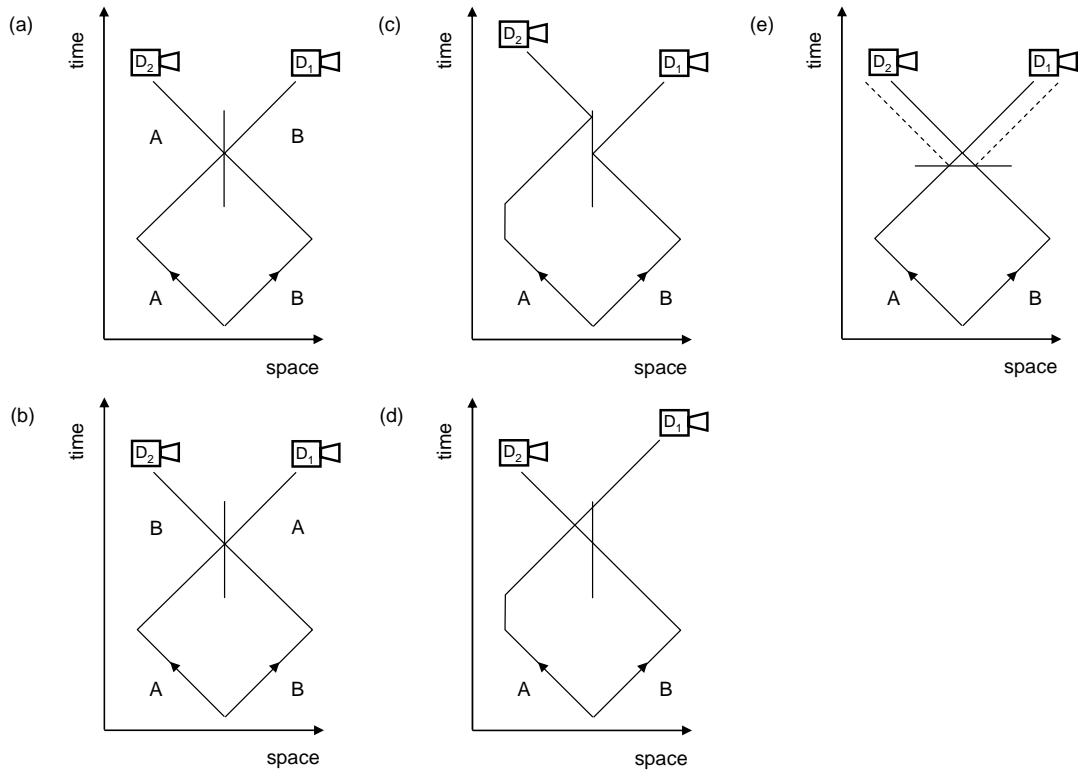


Figure 2-13 Feynman diagrams illustrating the coincidence probability amplitudes for (a)-(b) a well aligned and optical path-balanced interferometer, (c)-(d) a well aligned but optical path-imbalanced interferometer, (e) Two amplitudes corresponding to a misaligned but optical path-balanced interferometer. The 'twice reflected' amplitude is given shown by broken lines, the 'twice transmitted' amplitude given shown by solid lines.

2.6.3 Alignment of the optical paths through two-beam laser interference

The low-flux and broadband nature of the downconverted photons makes them unsuitable for direct use in a second order interference alignment procedure. Alignment was aided by merging the framework of the HOM interferometer with a Mach-Zehnder interferometer illuminated by a 633 nm helium-neon (HeNe) laser, see Figure 2-14. The required non-collinear amplitude-split alignment laser beams to match the downconversion beam paths were provided by passing the HeNe laser beam through a beam splitter BS_1 positioned in place of the non-linear crystal, and oriented such that the beam enters the cube at an angle to the surface normal.

A key feature of the method is that aperture pairs A_1 and A_2 (500 μm diameter) were positioned for collection of the 702.2 nm downconversion and define the trajectories in both the HOM and Mach-Zehnder interferometers. When the downconversion crystal and single photon counters were arranged such that the singles and coincidence counting rates were

2. Hong-Ou-Mandel interferometer design & build

maximized (see Figure 2-9) each of the four apertures were positioned in-turn while maintaining the singles and coincidence counting rate as far as possible.

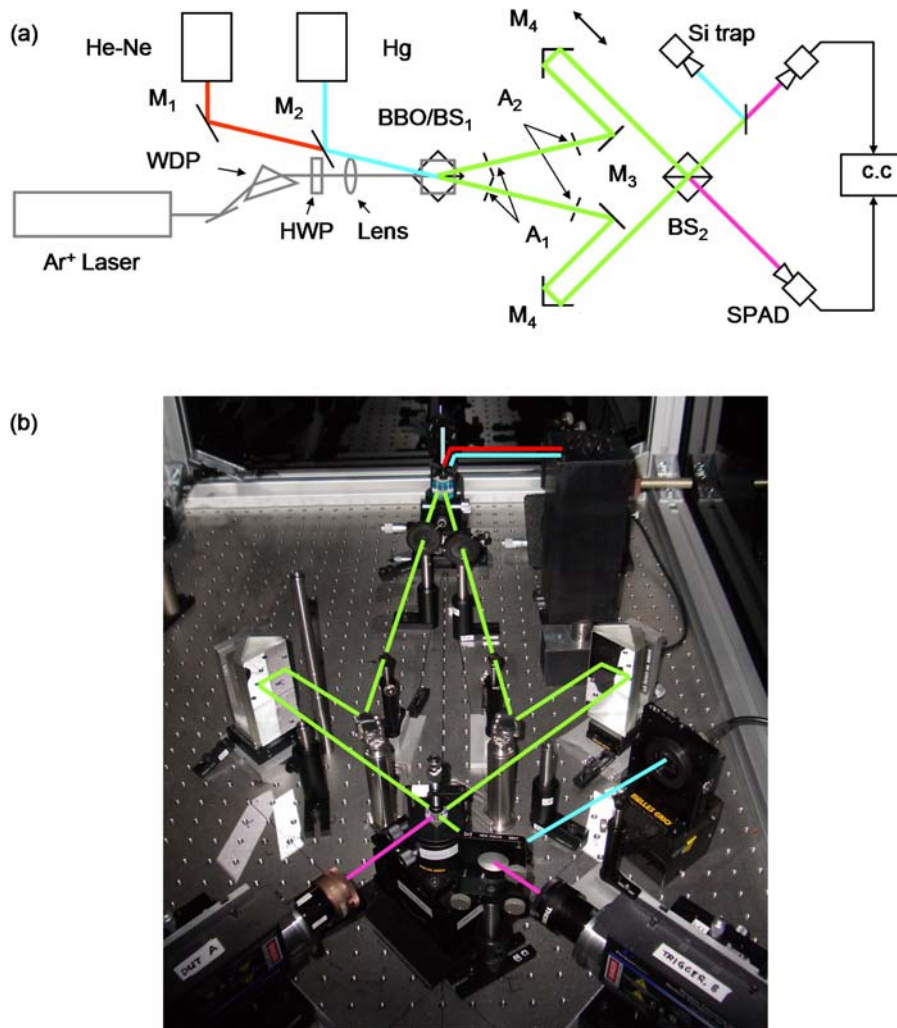


Figure 2-14 (a) Schematic of alignment/balancing interferometer and HOM interferometer. The flip mirror M_2 , switches between HeNe and Hg illumination of the Mach-Zehnder interferometer. The deflecting mirrors M_3 and roof mirrors M_4 precede the beam splitter BS_2 . The coincidence counter (c.c) records the coincident detection events between the SPADs. The optical paths in (a) are drawn with the same colour scheme applied to the photo of the setup in (b).

The alignment procedure then proceeded with BS_1 in place of the non-linear crystal. In order for the laser light to be guided through the HOM apertures thus ensuring overlap of the downconversion with the laser beams in the near and far field, rotation of BS_1 in the plane of the optical bench was necessary in addition to translation of BS_1 perpendicular to the reflecting surface and also directional control of the beam through tilting of M_1 . The beam steering mirrors M_3 , roof mirrors M_4 and beam splitter BS_2 were positioned with the aid of

2. Hong-Ou-Mandel interferometer design & build

the alignment laser beam. The tilt of M_3 and BS_2 were adjusted such that a single interference fringe was observed by eye on a viewing screen at one output port of BS_2 .

One optical path of the interferometer could be scanned through the movement of the roof mirror M_4 , which was mounted on a piezo translation stage (Physik Instrumente P-625.1). The interference fringes obtained by temporally scanning the interferometer, shown in Figure 2-15, were measured using a silicon trap detector [50]. The uniformity and smoothness of the measured fringes were indicative of good mechanical properties of both the optical delay mechanism and beam steering optics.

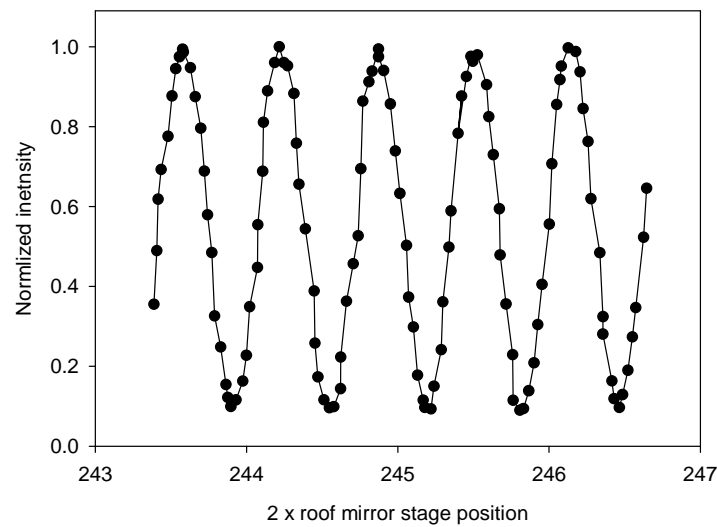


Figure 2-15 Interference fringes measured when illuminating the interferometer framework with a 633 nm He-Ne alignment laser, and then scanning one optical path.

2.6.4 Balancing of the interferometer optical paths using 2-beam interference of a short coherence length source

At the stage where high visibility laser interference fringes could be measured, the interferometer was aligned, but since the laser coherence length was long, the optical paths were unlikely to be balanced. Due to the low count rates involved, replacing the laser / BS_1 combination with the downconverter and attempting to find the coincidence counting interference feature by scanning the optical path over a distance that would cover the uncertainty in the mirror position corresponding to the ‘zero-path difference’ condition, would be time-consuming.

2. *Hong-Ou-Mandel interferometer design & build*

The paths of the interferometer were instead balanced by retaining the Mach-Zehnder framework and exchanging the laser for a spectrally broad emitter (a 100 W high-pressure Hg lamp) by use of a flip-mirror M_2 , Figure 2-14. The light was focussed through a 50 μm pinhole to ensure good spatial coherence of the beam and then collimated. Interference was only observable at the output port of the recombining beam splitter when the optical paths of the interferometer were balanced to within $\sim 30 \mu\text{m}$. The balancing was achieved through manual adjustment of the roof mirror such that strongly modulated fringes were observed by eye on a viewing screen.

The profile of the Hg interferogram measured upon scanning the interferometer is shown in Figure 2-16 (a), together with the Fourier transform of the interferogram and the emission spectra of the lamp measured using a SAD portable spectrophotometer. The main peak in the Fourier transform corresponds well to the 577 nm Hg doublet, and the shorter wavelength secondary peak corresponds well to the 546 nm Hg emission line. The line at 546 nm is more intense than the line at 577 nm in the directly measured spectrum whereas in the interferogram Fourier transform the opposite is true; this is because the reflectivity of the interferometer mirrors fall off rapidly in going from 577 nm to 546 nm.

Another useful feature of the Hg source was that although the emission lines of Hg do not coincide with the SPAD pass bands, there was sufficient optical noise at the filter wavelengths for a singles count of $\sim 10^6 \text{ s}^{-1}$ at the SPADs, the bright signal therefore aided the repositioning of the detectors from their locations in Figure 2-9 to those shown in Figure 2-14.

To complete the alignment process, the non-linear crystal was repositioned in place of BS_1 and the pump applied. The phase match angle was fine-tuned for maximum counts at the SPADs.

2. Hong-Ou-Mandel interferometer design & build

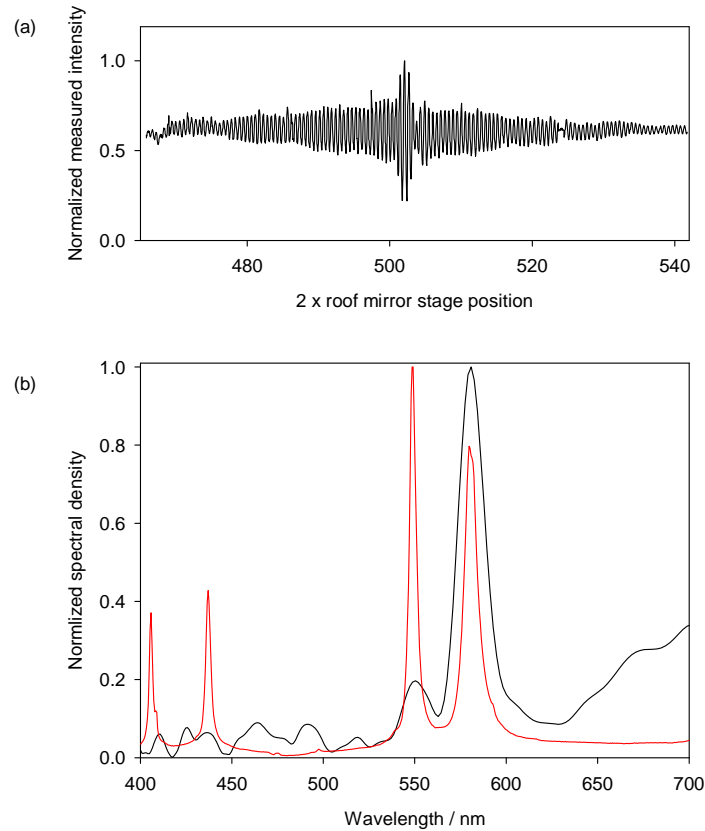


Figure 2-16 (a) Interference fringes measured when illuminating the interferometer framework with a Hg lamp, and then scanning one optical path about the point where it is equal to the other path. The black trace in (b) is the Fourier transform of the interferogram in (a) and the red line is the measured emission spectrum from the lamp.

2.6.5 Comparison of the alignment technique with a published alternative

The observed two-photon interference visibilities are comparable to those measured in recent experiments of similar design [23, 51]. Averaged over five separate builds, the centres of the Hg and Hong-Ou-Mandel interference features differ by $11.7 \mu\text{m}$, which compares favourably to the $61 \mu\text{m}$ reported in ref. [52], where a contrasting method for path alignment and balancing was implemented. Although that procedure also made use of long and short coherence length sources for the alignment and balancing respectively, that technique required a custom grating to produce non-collinear alignment beams from an initial input; alignment of the first-order diffracted beams with the downconverted field in the near field was achieved through an estimation of the necessary grating position through calculation, while far-field overlap was achieved by examination with a low-light detector array.

2. *Hong-Ou-Mandel interferometer design & build*

Here, pairs of apertures in each arm of the interferometer ensure that the alignment beams align with the downconverted fields. The use of a beamsplitter to split the alignment beam ensures that all of the source light is used, facilitating a fully visual alignment procedure without need for an expensive detector array, or the positioning of components based upon calculation.

Closer inspection of the optical paths obtained when using the method described here shows that the alignment beams do not overlap with the downconverted beams back to the point of their creation, instead the alignment beams emerge at a greater angle with respect to the pump beam direction, and refraction at the glass-air surface of the beam splitter parallelizes and overlaps them with the downconverted beams. Figure 2-17(a) shows that the two alignment beams share the same path symmetry about the pump as the downconverted fields, meaning that the path deviation of the alignment beams from the downconverted fields does not have a deleterious effect on the balancing procedure. Note that if the cube beam splitter was replaced with a plate beam splitter, the shared symmetry would be lost and an error would occur in the found balanced state of the downconversion HOM interferometer.

The method described previously in the literature [52] will only work for one downconversion emission angle, pre-determined by the grating characteristic and the wavelength of the alignment laser. The method described here may be applied to the construction of an interferometer where the parametric photons have arbitrary crystal emission angles. For smaller emission angles, the input trajectory of the alignment laser should be set at a smaller angle with respect to the beam splitting surface, and the split alignment beams will emerge from the cube closer to the forward edge. If the angle becomes very small so as to limit the aperture of the output beams, then the beamsplitter should be moved along the pump propagation direction. Figure 2-17(b) shows a suitable scheme for the HOM interferometer of ref. [52] where the crystal and lab downconversion emission angles were 0.66° and 1.0° respectively.

For larger emission angles, the beam splitter should be moved backwards relative to the pump propagation direction and when the parametric photons are emitted at 90° relative to one another, the splitting of the alignment beam should coincide exactly with the centre of the downconversion crystal. In general, the size of cube required is dictated by the separation of the downconverted beams at the point from which overlap with the alignment beam is required; a larger separation may require a larger beamsplitter. Secondly, a smaller

2. Hong-Ou-Mandel interferometer design & build

downconversion emission angle may require a larger beam splitter due to the shallow angle between the input alignment beam and beam splitting surface.

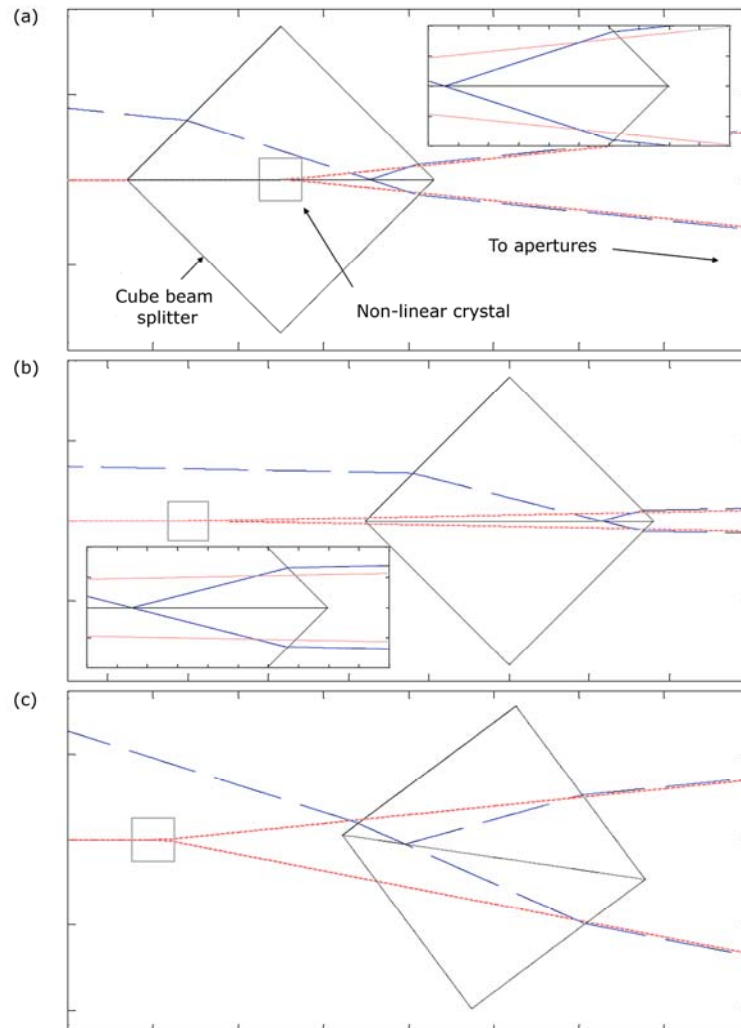


Figure 2-17 How the cube beam-splitter alignment technique may be applied to various experimental schemes; the graduations correspond to 10 mm intervals in the main figure and 1 mm intervals in the insets. The blue lines represent the alignment beams while the red lines represent the paths of the pump and downconverted fields. The downconverted and alignment fields are displaced for clarity, although they overlap. (a) For the experiment of this chapter, the cube beam splitter was positioned in place of the downconverter. (b) For smaller emission angles, or situations where the downconverter cannot be removed for the alignment, the cube beam splitter may be placed a distance in front of the crystal. (c) By changing the tilt of the beam splitter and its position perpendicular to the pump, the alignment beams may be made to overlap with downconverted beams having different angles about the pump beam.

If temporary removal of the crystal for the alignment is difficult for a particular setup, the beam splitter may be moved a distance along the pump direction. In this situation, the split

2. *Hong-Ou-Mandel interferometer design & build*

alignment beams will emerge from the cube further from the front edge and alignment with the downconversion fields will hold from a point slightly further along the optical path, see Figure 2-17(b).

The beamsplitter technique may also prove useful in aligning experiments incorporating non-degenerate photon pairs where the two photons of a pair are emitted at different angles relative to the pump beam. Alignment of the downconverted field with an alignment beam may be achieved through a translation of the beam splitter perpendicular to the pump direction accompanied by a rotation in the plane of the non-linear interaction. Figure 2-17(c) shows a possible alignment solution for the experiment described in ref. [53] where photon pairs are emitted at lab angles of 5.9° and 11° . Although this scheme may be of use for alignment of optics, the shared symmetry about the pump beam of the alignment and downconverted fields observed in Figure 2-17(a)-(b) is lost, and the technique is therefore of less value for path balancing. However a non-degenerate source is unlikely to be used in a HOM type experiment due to the spectral distinguishability between the photons and they will not interfere even if the temporal distinguishability is removed.

2.7 *Interferometer characteristics*

The interferometer collection angle $\Delta\theta_{collect}$ was defined by $2 \times \arctan(d/2s)$ where d is diameter of the second aperture in each interferometer path and s is the distance of the aperture from the BBO crystal centre. $\Delta\theta_{collect}$ was changed by exchanging the aperture for another with different d . The horizontal axis of the collection angle cuts across concentric rings of correlated emission at different wavelengths (see Figure 2-4) where as the vertical axis of the collection angle is at a tangent to the emission rings of particular frequency. (See Figure 2-7) As a result, the features of the HOM interference dip change with $\Delta\theta_{collect}$ and the spectral filtering conditions. The measured effects are discussed in the following sections. Also discussed are other interesting characteristics of the interferometer that have been reported elsewhere in the literature.

2. Hong-Ou-Mandel interferometer design & build

2.7.1 Interference dip bandwidth for different interferometer collection angles and frequency filtration

The bandwidth of the HOM dip interferogram is indicative of the spectral bandwidth of the interfering photons; a wider spectral bandwidth corresponds to a narrower interference feature. (c.f. classical two beam interferometry). Figure 2-18 shows that increasing the collection angle has little effect on the dip bandwidth when 3 nm interference filters were used, suggesting that over the entire range of tested $\Delta\theta_{collect}$ the filters limited the bandwidth of the interfering photons. Confirmation that the emission bandwidth into 1 mrad was > 3 nm was indicated by a halving of the dip FWHM when 12 nm filters were used. For the 12 nm filter system, the data suggested that the interfering photon spectral bandwidth increased up to $\Delta\theta_{collect} \sim 6$ mrad where the HOM dip bandwidth starts to level off, therefore the data indicates that there is a transition from an aperture limited bandwidth $\Delta\lambda_{collect}$ to a filter limited bandwidth through the increasing range of $\Delta\theta_{collect}$.

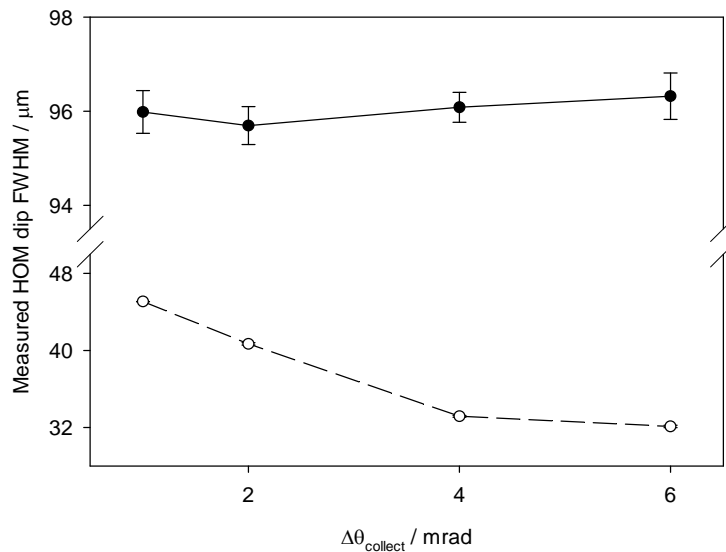


Figure 2-18 Measured HOM dip bandwidth with varying two photon interferometer collection angle. The filled circles joined by a solid line correspond to measurements where 3 nm filters were mounted at the front of the detectors. The unfilled circles joined by broken lines are associated with measurements using 12 nm bandwidth filters

From the phase matching curve in Figure 2-7, it was found that when $\Delta\theta_{collect} = 1$ mrad, $\Delta\lambda_{collect} = 6.2$ nm. This is consistent with the observation that the 3 nm filter limited the bandwidth at this collection angle, and is also consistent the inference that $\Delta\lambda_{collect}$ was less than the bandwidth of the 12 nm spectral filters. From the phase matching curve $\Delta\lambda_{collect}$ is

2. *Hong-Ou-Mandel interferometer design & build*

expected to exceed 12 nm when $\Delta\theta_{collect} = 1.8$ mrad which is a slightly smaller angle than that inferred from the data. The difference was likely to due the calculation of the phase matching curve not accounting for many effects such as focussing of the pump beam etc. In addition the there may be some experimental error due to a tolerance in positioning each $\Delta\theta_{collect}$ defining aperture in the mount.

2.7.2 *Visibility for different interferometer collection angles and frequency filtration*

Figure 2-19 shows that as $\Delta\theta_{collect}$ increases the visibility of the HOM dip decreases, where the visibility is defined by equation (2.6.1). This can be explained in terms of the influence of phasematching over the emission direction. Consider only those photon pairs emitted into the horizontal plane; the degenerate pairs emerge from the crystal at equal and opposite angles of $\pm 5.9^\circ$, pass through the central region of the collection angle and are made to overlap spatially and temporally at the beam splitter using the outlined method and therefore interfere. There are slightly non degenerate pairs that emerge at opposite but unequal angles to one another, such photons have lower spectral overlap with each other, take trajectories that lie towards the limits of the collection angle and have a lower degree of spatial and temporal overlap at the beam splitter, therefore the probability amplitudes associated with such photons will interfere less, reducing the overall measured interference visibility. This effect will be more pronounced with increasing collection angle, as the horizontal component of $\Delta\theta_{collect}$ cuts through the increasingly non-degenerate concentric emission rings.

Similarly, for the emission that occurs above and below the horizontal plane (i.e. along the tangents of the emission rings), in order to maintain phase matching a photon with an upward trajectory must be correlated with a photon with a downward trajectory. Since the interferometer was aligned for optimum overlap of photons in the horizontal plane, photon pairs with increasing trajectories out of the horizontal plane will overlap to a lesser at the HOM recombiner, and the probability amplitudes associated with such trajectories will interfere correspondingly less. As $\Delta\theta_{collect}$ increases photons are collected from larger tangents to the emission rings, and therefore the proportion of collected photons that are suitable for interference decreases.

2. Hong-Ou-Mandel interferometer design & build

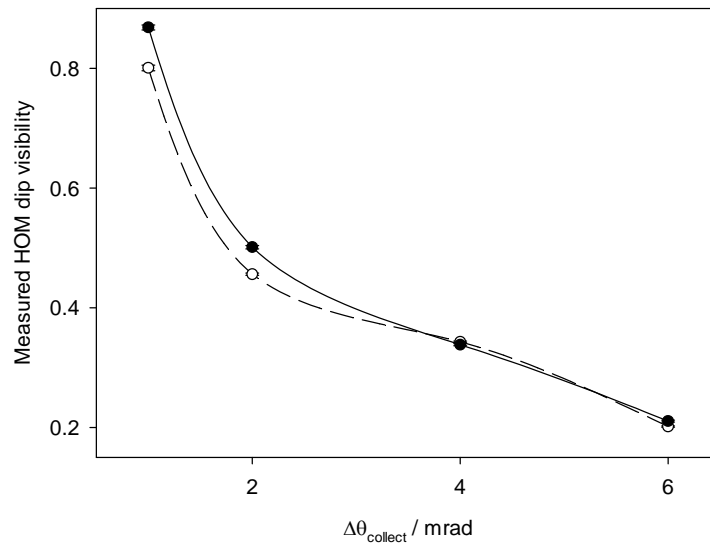


Figure 2-19 Measured HOM dip visibility with varying two photon interferometer collection angle. The filled data points joined by a solid line correspond to measurements where 3 nm (centred at 702.2 nm) filters were mounted on the detectors, while the unfilled data points joined by broken lines are associated with measurements with 12 nm filters (also centred at 702.2 nm).

Figure 2-19 shows that over all collection angles, the interference visibility is lower when using wider bandwidth filters, this is mostly likely due to a greater proportion of non-degenerate photons allowed to pass through the interferometer with the wider band filters. Greater non-degeneracy is associated with non-equal emission angle of the photon pairs, and therefore increasing the spectral bandwidth adds spatial distinguishability to the photons in addition to frequency distinguishability.

2.7.3 Interferometer singles count rate, coincidence counting rate and collection efficiency

Figure 2-20 shows that there was a dramatic increase in both the singles (a) and coincidence (b) counting rates upon increasing the interferometer collection angle.

In section 2.7.1 it was determined that the 3 nm filters limited the photon flux through the interferometer for even the smallest $\Delta\theta_{\text{collect}}$. In addition, equation (2.4.5) indicates that the downconverted photons are collected from the entire length of the crystal for even the smallest $\Delta\theta_{\text{collect}}$. Therefore the increase in single photon and coincidence counting rates with increasing $\Delta\theta_{\text{collect}}$ when 3 nm filters were used must be due to the collection of photons along

2. Hong-Ou-Mandel interferometer design & build

increased tangents to the near degenerate emission rings. This is consistent with the accompanying reduction in the dip visibility (see section 2.7.2).

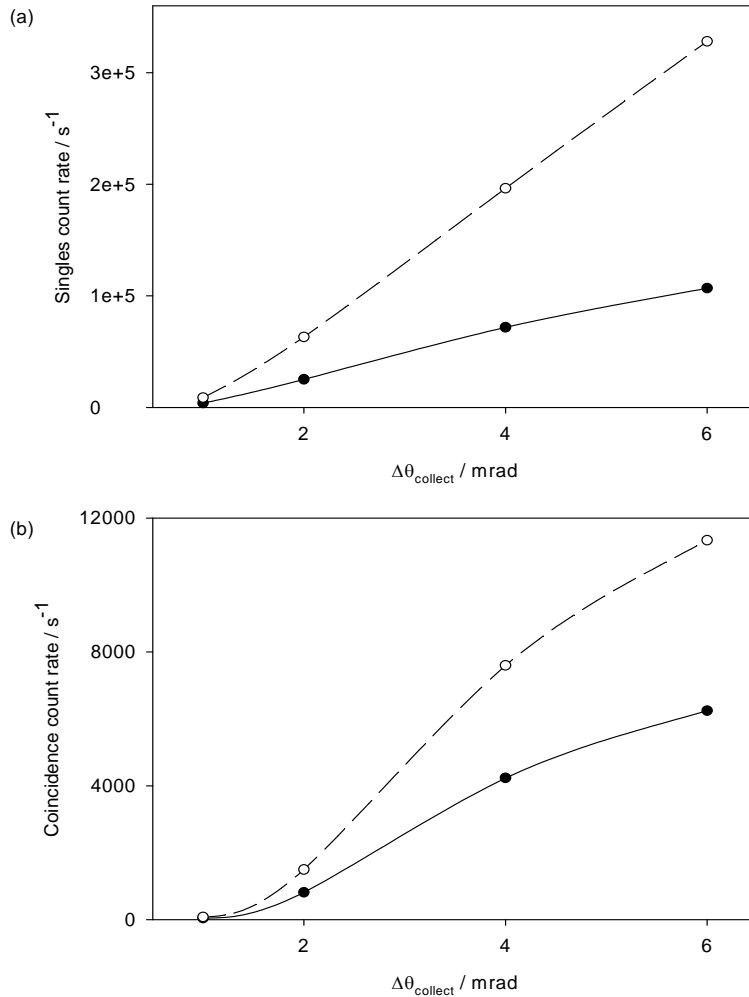


Figure 2-20 Plots of (a) single photon count rate and (b) coincidence counting rates in the two photon interferometer configuration for a range of collection angles defined by apertures in each beam path. The filled data points joined by a solid line correspond to measurements where 3 nm filters were mounted on the detectors. The unfilled data points joined by broken lines are associated with measurements with 12 nm filters.

For the 12 nm system, the bandpass was found to be aperture limited when $\Delta\theta_{\text{collect}} < 4$ mrad, therefore in addition to the increased collection of photons along the tangent to the near-degenerate emission rings, as $\Delta\theta_{\text{collect}}$ is increased to 4 mrad, increasingly non-degenerate photon pairs from other concentric emission rings were also passed to the interferometer. This could explain the factor of ~ 21 increase in the single photon count rate with $\Delta\theta_{\text{collect}}$ from 1 mrad to 6 mrad compared to a factor ~ 18 for the 3 nm filtered system.

2. *Hong-Ou-Mandel interferometer design & build*

In order to obtain a relatively high HOM dip visibility, the majority of the interferograms studied in the following chapter were taken with collection angles ~ 1 mrad. In this configuration the measured collection efficiency η_{12} as defined by equation (2.5.1) was typically around 0.02. Considering the difference between the crystal-aperture distance in the HOM interferometer compared with that associated with the setup for $\eta_{12}(a)$ measurements in section 2.5 (Figure 2-9), the 1 mrad HOM interferometer collection angle was equivalent to an aperture diameter $a \approx 300 \mu\text{m}$ for the measured $\eta_{12}(a)$ data in Figure 2-11. The pump beam for the HOM interferometer had the same focussing condition as for the ‘with-lens’ data in Figure 2-11, therefore taking the fitted curve associated with the ‘with-lens’ data; when $a = 300 \mu\text{m} \rightarrow \eta_{12} = 0.117 \pm 0.015$, which is significantly higher than the measured HOM interferometer collection efficiencies.

The disparity between the predicted and measured η_{12} associated with the HOM interferometer can be partly explained by the additional losses associated with the interferometer setup such as the roof mirror surfaces ($R=0.92$) and the beam steering mirror surfaces ($R = 0.99$). In addition, the recombiner results in half of the coincidences being lost. Inserting the additional losses into equation (2.5.3) gives $B_{HOM} = 0.12 \pm 0.008$. Rescaling the η_{12} axis of the ‘with-lens’ fitted curve in Figure 2-11 by the factor B_{HOM}/B_{η} (B_{η} was estimated in section 2.5), gives an estimate for the $\eta_{12}(a)$ relationship for the HOM interferometer that accounts for the additional losses. The new curve predicts that $B_{HOM} = 0.049 \pm 0.008$ at $a = 300 \mu\text{m}$. The remaining difference between the measured and predicted η_{12} for the HOM interferometer is almost certainly due to the ~ 30 cm reduction in optical path from the pump focussing lens to the collection (aperture) plane that is introduced upon transforming from the setup in Figure 2-9 (where the lens-detector position was optimal) to the two photon interferometer in Figure 2-14 (a), meaning that w was larger at the collection plane of the two photon interferometer. The collection efficiency could therefore be increased using a shorter focal length lens for the pump focussing.

2.7.4 *Observed dip in singles count rate*

The silicon APD detectors are unable to resolve between one incident photon, or two arriving simultaneously, and therefore when two photons arrive simultaneously, one photon of the pair is effectively ‘lost’ from the system when its partner is detected. The proportion of simultaneous photon arrivals at *one* detector is greater within the interference regime as the

2. Hong-Ou-Mandel interferometer design & build

photons emerge from the same output of the beam splitter, and therefore the number of ‘lost’ photons increases, resulting in a dip in the measured singles counting rate.

Using a classical model that ignores correlation effects between the photons, it has been shown that the visibility of the measured coincidence counting rate dip V_c , and the visibility of the single photon counting rate dip at one detector V_s are related by [54]:

$$V_s = V_c \frac{\eta}{(4 - \eta)} \quad (2.7.1)$$

where η is the single photon detection efficiency of the detector concerned.

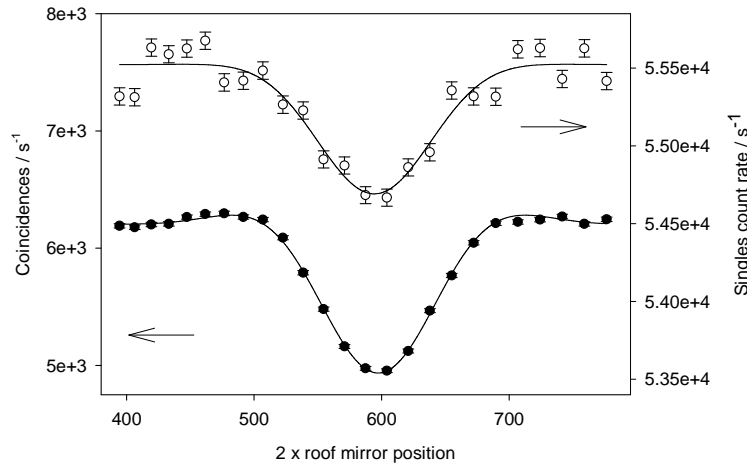


Figure 2-21 The black data points show the coincidence interference feature and the white data points show the associated dip in singles counts at one of the detectors. 3 nm band pass filters were mounted on both detectors. The fitted curves are based on the model described by equation 3.2.4.

Figure 2-21 shows a coincidence interference feature measured on the setup in Figure 2-14 together with the associated dip in the single photon count rate at one of the detectors. In order to maximize the pair collection efficiency and count rates, a large $\Delta\theta_{collect}$ (6 mrad) was set at the expense of coincidence interference visibility. From the fitting procedure $V_c = 0.205 \pm 0.002$ and taking η to be the product of the detector quantum efficiency and the measured average filter transmission (see section 2.5) predicts a value of $V_s = 0.0158$, which is in reasonable agreement with the value of 0.0149 ± 0.006 measured from the fitted curve to the singles count dip data. Note that when small interferometer collection angles were used, the pair collection efficiency was small, and therefore the dip in the single photon count rate was too small to observe.

2. Hong-Ou-Mandel interferometer design & build

2.7.5 Beam attenuation effects on the measured two photon interferograms

In classical two beam interference, the beams are spatially superimposed and the resulting intensity is measured. Attenuation of one beam results in an intensity measurement is that either increased or decreased depending on the relative phase of the beams and a reduced temporal interference visibility results. In HOM interference experiments the elementary measure is not intensity but the rate of coincident arrivals between two detectors. Attenuating one of the beams results in the occasional removal of photons from that beam, and with it the possibility for a coincidence measurement between the associated coincidence pair. It follows that attenuating one beam results in a reduction in the measured coincidence rate for all relative delays of the interferometer arms, but the attenuation does not effect the visibility of the dip.

Figure 2-22 shows two coincidence interferograms, in one interferogram both beams are un-attenuated where as in the second one beam is attenuated by a factor of three. The visibility of the interferogram where there was no beam-attenuation was 0.824 ± 0.014 while the visibility of the beam-attenuated interferogram was 0.791 ± 0.026 . The measured coincidence rate for a given roof mirror position was \sim a factor of three greater in the non beam attenuated interferogram as would be expected.

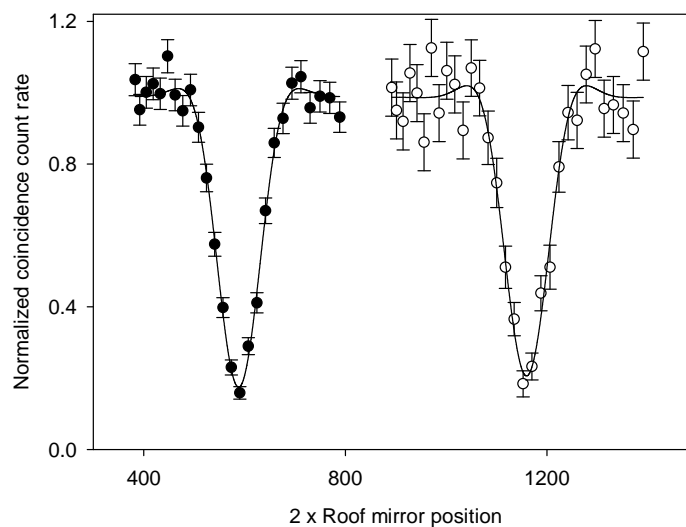


Figure 2-22 Two HOM coincidence interferograms taken under otherwise identical conditions except that for the measurements corresponding to unfilled data points, one of the two interferometer beams was attenuated by a factor of three. The interferograms have been displaced relative to each other along the horizontal axis for clarity.

2.8 *Conclusions*

The design of a Hong-Ou-Mandel interferometer was formulated. A parametric pair downconverter was used as the source. The photons were chosen to be at 702.2 nm because this was near the optimal response of cheap and high performance silicon photon counting technology, and a pump source at 351.1 nm was available. The photon source was chosen to have non-collinear geometry because this precluded the use of an additional beam splitting optic to separate the photons necessary for temporal adjustment of the interferometer paths. Type I phase matching was chosen for the source since no polarising optics were then required for erasing polarisation information that would have destroyed the HOM interference, and type-I interactions are also associated with higher non-linear coefficients and are therefore brighter. BBO was chosen as the source as it is highly transmitting at both the downconversion and UV pump wavelengths in addition to a relatively high non-linear coefficient. It also offers the additional benefits of being mechanically robust and non-hydroscopic.

The single photon counting detection scheme was introduced. Using a photon counting method outlined in the literature, the effective non-linear coefficient of BBO for the interaction was measured to be 1.03 ± 0.04 pm/V, the largest contribution to the uncertainty was associated with the uncertainty estimate of the photon counter detection efficiency.

The two photon coincidence detection scheme was introduced. The two photon collection efficiency of the generated pairs was investigated as a function of the collection aperture radius defining each detector. Using available theory it was found that the pair collection efficiency at low aperture radii could be improved through focussing the pump beam in order to form a waist a distance after the crystal equal to the optical path travelled by the downconversion from the crystal to the detectors.

The importance of good spatial beam alignment and temporal control over the photons in a HOM interferometer was explained. The difficulties in achieving the required alignment and path balancing directly using second order interference of the downconverted light was stated in terms of the low source brightness. A procedure was developed for aligning the interferometer that involved the merging of the HOM framework with that of a Mach-Zehnder interferometer through which visible He-Ne laser radiation was coupled. Alignment was then achieved through optimisation of intensity interference fringes formed by the laser beams at the HOM recombiner. The optical paths of the interferometer were then balanced

2. Hong-Ou-Mandel interferometer design & build

by replacing the He-Ne laser radiation with a bright but spectrally broad Hg lamp. The procedure was found to balance the optical paths to within $\sim 10 \mu\text{m}$ and result in high visibility HOM dip interference fringes. The alignment procedure was contrasted to an existing procedure in the literature.

Interferometer characteristics such as HOM dip visibility, dip FWHM, singles and coincidence counting rate and pair collection efficiencies were investigated as a function of the aperture radii defining the interferometer collection angles for the downconverted light and different spectral filtering conditions. Explanations were given for the observed characteristics. Interesting characteristics observed here and documented elsewhere, such as the persistence of coincidence interference visibility upon attenuating one beam of the interferometer, and the measurement of a dip in the single photon counting rate at the same temporal state of the interferometer as the HOM coincidence dip were documented and explained.

2. *Hong-Ou-Mandel interferometer design & build*

3 Measurement of photon indistinguishability to a quantifiable accuracy

3.1 Introduction

Despite the wide-ranging set of experiments and applications with the HOM scheme at their focus, little attention has been paid to the accuracy aspects to such experiments. Invariably the HOM experiments involve the measurement of the HOM ‘dip’ visibility, but the accuracy of the measurement is rarely given. Measurements have been largely restricted to the research laboratory but with many quantum technologies approaching commercial realization, measurement uncertainty will become more important. Deterministic single photon sources are perhaps the most important example of an emerging technology requiring HOM dip visibility measurements for their characterization [30-36, 55]. The HOM dip visibility carries indistinguishability information relating to the interfering photons and such information is important for determining the suitability of a photon source to quantum optical computation protocols [29]. Quantifying the accuracy of indistinguishability measurements is important to facilitate the comparison of different single photon source technologies and to ensure a source meets required indistinguishability thresholds for a particular protocol [56].

This chapter develops a procedure for using a HOM interferometer to measure photon indistinguishability with an estimated uncertainty. The interferometer source studied was a cw-pumped downconverter emitter of photon pairs, as described in the previous chapter. The design and construction of the interferometer was also presented in the previous chapter. In order to quantify the HOM dip visibility from experimental data, analytical and numerical curve fitting models were investigated, with consideration for corrections and uncertainties on the coincidence rate and optical delay coordinates of the data. A measurement equation is presented which describes how the photon indistinguishability is related to the measured HOM dip visibility. The terms of the equation correspond to experimental variables and these normally conspire to reduce the measured visibility relative to the intrinsic photon indistinguishability. Measurements were made to quantify each term under the experimental conditions of the indistinguishability measurement. The uncertainties associated with the

3. Measurement of photon indistinguishability to a quantifiable accuracy

quantified measurement equation terms were combined to give an overall uncertainty for the indistinguishability measurement. The largest factor relating the dip visibility to the indistinguishability measurement was found to be associated with surface effects of the interferometer, the same factor also contributed the largest uncertainty to the overall indistinguishability measurement. The sub-unity photon indistinguishability measured for the pair downconverter was attributed to the wavelength anti-correlation between the interfering photons and the interferometer acceptance angle being sufficiently large to allow through distinguishable photon trajectories. Changes to the experimental method are proposed with the aim to reduce the indistinguishability measurement uncertainty and the disparity between the measured dip visibility and photon indistinguishability.

Many of the metrology principles and concepts discussed in this chapter are summarized in the ISO Guide to the Expression of Uncertainty of Measurement, known as the GUM [57].

3.2 Quantifying the visibility of the measured interferogram – V_{HOM} – with an associated uncertainty

3.2.1 The HOM dip visibility from the coincidence counting experimental measurements

The experimentally measured two photon interferogram is the photon arrival coincidence rate N_c at the two output ports of the HOM recombiner measured as a function of optical delay between the two paths through the interferometer $\Delta\tau$. The widely accepted definition for the two photon measured HOM dip visibility is given by [58-60]:

$$V_{HOM} = \frac{N_{c,\Delta\tau \gg \tau_c} - N_{c,\Delta\tau=0}}{N_{c,\Delta\tau \gg \tau_c}} \quad (3.2.1)$$

where τ_c is the biphoton coherence time. $N_{c,\Delta\tau \gg \tau_c}$ is the measured coincidence rate far from the interference region and $N_{c,\Delta\tau=0}$ is the measured coincidence rate at the bottom of the dip. Each datapoint in the $N_c(\tau)$ curve will be subject to an uncertainty. The process of photon pair coincidence counting can be well modelled by a Poisson distribution [61], i.e. the coincidences occur randomly in time with a distribution having a mean equal to its variance.

3. Measurement of photon indistinguishability to a quantifiable accuracy

The associated \sqrt{N} Poisson noise was the dominant uncertainty in the measurements of N_c , and was typically equal to $\sim 2\%$ of the number of coincidences recorded for each data point. A correction was also made for accidental coincidences (see section 3.5) which has its own uncertainty. Although the correction algorithm accurately removes the accidental coincidences from outside the main peak in the coincidence histogram, the algorithm makes an estimate of the number of accidentals within the peak and may therefore erroneously remove genuine coincidences or leave some accidental coincidences behind. In a typical measurement, the estimated accidental coincidences accounted for only $\sim 1\%$ the total number of coincidences, and since the peak width was small (5 ns) compared to the entire range over which the correction was applied (80 ns), the uncertainty due to this correction was ignored.

In practice the HOM interferogram many take many minutes to measure, meaning fluctuations in the pump power may become significant. Therefore a further correction was made to each point of the $N_c(\tau)$ dataset in order to account for the resulting fluctuation in the singles count rate. Equation (2.5.1) shows that for a given pair collection efficiency the coincidence rate is proportional to the square rooted product of the single photon count rates at the two detectors. Therefore the corrected value of the datapoint $N_{c,measured}$ is given by:

$$N_{c,corrected} = \frac{\left\{ \sqrt{N_{s1}N_{s2}} \right\}_\mu}{\sqrt{N_{s1}N_{s2}}} \times N_{c,measured} \quad (3.2.2)$$

where N_{s1} and N_{s2} are the dark count corrected single photon count rates measured at detectors one and two respectively. The numerator is the mean value of $\sqrt{N_{s1}N_{s2}}$ across all data points of the interferogram. The denominator concerns the single photon count rates associated with a specific $N_{c,measured}$. Typically the corrections to each point were within the range $\pm 2\%$. The uncertainty on the corrected data point value was given by:

$$u_{correction_{N_s}} = N_{c,corrected} \times \sqrt{\left(\frac{\left\{ \sqrt{N_{s1}N_{s2}} \right\}_\sigma}{\left\{ \sqrt{N_{s1}N_{s2}} \right\}_\mu} \right)^2 + \left(\frac{u_{\sqrt{N_{s1}N_{s2}}}}{\sqrt{N_{s1}N_{s2}}} \right)^2 + \left(\frac{u_{N_{c,measured}}}{N_{c,measured}} \right)^2} \quad (3.2.3)$$

3. Measurement of photon indistinguishability to a quantifiable accuracy

$\{\sqrt{N_{s1}N_{s2}}\}_\sigma$ is the standard deviation of $\sqrt{N_{s1}N_{s2}}$ across all datapoints of the interferogram, $u_{\sqrt{N_{s1}N_{s2}}}$ is the Poissonian derived uncertainty on $\sqrt{N_{s1}N_{s2}}$ associated with the coincidence data point to which the correction is made and $u_{N_{c,measured}}$ is the Poissonian uncertainty on $N_{c,measured}$. Typically $u_{correction_{N_s}}$ was $< 0.5\%$ greater than $u_{N_{c,measured}}$.

The above discussion is predicated on the assumption that the single photon count rates are not affected by the HOM effect; this is reasonable because the interferometer collection angles were small, leading to a low pair collection efficiency (see section 2.7.4).

3.2.2 The slit aperture model for fitting interferogram data

In order to quantify V_{HOM} , a least squares procedure was used to fit a curve to the $N_{c,corrected}(\tau)$ data points [62]. The coincidence counting rate is proportional to the second order correlation function $G^{(2)}$ associated with the two photon field [63], see appendix 2. Therefore by calculating the $G^{(2)}(\tau)$ function associated with the output state of a HOM interferometer, it is possible to model the form of the HOM dip.

For a type-I non-collinear degenerate (and therefore symmetrically emitting) downconversion process, an interferometer defined by apertures with dimensions only along one transverse axis (i.e. slit apertures) and assuming no spectral filtering, derivation of the associated $G^{(2)}$ field leads to a simple expression for the coincidence rate in a HOM interferometer [64]:

$$N_c(\tau) = A \left(1 - V_{HOM} \exp[-B(\tau - C)^2] \times \text{sinc}[D(\tau - C)] \right). \quad (3.2.4)$$

V_{HOM} , A , B , C and D are fitting parameters, A is the rate of coincidences in the absence of two photon interference, C is the HOM dip centre position, and B and D are given by:

$$B = \frac{1}{2\sigma^2 \sin^2 \theta}, \quad D = \frac{\omega_0 \Delta \theta_{collect}}{2c \tan \theta}$$

3. Measurement of photon indistinguishability to a quantifiable accuracy

where σ is the pump beam diameter, θ is the downconversion emission angle, ω_0 is the angular frequency of the pump and $\Delta\theta_{collect}$ is the interferometer collection angle defined by the apertures.

The described ‘slit-aperture’ fitting model was applied to an interferogram measured when 3 nm spectral filters were mounted on the detectors and the apertures defined the collection angle in each arm of the interferometer ($\Delta\theta_{collect}$) at 1 mrad. Figure 3-1 shows the model to give an excellent fit to the experimental data, however the fitted curve corresponds to a pump beam diameter of 1.1 mm (1.5 mm measured at crystal) and an interferometer collection angle of 0.13 mrad. The discrepancy between the fitted and measured parameters are most likely due to invalidity of the assumptions made by the model, the most inappropriate being that the apertures define the two photon spectral profile whereas the narrowband spectral filters have been shown to dominate the spectral profile (see section 2.7.1). In addition the model ignores the focussing of the pump beam in order to maximize the photon pair collection efficiency (see section 2.5).

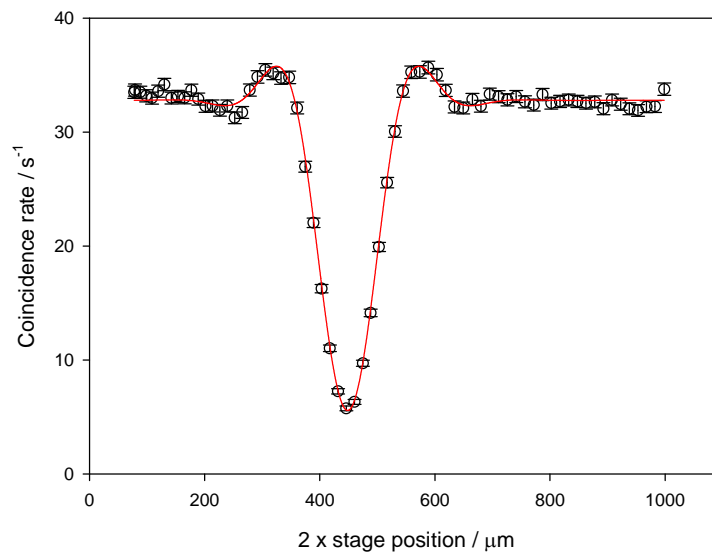


Figure 3-1 Interferogram from a HOM interferometer incorporating 1 mrad collection angles and 3 nm narrow band spectral filtering. The solid red line is a least squares fit using the slit aperture model.

3.2.3 Spectral filter model for fitting interferogram data

A second fitting model was investigated that assumed the two photon spectral profile to be dominated by the spectral filters. The ‘spectral filter’ model is also based on knowledge of

3. Measurement of photon indistinguishability to a quantifiable accuracy

$G^{(2)}(\tau)$ and it has been shown that in general the HOM dip shape in the *absence* of spectral filtering is described by [65-66]:

$$G^{(2)}(\tau) = N_c(\tau) = \frac{1}{2} \{1 \pm G^{(1)}(2\tau)\} \quad (3.2.5)$$

$G^{(1)}(\tau)$ is the first order correlation function and is directly related to the photon spectrum through a Fourier transform. Equation (3.2.5) means that the HOM dip form equals the envelope of the spectrum Fourier transform, but squeezed by a factor of two along the τ axis, see appendix 2. A different τ scaling factor is required to relate $G^{(1)}(\tau)$ and $G^{(2)}(\tau)$ for spectrally filtered light, but the form of the two curves are still the same. Therefore provided the photon spectrum is known, the form of the HOM dip is calculable and this is the basis of the ‘spectral-filter’ fitting procedure. The mechanics of the fitting procedure are depicted in Figure 3-2.

Under normal measurement conditions, the spectral filters dominate the photon spectrum, therefore it was necessary to measure the spectral transmittance profile with frequency. The filter transmittance profile was measured using a spectrophotometer (Cary 5E) with a spectral resolution of 0.05 nm. The Fast Fourier Transform (FFT) algorithm was used to evaluate the Fourier transform of the measured transmittance profile. Subsequently an envelope detection algorithm incorporating a Hilbert transform [67] was used to acquire the transform envelope. Note that only the lower half of the $G^{(1)}(\tau)$ envelope was required for the fitting procedure since the HOM interferometer was configured to produce only a half-envelope ‘dip’ (it is possible to produce a HOM ‘peak’ corresponding to the upper portion of the $G^{(1)}(\tau)$ envelope by positioning analyzers in front of each detector; the analyzers are required to have orthogonal orientations at +45° and -45° to the polarisation basis of the downconversion [21]).

3. Measurement of photon indistinguishability to a quantifiable accuracy

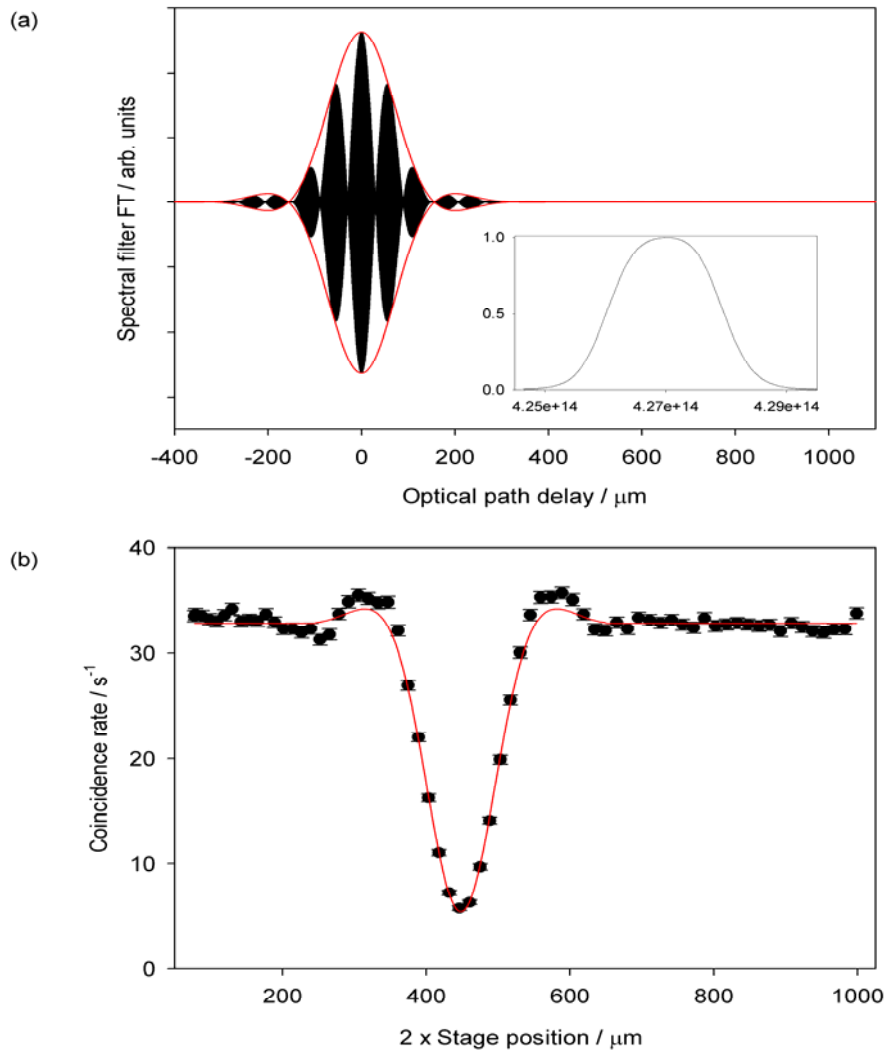


Figure 3-2 (a) Inset shows the measured transmittance of the spectral filters used in this chapter for HOM measurement. The main figure shows the Fourier transform of the filter spectrum and associated envelope function (red line). (b) The lower portion of the envelope in (a) was fitted to the experimental data (same data as Figure 3-1) using a least squares technique.

The calculated $G^{(1)}(\tau)$ envelope was then fitted to the measured HOM interference data using a least squares algorithm. The fitting parameters were those that describe the centre position and extent of the envelope function along the position axis, together with parameters that correspond to the coincidence rate at the dip centre and the coincidence rate far from the interference regime. As the result of the fitting procedure, the form of the $G^{(1)}(\tau)$ envelope was maintained but the coincidence rate and τ axes were rescaled to fit the experimental data. The HOM dip visibility could be evaluated using the two fitting parameters associated with

3. Measurement of photon indistinguishability to a quantifiable accuracy

the coincidence counting rate while the FWHM of the dip feature could be estimated numerically from the final fit.

The described spectral filter model was applied to the dataset from the previous section, see Figure 3-2 (b). In order to fit the data, the calculated $G^{(1)}(\tau)$ envelope was compressed along the τ axis by 1.46. An analogous expression to equation (3.2.5) but corresponding to the situation of a Gaussian filtered spectrum is given by:

$$G^{(2)}(\tau) = N_c(\tau) = 1 - \frac{1}{2\pi} \int \exp\left\{-\frac{(\Omega)^2}{4\sigma^2}\right\} \cos \Omega \tau d\Omega \quad (3.2.6)$$

Where $\Omega = \omega_s - \omega_p/2$, and σ is the width parameter of the filter. The function described by (3.2.6) is compressed along the τ -axis by $\sqrt{2}$ relative to the corresponding $G^{(1)}(\tau)$ function, which is close to compression required to fit the $G^{(1)}(\tau)$ function calculated from the spectral filter profiles to the experimental data in Figure 3-2 (b). The fit is excellent near the dip centre and in the region of no interference but deviates slightly from the data points about the maxima of the $N_c(\tau)$ curve at the edge of the dip. This deviation is due to the rigid assumption that the fitting curve takes the exact form of the spectrum transform. Although the spectral filters were determined to dominate the spectral bandwidth of the emission (and therefore the form of the $G^{(1)}(\tau)$ fitting function), there may have been other subtle influences such as aperturing of the downconversion or the nature of the pump spectral profile that caused the $G^{(1)}(\tau)$ function of the downconversion to be slightly different from that calculated for the spectral filters.

3.2.4 More on the fitting procedure and comparison between slit aperture and spectral filter models

The primary purpose of the fitting models was to evaluate the interference visibility associated with an interferogram, and in order to compare the models for this purpose each were fitted to ten interferograms, all taken from the same basic interferometer configuration (3 nm filters and $\Delta\theta_{collect} \sim 1$ mrad collection angle) but taken on different occasions. The metric used for the quality of the fit was given by the ‘goodness of fit’, *GOF*:

3. Measurement of photon indistinguishability to a quantifiable accuracy

$$GOF = \sqrt{\frac{R_{N_c}}{n_{data} - n_{parameter}}} \quad (3.2.7)$$

Where n_{data} is the number of experimental data points, $n_{parameter}$ is the number of fitting parameters used in the model and R_{N_c} is the minimized residual. The minimisation of R_{N_c} is the key operation of the fitting procedure. R_{N_c} is given by:

$$R_{N_c} = \sum_{i=1}^{n_{data}} \frac{(N_{c,model} - N_{c,measured})_i^2}{(u_{N_{c,corrected}}^2)_i} \quad (3.2.8)$$

$(N_{c,model})_i$ is the value of the fitted curve at τ_i , evaluated by inserting the fit parameters together with τ_i into the associated fitting model. $(N_{c,measured})_i$ is the N_c ordinate of data point i . $u_{N_{c,corrected}}$ is the standard uncertainty on the $N_{c,measured}$ measurement, estimated through equation (3.2.3). A *GOF* equal to one corresponds to the situation where the model gives the best possible fit given the uncertainties estimated for the data points. A value significantly higher than one may indicate either that the uncertainties have been underestimated or that the fitting model is incorrect. A value lower than one may indicate that either the uncertainties have been overestimated or that the model is erroneously fitting to noise. For the slit aperture model the *GOF* over ten datasets was measured to be 0.99 ± 0.11 where as for the spectral filter model the *GOF* averaged over the same datasets was 1.11 ± 0.20 . The better suitability of the slit aperture model indicated by the *GOF*s is consistent with the comparison between the fits of Figure 3-1 and Figure 3-2. There appeared to be some variability in the extent of the minor peaks in the coincidence rate at the edges of the dip between different interferogram datasets. (This is consistent with the suggestion made in section 3.2.3 that there may some factor influencing the two-photon spectral profile other than the spectral filters). While the slit aperture model was able to adjust to small changes in the ‘wings’ of the measured interferograms, the spectral model was locked to the same basic shape of the spectral filter $G^{(1)}(\tau)$ function, and as a result the *GOF* for the slit aperture model was more consistently closer to one and had a smaller standard deviation about the mean *GOF* value.

3. *Measurement of photon indistinguishability to a quantifiable accuracy*

Despite the difference between the *GOF* properties, the dip visibilities reported by the two models consistently agreed to within the estimated uncertainties which were 1.1 % and 1.3 % for the slit aperture and spectral filter models respectively, averaged over the ten datasets. The FWHM values reported from the fits using the two models differed by 0.1 % averaged over ten interferograms which is insignificant since the average uncertainty on the FWHM was 2.7 % and 2.5 % for the slit aperture and spectral filter models respectively.

Every iteration of the fitting procedure required the evaluation of an $n_{data} \times n_{parameter}$ matrix, and because the slit model was based upon an analytical expression the matrix could be evaluated using computationally fast vector operations, as a result the computation time required for convergence of the model to fit the data was typically < 1sec. The computation required time for convergence of the spectral filter model often spanned several minutes because the $n_{data} \times n_{parameter}$ matrix needed to be evaluated through a series of nested loops (a computationally slow structure) due to the numerical nature of the fitting function.

Based upon the above fitting quality and computation time arguments the slit aperture model was used as the standard curve fitting procedure for interferograms measured for the purposes of this chapter, and also for the analysis of those interferograms measured for characterisation of the interferometer in the previous chapter.

3.2.5 *Corrections and uncertainties associated with τ*

The previous sections dealt only with corrections and uncertainties associated with the coincidence rate axis of interferogram data. Investigations were carried out to determine whether corrections and uncertainties associated with the τ axis had any influence on the interferogram parameters determined from the fitting of the slit aperture model [equation (3.2.4)] to the experimental data.

The τ - delay roof mirror in the HOM interferometer was mounted on a piezo driven translation stage, and the position of the stage was recorded at a frequency of 1 Hz using a capacitive sensor. The profile of the stage position with time during the measurement of an interferogram is shown in Figure 3-3(a). The profile shows a series of $\sim 5 \mu\text{m}$ steps, interspaced with periods of time where the stage is approximately stationary corresponding to when coincidence events were counted. In the two second time period before and after each

3. Measurement of photon indistinguishability to a quantifiable accuracy

main step movement, the stage position appeared to show transient behaviour, and these time periods were excluded from the time during which coincidence measurements were made.

For the analysis in the previous section, the position corresponding to a coincidence counting measurement was taken to be the measured stage position shortly after the transient movement. Although Figure 3-3 (a) indicates that the stage position was relatively constant during the coincidence measurement, closer examination reveals a drift in the stage position, see Figure 3-3 (b). Therefore, the *mean* stage position over the measurement time was instead associated with a coincidence measurement, with the uncertainty u_x given by the standard deviation about the mean of the position readings. The uncertainty ranged between ~ 20 nm and 100 nm, with larger uncertainties associated with large step sizes suggesting that the jitter was produced by residual momentum of the roof mirror assembly gained during the step movement.

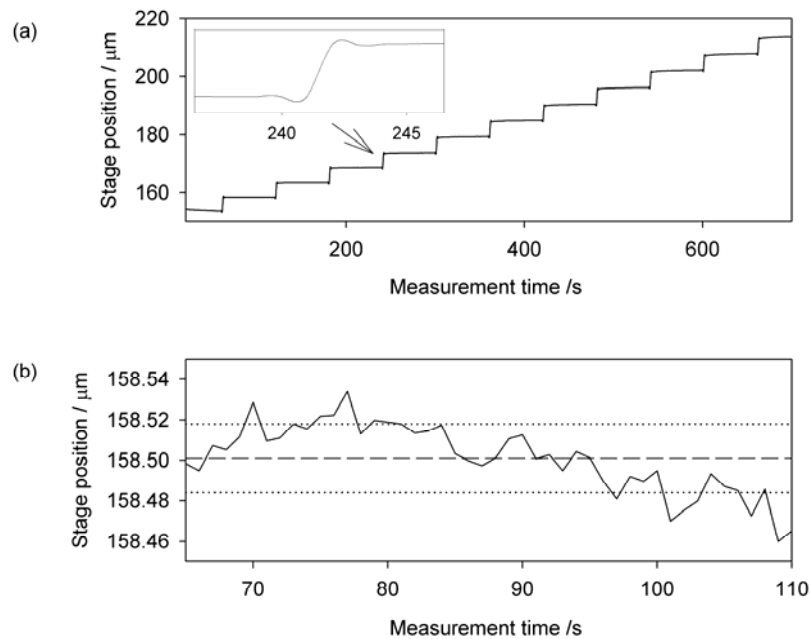


Figure 3-3 (a) Profile of the HOM interferometer optical delay translation stage with time during the measurement of a complete HOM interferogram, the inset shows the profile of the stage position about the time of a step. (b) Profile of the stage position over the measurement time of a single coincidence data point. Note that the transient movement of the stage position immediately before and after the positional step is not included within the coincidence measurement time frame. The broken line shows the mean stage position while the dotted lines denote the standard deviation about the mean position.

3. Measurement of photon indistinguishability to a quantifiable accuracy

The least squares algorithm for fitting of the slit aperture model described by equation (3.2.4) to the interferogram data was modified to include u_τ . The function of the algorithm was to minimise the residual $R_{N_c, \tau}$:

$$R_{N_c, \tau} = \sum_{i=1}^{n_{data}} \left\{ \frac{(N_{c,model} - N_{c,measured})_i^2}{(u_{N_c,corrected})_i^2} + \frac{(\tau_i - \tau_{var})_i^2}{(u_\tau)_i^2} \right\} \quad (3.2.9)$$

Unlike the fitting procedure associated with R_{N_c} (equation 3.2.8), the final τ co-ordinates of the fit are not restricted to τ_i and can take any values $\tau_{var,i}$ provided this reduces $R_{N_c, \tau}$. $(N_{c,model})_i$ is the value of the fitted curve at τ_{var} . Using the ‘new’ τ values with their uncertainties, the $R_{N_c, \tau}$ minimisation curve fitting procedure using the slit aperture model was applied to the same ten interferograms referred to in section 3.2.4. ; the averaged uncertainty was 3.1 % compared to 2.7 % when then the R_{N_c} minimisation fitting procedure was used. Therefore it was inferred that the τ uncertainties made a contribution of ~ 0.4 % to the measured FWHM uncertainty.

The possibility of influences on the HOM interferogram data due to any misalignment of the stage movement direction and the beam propagation direction was studied. A split HeNe laser beam was coupled into the interferometer framework using the method outlined in section 2.6, and the intensity interference fringes formed at the HOM recombiner as the stage position was scanned were measured. The intensity measurements were made using a three-element trap detector connected to a computer through a DVM. The stage was moved in steps of 30 nm and typically five intensity measurements were made at each interval within a 1 s time period. The resulting interferogram was a sinusoidal intensity modulation with the stage position. Using a least squares procedure the following model was fitted to the data points:

$$I = A \cos^2(Bx - C)D \quad (3.2.10)$$

where x is the stage position, and A , B , C and D are fitting parameters. Typically ten consecutive fringes were measured but a small variation in the period of consecutive fringes (upto $\sim \pm 2\%$) meant that it was not always possible to find a converging fit solution when all fringes were considered. Therefore the fitting procedure was applied to each measured fringe

3. Measurement of photon indistinguishability to a quantifiable accuracy

in turn, and from an interferogram consisting of N - fringes there would be a set of N A - D parameters after application of the fitting procedure.

The wavelength of the interfering light $\lambda_{measured}$ was given through the fitting parameter $B = 2\pi/\lambda_{measured}$ and therefore the average wavelength $\lambda_{measured,N}$ over all fringes was estimated by:

$$\lambda_{measured,N} = 2\pi/\overline{B_w} \quad (3.2.11)$$

where $\overline{B_w}$ is the weighted average of the B values over N fringes:

$$\overline{B_w} = \frac{\sum_{i=1}^N w_i B_i}{\sum_{i=1}^N w_i} \quad (3.2.12)$$

B_i is the fitting parameter for fringe i with reciprocal uncertainty w_i . The overall uncertainty in the wavelength of the interfering light was estimated as:

$$u_{\lambda_{measured,N}} = 2\pi \left(\frac{1}{\overline{B_w} + u_{\overline{B_w}}} - \frac{1}{\overline{B_w}} \right) \quad (3.2.13)$$

where the overall uncertainty on $\overline{B_w}$, $u_{\overline{B_w}}$ is given by the weighted standard deviation of the set of measured B parameters:

$$u_{\overline{B_w}} = \sqrt{\frac{\sum_{i=1}^N w_i (B_i - \overline{B_w})^2}{(N-1) \sum_{i=1}^N w_i}} \quad (3.2.14)$$

The laser wavelength was well defined at 633 nm and any deviation of $\lambda_{measured,N}$ from this would signify an angle between the delay translation stage movement and the interferometer beam propagation direction towards and away from the roof mirror. Therefore in principle, a ‘stretch’ factor of $633\text{nm}/\lambda_{measured,N}$ could be applied to the 2τ position axis of the HOM

3. Measurement of photon indistinguishability to a quantifiable accuracy

interferograms measured under the same alignment condition. $u_{\lambda_{\text{measured}}}$ was $\sim 2\%$ and $\lambda_{\text{measured},N}$ was consistently within $\pm 2\%$ of 633 nm, however $u_{\lambda_{\text{measured}}}$ corresponded to a $\sim \pm 10^\circ$ uncertainty on the angle between the optical delay travel and the interferometer beams entering and exiting the roof mirror. Therefore the ‘stretch’ factor correction $633\text{ nm}/\lambda_{\text{measured},N}$ was not useful. The uncertainty on $u_{\lambda_{\text{measured}}}$ could have been due to some uncertainty in the stage position measurement, or perhaps due to some irregular jitter in the stage position as the intensity measurement was made. It was inferred from the smoothness and regularity of the fringe modulation that any irregular jitter on the stage position did not significantly effect the measured interference visibility.

The uncertainty on the interferogram axis rescaling factor was combined with the estimated uncertainty on the HOM dip FWHM found from the least squares fit procedure to give an overall uncertainty on the dip width; nominally $\sim 3.5\%$.

Unsurprisingly, none of the above corrections or additional uncertainty considerations had any significant influence (i.e. $> 0.1\%$) on either the value of the measured HOM dip visibility or its uncertainty.

3.3 Photon indistinguishability and its determination from V_{HOM}

The degree of photon indistinguishability for a particular source refers to all possible means for discriminating the emitted photons. A source that emits photons with identical temporal, spatial, spectral and polarization properties is associated with a degree of indistinguishability of one, a value of zero is attributed to a source that emits photons that are completely distinguishable.

The degree of indistinguishability for photons from a source may be inferred from the visibility of its HOM interferogram. However, in a HOM experiment the interferometer is not a perfect instrument. The photons interact with the optical elements of the interferometer and the observed visibility carries not only photon indistinguishability information but also information about the parameters of the experimental setup; in order to determine the ‘true’ indistinguishability the effects of these parameters need to be quantified and corrected for. The uncertainty associated with each parameter’s effect will contribute to the uncertainty of

3. Measurement of photon indistinguishability to a quantifiable accuracy

the indistinguishability. The first stage in quantifying photon indistinguishability and estimating its uncertainty is the derivation of a measurement equation that expresses the indistinguishability P_{ind} as a function of the dominant influencing parameters.

The parameters of concern are those that contribute most to the non-ideal performance of the interferometer. The uncertainties in τ have already been considered in section 3.2.5, and therefore we are only concerned with parameters which affect the visibility above and beyond those described there. The dominant non-ideal aspects of the interferometer which affect the visibility are: polarization bias imparted on the interfering photons, departure of the beam splitter reflectance and transmittance from 50%; the centre-centre separation of the interferometer optical paths, the angular separation of the interferometer optical paths, the surface properties of the interferometer that are imparted onto the photons. These effects can be expressed analytically using the following measurement equation, where $f_{\Delta\phi_{\text{int}}}$, $f_{R,T}$, f_{ϵ} , f_{θ} , f_{surface} respectively relate to the effects described above:

$$P_{ind} = \frac{V_{HOM}}{f_{\Delta\phi_{\text{int}}} \cdot f_{R,T} \cdot f_{\epsilon} \cdot f_{\theta} \cdot f_{\text{surface}}} \quad (3.2.15)$$

In order to quantify P_{ind} , each term in the measurement equation needs to be evaluated. The evaluation of each term will have an associated uncertainty and these can be combined through the standard formulae for uncertainty propagation to give the overall uncertainty of the indistinguishability measurement:

$$u_{P_{ind}}^2 = \sum_{i=1}^N \left(\frac{\partial P_{ind}}{\partial f_i} \right)^2 \cdot u_{f_i}^2 + 2 \sum_{i=1}^{N-1} \sum_{j=i+1}^{N-1} \left(\frac{\partial P_{ind}}{\partial f_i} \right) \left(\frac{\partial P_{ind}}{\partial f_j} \right) u(f_i, f_j) \quad (3.2.16)$$

where f_i and u_{f_i} are the measurement equation terms and their associated uncertainties respectively. The first term applies for independent uncertainty components while the second term accounts for quantities that are correlated and is zero if there are no correlations. The partial derivatives within the summations are known as sensitivity coefficients. The sensitivity coefficient corresponding to a particular parameter determines the influence that the associated uncertainty has on the overall uncertainty of the indistinguishability measurement.

3. Measurement of photon indistinguishability to a quantifiable accuracy

The uncertainties can be evaluated using statistical methods (Type A uncertainties as defined by the GUM), or otherwise (Type B). The final uncertainty is the standard combined uncertainty for the indistinguishability measurement.

Sections 3.4-3.8 detail the experimental procedures and theoretical models that were used in order to estimate each term of the measurement equation, and their uncertainties. The determined quantities are tabulated in section 3.9 together with the uncertainty budget for the system.

3.4 Polarisation effects influencing the measured visibility - $f_{\Delta\varphi_{\text{int}}}$

The interferometer influence on relative polarization angle between the interfering photons, and the polarization properties of the photon source itself will be manifested in V_{HOM} , but only the photon source characteristics should affect P_{ind} . Therefore the factor $f_{\Delta\varphi_{\text{int}}}$ which accounts for interferometer polarization influence is required to relate V_{HOM} and P_{ind} .

Consider two photons with identical polarizations H that are input into separate paths of a HOM interferometer. One arm of the interferometer rotates the polarization of one photon by $\Delta\varphi_{\text{int}}$ while the other arm of the interferometer leaves the photon polarization unchanged. When $\Delta\tau = 0$, the spatially entangled state across the two output ports of the recombiner is [21]:

$$|\psi\rangle_{\Delta\tau=0} = \frac{1}{2} \left[|1_1^H 1_2^{H+\Delta\varphi_{\text{int}}}\rangle - |1_1^{H+\Delta\varphi_{\text{int}}} 1_2^H\rangle \right] \quad (3.3.1)$$

where each ket term gives the photon occupation number of each output mode of the recombiner. The output mode is given by the subscripts, while the superscripts denote the associated polarisation. The probability for coincident detection of two photons in this state is given by the second order correlation function, for $\Delta\tau = 0$ [21,63]:

$$N_{c,\Delta\tau=0} = \langle \psi | \hat{a}_1^\dagger \hat{a}_2^\dagger \hat{a}_2 \hat{a}_1 | \psi \rangle = \frac{1}{2} \sin^2 \Delta\varphi_{\text{int}} \quad (3.3.2)$$

3. Measurement of photon indistinguishability to a quantifiable accuracy

where the \hat{a}^\dagger and \hat{a} terms are the positive and negative vector operators respectively for the photon fields. Evaluating $|\psi\rangle$ and the second order correlation function when $\Delta\tau \gg \tau_c$ gives:

$$N_{c,\Delta\tau \gg \tau_c} = \frac{1}{2} \quad (3.3.3)$$

For otherwise ideal experimental conditions i.e., $f_{R,T} = f_\varepsilon = f_\theta = f_{surface} = 1$ and indistinguishable photons $P_{ind} = 1$, such that $V_{HOM} = f_{\Delta\phi_{int}}$, combining equation, (3.2.15), (3.2.1), (3.3.2) and (3.3.3) gives:

$$f_{\Delta\phi_{int}} = \cos^2 \Delta\phi_{int} \quad (3.3.4)$$

Equation (3.3.4) gives the dependency of the HOM dip visibility on the polarization angle between the interfering photons reported elsewhere in the literature [21]. The HOM dip visibility is a maximum when $\Delta\phi_{int} = 0$, and any change from this condition will degrade the visibility. $f_{\Delta\phi_{int}}$ was evaluated under the conditions at which the indistinguishability measurement was made; the polarization angle of the downconversion was measured in each path of the interferometer before the input aperture pairs (A_1 in Figure 2-14) and then again after double reflection at the roof mirrors. $\Delta\phi_1$ and $\Delta\phi_2$ are the measured polarization rotations angles along arms 1 and 2 of the interferometer respectively, and $\Delta\phi_{int} = \Delta\phi_1 - \Delta\phi_2$, from which $f_{\Delta\phi_{int}}$ can be evaluated.

The required polarization angles were quantified by measuring the relationship between the intensity (photon count rate) transmitted through a polarizer as it was rotated through a range of angles, and then fitting a Malus' law \cos^2 curve to the data:

$$I_{transmitted} = A \cos^2(B\theta - C) + D \quad (3.3.5)$$

where A , B , C and D are fitting parameters, and C gives the photon polarisation direction. From the measurements shown in Figure 3-4, $\Delta\phi_{int}$ was found to be $0.07 \pm 0.02^\circ$. Inserting the measured value of $\Delta\phi_{int}$ into equation (3.3.4) gives $f_{\Delta\phi_{int}} = 1.000 \pm 0.001$. This

3. Measurement of photon indistinguishability to a quantifiable accuracy

means that interferometer polarisation rotation effects make a negligible contribution to any disparity between P_{ind} and V_{HOM} . The uncertainty on $f_{\Delta\phi}$ was given by:

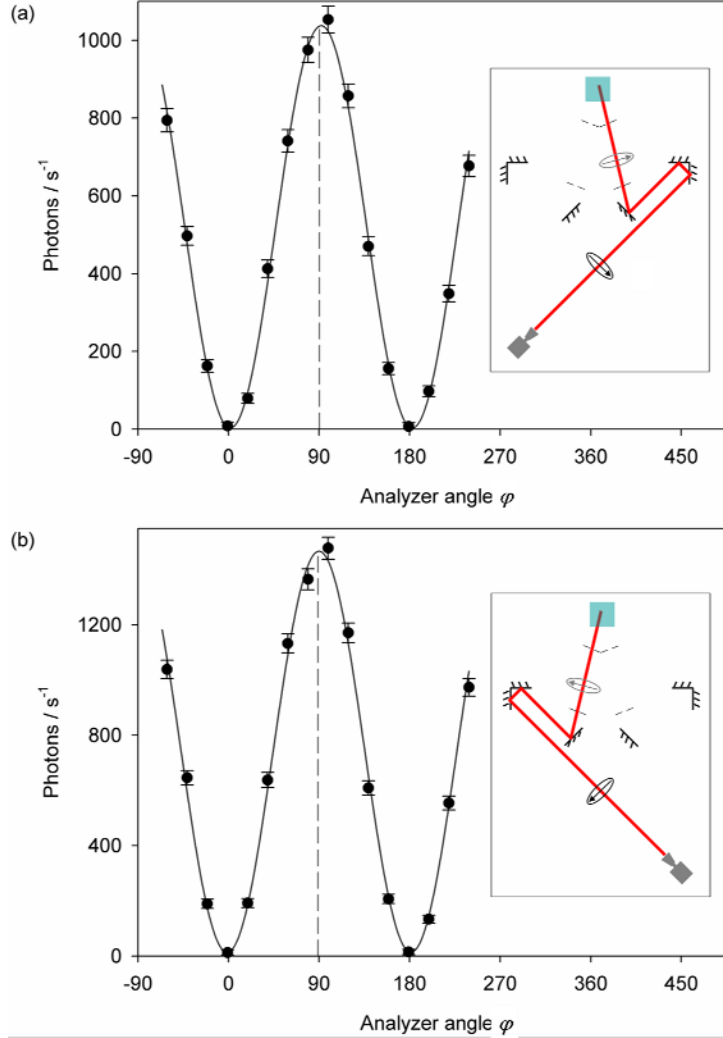


Figure 3-4 (a) The data show the dark count-corrected photon count rate transmitted through a polarisation analyzer with location indicated by the black arrow in the inset. From the fit, the polarisation orientation was measured to be $89.88 \pm 0.01^\circ$. When the analyzer was moved to the position indicated by the grey arrow the polarisation orientation was $89.97 \pm 0.01^\circ$, therefore $\Delta\phi_1 = 0.09 \pm 0.01$ (b) Analogous measurements to (a) but associated with the left arm of the interferometer; Measured polarisation angle when analyzer was located by the black arrow (grey arrow) $89.43 \pm 0.01^\circ$ ($89.59 \pm 0.01^\circ$), therefore $\Delta\phi_2 = 0.16 \pm 0.01$.

$$u_{f_{\Delta\phi_{int}}} = \left(\frac{df_{\Delta\phi_{int}}}{d\Delta\phi_{int}} \right) \cdot u_{\Delta\phi_{int}} = -2 \cos(\Delta\phi_{int}) \sin(\Delta\phi_{int}) \cdot u_{\Delta\phi_{int}} \quad (3.3.6)$$

3. Measurement of photon indistinguishability to a quantifiable accuracy

where $u_{\Delta\phi_{int}}$ was estimated by combination of $u_{\Delta\phi_1}$ and $u_{\Delta\phi_2}$, both of which were derived from the uncertainties on the C parameter associated with the fitted curves to the data. The sensitivity coefficient that dictates the influence of $u_{f_{\Delta\phi_{int}}}$ on $u_{P_{ind}}$ is given by:

$$\left(\frac{\partial P_{ind}}{\partial f_{\Delta\phi_{int}}} \right)_{\Delta\phi_{int}=0.07^\circ} = \frac{V_{HOM}}{f_{R,T} \cdot f_\varepsilon \cdot f_\theta \cdot f_{surface} \cdot (f_{\Delta\phi_{int}})_{\Delta\phi_{int}=0.07^\circ}^2} \approx \frac{V_{HOM}}{f_{R,T} \cdot f_\varepsilon \cdot f_\theta \cdot f_{surface}} \quad (3.3.7)$$

The resulting contribution that $u_{f_{\Delta\phi_{int}}}$ makes to the uncertainty on P_{ind} is negligibly small. For an interferometer with less symmetrical paths the nominal value and uncertainty contribution from $f_{\Delta\phi_{int}}$ may be more significant.

3.5 Beam splitter influence on the measured visibility - $f_{R,T}$

Assuming indistinguishable photons, the four equally probable classical outcomes to a recombination of two photons incident on separate input ports of a recombiner are described by tt , rr , rt and tr where r and t are the reflection and transmission probability amplitudes at the beamsplitter respectively. tt and rr correspond to the events that can register a coincident detection at separate output ports of the beam splitter (see figure 3-1). The HOM interference visibility is a maximum if $r = t$ but further from 50:50, the probability amplitudes associated with the tt and rr events will become increasingly different in magnitude, and since HOM interference is the interference between these amplitudes a decrease in the HOM dip visibility will result. Therefore the formulated measurement equation (3.2.15) comprises a factor $f_{R,T}$ that ensures P_{ind} is not affected by a V_{HOM} value degraded by any non-equal reflection and transmission property of the recombiner.

Considering Feynman's interpretation for evaluating event probabilities in quantum mechanics, [68] when $\Delta\tau \gg \tau_c$, the two probability amplitudes rr and tt are distinguishable, therefore the total probability for the two incident photons registering a coincidence is given by the sum of the squares of the two amplitudes:

3. Measurement of photon indistinguishability to a quantifiable accuracy

$$N_{c,\Delta\tau\gg\tau_c} \propto P_{12} = |rr|^2 + |tt|^2 = R^2 + T^2 \quad (3.4.1)$$

Where R and T are the reflection and transmission probabilities respectively. When $\Delta\tau \approx 0$, the two probability amplitudes describing photons leaving different output ports of the recombiner are indistinguishable, therefore the total probability for the two incident photons registering a coincidence is given by the square of the sum of the individual amplitudes:

$$N_{c,\Delta\tau=0} \propto P_{12} = |rr + tt|^2 = R^2 + T^2 + 2RT \quad (3.4.2)$$

The measured interference visibility obtained by combining equations (3.2.1), (3.4.1) and (3.4.2) is:

$$V_{HOM} = \frac{2RT}{R^2 + T^2} \quad (3.4.3)$$

The above analysis assume otherwise ideal experimental conditions, i.e. $f_{\Delta\phi_{int}} = f_{\theta} = f_{\varepsilon} = P_{ind} = 1$, and therefore from equation (3.2.15):

$$f_{R,T} = \frac{2RT}{R^2 + T^2} \quad (3.4.4)$$

Equation (3.4.4) shows the dependency of the HOM dip visibility on R and T reported elsewhere in the literature [8]. The HOM dip visibility is a maximum when $R=T$, and any change from this condition will degrade the visibility. R and T were evaluated from the reflected and transmitted intensity through the beamsplitter of a collimated white light source that was narrow band-pass (3nm) filtered about the centre wavelength of the downconversion; a schematic of the setup is shown in Figure 3-5. Two silicon trap detectors were used for each intensity measurement, one to detect the reflected or transmitted intensity from the beam splitter, and a monitor. The detectors were connected to separate DVMs (Keighley). Each intensity measurement read from a DVM was the average value of 50 measurements over a one second time period. For the R measurement, ten such measurements of the reflected beam intensity were made with simultaneous measurements of the intensity at the monitor, similarly for the T measurement. In addition for both the R and T measurements, the background intensity levels were measured ten times at each of the two detectors. For each

3. Measurement of photon indistinguishability to a quantifiable accuracy

dataset of ten intensity measurements, the mean of the ten measurements was taken as the value for analysis, with uncertainty given by the standard deviation about the mean.

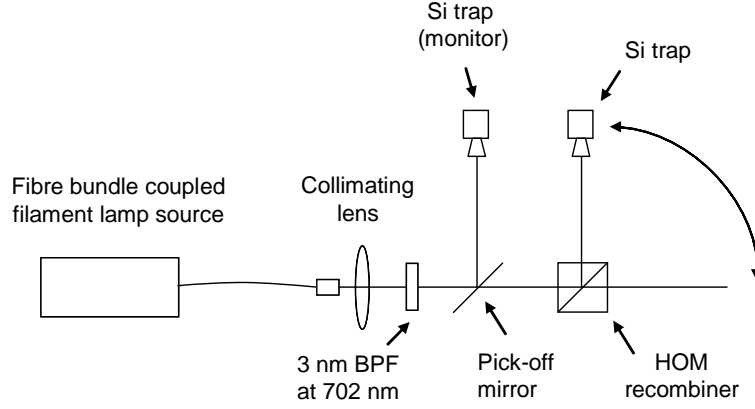


Figure 3-5 Setup for measuring the reflection and transmittance of the HOM recombiner

In order to ensure signal parity between the background corrected reflected and transmitted light intensity measurements (I_{ref} and I_{trans} respectively), I_{ref} was applied with a further correction:

$$I_{ref(adjusted)} = I_{ref} \times \frac{I_{monitor,trans}}{I_{monitor,ref}} \quad (3.4.5)$$

Where $I_{monitor,trans}$ and $I_{monitor,ref}$ are the back ground corrected intensity measurements at the monitor detector during the transmittance and reflectance measurements respectively. The total uncertainty on the reflection measurement was therefore:

$$u_{I_{ref(adjusted)}} = I_{ref(adjusted)} \sqrt{\left(\frac{u_{I_{ref}}}{I_{ref}}\right)^2 + \left(\frac{u_{I_{monitor,trans}}}{I_{monitor,trans}}\right)^2 + \left(\frac{u_{I_{monitor,ref}}}{I_{monitor,ref}}\right)^2} \quad (3.4.6)$$

There was a measured 7.8 % loss through the beam splitter, but the only effect of loss on a HOM interferogram is to reduce the overall coincidence counting rate, and there is no influence on the dip visibility. Therefore the sum of $I_{ref(adjusted)}$ and I_{trans} were normalized to one to give R and T respectively. For the HOM recombiner it was found that $R = 0.414 \pm 0.005$ and $T = 0.586 \pm 0.004$; equation (3.4.4) gives $f_{R,T} = 0.943$. For the uncertainty $u_{f_{R,T}}$, since $T = 1 - R$:

3. Measurement of photon indistinguishability to a quantifiable accuracy

$$f_{R,T} = \frac{2RT}{R^2 + T^2} = \frac{2R(1-R)}{R^2 + (1-R)^2} \quad (3.4.7)$$

$$u_{f_{R,T}} = \left(\frac{df_{R,T}}{dR} \right)_{R=0.414} \cdot u_R \quad (3.4.8)$$

Evaluating expression (3.4.8) gives $u_{f_{R,T}} = 6.49 \times 10^{-3}$, representing a 0.7% uncertainty on $f_{R,T}$. The influence that $u_{f_{R,T}}$ has on the indistinguishability uncertainty is given by the sensitivity coefficient:

$$\left(\frac{\partial P_{ind}}{\partial f_{R,T}} \right)_{R=0.414} = \frac{V_{HOM}}{f_{\Delta\varphi_{int}} \cdot f_{\varepsilon} \cdot f_{\theta} \cdot f_{surface} \cdot (f_{R,T})^2_{R=0.414}} = \frac{1.13 \cdot V_{HOM}}{f_{\Delta\varphi_{int}} \cdot f_{\varepsilon} \cdot f_{\theta} \cdot f_{surface}} \quad (3.4.9)$$

3.6 Influence of angular interferometer alignment on the measured visibility – f_{θ}

3.6.1 The approach for determining f_{θ}

The simplified wavefunction at the output of a HOM recombiner is given by the state:

$$|\psi\rangle = \frac{1}{2} [|1_1, 1_2\rangle + i |2_1, 0_2\rangle + i |0_1, 2_2\rangle - |1_1, 1_2\rangle] \quad (3.5.1)$$

where each ket term gives the photon occupation number of each output mode of the recombiner, the output mode is denoted by the subscripts. For perfect HOM interference to occur, the two $|1_1, 1_2\rangle$ terms must cancel and this is only possible if the two corresponding coincidence events are indistinguishable. If the trajectories of the two photons entering the beam splitter are not matched (i.e. if the interferometer is poorly aligned), the two $|1_1, 1_2\rangle$ terms will be spatially distinguishable (see figure 2-13) and loss of interference will result. The photon trajectories are broadly governed by the interferometer alignment rather than any

3. Measurement of photon indistinguishability to a quantifiable accuracy

property of the photons themselves. Therefore the factor f_θ of the measurement equation ensures that a reduced V_{HOM} value due to non-optimal angular alignment of the beams does not translate into a reduction in the measured photon indistinguishability. A factor accounting for non-perfect beam centre alignment is treated in section 3.7.

$f_{R,T}$ and $f_{\Delta\phi_{int}}$ were estimated by expressing them in terms of the associated variable parameters (i.e. R/T and $\Delta\phi_{int}$ respectively) and then making accurate measurements of the parameters. However, an analytic expression for f_θ would be far more complex, requiring the augmentation of $|\psi\rangle$ to consider τ , θ , x and y variables, where τ is the optical delay between the recombining photons, θ is the angle between two photons emerging from the same output port of the HOM recombiner while x and y are transverse spatial coordinates. $|\psi\rangle$ could then be used to calculate the second order correlation function $G^{(2)}$, which describes the coincidence counting rate between the two output ports of the HOM recombiner. Therefore assuming an otherwise perfect interferometer and indistinguishable photons, from equations (3.2.1) and (3.2.15) f_θ could be determined by evaluating:

$$f_\theta = \frac{\iint_{all\ space} [G^{(2)}(\tau \gg \tau_c, \theta, x, y) - G^{(2)}(\tau = 0, \theta, x, y)] dx dy}{\iint_{all\ space} G^{(2)}(\tau \gg \tau_c, \theta, x, y) dx dy} \quad (3.5.2)$$

Even with an explicit expression for $|\psi(\tau, \theta, x, y)\rangle$, evaluating equation (3.5.2) would be problematic because quantifying θ absolutely is difficult. For these reasons f_θ was instead estimated by a process of measuring V_{HOM} as a function of θ , and then fitting a curve to the data. The maximum of the fit gives an estimate for the location of $\theta = 0$ (perfect alignment), giving a basis for the definition of f_θ .

In the absence of a full expression for $G^{(2)}(\tau, \theta, x, y)$ to base a fitting model, the HOM visibility relationship with θ was assumed to take the same form as the variation with θ of the visibility associated with an intensity interferogram formed by two Gaussian beams at the recombiner. Experimental measurements of the HOM and intensity interference visibility relationships with θ [where the intensity interference measurements were made using a

3. Measurement of photon indistinguishability to a quantifiable accuracy

HeNe laser coupled into HOM framework, see section 2.6.3] revealed a common form and so the use of the intensity interference model for fitting to HOM dip visibility data was justified.

The model for the intensity interference visibility involves the calculation of the intensity distribution at the detection (x, y) plane due to the presence of two Gaussian beams $I(\tau, \theta, x, y)$. Consider $I(\tau, \theta, x, y)$ at the detection (x, y) plane, where two Gaussian beams of width σ propagate at angles of $\pm\theta$ to the y -axis, and have phase delays of $\exp(i\omega t_1)$ and $\exp(i\omega t_2)$. Also considered is the separation of the beam centres along the x -axis, $\pm\varepsilon$, see Figure 3-6. The amplitudes of beams one and two are given respectively by [69]:

$$U_1(t_1, \theta, \varepsilon, x, y) = A \exp\left(-\frac{(x + \varepsilon)^2 \cos^2 \theta + y^2}{\sigma}\right) \times \exp(-i\omega t_1 + ikx \sin \theta - ikz \cos \theta) \quad (3.5.3)$$

$$U_2(t_2, -\theta, -\varepsilon, x, y) = A \exp\left(-\frac{(x - \varepsilon)^2 \cos^2 \theta + y^2}{\sigma}\right) \times \exp(-i\omega t_2 + ikx \sin \theta - ikz \cos \theta) \quad (3.5.4)$$

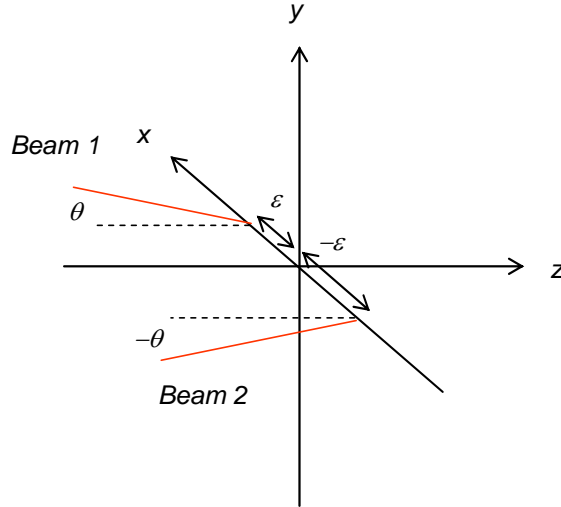


Figure 3-6 Geometry of 2 beam interference model used for fitting to HOM visibility versus θ data.

The intensity distribution in the detection plane is given by:

$$I(\tau, \theta, \varepsilon, x, y) = |U_1|^2 + |U_2|^2 + U_1 U_2^* + U_1^* U_2 \quad (3.5.5)$$

3. Measurement of photon indistinguishability to a quantifiable accuracy

where $\tau = t_2 - t_1$. The integral of equation (3.5.5) over x and y , gives the total intensity $I(\tau, \theta, \varepsilon)$ in the detection plane. Figure 3-7 (a) and (b) show $I(\tau, \theta, \varepsilon = 0)$ plotted as a function of τ for zero and non-zero θ respectively. The insets of Figure 3-7 (a) show the calculated $I(\tau, \theta = 0, \varepsilon = 0, x, y)$ distributions at different values of τ , which correspond well to the observed HeNe laser interference patterns in the HOM framework when the system was well aligned, similarly the insets of Figure 3-7(b) show calculated intensity distributions that correspond well to the observed HeNe laser interference patterns when the system was slightly mis-aligned with respect to θ . The visibility of the modulation $V(\theta)$ is calculated from:

$$V(\theta) = \frac{I(\tau = 0, \theta, \varepsilon = 0) - I(\tau = \pi/\omega, \theta, \varepsilon = 0)}{I(\tau = 0, \theta, \varepsilon = 0) + I(\tau = \pi/\omega, \theta, \varepsilon = 0)} \quad (3.5.6)$$

Equation (3.5.6) formed the basis for the model used to fit a curve to the HOM visibility data with θ , $V_{HOM}(\theta_{HOM})$, where the *HOM* subscript denotes that θ relates specifically to the downconversion sourced interferometer. The least squares fitting parameters were σ , a pre-factor A that rescales the $V(\theta)$ axis in order to account for the non-unity value of the observed maximum in the visibility data, and a parameter B that determines the position of the fit maximum along the θ axis. The effects of the fitting parameters A and B are shown diagrammatically in Figure 3-7 (c). The maximum value of $V_{HOM}(\theta_{HOM})$ (Given by the ‘ A ’ fitting parameter) by definition occurs when $\theta_{HOM} = 0$, and gives an estimate of the visibility when the HOM interferometer paths are perfectly aligned with respect to angle. Therefore the factor f_θ in the measurement equation is given by:

$$f_\theta = \frac{V_{HOM}(\theta_{opt})}{V_{HOM}(\theta_{HOM} = 0)} \quad (3.5.7)$$

θ_{opt} is the optimal value for θ determined from the alignment procedure, and therefore $V_{HOM}(\theta_{opt})$ corresponds to V_{HOM} in the measurement equation for photon indistinguishability (3.2.15). Equation (3.5.7) conveys that when the interferometer is perfectly aligned with respect to θ , the measured HOM dip visibility $V_{HOM}(\theta_{opt})$ is a maximum and equal to $V_{HOM}(\theta_{HOM} = 0)$. Any misalignment with respect to θ causes the visibility to decrease.

3. Measurement of photon indistinguishability to a quantifiable accuracy

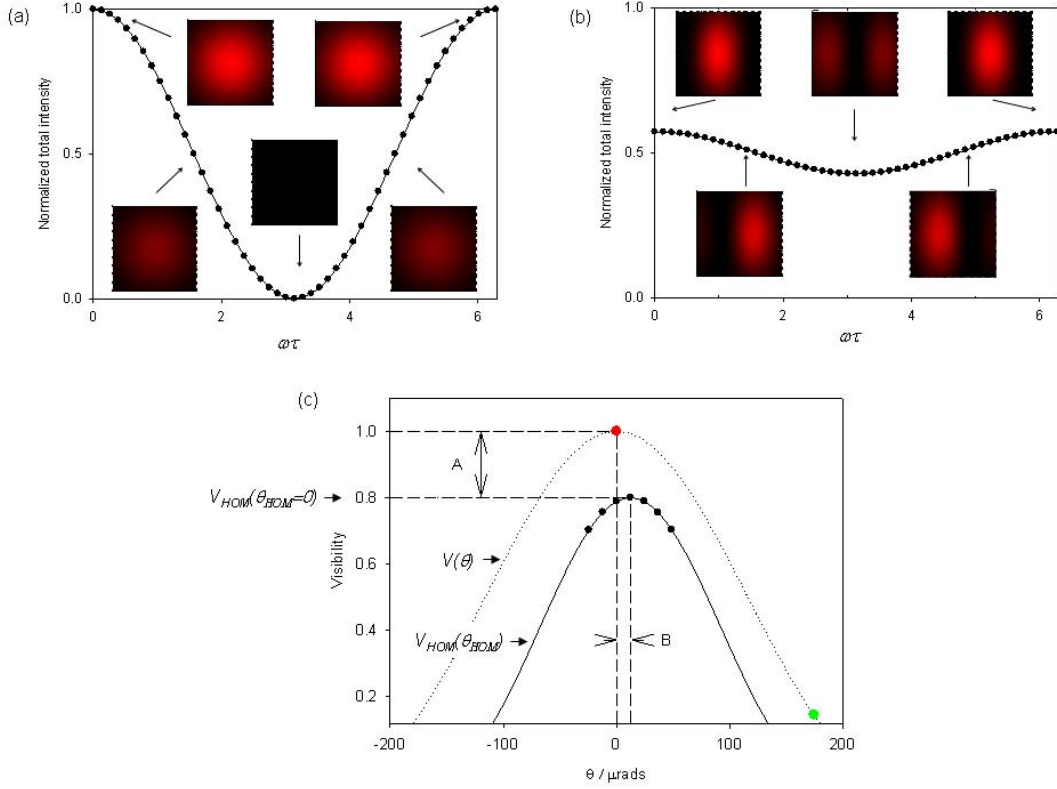


Figure 3-7 Two beam intensity interference model calculations; For $I_1 = I_2$, $\sigma = 1.2 \text{ mm}$ and $\varepsilon = 0$
 (a) Calculated intensity in the detection plane as a function of τ when and $\theta = 0 \text{ rads}$ [visibility of modulation denoted by red circle in (c)] and when (b) $\theta = 175 \mu\text{rads}$ [green circle in (c)]. The insets of (a) and (b) show the calculated x-y intensity distribution at the indicated τ and define $2 \text{ mm} \times 2 \text{ mm}$ areas. (c) Mechanism for the fitting procedure of the two-beam Gaussian interference model to $V_{HOM}(\theta)$ data (black circles). The dotted line is the calculated relationship of the visibility versus θ which is transformed to fit the data (solid line) using the parameters A , B and σ .

The uncertainty on f_θ is:

$$u_{f_\theta} = f_\theta \sqrt{\left(\frac{u_{V_{HOM}(\theta_{opt})}}{V_{HOM}(\theta_{opt})} \right)^2 + \left(\frac{u_{V_{HOM}(\theta_{HOM}=0)}}{V_{HOM}(\theta_{HOM}=0)} \right)^2} \quad (3.5.8)$$

Where $u_{V_{HOM}(\theta_{opt})}$ is taken as the uncertainty on the visibility measurement at θ_{opt} while

$u_{V_{HOM}(\theta_{HOM}=0)}$ is taken as the uncertainty on the A parameter from the fitting procedure.

3. Measurement of photon indistinguishability to a quantifiable accuracy

3.6.2 Implementation of approach for determining f_θ

The most obvious method for changing the θ alignment condition would be to change the steering angle of one of the beams onto the beam splitter, see Figure 3-8 (a). However this method would require an additional beam steering optic. Figure 3-8 (b) shows that an equivalent operation is achieved by rotating the beam splitter in the plane of the interferometer, i.e. the opening of a 2θ angle between the recombined beams. Therefore the beam splitter rotation mechanism was used. Note that the angle between the beams caused by the rotation creates a spot separation $\varepsilon \approx D_{i,ii}2\theta$ which must be incorporated into the fitting model.

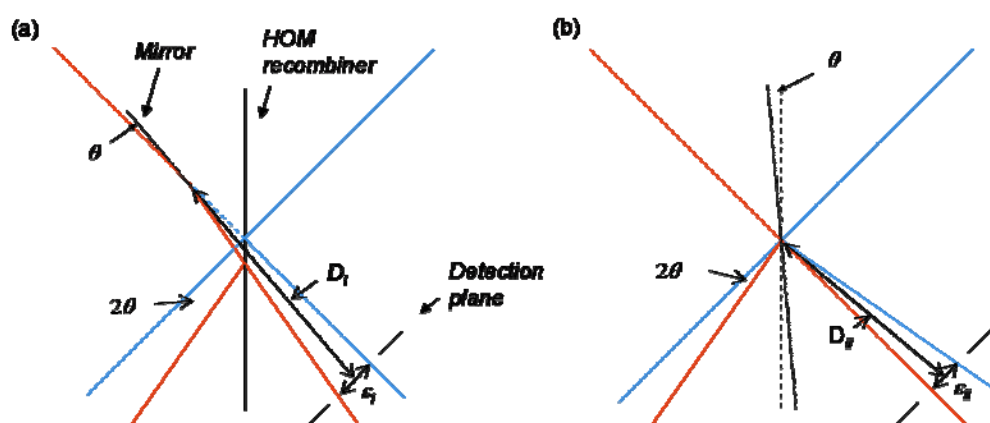


Figure 3-8 Mechanisms for simulating interferometer angular alignment change. (a) changing the steering of one beam before the recombiner and (b) through beam splitter rotation. In (a) D_i is distance from the beam steering surface to the detector while D_{ii} in (b) is the distance from the recombiner surface to the detector.

Figure 3-9 shows experimentally measured HOM dip visibility data against θ in addition to data for the visibility of intensity interferograms formed by a He-Ne laser coupled into the HOM framework. The visibility of the laser intensity interference fringes are quantified by:

$$V_{laser} = \frac{I_{max} - I_{min}}{I_{max} + I_{min}} \quad (3.5.9)$$

3. Measurement of photon indistinguishability to a quantifiable accuracy

I_{max} and I_{min} are the measured maximum and minimum intensities at the interferometer output upon scanning the optical delay. V_{laser} and its uncertainty was determined through a least squares fit of a cosine function to the measured data.

Also shown in Figure 3-9 are the fitted curves to both data sets, [$V_{HOM}(\theta_{HOM})$ and $V_{laser}(\theta_{laser})$ respectively] using the model described in section 3.6.1. The fits to both the HOM visibility and intensity interference visibility are excellent, in particular the quality of fit to the HOM visibility data justifies the use of the fitting model for the purposes of evaluating f_{θ} .

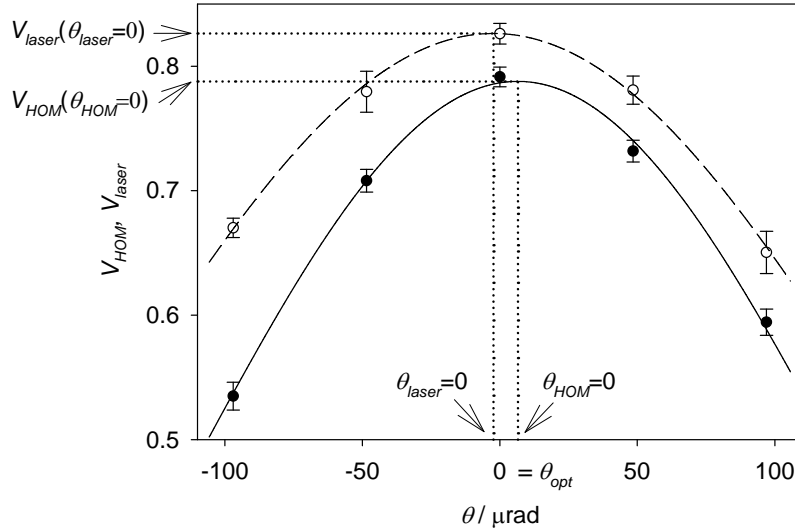


Figure 3-9 Measured interference visibility with change in beam splitter rotation angle for the downconversion sourced HOM (filled data points) interferometer and the HeNe sourced interferometer sharing the HOM framework (unfilled data points). The curves are fits to the data using a Gaussian 2-beam intensity interference model.

For the $V_{laser}(\theta_{laser})$ fit solution, the fit parameter $\sigma = 1.38 \pm 0.05$ mm, agreeing well with the measured HeNe spot diameter in the detector plane of 1.45 ± 0.05 mm. For the HOM interference fit solution $\sigma = 1.72 \pm 0.05$ mm. Although no direct measurement of downconversion spot diameter was made, this seems a little large as the downconversion and laser beams were subject to identical aperturing. The zero of the horizontal axis in Figure 3-9 corresponds to the angle θ_{opt} of the beam splitter rotation stage that was determined to be optimal for interference during the alignment process. From the fitting parameter B_{laser}

3. Measurement of photon indistinguishability to a quantifiable accuracy

associated with $V_{laser}(\theta_{laser})$, the required orientation of the beam splitter stage for perfect angular alignment of the laser beams ($\theta_{laser} = 0$ Figure 3-9) was -2.3 ± 0.3 μ rad relative to θ_{opt} , which is indicative of high quality alignment for the laser interferometer at θ_{opt} . This was because the alignment of the laser interferometer with respect to θ was marked by the observation of a rapidly expanding fringe pattern within the intensity spot such that only one fringe became observable.

From the fitting parameter B_{HOM} associated with $V_{HOM}(\theta_{HOM})$, the required orientation of the beam splitter to give perfect angular alignment of the downconversion beams ($\theta_{HOM} = 0$ in Figure 3-9) was determined to be 6.6 ± 1.8 μ rad relative to θ_{opt} . The small separation of $\theta_{laser} = 0$ and $\theta_{HOM} = 0$ indicates high accuracy of the alignment procedure with respect to angular trajectory matching of the downconversion and laser interferometer beams.

From the HOM visibility data and fitted curve, evaluation of equations (3.5.7) and (3.5.8) gives $f_{\theta} = 1.004 \pm 0.014$. The near unity value is a further indication of excellent interferometer angular alignment. This value for f_{θ} concerns only the angular alignment of the beams in the plane of the optical bench, i.e. the horizontal plane. There is also a further angular alignment degree of freedom in the perpendicular (vertical) plane, and this needs to be accounted for in the measurement equation and uncertainty analysis for P_{ind} . Due to the small collection angles defining the interferometer arms, any difference between the spatial properties of the downconversion emission in the horizontal and vertical direction will be small, and therefore the following assumption was made:

$$f_{\theta_H} = f_{\theta_V} \quad u_{f_{\theta_H}} = u_{f_{\theta_V}} \quad (3.5.10)$$

Where f_{θ_H} and f_{θ_V} are the parameters associated with the horizontal and vertical degrees of angular freedom, while $u_{f_{\theta_H}}$ and $u_{f_{\theta_V}}$ are their uncertainties respectively. Since f_{θ_H} and f_{θ_V} are independent variables, f_{θ} in equation (3.2.15) is given by:

$$f_{\theta} = f_{\theta_H} \cdot f_{\theta_V} \quad (3.5.11)$$

3. Measurement of photon indistinguishability to a quantifiable accuracy

The sensitivity coefficient that determines the influence of $u_{f_{\theta_H}}$ on $u_{P_{ind}}$ is given by:

$$\left(\frac{\partial P_{ind}}{\partial f_{\theta_H}} \right)_{\theta_H=6.6\mu\text{rads}} = \frac{V_{HOM}}{f_{R,T} \cdot f_{\varepsilon} \cdot f_{\Delta\phi_{int}} \cdot f_{surface} \cdot f_{\theta_V} \cdot (f_{\theta_H})^2_{\theta_H=6.6\mu\text{rads}}} \approx \frac{0.99 \cdot V_{HOM}}{f_{R,T} \cdot f_{\varepsilon} \cdot f_{\Delta\phi_{int}} \cdot f_{\theta_V} \cdot f_{surface}} \quad (3.5.12)$$

Equation (3.5.12) is also equal to $\left(\frac{\partial P_{ind}}{\partial f_{\theta_V}} \right)$.

3.7 Influence of beam centre Interferometer alignment on the measured visibility – f_{ε}

Like f_{θ} , the term f_{ε} of the measurement equation refers to the alignment of the interferometer. f_{ε} ensures that a reduced V_{HOM} due to poor transverse overlap of the interferometer paths does not translate into a reduction of the measured indistinguishability. f_{ε} was estimated in a similar fashion to f_{θ} ; through measurement of the HOM dip visibility as a function of the beam centre-centre separation (given by ε , see Figure 3-6) and then fitting a curve to the data. The maximum of the fit gives an estimate for the location of $\varepsilon = 0$, giving a basis for the definition of f_{ε} . The intensity interference model based on equation (3.5.6) was used for curve fitting to the HOM dip visibility vs. ε data. The mechanism for the fitting procedure was similar to that shown in Figure 3-7, and the fitting parameters were σ , A and B where B now describes the ε -shift of the calculated curve required for a fit the data.

The maximum value of the fitted curve $V_{HOM}(\varepsilon_{HOM})$ (Given by the ‘ A ’ fitting parameter) by definition occurs when $\varepsilon_{HOM} = 0$, and gives an estimate of the visibility when the HOM interferometer paths are perfectly aligned with respect to angle. Therefore the factor f_{ε} in the measurement equation is given by:

3. Measurement of photon indistinguishability to a quantifiable accuracy

$$f_{\varepsilon} = \frac{V_{HOM}(\varepsilon_{opt})}{V_{HOM}(\varepsilon_{HOM} = 0)} \quad (3.6.1)$$

ε_{opt} is the optimal value for ε determined from the alignment procedure, and therefore $V_{HOM}(\varepsilon_{opt})$ corresponds to V_{HOM} in the measurement equation for photon indistinguishability (3.2.15). Equation (3.6.1) conveys that when the interferometer is perfectly aligned with respect to ε , the measured HOM dip visibility is a maximum and equal to $V_{HOM}(\varepsilon_{HOM} = 0)$. Any misalignment with respect to ε causes the visibility to decrease.

The uncertainty on f_{ε} is:

$$u_{f_{\varepsilon}} = f_{\varepsilon} \sqrt{\left(\frac{u_{V_{HOM}(\varepsilon_{opt})}}{V_{HOM}(\varepsilon_{opt})}\right)^2 + \left(\frac{u_{V_{HOM}(\varepsilon_{HOM}=0)}}{V_{HOM}(\varepsilon_{HOM}=0)}\right)^2} \quad (3.6.2)$$

where $u_{V_{HOM}(\varepsilon_{opt})}$ is taken from the uncertainty of the data point associated with the indistinguishability measurement and $u_{V_{HOM}(\varepsilon_{HOM}=0)}$ is taken from the uncertainty on the A parameter of the fitting procedure.

The beam separation in the plane of the optical bench was changed through movement of the τ -scanning roof mirror in the direction perpendicular to the slide of the trombone, see Figure 3-10.

Figure 3-11 shows experimentally measured HOM dip visibility data against ε in addition to data for the visibility of intensity interferograms formed by a He-Ne laser coupled into the HOM framework. Also shown in Figure 3-11 are fitted curves to both data sets, [$V_{HOM}(\varepsilon_{HOM})$ and $V_{laser}(\varepsilon_{laser})$ respectively] using the model described in section 3.6.1. For both the laser and downconversion data, the beam width fitting parameter σ ($161 \pm 4\mu\text{m}$ and $174 \pm 5\mu\text{m}$ respectively) was a lot lower than the measured value from the HeNe beam profile at the detector plane (1.45 mm). The underestimation is almost certainly due to a change in θ as ε was varied; further calculations show that when σ is fixed at 1.45 mm, the model curves describe the HOM dip visibility vs. ε data well if $|\theta|$ increases linearly from 0 to 35

3. Measurement of photon indistinguishability to a quantifiable accuracy

μrads over the range that $|\varepsilon|$ increases from 0 to 40 μm . This shows that only a small change of $|\theta|$ with $|\varepsilon|$ is required to cause the observed behaviour.

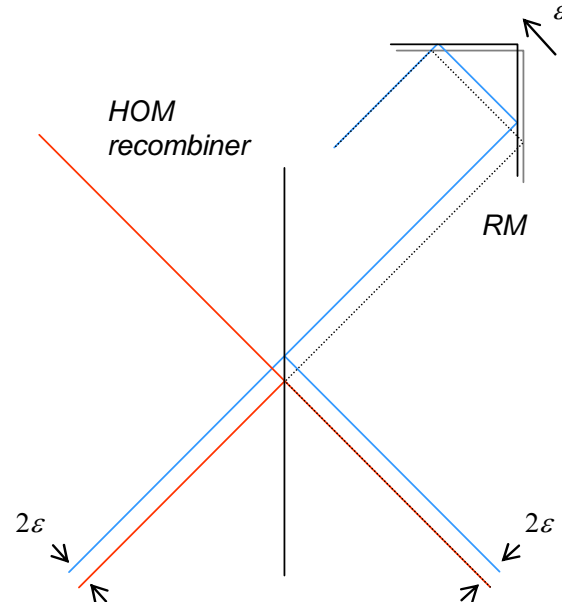


Figure 3-10 Mechanism for changing beam centre- beam centre separation 2ε by translation of a roof mirror (RM) The dotted line represent the optical path followed by the beam through RM before the movement of RM ε shown by the arrow. The blue line shows the optical path of the beam through RM after the movement. The red line represents the beam occupying the stationary arm of the interferometer.

The zero of the horizontal axis in Figure 3-11 corresponds to the position ε_{opt} of the roof mirror that was determined to be optimal for interference during the alignment process. From the fitting parameter B_{laser} associated with $V_{laser}(\varepsilon_{laser})$, the required position of the roof mirror stage for perfect spatial alignment of the laser beams ($\varepsilon_{laser} = 0$ in Figure 3-11) was $-9.6 \pm 1.9 \mu\text{m}$ relative to ε_{opt} , which is indicative of high quality alignment for the laser interferometer at ε_{opt} . However, comparing the relative separation of $\theta_{laser} = 0$ and θ_{opt} in Figure 3-9 to the relative separation of $\varepsilon_{laser} = 0$ and ε_{opt} in Figure 3-11, indicates better θ alignment at θ_{opt} relative to the ε alignment at ε_{opt} . This is plausible since perfect ε_{laser} alignment of the interferometer was less easy to determine from the observed interference pattern than for perfect θ_{laser} alignment.

3. Measurement of photon indistinguishability to a quantifiable accuracy

From the fitting parameter B_{HOM} associated with $V_{HOM}(\varepsilon_{HOM})$, the position of the roof mirror required to give perfect ε alignment of the downconversion beams ($\varepsilon_{HOM} = 0$ in Figure 3-11) was determined to be $-3.3 \pm 1.1 \mu\text{m}$ relative to θ_{opt} . The small separation of $\varepsilon_{laser} = 0$ and $\varepsilon_{HOM} = 0$ ($\ll \sigma$) indicates high accuracy of the alignment procedure with respect to beam centre overlap of the downconversion and laser interferometer beams.

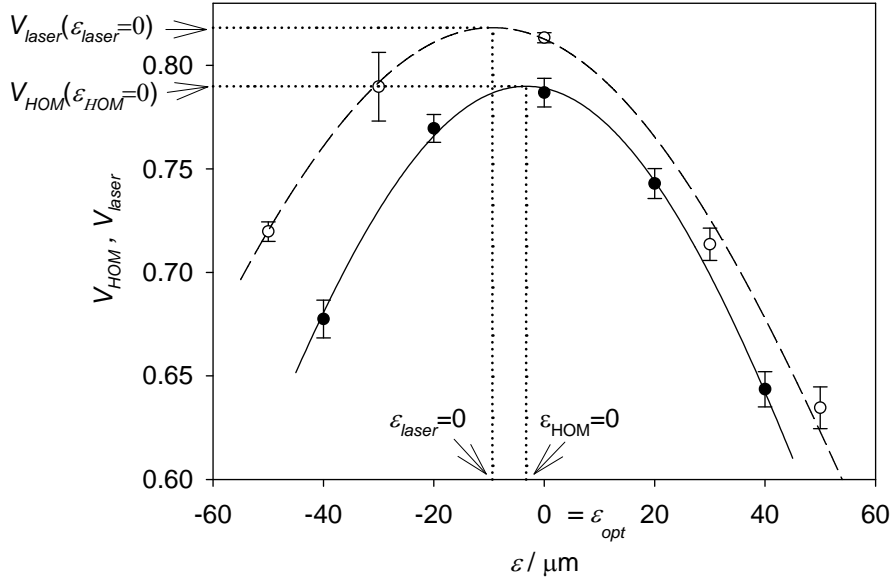


Figure 3-11 Measured interference visibility with roof mirror position (see Figure 3-10) for the reference (hollow data points) and HOM (solid data points) interferometers. The lines are fitted curves to the data based on a model given by equation (3.5.6).

From the HOM visibility data and fitting procedure, evaluating equations (3.6.1)-(3.6.2) gives $f_\varepsilon = 0.996 \pm 0.012$. Figure 3-11 suggests that the near unity f_ε which results from the close proximity of ε_{opt} to ($\varepsilon_{HOM} = 0$) may be due to a partial cancelling out of the error in aligning the reference interferometer and the error associated with overlapping the reference and HOM interferometers.

f_ε only accounts for the effect on V_{HOM} due to downconversion beam overlap in the horizontal plane. A further factor is required to account for the degree of freedom in the perpendicular plane. From the small aperture assumption that was used in the definition of equations (3.5.10):

$$f_{\varepsilon_H} = f_{\varepsilon_V}, \quad u_{f_{\varepsilon_H}} = u_{f_{\varepsilon_V}} \quad (3.6.3)$$

3. Measurement of photon indistinguishability to a quantifiable accuracy

Assuming that f_{ε_x} and f_{ε_y} are independent variables, they are related to f_{ε} in the measurement equation by:

$$f_{\varepsilon} = f_{\varepsilon_H} \cdot f_{\varepsilon_V} \quad (3.6.4)$$

The sensitivity coefficient that determines the influence of $u_{f_{\varepsilon_H}}$ on $u_{P_{ind}}$ is given by:

$$\left(\frac{\partial P_{ind}}{\partial f_{\varepsilon_H}} \right)_{\varepsilon=3.3\mu m} = \frac{V_{HOM}}{f_{R,T} \cdot f_{\theta} \cdot f_{\Delta\phi_{mt}} \cdot f_{surface} \cdot f_{\varepsilon_V} \cdot (f_{\varepsilon_H})_{\varepsilon_H=3.3\mu m}^2} \approx \frac{V_{HOM}}{f_{R,T} \cdot f_{\Delta\varepsilon} \cdot f_{\Delta\phi_{mt}} \cdot f_{\varepsilon_V} \cdot f_{surface}} \quad (3.6.5)$$

Which is equal to $\left(\frac{\partial P_{ind}}{\partial f_{\varepsilon_V}} \right)$.

3.8 Surface effects on the measured visibility - $f_{surface}$

3.8.1 Measurement equation associated with the laser interferometer within the HOM framework

In a HOM type indistinguishability measurement, the interfering photons follow separate optical paths through the interferometer, and are therefore incident on surfaces with different properties. A degree of distinguishability will therefore be imparted on the photons and V_{HOM} will be reduced. The factor $f_{surface}$ ensures that a reduced V_{HOM} due to interferometer surface effects does not translate to a reduction in the measured photon indistinguishability.

In order to quantify $f_{surface}$, we first formulate an analogous measurement equation to (3.2.15) for the laser interferometer occupying the HOM framework (see Figure 3.6.2):

$$P_{ind,laser} = \frac{V_{laser}}{f_{\phi_{mt,laser}} \cdot f_{I_1 I_2} \cdot f_{\varepsilon_{laser}} \cdot f_{\theta_{laser}} \cdot f_{surface}} \quad (3.7.1)$$

3. Measurement of photon indistinguishability to a quantifiable accuracy

where the terms V_{laser} , $f_{\phi_{int,laser}}$, $f_{I_1 I_2}$, $f_{\epsilon_{laser}}$, and $f_{\theta_{laser}}$ are analogous to the terms V_{HOM} , $f_{\Delta\phi_{int}}$, $f_{R,T}$, f_{ϵ} and f_{θ} in equation (3.2.15) respectively. The laser and downconversion wavelengths are similar and both follow the same paths through the interferometer; also the spot sizes of the laser and downconversion beams are both limited by small apertures. Therefore the $f_{surface}$ factors in equations (3.2.15) and (3.7.1) can be assumed to be equivalent. $P_{ind,laser}$ is the ‘indistinguishability’ of the laser photons; although indistinguishability is an incorrect metric for many photon sources, there exists a well established notion that a high degree of indistinguishability in quantum mechanics is related to a high degree of coherence in classical mechanics [70]. Since the laser beam has high coherence, substituting $P_{ind,laser} = 1$ into equation (3.7.1) and rearranging gives:

$$f_{surface} = \frac{V_{laser}}{f_{\phi_{int,laser}} \cdot f_{I_1 I_2} \cdot f_{\epsilon_{laser}} \cdot f_{\theta_{laser}}} \quad (3.7.2)$$

$f_{surface}$ given by equation (3.7.2) can be considered equal to the $f_{surface}$ required for the measurement equation (3.2.15). The following sections elaborate on the terms on the right hand side of equation (3.7.2), in particular the method for their evaluation.

3.8.2 Measured visibility of laser intensity interference fringes within HOM framework -

$$V_{laser}$$

Measurement carried out as described in section 3.6.2.

3.8.3 Polarisation influences on the measured laser interference visibility in the HOM framework - $f_{\Delta\phi_{int,laser}}$

The intensity at one output port of the recombiner is given by squaring the sum of the amplitude vectors of the two waves \bar{A}_1 and \bar{A}_2 with respective polarisations ϕ_1 and ϕ_2 at that port:

$$I_{total} = (\bar{A}_1 + \bar{A}_2)^2 = \bar{A}_1 \cdot \bar{A}_1 + \bar{A}_2 \cdot \bar{A}_2 + 2\bar{A}_1 \cdot \bar{A}_2$$

3. Measurement of photon indistinguishability to a quantifiable accuracy

$$= I_1 + I_2 + 2\sqrt{I_1}\sqrt{I_2} \cos(\theta_1 - \theta_2) \cos(\varphi_1 - \varphi_2) \quad (3.7.3)$$

Where $\theta_1 - \theta_2$ is the relative phase of the recombined beams. Taking $I_{total} = I_{max}$ when $\theta_1 = \theta_2$ and $I_{total} = I_{min}$ when $|\theta_1 - \theta_2| = \pi$, from equation (3.5.9):

$$V_{laser} = \frac{2\sqrt{I_1 I_2}}{I_1 + I_2} \cos(\Delta\varphi) \quad (3.7.4)$$

where $\Delta\varphi = \varphi_1 - \varphi_2$. Assuming that the two beams have identical polarisations at the interferometer input, the two beams to have equal intensity $I_1 = I_2$ ($f_{I_1 I_2} = 1$), and assuming perfect interferometer alignment ($f_{\epsilon_{laser}} = f_{\theta_{laser}} = 1$), combining equations (3.7.2) and (3.7.4) gives:

$$f_{\Delta\varphi_{int,laser}} = |\cos \Delta\varphi_{int,laser}| \quad (3.7.5)$$

where $\Delta\varphi_{int,laser} = \Delta\varphi_{laser,1} - \Delta\varphi_{laser,2}$. $\Delta\varphi_{laser,1}$ and $\Delta\varphi_{laser,2}$ are the measured polarisation rotations of the laser beam through paths one and two of the interferometer respectively. The $f_{\varphi_{int,laser}}$ term can be evaluated in an identical fashion to $f_{\varphi_{int}}$ through measuring the polarisation state of the split laser beam at the inputs and outputs of the interferometer optical paths. As before the polarisation orientations with uncertainty are quantified by fitting a \cos^2 curve to experimental data of the transmitted intensity through an analyzer as a function of analyzer orientation. The uncertainty on $f_{\Delta\varphi_{int,laser}}$ and the sensitivity coefficient are determined in a similar manner as were equations (3.3.6) and (3.3.7) respectively.

3.8.4 Beam intensity influence on the measured laser interference visibility in the HOM framework - $f_{I_1 I_2}$

$f_{I_1 I_2}$ is similar to the expression to $f_{R,T}$ in the measurement equation (3.2.15) but must be evaluated in a slightly different fashion. This is because although intensity interference like the HOM interference is sensitive to the beam splitter R/T ratio, unlike the HOM interference the laser interference is also sensitive to the relative intensity of the beams at the

3. Measurement of photon indistinguishability to a quantifiable accuracy

input of the recombiner. Taking equations (3.7.2) and (3.7.4), assuming equal beam polarisations, and perfect interferometer alignment conditions gives:

$$f_{I_1, I_2} = \frac{2\sqrt{I_1 I_2}}{I_1 + I_2} \quad (3.7.6)$$

The I_1, I_2 measurements were given by the mean of ten silicon trap detector measurements with an uncertainty given by the standard deviation about the mean. The final I_1 and I_2 measurements were corrected for background intensity. The uncertainty on f_{I_1, I_2} is given by:

$$u_{f_{I_1, I_2}} = \frac{2\sqrt{I_1 I_2}}{I_1 + I_2} \sqrt{\left(\frac{u_{I_1}}{2I_1}\right)^2 + \left(\frac{u_{I_2}}{2I_2}\right)^2 + \frac{(u_{I_1})^2 + (u_{I_2})^2}{(I_1 + I_2)^2}} \quad (3.7.7)$$

3.8.5 Alignment influences on the measured laser interference visibility in the HOM framework - $f_{\theta_{laser}}$ and $f_{\epsilon_{laser}}$

The $f_{\theta_{laser}}, f_{\epsilon_{laser}}$ factors and their uncertainties were evaluated in the same way as the f_{θ} (section 3.6) and f_{ϵ} (section 3.7) factors respectively; i.e. for $f_{\theta_{laser}}, V_{laser}$ was measured as a function of θ and a curve fitted to the data (see Figure 3-9), then by analogy to equation (3.5.7):

$$f_{\theta_{laser}} = \frac{V_{laser}(\theta_{opt})}{V_{laser}(\theta_{laser} = 0)} \quad (3.7.8)$$

where $V_{laser}(\theta_{opt})$ is the measured visibility of the laser interference fringes when the alignment condition corresponded to that at which the indistinguishability measurement was made. $V_{laser}(\theta_{laser} = 0)$ is the maximum value of the fitted curve to the data. The uncertainties on the $V_{laser}(\theta_{opt})$ data point and the curve fitting parameter associated with $V_{laser}(\theta_{laser} = 0)$ were combined to give $u_{f_{\theta_{laser}}}$ [c.f. equation (3.5.8)]. Also note that vertical degree of freedom needs to be considered [c.f equation (3.5.11)]. The associated sensitivity coefficient is similar to equation (3.5.12).

3. Measurement of photon indistinguishability to a quantifiable accuracy

A similar analysis applies for $f_{\epsilon_{laser}}$, where V_{laser} was measured as a function of ϵ and a fitted curve fitted to the data (see Figure 3-10) yielding:

$$f_{\epsilon_{laser}} = \frac{V_{laser}(\epsilon_{opt})}{V_{laser}(\epsilon_{laser} = 0)} \quad (3.7.9)$$

The uncertainties on the $V_{laser}(\epsilon_{opt})$ data point and the fitting parameter associated with $V_{laser}(\epsilon_{laser} = 0)$ were combined to give $u_{f_{\epsilon_{laser}}}$ [c.f. equation(3.6.2)]. Also note that vertical degree of freedom needs to be considered [c.f equation (3.6.4)]. The associated sensitivity coefficient is similar to equation (3.6.5).

3.8.6 $f_{surface}$ quantified

The variables on the right hand side of equation (3.7.2) were quantified with their uncertainties according to the sections 3.8.2-3.8.5, and are summarized in Table 3-1. The table also shows the $f_{surface}$ value that was calculated from the set of measurements under the assumption that $P_{ind,laser} = 1$. The quoted uncertainty on $f_{surface}$ is the standard combined uncertainty associated with the measurement equation (3.7.2), i.e.:

$$u_{f_{surface}}^2 = \sum_{i=1}^N \left(\frac{\partial f_{surface}}{\partial f_i} \right)^2 \cdot u_{f_i}^2 \quad (3.7.10)$$

where f_i are the measurement equation terms, and correlations between uncertainty components have been ignored.

3. Measurement of photon indistinguishability to a quantifiable accuracy

Measurement equation (3.7.2) term	Value	Uncertainty	Sensitivity coefficient	Contribution to standard uncertainty on $f_{surface}$
V_{laser}	0.819	8.61×10^{-3}	1.221	1.05×10^{-2}
$f_{\phi_{int,laser}}$	1.000	1.04×10^{-3}	1.000	1.04×10^{-3}
$f_{I_1 I_2}$	0.953	5.10×10^{-3}	1.049	5.35×10^{-3}
$f_{\theta_{H,laser}} = f_{\theta_{V,laser}}$	0.996	1.24×10^{-2}	1.004	1.25×10^{-2}
$f_{\varepsilon_{H,laser}} = f_{\varepsilon_{V,laser}}$	0.994	4.62×10^{-3}	1.006	4.64×10^{-3}
$f_{surface}$	0.877		$u_{f_{surface}} =$	2.22×10^{-2}

Table 3-1 Summary of the measured values with uncertainties for the components on the right hand side of the laser interferometer measurement equation (3.7.2) used to determine $f_{surface}$. The given uncertainty on $f_{surface}$ is the combined standard uncertainty, with $k = 1$.

3.9 Compiled uncertainty budget for photon distinguishability measurement and discussion

The experimentally determined values of the terms on the right hand side of the measurement equation (3.2.15), together with their associated uncertainties are compiled in Table 3-2. Also shown is the determined P_{ind} value; the associated uncertainty, $u_{P_{ind}}$, is the standard combined uncertainty calculated using equation (3.2.16). The various degrees of freedom associated with the interferometer (f_i) were assumed to be independent in calculating $u_{P_{ind}}$.

The largest single contributor to $u_{P_{ind}}$ was $u_{f_{surface}}$. This was because $u_{f_{surface}}$ was derived from the combined uncertainties associated with the terms of the measurement equation (3.7.2) for the laser interferometer. $u_{f_{surface}}$ could be reduced if an intensity stabilized laser was used for the evaluation of the component uncertainties.

3. Measurement of photon indistinguishability to a quantifiable accuracy

Another important contributor to $u_{P_{ind}}$ was $u_{V_{HOM}}$. $u_{V_{HOM}}$ was dominated by the \sqrt{N} Poisson statistical uncertainty for coincidence counting and this would be greatly reduced if a brighter photon source were being characterized and/or longer integration times were used for interferogram acquisition.

Measurement equation (3.2.15) term	Value	Uncertainty	Sensitivity coefficient	Contribution to standard uncertainty on P_{ind}
V_{HOM}	0.789	7.9×10^{-3}	1.21	9.55×10^{-3}
$f_{\phi_{int}}$	1.000	6.72×10^{-4}	0.954	6.41×10^{-4}
$f_{R,T}$	0.943	6.49×10^{-3}	1.012	6.57×10^{-3}
$f_{\theta_H} = f_{\theta_V}$	1.004	1.38×10^{-2}	0.949	1.31×10^{-2}
$f_{\varepsilon_H} = f_{\varepsilon_V}$	0.996	1.19×10^{-2}	0.957	1.14×10^{-2}
$f_{surface}$	0.877	2.22×10^{-2}	1.088	2.42×10^{-2}
P_{ind}	0.954		$u_{P_{ind}} =$	3.64×10^{-2}

Table 3-2 Summary of the measured values with uncertainties for the components on the right hand side of the HOM interferometer measurement equation (3.2.15) used to determine P_{ind} . The given uncertainty on P_{ind} is the combined standard uncertainty with $k = 1$.

The uncertainties on f_{θ} and f_{ε} represented significant contributions to $u_{P_{ind}}$. $u_{f_{\varepsilon}}$ and $u_{f_{\theta}}$ were both dependent primarily on the uncertainty of HOM visibility measurements and therefore the $u_{f_{\varepsilon}}$ and $u_{f_{\theta}}$ contributions could be reduced if longer integration times and/or a brighter source were employed for interferogram acquisition. By increasing the dataset of ε and θ for which V_{HOM} was measured, $V_{HOM}(\theta_{HOM} = 0)$ and $V_{HOM}(\varepsilon_{HOM} = 0)$ could be more accurately determined, thereby reducing the uncertainties on f_{θ} and f_{ε} .

It would be possible to reduce the uncertainty on $f_{R,T}$ to $< 0.1\%$ using a stabilized laser source for the reflectance and transmittance measurements [71]. In addition the contribution of $u_{f_{R,T}}$ to $u_{P_{ind}}$ could be reduced by choosing a beam splitter with $R = T \sim 0.5$, where the sensitivity coefficient ($\partial f_{R,T} / \partial R$) approaches zero.

3. Measurement of photon indistinguishability to a quantifiable accuracy

In an ideal experiment, V_{HOM} would equal P_{ind} . In this investigation, the most significant contributors to the disparity of the two quantities were $f_{R,T}$ and $f_{surface}$. Although $f_{R,T}$ could be made closer to unity by obtaining a recombiner with similar values for R and T , it would be difficult to force $f_{surface}$ close to one in a free space interferometer. This is because although optical surfaces can be produced to a high degree of flatness, there are many such surfaces comprising the interferometer, each making a small contribution to the overall wavefront distortion. Also, in addition to the effect of the surface roughness specified by the manufacturer, the $f_{surface}$ term takes into account the effects due to the presence of surface dust and tarnish on the interference visibility. Since optical fibres can be drawn to a high degree of uniformity, replacing the beamsplitter and beam steering mirrors with a single mode optical fibre recombiner would mean that $f_{surface}$ would be replaced with an equivalent wave front distortion term approaching unity. A single mode fibre recombiner would also circumvent the need for the f_ε and f_θ terms, further reducing uncertainties. However the benefits of a single mode fibre recombiner would be countered by reduced count rates due to coupling inefficiencies. In addition spatial filtering and depolarization of the photons by the fibre could mimic high photon indistinguishability, which would be a difficult effect to quantify. Note however that the reduced count rates due to the inefficiency of coupling photons into fibre would not effect the HOM visibility measurement.

For the curve fitting analysis of the HOM dip visibility data versus ε and θ , required for the determination of f_ε and f_θ respectively, a model based on 2-beam intensity interference was used. Although the model did not represent the true mechanism behind the measured data, the fits to the data were good which was the primary requirement from the model in the procedure for determining f_ε and f_θ .

In order to determine f_ε it was necessary to vary ε , and the curve fitting analysis of the visibility versus ε data indicated that the mechanism for changing ε was not independent of θ . As a result the influence of the parameter f_ε on the measured visibility may have been underestimated (i.e. the value of f_ε was overestimated) because the true maximum of the visibility relationship with ε may have been masked by the effect on the visibility of the θ change, i.e. the true $V_{HOM}(\varepsilon_{HOM} = 0)$ value could be greater relative to $V_{HOM}(\varepsilon_{opt})$ than was estimated. From experience of aligning the interferometer many times to find repeatable

3. Measurement of photon indistinguishability to a quantifiable accuracy

visibility measurements within the estimated uncertainty it was felt that the procedure for ε alignment was not subject to a significant random error, and a systematic error for the alignment seems unlikely. Therefore any overestimation of f_ε due to the θ dependence of the visibility measurements with ε is likely to be small. In the event of a significant systematic error on the ε alignment, f_ε may have been overestimated, but assuming that the systematic alignment error also effected the He-Ne interferometer, $f_{surface}$ would then be underestimated such that P_{ind} was not effected [see equation (3.7.2)]. The (small) θ change with ε probably occurred because the travelling beam of the ε change mechanism walked across the two optical surfaces of a roof mirror; since the roof-mirror surfaces may not be completely flat, there might be a slight dependency of the steer direction on the surface position at which the beam is incident. The method for determining f_ε could therefore be improved by establishing a mechanism for varying ε that does not cause the travelling interferometer beam to walk across optical surfaces; a periscope may be a better alternative.

This investigation concerned a parametric photon pair source, and the cw-pump meant that the pairs arrived randomly in time at the recombiner. For linear optics quantum computation experiments, single photon sources are required and it is essential that the source has a high timing resolution, implying a pulse-pump configuration. The most convenient method of characterizing a pulsed source is to interfere consecutive photons from a photon train. The measurement equation for such an experiment would take an identical form to the one given here, but there would be subtle (and possibly small) differences in the relative uncertainty contributions from each component. For example, in this experiment the coincidences are measured from the area under a coincidence-time histogram consisting of a single peak on a flat background, meaning accidental coincidence counts could be discriminated with an algorithm that made a negligibly small contribution to the raw data uncertainties that propagate to V_{HOM} [47]. In the case of a HOM experiment incorporating a train of photons passing at a regular interval, the coincidence-time histogram would consist of a series of equally spaced peaks, corresponding to the dual detection of photons that arrive at the recombiner with different time separations; only the area under one of the peaks, corresponding to where the received photons arrived at the recombiner simultaneously, contributes to the HOM dip measurement [36]. Therefore subtracting the unwanted coincidences will require an algorithm that may have different uncertainties to the one used here.

3. Measurement of photon indistinguishability to a quantifiable accuracy

The overall indistinguishability value for the downconverted photons is a reflection of the polarization, temporal spatial and spectral properties of the photons. Phase matching constraints dictate that the photons have indistinguishable polarizations, and energy conservation dictates that the interfering photons are created simultaneously, ensuring temporal indistinguishability for equal interferometer paths. Although the spectral properties of the interfering photons are partially influenced by identical filters on each detector, the interfering photons of a pair are wavelength anti-correlated and consequently will be inherently partially distinguishable. In addition, phasematching dictates that while degenerate photon pairs are launched into the interferometer with equal and opposite angles about the pump beam, lower and higher energy photons are launched at larger and smaller angles respectively. Therefore in the case of non-degenerate pairs there is further reduction of indistinguishability due to their differing spatial properties. The above arguments are consistent with the measured high, but sub-unity indistinguishability.

3.10 Conclusions

The fitting of model curves to HOM interferogram data was presented as a method for quantifying HOM interference dip visibilities. The test data was taken from the HOM interferometer built in the previous chapter. A fitting model was tested that was based upon an expression for the dip shape assuming that the spectral profile of the HOM source photons were defined by slit apertures. In addition a fitting model was tested that was based upon the Fourier transformed frequency transmission profile of the narrowband filters through which the HOM downconversion was passed. The quicker computation time and superior fitting properties of the ‘slit aperture’ model meant that this method was used in the standard curve fitting procedure to HOM interferogram data.

The corrections made to raw interferogram data with respect to both coordinates were discussed. The most significant correction to the measured coincidence rate was due to fluctuations in pump power, and lead to an additional uncertainty of $\sim 0.5\%$, but this was still less than the Poissonian statistical uncertainty associated with typical data. The corrections associated with the optical delay axis were found to make negligible contributions to the HOM dip visibility inferred from the interferogram.

3. Measurement of photon indistinguishability to a quantifiable accuracy

A measurement equation for the quantification of photon distinguishability using a Hong-Ou-Mandel interferometer was presented. The equation relates photon indistinguishability to the HOM dip visibility measurement associated with the photons, the other terms of the equation relate to the properties of the interferometer. The rationale for each term of the equation was given, with details of the experimental measurements required for their evaluation. The measurement equation methods were applied to the interferometer described in the previous chapter. From the interferogram data and the other quantified terms of the measurement equation, the pair photon indistinguishability was estimated to be 0.954 ± 0.036 . The most significant component separating the magnitude of the measured interference visibility and the indistinguishability was attributed to the influence of optical surface imperfection properties of the interferometer. The estimated uncertainty on the surface effect quantity made the greatest contribution to the indistinguishability measurement uncertainty; this was because the surface effect uncertainty was estimated from the combined uncertainties associated with the terms of a second measurement equation, relating to a laser interferometer occupying the HOM framework. The interferometer build procedure was found to give near-optimal alignment resulting in minimal degradation of the measured visibility, however it was likely that the mechanism used to vary the transverse overlap of the interfering beams in order to determine its influence on the interference visibility was not independent of the angular alignment. As a result, the influence of the associated measurement equation term on the indistinguishability may have been underestimated. A change to the experimental method was proposed with a view to remedy this. Other changes to the experimental method were proposed with the aim to reduce the uncertainty on the indistinguishability measurement, and also to reduce the disparity between the measured HOM dip visibility and the photon indistinguishability.

4 Pump enhanced source of correlated photons in the telecoms band

4.1 Introduction

Entangled states generated from SPDC photon pair processes are a key element in quantum computation, quantum key distribution schemes and fundamental tests of quantum mechanics. In addition photon pair sources have demonstrated applicability in metrology such as the absolute calibration of single photon counting detectors [72], polarisation mode dispersion measurements in optical fibre and quantum optical coherence tomography [28].

The vast majority of SPDC investigations concerning the above applications have focussed mainly on the 600-900 nm spectral region, often for the reason that it is possible to use silicon avalanche photodiodes for detection. Such detectors are ubiquitous, have high quantum efficiencies, low dark counts, short dead times, in addition to being compact and relatively low cost.

While the visible wavelength experiments are generally carried out in free space, for communications it is often desirable to transport the photons through optical fibre where the most advantageous wavelengths in terms of low absorption are at 1.3 and 1.55 μm . This is therefore likely to be an important spectral region for the development of optical quantum information technologies. Historically one problem working in this regime has been the need to use InGaAs/InP based detection schemes that have poor quantum efficiencies, high dark counts and dead times in addition to high cost. However the technology is improving and it is possible to obtain detectors with quantum efficiencies $>20\%$.

A second reason for the general lack of development work towards telecoms photon counting sources is that large frame pump lasers are required to achieve sufficiently high source brightness for high data rates in communication schemes, and low data acquisition time in metrology applications. In recent years relatively low cost, compact and powerful diode laser systems at wavelengths suitable for pumping telecoms downconversion processes have become more available; at the time of writing a 1.5 W CW (780 nm) laser diode and a 100

4. Pump enhanced source of correlated photons in the telecoms band

mW tuneable laser diode covering the 792 nm region are commercially available from Toptica photonics [73]. For schemes where it is necessary to know accurately the time of photon generation, compact fibre-laser systems are commercially available (also from Toptica photonics) and such systems can generate fs pulses with 100s' mW average powers at 780 nm.

The advances in detector and pump source technologies have opened up the possibility to develop photon counting sources in the telecoms band. This chapter presents the design work and building of such a pair photon source.

The first aim of this chapter was to identify a suitable downconversion material for degenerate photon pair generation in the telecoms band. In order to maximize the brightness of the downconversion process the possibility of incorporating waveguide morphology nonlinear material was investigated as was the concept of a bulk downconversion medium in an optical resonator. The relative merits of the two methods are discussed in addition to the decision to incorporate a pump enhancement cavity into the final design. Following the initial choice of source configuration, it was necessary to determine design parameters such as enhancement cavity mirror curvatures/reflectivities and mode matching of the pump to the mode of the enhancement cavity, and the details of these design processes are given.

The source was built at the University of St. Andrews, and characterisation experiments were carried out such as the estimation of the photon pair generation rate and the incorporation of the source into a HOM interference experiment.

4.2 Non-linear crystal choice

The brief for this work was to design and produce a $\chi^{(2)}$ source of correlated photons in the telecoms band. The emitted photons should be orthogonally polarised and collinear to the pump for compatibility with a scheme for polarisation entanglement (see following chapter). This section details the $\chi^{(2)}$ crystal materials that were considered and the reasons behind their subsequent selection or exclusion from the source design.

4. Pump enhanced source of correlated photons in the telecoms band

4.2.1 KDP and BBO

When choosing the non-linear crystal for the visible wavelength two-photon interferometer (see chapter 2), KDP and BBO were considered as candidate materials primarily because of their ubiquity and high transmittance at the 351.1 nm pumping wavelength. The transmittance window for these crystals also extends across both the pump and downconversion wavelengths concerned with this investigation.

Using similar calculations to those outlined in chapter 2, a phase matching solution in BBO for the 775 nm (*e*) → 1550 (*e*) + 1550 nm (*o*) downconversion process was found with $\theta_{pm} = 28.8^\circ$ and $\phi_{pm} = 30.0^\circ$. Given the pump wavelength and calculated crystal parameters, using a numerical method (see chapter 7) the efficiency of the degenerate downconversion process was calculated over all emission angles relative to the pump beam. The calculations showed that the degenerate wavelength emission travels at different angles to the pump beam depending on the azimuthal angle about the pump beam, resulting in the orthogonally polarized photons being emitted into two cones. The calculated cone cross sections are shown in Figure 4-1(a), the required collinear emission occurs only along the tangent of the cone intersection. The effective nonlinearity for the type II process in BBO is given by [45]:

$$d_{eff,II}(BBO) = d_{22} \cos^2 \theta \sin 3\phi \quad (4.2.1)$$

which is evaluated as 0.77 pm/V for the phase matched solution. From Figure 4-1 (a) it is clear that a large proportion of the downconverted power for the interaction is emitted non-collinearly and therefore not suitable for incorporation into the proposed entanglement source.

A phasematching solution for the same interaction in KDP was found to be $\theta_{pm} = 71.1^\circ$ and $\phi_{pm} = 0^\circ$ [Figure 4-1 (b)], and the emission profile showed a similar azimuthal symmetry for the BBO interaction, except that in KDP a greater proportion of the downconverted power is collinear with the pump. The relevant nonlinear coefficient for the interaction is:

$$d_{eff,II}(KDP) = d_{36} \sin 2\theta \cos 2\phi \quad (4.2.2)$$

which is evaluated to be 0.38 pm/V. Clearly the brightness of the birefringently phasematched type II collinear process will be low in both BBO and KDP.

4. Pump enhanced source of correlated photons in the telecoms band

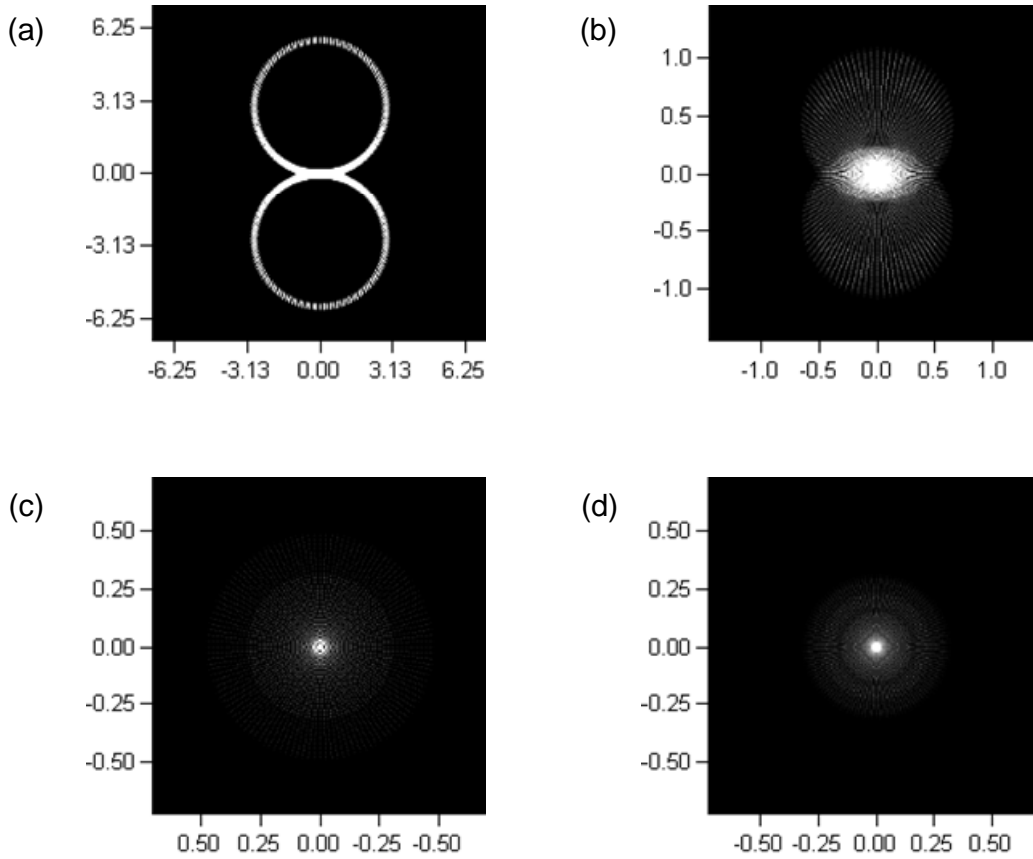


Figure 4-1 Angular emission profile from collinearly phase-matched $775 \text{ nm} \rightarrow 1550 + 1550 \text{ nm}$ processes in (a) BBO, $e \rightarrow e+o$, (b) KDP, $e \rightarrow e+o$, (c) PPLN $o \rightarrow e+o$ and (d) PPKTP $y \rightarrow y+z$. The horizontal and vertical axis of the plots are lab angles in degrees.

4.2.2 PPLN and PPKTP

Due to the apparent non-suitability of BBO and KDP for the application, additional non-linear crystals, lithium niobate (LiNbO_3) and potassium titanyl phosphate (KTiOP_4) with transmission windows in the region of interest were also considered. Both crystals are ferroelectric and can therefore be periodically poled for quasi-phase matched interactions. For PPLN, a non-critically phase-matched solution for the $775 \text{ nm} (o) \rightarrow 1550 (e) + 1550 \text{ nm} (o)$ process was found at $\theta_{pm} = 0^\circ$ and $\phi_{pm} = 0^\circ$ with a grating period of $16.3 \mu\text{m}$ at a temperature of 35°C . A temperature of 35°C was preferred since it was felt that in the absence of expensive temperature control measures, the crystal may operate as desired at laboratory temperature, but if that had turned out not to be the case then a temperature slightly above laboratory ambient temperature would be the simplest one to stabilize to.

4. Pump enhanced source of correlated photons in the telecoms band

A second solution was found with $\theta_{pm} = 90^\circ$ and $\phi_{pm} = 0^\circ$ and a grating period of $9.3 \mu\text{m}$ at the same temperature. The effective non linearity for the two interactions in the poled material is given by:

$$d_{eff,II}(PPLN) = \frac{2}{\pi} d_{31} \sin \theta - d_{22} \cos \theta \sin 3\phi \quad (4.2.3)$$

Equation (4.2.3) is maximized by taking the second solution, giving 3.78 pm/V . The numerically evaluated emission profile of the degenerate wavelength is shown in Figure 4-1 (c), and shows that most of the downconverted power is transferred into the collinear mode, indicating a high percentage of the generated power could be used in the proposed entanglement source.

For PPKTP, there is a non-critically phase matched solution for the $775 \text{ nm (fast, } y) \rightarrow 1550 \text{ nm (fast, } y) + 1550 \text{ nm (slow, } z)$ interaction by taking $\theta_{pm} = 90^\circ$ and $\phi_{pm} = 0^\circ$ with a grating period of $46.1 \mu\text{m}$ at 35°C . These phase matching angles also correspond to maximization of the effective nonlinearity for the interaction the $x - y$ plane:

$$d_{eff,II}(PPKTP) = \frac{2}{\pi} d_{31} \sin \theta \quad (4.2.4)$$

Equation (4.2.4) evaluates to 2.50 pm/V . As for the PPLN emission, the PPKTP spatial emission profile is [shown in Figure 4-1 (d)] constrained to a tight angle about the pump beam.

Under the $\theta_{pm} = 90^\circ$ phase matching condition described above for the PPLN crystal, Figure 4-2 (a) shows the variation in wavelength of the signal and idler photons emitted collinearly to the pump as the pumping wavelength is varied. At $\lambda_p = 775 \text{ nm}$ as expected the signal and idler photons are degenerate, but the emission goes rapidly non degenerate as λ_p is varied. In the short term the crystal will be incorporated into a cw-pumped device and therefore the non-degeneracy of the emission would be avoided because the pump is monochromatic, but in future experiments it may be necessary to have greater control over when photons are likely to be generated, in such an experiment it would be necessary to pump with pulses. A 200 fs pulse centred at 775 nm corresponds to a minimum Heisenberg bandwidth of $\Delta\lambda \sim \lambda^2/4\pi c\Delta\tau \sim 0.8 \text{ nm}$, and therefore a significant proportion of the pump power will be

4. Pump enhanced source of correlated photons in the telecoms band

downconverted to non-degenerate pairs that are less useful for quantum optics experiments because of the distinguishing information they carry.

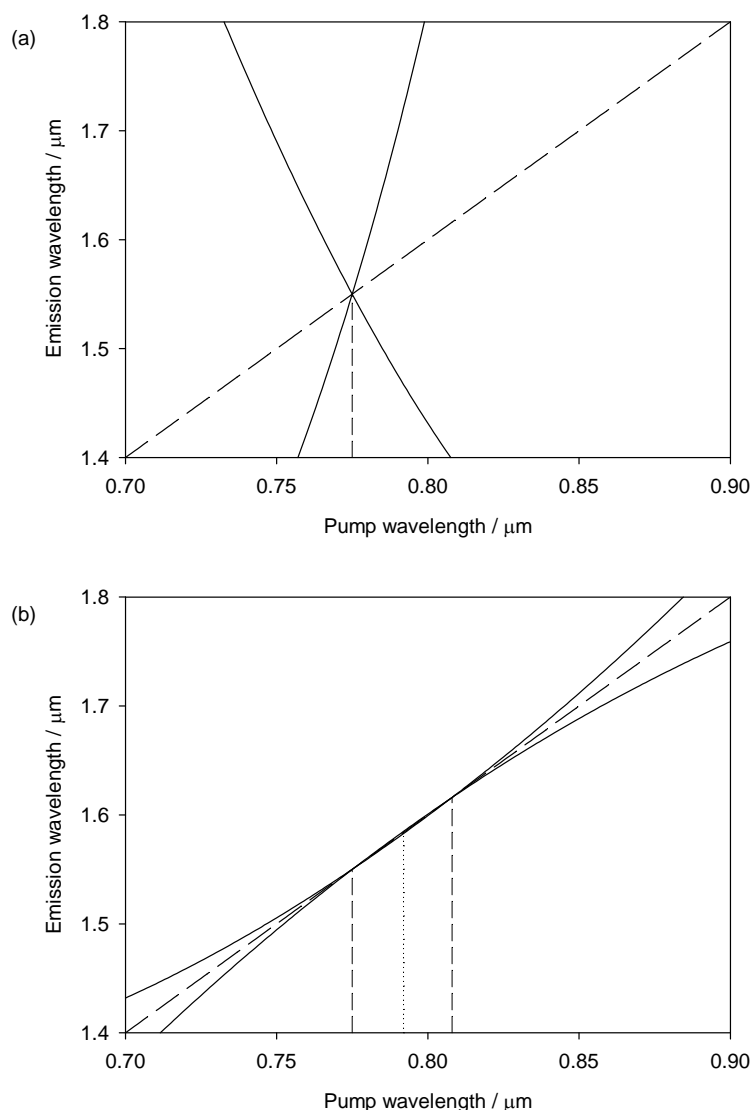


Figure 4-2 Plot of collinear emission wavelength versus pump wavelength in (a) PPLN $\Lambda= 9.35 \mu\text{m}$ grating (b) PPKTP, (---) denotes intersection of signal of idler curve when $\Lambda= 46.2 \mu\text{m}$, (....) denotes intersections when $\Lambda= 46.1 \mu\text{m}$.

In contrast the collinear downconversion emission wavelength vs. pump wavelength relationships for PPKTP crystal shows that approximately degenerate photons are produced over a $\sim 30 \text{ nm}$ bandwidth of pump wavelengths, see Figure 4-2 (b). Therefore the PPKTP crystal would be more suited to pulsed pumping applications.

In addition to the above arguments PPKTP and PPLN are both robust materials with high resistance to laser damage and high powers. In PPLN, the greatest refractive index partial derivative with respect to temperature is $(\partial n_e / \partial T)_{LN}$ and is about ~ 2.5 larger than

4. Pump enhanced source of correlated photons in the telecoms band

$(\partial n_z / \partial T)_{KTP}$, the largest corresponding quantity in PPKTP. This indicates that's PPLN would be preferable if broad wavelength tune-ability was an important feature but a PPKTP based system would be less demanding in terms of the required temperature stabilisation.

PPKTP and PPLN are both more expensive than the BBO and KDP, mainly due to the poling process. Raicol crystals [74] are able to produce antireflection coated $1 \times 6 \times 10$ mm PPKTP crystals for ~4000 Euros at the time of writing while HC photonics [75] are able to produce coated PPLN crystals of the same dimensions for ~ 4000 U.S dollars. In either case an additional 2000 U.S dollars (equiv.) was payable if the manufacturer did not already have a suitable photolithographic mask. Raicol did possess a suitable mask for the required interaction in PPKTP but HC photonics did not have a $9.3 \mu\text{m}$ mask for the PPLN interaction, although they did have a $9.5 \mu\text{m}$ mask corresponding to a higher phasematching temperature of 60°C for the required process.

The combination of the possibility to pulse pump PPKTP in future experiments requiring indistinguishable photons, a reduced temperature sensitivity of the phasematching process in PPKTP and the reduced cost of PPKTP were three key reasons why a PPKTP solution was chosen over PPLN.

4.3 Waveguide and bulk pump-enhanced approaches to improved downconversion efficiencies

In parallel to the investigation of choosing a non-linear material for the source, two approaches for further improving the efficiency of photon pair generation were investigated. The first involves fabricating the downconversion medium in the conformation of waveguide. Photolithography techniques are used to create the waveguides from wafers of the parent crystal. PPKTP waveguides are available commercially from AdvR [76], while HC photonics supply waveguided PPLN. The second approach would be to use bulk non-linear material placed in an optical resonator for the pump beam. This section compares the relative merits of the two approaches in terms of the spectral brightness, spectral bandwidth and spatial mode of the emitted light, in addition to factors such as cost and susceptibility to damage.

4. Pump enhanced source of correlated photons in the telecoms band

For the case of a waveguide nonlinear crystal with nonlinearity d_{eff} , length L , cross-sectional A_I , the spectral density of the signal photons emitted with wavelength λ_s within an interval $d\lambda_s$ can be calculated through Fermi's golden rule to be [77]:

$$dP_{s,WG} = \frac{16\pi^3 \hbar d_{eff}^2 L^2 c P_p}{\epsilon_0 n_s n_i n_p \lambda_s^4 \lambda_i A_I} \text{sinc}^2\left(\frac{\Delta k L}{2}\right) d\lambda_s \quad (4.3.1)$$

where P_p is the incident pump power. In the bulk case, the spectral density is found through a similar analysis to be [77]:

$$dP_{s,bulk} = (2\pi)^4 f(\lambda_s) \frac{2\hbar c d_{eff}^2 L \lambda_p P_p}{\epsilon_0 n_p^2 \lambda_s^5 \lambda_i^2} d\lambda_s \quad (4.3.2)$$

Considering the 792 nm (y) \rightarrow 1584 nm (y) + 1584 nm (z) interaction in PPKTP, Figure 4-3 plots the spectral densities for the waveguide and bulk configurations. The spectrally broad and flat curve for the bulk source contrasts with the narrow band nature of the waveguide source. The spectral density for the bulk material would be flat except for the factor $f(\lambda_s)$ that was introduced in order to distinguish between the emission power associated with the signal photons (defined as longer wavelength photon here) from that associated with the idler photons; this is necessary because without $f(\lambda_s)$, equation (4.3.2) relates to the total parametric fluorescence power, (i.e. $P_s + P_i$).

The form of the waveguide emission profile can be interpreted as follows; the pump and downconverted photons are limited to the modes of propagation allowed by the thin waveguide. As a result the only wave vectors that need to be considered for phasematching are those that are almost collinear. The collinear wave vectors are enshrined within $\Delta k = k_p - k_s - k_i - 2\pi/\Lambda$ of the sinc^2 term in equation (4.3.1), and only a limited number of emission wavelengths correspond to a small Δk consistent with significant conversion. Therefore in the waveguide, the downconverted power can be seen to be 'squeezed' into relatively few modes spectral modes. It follows that the downconversion emission from a waveguide source is spectrally bright but narrowband.

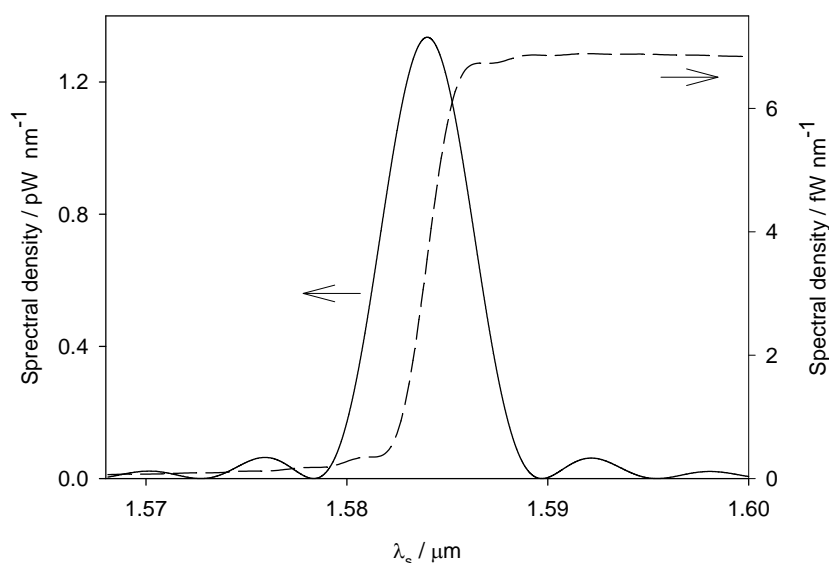


Figure 4-3 Calculated spectral density profiles for 1mW pump through waveguided PPKTP (solid line, left axis) and bulk PPKTP (broken line, right axis) profiles.

In contrast, the flatness of the bulk spectral density is due to freedom of the pump and downconverted photons to occupy any number of free space modes. Since the wavevector describing the propagation of a photon at a fixed wavelength is different for each propagation mode, the wavelength must change with mode in order to maintain phasematching and this results in an emission characterized by broad spectral bandwidth and a broad range of emission directions. Analytically equation (4.3.2) corresponds to an integration of a sinc^2 term similar to that in equation (4.3.1), over a continuum of modes.

Based on equations (4.3.1) and (4.3.2), Figure 4-4 shows the calculated pair generations rates expected from waveguided PPKTP, bulk PPKTP and pump enhanced bulk PPKTP configurations. The dimensions for the waveguide are taken from the example in ref [77] having $A_t = 15 \mu\text{m}^2$ and $L = 10 \text{ mm}$. The bulk crystal was also taken to have $L = 10 \text{ mm}$. Coupling into optical fibre is a necessary requirement for any telecoms band source, and the calculations assume that all of the photon pairs from the waveguide are ‘useable’ since they may be mode matched efficiently to single mode fibres. Only a limited range of angles are collectable from a bulk source, and equation (4.3.2) describes the emitted power at a given wavelength but makes no reference to the emission angle. Therefore it was necessary to assume $\Delta k = 0$ and calculate the relationship between emission angle θ_s and λ_s , allowing for λ_s in equation (4.3.2) to be limited according to the collectable θ_s ; this is based on exactly

4. Pump enhanced source of correlated photons in the telecoms band

the same principle as was used for determining d_{eff} in BBO, see section 2.4.2. For the bulk calculations, a collection cone angle of 1° about the pump beam was considered.

Although coupling of the emission from the waveguide mode to single mode optical fibre will be greater than the coupling from the bulk emission, the benefit will be offset to a degree by the relatively low coupling efficiency of pump light into the waveguide, taken as 60% for the calculation [78]. The relatively low coupling efficiency of the pump to the waveguide also eliminates the possibility to incorporate the waveguide within an optical cavity for further enhancement of the pump field, unless the cavity mirrors form the ends of the waveguide.

For low pump powers, the waveguided PPKTP benefits from the additional spectral brightness conveyed by Figure 4-3 (a). However the small size of the waveguide mode means that the damage threshold is reached at relatively low pump powers. Since the damage threshold is dependent on both the wavelength and temporal properties of the light, there is no damage data exactly relevant to the experiment here, and although damage-free pumping with ~ 400 nm cw light at a power density of 1.3×10^5 W/cm² has been reported [77], there have been reports of damage from cw pumping for lower power densities at visible wavelengths [79]. Therefore it is unclear whether the waveguide could be used for pump powers > 10 's mW.

In the bulk the diameter of the pump mode can be several hundred microns, therefore neither the bulk nor pump enhanced schemes would reach the likely damage threshold even for several watts of pump power. Cheap single longitudinal mode diode lasers at 780 nm with powers up to 1.5 W are commercially available [73], and using such a device it would be feasible to access pair generation rates $> 10^9$ s⁻¹ in association with a pump enhanced scheme (enhancement factor > 10).

The small aperture of the waveguide means that the device could be rendered useless by damage to a relatively small volume of the material where as the bulk material is routinely fabricated with large aperture dimensions giving ample redundancy should damage occur.

At the time of writing, a PPKTP waveguide costs $\sim 30\%$ more than a bulk PPLN waveguide of the same length.

On balance of the factors discussed it was decided that a bulk, pump enhanced configuration would be incorporated into the source design.

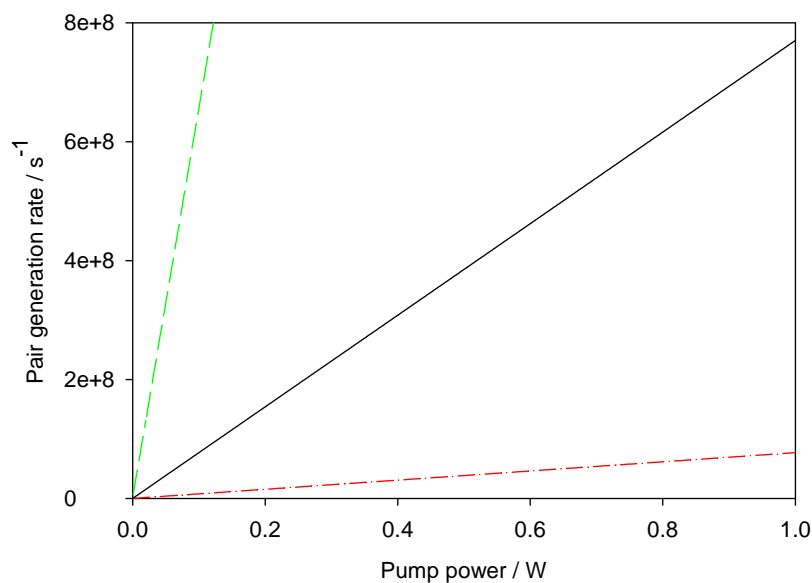


Figure 4-4 Predicted pair generation rates under different cw pumping regimes for the PPKTP waveguide (---), PPKTP bulk (-.-) and PPKTP bulk pump enhanced (—) setups, for the pump enhanced system the enhancement factor was 10.

4.4 Pump enhancement cavity design

This section presents the theory of the pump enhancement cavity and communicates the chosen parameters for the cavity incorporated into the pair photon source design in the context of design requirements.

4.4.1 Cavity mirror reflectivities

The pump enhancement cavity consists of two mirrors that are reflective at the pump wavelength but transmit at the downconverted wavelengths. One of the mirrors M_1 , with reflectivity and transmission amplitudes r_1 and t_1 respectively is designated the input coupler, and the second mirror M_2 with reflectivity r_2 and transmission t_2 is designated the output coupler. For the source design here, the nonlinear crystal is positioned centrally between the input and output coupler.

4. Pump enhanced source of correlated photons in the telecoms band

Figure 4-5 shows the schematic of the beam path taken by the pump light through the resonator. The incident beam has amplitude E_0 . In order to determine the transmitted amplitude E_T it is necessary to sum the individual amplitudes transmitted through M_2 corresponding to the consecutive half-integer round trips of the beam in the resonator:

$$\begin{aligned}
 E_T &= E_{T,1/2} + E_{T,3/2} + E_{T,5/2} + \dots \\
 &= E_0 t_1 t_2 (1-\alpha) e^{i\phi} \left[1 + r_1 r_2 (1-\alpha)^2 e^{2i\phi} + r_1^2 r_2^2 (1-\alpha)^4 e^{4i\phi} + \dots \right] \\
 &= \frac{E_0 t_1 t_2 (1-\alpha) e^{i\phi}}{1 - r_1 r_2 (1-\alpha)^2 e^{2i\phi}}
 \end{aligned} \tag{4.4.1}$$

where α is the single pass loss through the cavity, and accounts for absorption, scattering and Fresnel losses, including those incurred by the presence of the non linear crystal. ϕ is the single pass phase shift. The back reflected amplitude E_R is found by summing the amplitudes resulting from the initial back reflection of E_0 from M_1 and the amplitudes transmitted through M_1 after successive integer round trips around the cavity:

$$\begin{aligned}
 E_R &= E_{R,0} + E_{T,1} + E_{T,2} + \dots \\
 &= -r_1 E_0 + E_0 t_1^2 r_2 (1-\alpha)^2 e^{2i\phi} \left[1 + r_1 r_2 (1-\alpha)^2 e^{2i\phi} + r_1^2 r_2^2 (1-\alpha)^4 e^{4i\phi} + \dots \right] \\
 &= \frac{-r_1 E_0 + E_0 r_2 (1-\alpha)^2 e^{2i\phi} (r_1^2 + t_1^2)}{1 - r_1 r_2 (1-\alpha)^2 e^{2i\phi}}
 \end{aligned} \tag{4.4.2}$$

The minus sign on the term associated with $E_{R,0}$ is due to the pi phase change upon reflection at M_1 . The π phase change due to the reflection from M_2 associated with the other terms has been ignored as π is small in comparison to ϕ .

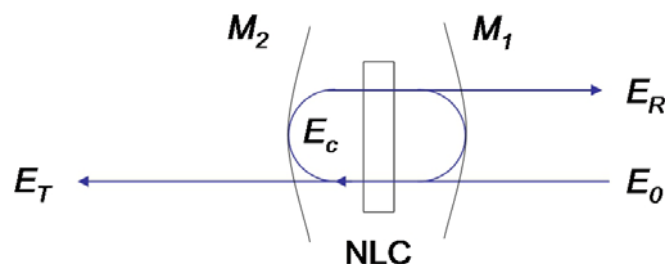


Figure 4-5 A pump enhancement cavity with an intracavity nonlinear crystal (NLC).

4. Pump enhanced source of correlated photons in the telecoms band

The intensity of the reflected beam I_R as a fraction of the incident intensity I_0 is:

$$\begin{aligned} \frac{I_R}{I_0} &= \frac{E_R E_R^*}{E_0 E_0^*} = \frac{\left[-r_1 + r_2 (1-\alpha)^2 e^{2i\phi} (r_1^2 + t_1^2) \right] \left[-r_1 + r_2 (1-\alpha)^2 e^{-2i\phi} (r_1^2 + t_1^2) \right]}{\left[1 - r_1 r_2 (1-\alpha)^2 e^{2i\phi} \right] \left[1 - r_1 r_2 (1-\alpha)^2 e^{-2i\phi} \right]} \\ &= \frac{R_1 + R_2 e(1-\alpha)^4 - 2\sqrt{R_1} \sqrt{R_2} (1-\alpha)^2 \cos 2\phi}{1 + R_1 R_2 (1-\alpha)^4 - 2\sqrt{R_1} \sqrt{R_2} (1-\alpha)^2 \cos 2\phi} \end{aligned} \quad (4.4.3)$$

where the intensity reflection and transmission coefficients for M_1 are $R_1 = r_1^2$ and $T_1 = t_1^2$ respectively, and scattering and absorption losses are assumed to be negligible i.e. $R_1 + T_1 = 1$. Similarly for mirror M_2 , the reflected and transmitted intensities are $R_2 = r_2^2$ and $T_2 = t_2^2$ respectively.

A plot of I_R/I_0 versus ϕ is shown in Figure 4-6 taking $R_1 = R_2 = 0.95$, and $\alpha = 0$. The maximum value of I_R/I_0 corresponds to the situation where almost all of the incident power is reflected by M_1 . When $\phi = n\pi$ where n is an integer, I_R is a minimum and corresponds to the cavity resonance condition. I_R goes to zero in Figure 4-6 and this corresponds to a special case known as impedance matching. Impedance matching occurs when R_1 is equal to $\left[R_2 (1-\alpha)^4 \right]$.

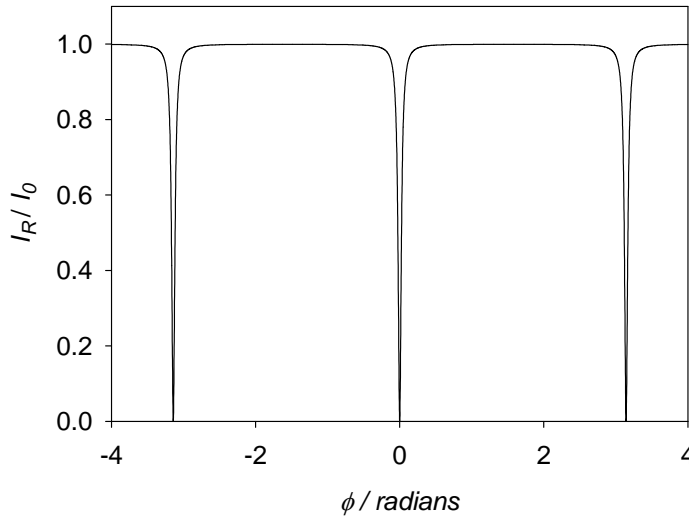


Figure 4-6 Back reflected intensity from enhancement cavity versus cavity single pass phase shift.

The transmitted intensity as a fraction of the incident light is given by:

4. Pump enhanced source of correlated photons in the telecoms band

$$\frac{I_T}{I_0} = \frac{E_T E_T^*}{E_0 E_0^*} = \frac{T_1 T_2 (1-\alpha)^2}{1 + R_1 R_2 (1-\alpha)^4 - 2\sqrt{R_1} \sqrt{R_2} (1-\alpha)^2 \cos 2\phi} \quad (4.4.4)$$

The pump field circulating within the cavity I_C , can be arrived at by realising that I_T is equal to I_C multiplied by the single pass loss through the resonator and the transmittance through M_2 , combining this and equation (4.4.4) gives:

$$\frac{I_C}{I_0} = \frac{T_1}{1 + R_1 R_2 (1-\alpha)^4 - 2\sqrt{R_1} \sqrt{R_2} (1-\alpha)^2 \cos 2\phi} \quad (4.4.5)$$

Equation (4.4.5) is referred to as the cavity enhancement or pump enhancement factor and is a maximum when the cavity is on resonance. The mechanism used for locking ϕ on resonance for the source design investigated here is described in section 4.5.3.

Through equations (4.4.3)-(4.4.5), R_1 and R_2 are key design parameters of the optical cavity. One of the design requirements for the correlated photon source is that the pump enhancement factor should be ≥ 10 in order to give a clear performance gain over the non-pump enhanced equivalent. A second requirement comes from the architecture for the polarization entangled photon pair scheme presented in the following chapter, for which the correlated photon source discussed here is a central component; for the entanglement scheme it is necessary that $I_R \approx I_T$ because I_R and I_T are input to separate arms of a two-beam interferometer, and are subsequently required to interfere at a recombiner with sufficient visibility in order that two optical paths of the interferometer can be locked relative to one another using an error signal derived from the interference fringes.

In addition, high reflectivity mirrors were avoided since when R is close to one, manufacturing limitations mean that losses often make up the balance, i.e. $T = 0$ and there is no transmission through the associated mirror. Using equations (4.4.4)-(4.4.5) and taking a relatively modest value for $R_2 = 0.98$, Figure 4-7 (a) shows how the pump enhancement varies with R_1 , I_R/I_0 and I_T/I_0 are shown as a function of R_1 in (b). $R_2 = 0.98$ and $R_1 = 0.88$ were chosen for the cavity mirror reflectivities for the pump enhancement cavity design since a pump enhancement > 10 is predicted with $I_R = I_T$, as required.

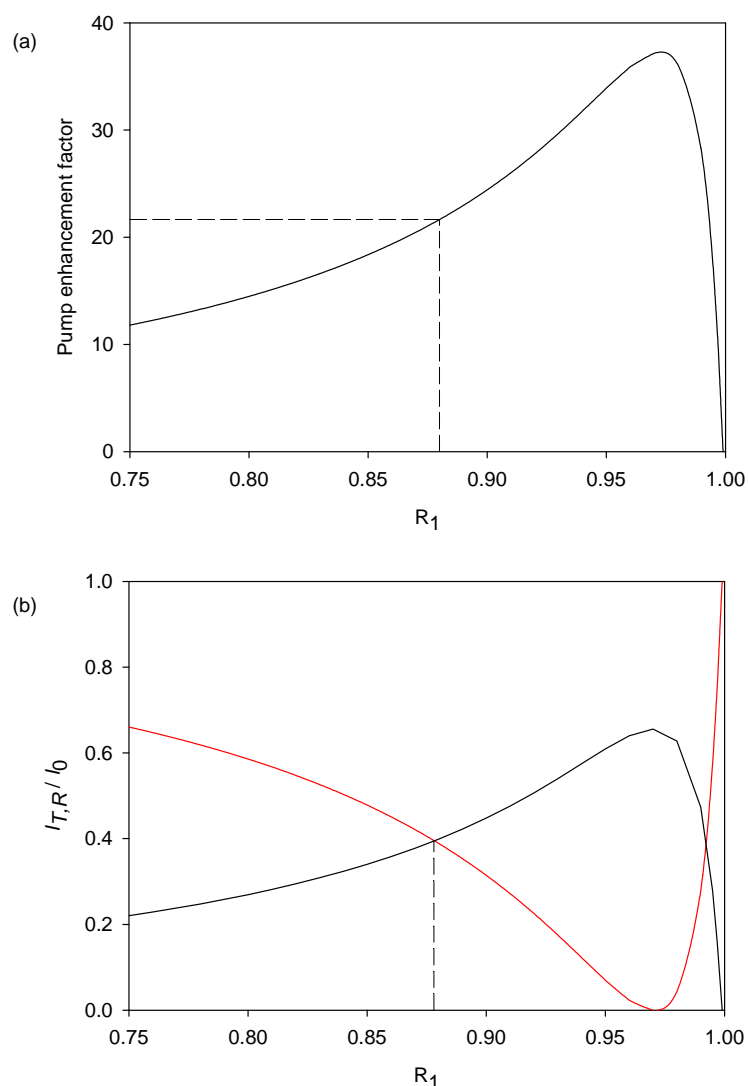


Figure 4-7 Plotted as a function of R_1 ; (a) the pump enhancement factor and (b) the transmitted (black line) and reflected (red line) intensity from the enhancement cavity. For both (a) and (b) $R_2 = 0.98$ and the vertical drop lines correspond to the chosen R_1 for the pump enhancement cavity.

4.4.2 Resonator dimension and mirror curvatures

In addition to the selection of the pump enhancement mirror reflectivities, it was necessary to establish the dimensions of the resonator. Unlike stimulated processes, for SPDC there is no enhancement in the conversion efficiency from focussing the pump beam to a small spot in the crystal since the conversion is dependent only on the total pump power [see equation (4.3.2)]. From the viewpoint of maximising photon indistinguishability it is desirable to have a large pump beam waist [80]. A large beam waist would also help to minimize diffraction losses. In order to maximize the beam waist of the resonator mode while preventing mode

4. Pump enhanced source of correlated photons in the telecoms band

clipping of the beam by the 1mm dimension of the crystal, it was decided that a cavity mode with a 200 μm beam waist diameter would be incorporated into the design.

Given the required mode size for the resonator, it was then necessary to find a configuration of cavity mirror curvatures and separations that enabled the mode to propagate in a stable fashion. The only constraint on the resonator design from a component size perspective was that the mirror separation needed to be greater than 40 mm in order to accommodate the crystal oven. The constraint of a symmetrical cavity was placed by the design for the polarisation entangled pair photon source presented in the next chapter. The mode analysis for the cavity could be carried out using a geometric approach described in the literature [81], or through matrix optics. Matrix optics was the principal method employed here.

Matrix optics provides a means to determine the effect that individual optical components have on the diameter and radius of curvature of a propagating beam. In the matrix approach, each optical component of a system is represented by a 2x2 “ABCD” matrix of the form $\begin{pmatrix} A & B \\ C & D \end{pmatrix}$ with elements characteristic to the associated optic. The relevant matrices for the cavity stability and mode matching (see section 4.4.3) problems are shown in Table 4-1 [82]. For a Gaussian beam, the wavefront radius of curvature and the transverse beam size can be described by a single complex radius of curvature q :

$$\frac{1}{q(z)} = \frac{1}{R(z)} - i \frac{\lambda}{\pi \omega(z)^2} \quad (4.4.6)$$

Where $\omega(z)$ and $R(z)$ are the beam width and radius of curvature at position z respectively. An optical element described by an $ABCD$ matrix acts upon an incident beam with complex radius q_{in} according to:

$$q_{out} = \frac{Aq_{in} + B}{Cq_{in} + D} \quad (4.4.7)$$

The radius of curvature and transverse size of the beam after the transformation are recovered from the real and imaginary components of q_{out} , according to equation (4.4.6). If the Gaussian beam propagates through further elements then the matrix operations for each element can be applied in turn, with q_{out} from the previous matrix transformation becoming

4. Pump enhanced source of correlated photons in the telecoms band

q_{in} for the new optical element. In this way complete optical systems can be modelled. The system matrix for a symmetrical optical cavity with a centrally positioned crystal is given by:

$$M_{cavity} = \begin{pmatrix} 1 & \frac{L}{2n_{y,KTP}} \\ 0 & 1 \end{pmatrix} \begin{pmatrix} 1 & \frac{d-L}{2} \\ 0 & 1 \end{pmatrix} \begin{pmatrix} 1 & 0 \\ -\frac{1}{f_1} & 1 \end{pmatrix} \begin{pmatrix} 1 & \frac{d-L}{2} \\ 0 & 1 \end{pmatrix} \begin{pmatrix} 1 & \frac{L}{n_{y,KTP}} \\ 0 & 1 \end{pmatrix} \begin{pmatrix} 1 & \frac{d-L}{2} \\ 0 & 1 \end{pmatrix} \\ \times \begin{pmatrix} 1 & 0 \\ -\frac{1}{f_2} & 1 \end{pmatrix} \begin{pmatrix} 1 & \frac{d-L}{2} \\ 0 & 1 \end{pmatrix} \begin{pmatrix} 1 & \frac{L}{2n_{y,KTP}} \\ 0 & 1 \end{pmatrix} \quad (4.4.8)$$

Component	ABCD matrix	Parameters
Free space	$\begin{pmatrix} 1 & d \\ 0 & 1 \end{pmatrix}$	$d =$ free space path
Thin lens	$\begin{pmatrix} 1 & 0 \\ -\frac{1}{f} & 1 \end{pmatrix}$	$f =$ focal length
Spherical dielectric interface	$\begin{pmatrix} 1 & 0 \\ \frac{n_2 - n_1}{n_2 \cdot R} & \frac{n_1}{n_2} \end{pmatrix}$	$R =$ Interface radius of curvature $n_1 =$ first medium refractive index $n_2 =$ second medium refractive index
Crystal	$\begin{pmatrix} 1 & \frac{L}{n} \\ 0 & 1 \end{pmatrix}$	$L =$ Crystal length $n =$ refractive index

Table 4-1 ABCD matrices used to study the enhancement cavity mode stability and to study the problem of mode matching the Ti-sapphire pump to the enhancement cavity

The complex radius of curvature for the ‘start’ q_{in} is calculated from the beam waist at the cavity centre, where $R \rightarrow \infty$. f_1 and f_2 are equal to half the curvature radii of mirrors M_1 and M_2 respectively. d is the mirror separation, L is the crystal length and $n_{y,KTP}$ is the refractive index of the pump wavelength in the crystal. A stable solution is found if the condition $q_{out} = q_{in}$ is satisfied, where $q_{out} = M_{cavity}q_{in}$. The PSST software suite [83] works under these principles and using the software a suitable stable mode was found with a cavity

4. Pump enhanced source of correlated photons in the telecoms band

configuration consisting of two concave mirrors with 75 mm curvature radii, separated by 60 mm and with a 10 mm length KTP crystal located centrally between the mirrors. The stable mode was symmetric with a 200 μm waist at the 792 nm pump wavelength.

4.4.3 Mode matching of the pump beam to the resonator

In order to maximize the power coupled into the chosen cavity mode it was necessary to match the cavity mode with that of the incoming pump beam. A mode matching lens can be used to transform the incoming pump beam waist with radius $w_{0,pump}$ at position $z_{0,pump}$, to a waist of radius $w_{0,cavity}$ centred within the cavity at $z_{0,cavity}$. The focal length and position of the mode matching lens required to do this was determined using the ABCD matrix propagation method.

The ‘start’ value of q and position for the mode matching system are given by $w_{0,pump}$ and $z_{0,pump}$ respectively. However the pump beam waist was inside the Ti-Sapphire cavity and therefore measurements for the beam waist and its position were unobtainable hence the pump was focussed through an artificial waist using a 300 mm focal length lens. The waist size and its location were then determined using a beam profiling system (Spiricon). Horizontal and vertical beam radius measurements as a function of position along the beam are shown in Figure 4-8: also shown are least squares fitted curves to the data following the equation for Gaussian beam propagation:

$$w(z) = w_0 \sqrt{1 + \left(\frac{zM^2\lambda}{\pi w_0^2} \right)^2} \quad (4.4.9)$$

where the beam waist radius w_0 , and M^2 values were fitting coefficients. The M^2 value is a measure of the laser beam mode quality. The M^2 value averaged across both fits was 1.50, while beam waist radii along the horizontal and vertical direction were found to be and 55.5 μm and 59.8 μm respectively.

For the mode matching analysis, the relevant ABCD system matrix was:

4. Pump enhanced source of correlated photons in the telecoms band

$$\begin{aligned}
 M_{MM} = & \begin{pmatrix} 1 & z_{MM} - z_{0,pump} \\ 0 & 1 \end{pmatrix} \begin{pmatrix} 1 & 0 \\ -\frac{1}{f_{MM}} & 1 \end{pmatrix} \begin{pmatrix} 1 & z_{M_1(convex)} - z_{MM} \\ 0 & 1 \end{pmatrix} \begin{pmatrix} 1 & 0 \\ \frac{n-1}{n \cdot R_1} & \frac{1}{n} \end{pmatrix} \begin{pmatrix} 1 & t_{M_1} \\ 0 & 1 \end{pmatrix} \\
 & \times \begin{pmatrix} 1 & 0 \\ \frac{1-n}{R_2} & n \end{pmatrix} \begin{pmatrix} 1 & \frac{d-L}{2} \\ 0 & 1 \end{pmatrix} \begin{pmatrix} 1 & L \\ 0 & 1 \end{pmatrix} \quad (4.4.10)
 \end{aligned}$$

where z_{MM} and $z_{M_1(convex)}$ are the positions of the mode matching lens and outer surface of the input coupler respectively. f_{MM} is the focal length of the mode matching lens, n and t_{M_1} are the refractive index and thickness of the input coupler respectively. R_1 and R_2 are the mirror curvatures experienced by the beam at the outer and inner surfaces of M_1 respectively. Note that for this investigation, meniscus mirrors were used. Therefore $R_1 = R_2$ and the matrix product of the fourth and sixth terms in the equation is the unit matrix and the system behaves as if the interfaces of M_1 were perpendicular to the beam wavefronts.

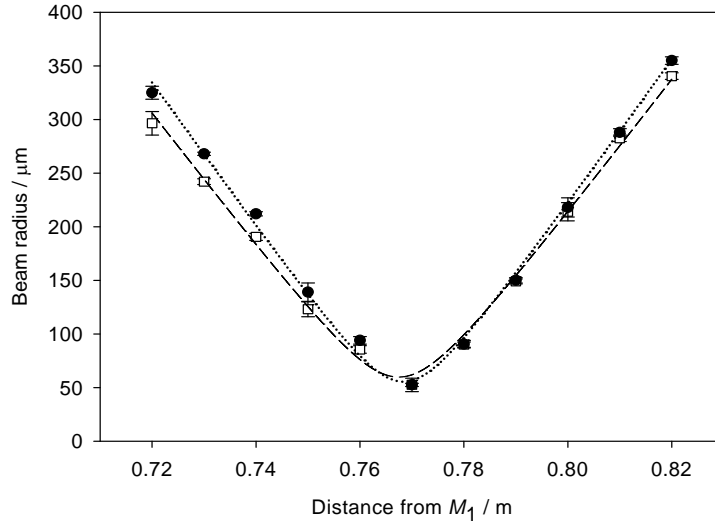


Figure 4-8 Measured Ti-sapphire beam radius in the horizontal (filled points) and vertical (unfilled points) directions (orthogonal to pump propagation direction).

$z_{0,pump}$ was fixed, while z_{MM} and f_{MM} were variable. The position of the cavity could be altered through $z_{M_1(convex)}$. The system matrix M_{MM} applied to $w_{0,pump}$ at $z_{0,pump}$ gives the beam curvature and radius at the cavity centre position z_{centre} , $R(z_{centre})$ and $w(z_{centre})$ respectively. Mode matching is characterized by (i) the waist radius of the formed mode $w(z_{waist})$ being equal to the calculated waist radius for the stable cavity mode in section 4.4.2, and (ii) the position of the formed waist z_{waist} being located at the centre of the cavity z_{centre} ,

4. Pump enhanced source of correlated photons in the telecoms band

as calculated for the symmetric stable mode. In order to verify that (i) and (ii) are satisfied, first write:

$$w(z_{centre}) = w(z_{waist}) \sqrt{1 + \left(\frac{(z_{centre} - z_{waist})}{z_R} \right)^2} \quad (4.4.11)$$

$$R(z_{centre}) = (z_{centre} - z_{waist}) \left[1 + \left(\frac{z_R}{(z_{centre} - z_{waist})} \right)^2 \right] \quad (4.4.12)$$

where $z_R = \pi w^2(z_{waist})/\lambda$. For $w(z_{waist})$, rearrange (4.4.11), substitute for $(z_{centre} - z_{waist})$ from equation (4.4.12) and assume that $(z_{centre} - z_{waist})$ is small such that

$(z_{centre} - z_{waist}) + \frac{z_R^2}{(z_{centre} - z_{waist})} \approx \frac{z_R^2}{(z_{centre} - z_{waist})}$ to give:

$$w(z_{waist}) = \frac{w(z_{centre})}{\sqrt{1 + \left(\frac{(z_{centre} - z_{waist})}{z_R} \right)^2}} = \frac{w(z_{centre})}{\sqrt{1 + \left(\frac{\pi w^2(z_{centre})}{\lambda R(z_{centre})} \right)^2}} \quad (4.4.13)$$

$z_{centre} - z_{waist}$ is estimated through rearranging (4.4.12) and then assuming that $(z_{centre} - z_{waist})$ is small:

$$(z_{centre} - z_{waist}) = \frac{R(z_{centre})}{\left[1 + \left(\frac{z_R}{(z_{centre} - z_{waist})} \right)^2 \right]} \approx \frac{R(z_{centre})}{\left[1 + \left(\frac{\lambda R(z_{centre})}{\pi w^2(z_{centre})} \right)^2 \right]} \quad (4.4.14)$$

From the ABCD calculation, and equation (4.4.13), Figure 4-9 (a) shows how $w(z_{waist})$ changes with $z_{M_1(convex)} - z_{MM}$ for different $z_{MM} - z_{0,pump}$ when $f_{MM} = 200$ mm. From equation (4.4.14), Figure 4-9 (b) describes how $(z_{centre} - z_{waist})$ changes with $z_{M_1(convex)} - z_{MM}$ and $z_{MM} - z_{0,pump}$. The figures show that favourable cavity mode conditions of a ~ 200 μ m beam waist located near the cavity centre are attained when the mode matching lens-cavity separation is ~ 0.5 m and the pump beam waist is positioned 0.3 m from the mode matching lens.

4. Pump enhanced source of correlated photons in the telecoms band

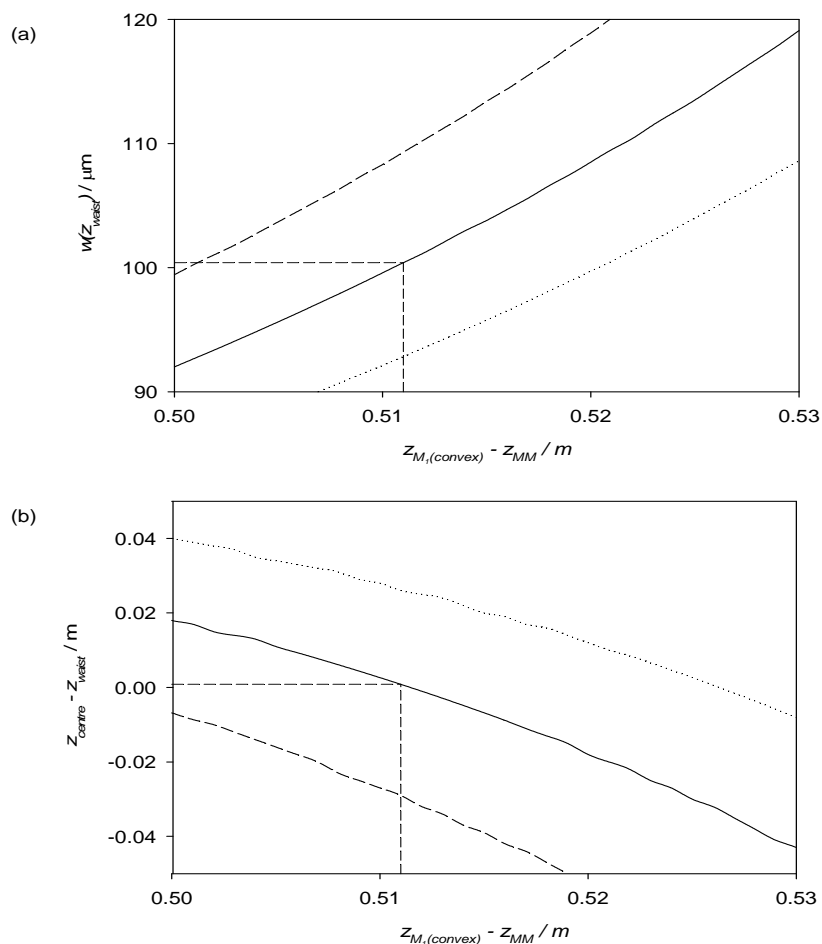


Figure 4-9 From ABCD analysis of cavity mode matching problem (a) Relationship between formed beam waist radius with input coupler to mode matching lens separation (b) Position of formed beam waist relative to cavity centre as a function of input coupler to mode matching lens separation. The broken, solid and dotted lines correspond to pump beam waist to mode matching lens separations of 0.29 m , 0.30 m and 0.31 m respectively. The points located by the horizontal and vertical drop lines correspond to the chosen design parameters.

4.5 Experimental setup for pump enhanced pair generation scheme

4.5.1 Layout of optical and electrical components

The experimental setup is shown in Figure 4-10, the following sections give a description of the purpose for the components and, where appropriate, design and setup procedures are also described.

4. Pump enhanced source of correlated photons in the telecoms band

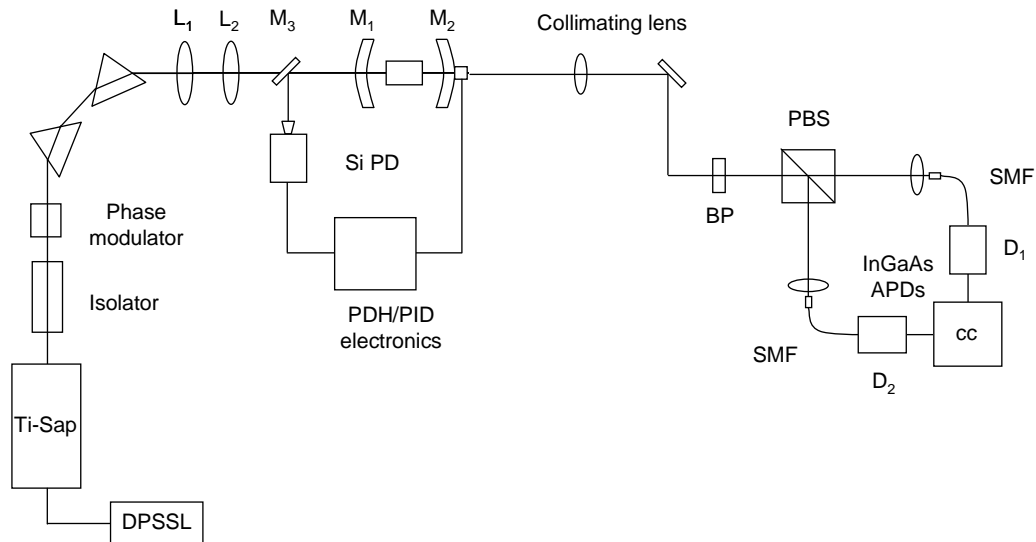


Figure 4-10 Setup for generating photon pairs in the telecom band through a pump enhanced downconversion process. Also shown is the setup for detection of single and pair photons.

4.5.2 Diode pumped solid-state laser and Ti-Sapphire pump laser schemes

The parent pump laser for the setup was a single longitudinal mode diode pumped solid state laser (DPSSL) emitting at 532 nm (Coherent Verdi V10). The 532 nm was used to pump a titanium-sapphire bow-tie resonator CW single frequency laser (Microlase MBR-100). The wavelength of the resonator was set to 792 nm: coarse tuning was achieved using a birefringent filter, and an intracavity etalon enabled finer but discrete control of the wavelength in addition to ensuring single frequency operation. The transmission of the etalon was locked to the laser frequency in order to prevent mode hops. An optical isolator was positioned after the Ti-sapphire laser in order to prevent perturbation of the laser due to back reflections.

4.5.3 Enhancement cavity alignment and locking

The lenses L_1 and L_2 are the 300 mm and 200 mm focal length lenses respectively that are involved in the problem of mode matching the pump beam to the enhancement cavity, see section 4.4.3. With the pump field circulating within the enhancement cavity defined by M_1 , M_2 and the position of M_2 ramped, interference fringes were observed between the pump light reflected back from M_1 and a component of the circulating field emerging out through M_1 . The fringes were measured on a silicon detector [SiPD, Osram BPX-65 silicon PIN

4. Pump enhanced source of correlated photons in the telecoms band

photodiode], see Figure 4-11(a). The minimum in the observed intensity corresponds to when the interfering light components are π out of phase, which is consistent with the cavity on-resonance, c.f. Figure 4-6. Note that good cavity alignment and mode matching was indicated by a single large fringe feature, as opposed to multiple smaller and different fringe features when the pump power is distributed to other cavity modes.

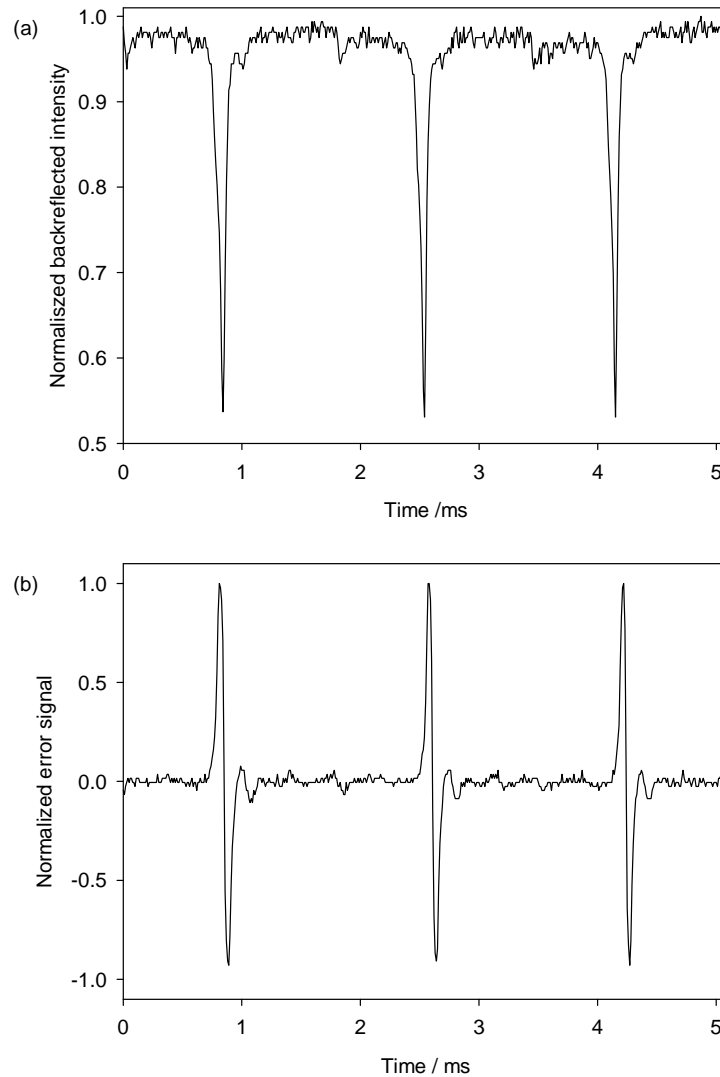


Figure 4-11 (a) Interference fringes observed on the silicon photodiode shown in figure Figure 4-10 when the enhancement cavity length was scanned (b) Pound-Drever-Hall locking signal resulting from the signal in (a).

The cavity was held on resonance for maximum pump enhancement using the Pound-Drever-Hall (PDH) technique [84]. The PDH technique relies on the principle that a cavity acts as a filter with transmission lines spaced in frequency by the free spectral range of the cavity $\Delta\nu = c/2L$. In the PDH scheme the pump beam is phase modulated, creating two frequency

4. Pump enhanced source of correlated photons in the telecoms band

sidebands at $\omega \pm \Omega$, where ω is referred to as the carrier frequency and Ω is the modulation frequency. The sidebands are normally outside the pass band of the cavity, and are therefore reflected back by the input coupler. The light back from the input coupler also contains a component from the intracavity field which is at the carrier frequency. Since the sidebands are at a different frequency to the returning cavity field and has a definite relation with it, a beat frequency is formed. The amplitude of the RF beat frequency measured at SiPD is dependent on the separation between the centre frequency of the laser beam from the cavity resonance peak: this dependency is the mechanism for the PDH error signal generation. The error signal [shown in Figure 4-11(b)] is then passed to the piezo-ceramic mounted mirror M_2 through PID feedback electronics such that the cavity is held on resonance.

A Pound-Drever-Hall locking scheme has many favourable properties such as being relatively insensitive to amplitude fluctuations of the laser, and allowing lock to the minimum of the back reflected interference fringe. PDH setups are also able to compensate for rapid frequency fluctuations of the laser that may cause resonance to be lost; the frequency fluctuations may occur on a time scale less than the cavity decay time hence the phase of the leakage component to the measured beat frequency will not be sensitive to the fluctuation but the directly reflected component will be, and this change will be fed to the error signal for adjustment of the cavity length.

For the investigations here a 50 MHz phase modulator was used (Leysop PM50). The electronics required for generation of the error signal from the beat frequency amplitude and the electronics for feedback control were produced in-house. The feedback control voltage was amplified (Piezomechanik SVR 500/3) and sent to an annular piezoceramic material on which the output coupler cavity mirror was mounted.

4.5.4 PPKTP oven calibration

The crystal was housed in an oven heated using a resistive element, and the power applied to the resistor was set by a control unit. The control unit displays a number N for a given adjustment of the applied power. It was necessary to calibrate the oven such that the N -values could be related to oven temperatures. The calibration curve shown in Figure 4-12 was measured using a thermocouple.

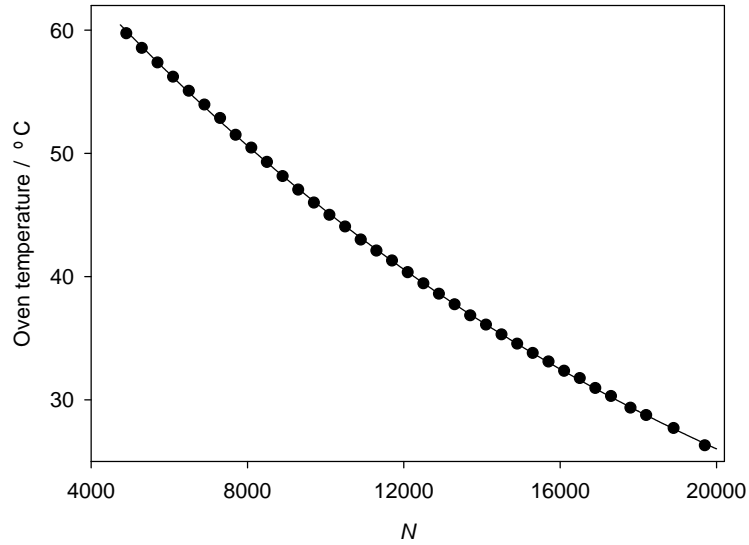


Figure 4-12 Crystal oven calibration curve relating the control unit variable N with oven temperature

4.5.5 Collection optics

The problem of collecting the downconversion generated within the PPKTP crystal into the single mode fibre (SMF) detector inputs is shown in Figure 4-13. The pump beam waist at the crystal centre ω_1 was measured to be $198 \mu\text{m}$. Since the detectors fibre inputs were ~ 0.5 m from the cavity centre some collimation was necessary to limit loss of downconversion signal through diffraction. The physical size of the cavity and cavity mirror mounts meant that the collimating lens could not be positioned closer than ~ 160 mm to the cavity centre, and therefore a 160 mm focal length lens (f_1) was chosen for the collimation and was positioned at its focal length from ω_1 . A lens was also required for coupling the collimated downconversion photons into the single mode fibre, the lens was positioned at its focal length f_2 from the fibre tip.

4. Pump enhanced source of correlated photons in the telecoms band

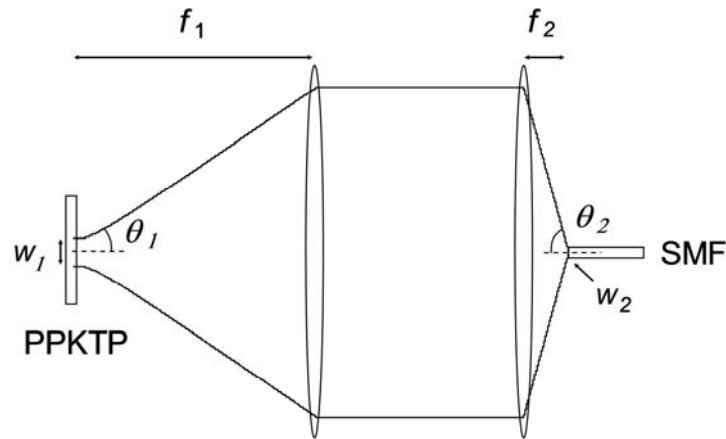


Figure 4-13 Gaussian beam analysis of the collection of downconverted photons from the crystal to the single mode optical fibre detector inputs.

The choice of f_2 was made through an ABCD analysis of the system in Figure 4-13. The downconversion beam was assumed to be at the degenerate wavelength (1584 nm), take the pump beam diameter at the crystal centre and have a diffraction profile of $M^2 = 1.5$, which is also the same as the pump. The parameters of interest for maximizing coupling to the fibre are the spot size formed by the beam at the fibre tip w_2 and the cone angle θ_2 of the beam formed by the coupling lens. w_2 and θ_2 were calculated for a range of f_2 values as shown in Figure 4-14. Ideally, w_2 should be within the 10 μm mode field diameter of the fibre, and θ_2 should be within the $\sim 5^\circ$ numerical aperture of the fibre mode. Although the figure indicates that there was no focal length f_2 that allowed both conditions to be fulfilled, the calculation shows that the optimum focal length was somewhere between 8 mm and 14 mm. Therefore 11 mm focal length lenses were used. As discussed in section 4.3, the downconversion emission is actually spread over a range of angles about the pump, and the calculation here effectively only considers the collinear emission. However since we are primarily interested in the degenerate collinear emission the approximation used is a reasonable one.

4. Pump enhanced source of correlated photons in the telecoms band

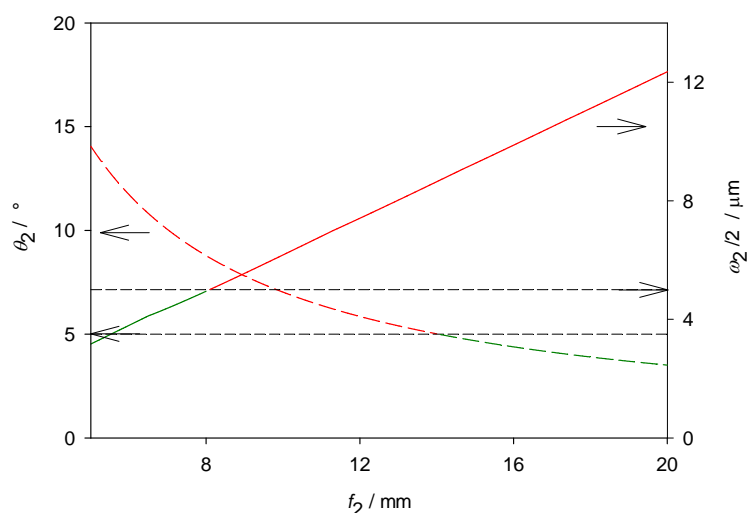


Figure 4-14 Plot of how the focussed cone angle (broken line) and focussed spot size (solid line) at the detector fibre inputs change with focal length of the fibre coupling lens. The upper horizontal broken line denotes the radius of the fibre mode and the lower broken horizontal line corresponds to the acceptance angle of the fibre. Green/red denote regions of favourable/unfavourable conditions with respect to the associated parameter.

4.5.6 Photon counting detectors

The detectors used for single photon counting of the generated pairs were InGaAs/InP Geiger Mode APDs (Princeton Lightwave PGA 600 series). The detector inputs were single mode fibre at telecoms wavelength. Unlike the silicon APDs used in chapter 2-3, the InGaAs /InP detectors are not ready to receive a photon continuously until detection but are operated in a gated fashion. These single photon counters suffer from higher dark counts than silicon detectors and the gated operation can greatly increase signal to noise for pulsed detection as well as help to suppress dark counts due to after pulses. Also using two gated detectors for measuring coincidence events due to correlated photon pairs can reduce the number of accidental coincidences recorded resulting from uncorrelated two-photon events: see section 4.5.9.

The APD is reverse biased above the breakdown voltage with a 1 ns, ~ 4 V amplitude pulse. During this time a photon incident at the APD can initiate an avalanche. The resulting flow of electrons is detected by the internal electronics, resulting in an output pulse from the detector. The detection unit also converted the raw output pulses into NIM-type (square) pulses provided that the raw pulse amplitudes exceeded a predetermined value. The discrimination was set by simultaneously observing the raw output and square wave pulses

4. Pump enhanced source of correlated photons in the telecoms band

and then choosing the highest discrimination threshold for which a raw detection pulse was always accompanied by a NIM pulse output from the detector. The NIM-type output pulses were compatible with the coincidence counter used for registering when simultaneous pulses were generated from two detectors (see following section). The detector reverse bias (before over biasing) was set by optimising the measured count rate while maintaining signal to noise ratio (SNR), where the noise was taken as the measured dark count rate. Figure 4-15 shows how the measured count rate and SNR varied with APD bias when sub-threshold fluorescence from a 1550 nm laser diode (Avanex A1905 LMI) was coupled into one of the detectors. Over the biasing range 59.5-60.5 V the SNR remains approximately constant while the measured count rate rises linearly. Beyond 62 V biasing, the dark counts begin to dominate the measured count rate. On the basis of SNR and count rate arguments an APD bias of 60.7 V was used for further measurements made from the detector associated with Figure 4-15.

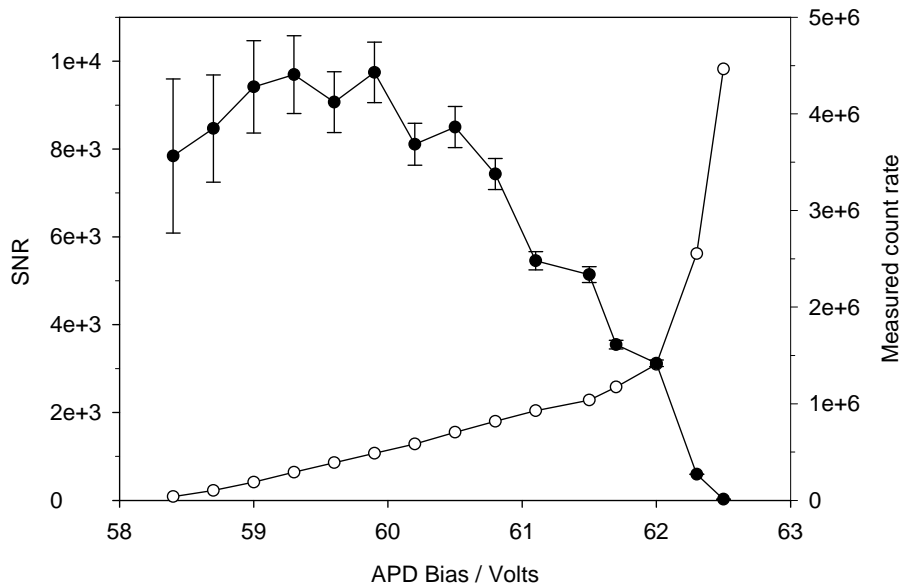


Figure 4-15 Measurements of SNR (filled circles) and photon count rate (unfilled circles) upon coupling 1550 nm fluorescence from a sub-threshold laser diode into an InGaAs/InP APD for different bias settings

4.5.7 Measurement of detector quantum efficiency

In order to estimate the brightness of the source it was necessary to know the effective loss due to non unity detection efficiency; a schematic of the quantum efficiency measurement setup is shown in Figure 4-16.

4. Pump enhanced source of correlated photons in the telecoms band

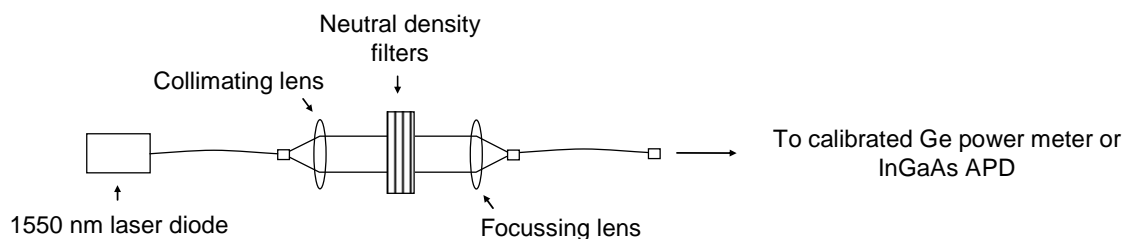


Figure 4-16 Schematic of setup used for measuring the quantum efficiency of the InGaAs/InP APDs

The calibration source was a 1550 nm laser diode (Avanex A1905 LMI). In order to ensure the power delivered to the detectors was low such that the measured count rate $N_{measured}$ was much less than the detector gate frequency $\nu_{gate} \sim 6$ MHz, the source was attenuated by a series of neutral density filters. The attenuation of the combined neutral density filters was assessed by operating the laser diode well above threshold corresponding to an output power of ~ 7 mW. The power transmitted to a calibrated meter (Melles Griot Universal power meter, germanium head) was recorded in the presence and absence of the neutral density filters, and from the two power values a filter transmittance of $(6.46 \pm 0.1) \times 10^{-6}$ was estimated.

In the absence of the filters, the laser current was then reduced for operation below threshold such that the signal level at the power meter was ~ 100 nW which is still comfortably within the measurable range. The filters were then positioned between source and detector. Upon connection of the output fibre to the InGaAs/InP APD, the number of photons per second delivered to the detector when the detector gate is ‘open’ is given by:

$$N_{QE=1} = \frac{P_{in} \lambda T_D}{hc} \quad (4.5.1)$$

where λ is the calibration wavelength, h and c are Plank’s constant and the speed of light in vacuum respectively. P_{in} is the power delivered to the APD through the fibre, given by multiplying the measured sub-threshold fluorescence power in the absence of the filters, with the transmittance of the filters. T_D is the detector duty cycle, which is a product of the gate opening time (1 ns) and ν_{gate} .

4. Pump enhanced source of correlated photons in the telecoms band

Provided that the measured photon count rate $N_{measured} \ll \nu_{gate}$ such that two photon events (that cannot be resolved by the detectors) can be discounted, an estimate of the detector quantum efficiency, η is given by:

$$\eta = \frac{N_{measured}}{N_{QE=1}} \quad (4.5.2)$$

Where $N_{measured}$ was corrected for dark counts. For the two detectors used in this chapter, quantum efficiencies of 4.87 ± 0.25 % (D_1) and 11.98 ± 0.25 % (D_2) were estimated. The count rates associated with the measurement were $\sim 10^3 \text{ s}^{-1}$ which is similar to the counting rates measured during most experiments incorporating these detectors in this portfolio. The relatively low measured quantum efficiency of D_1 was later found to be due to corrosion of the thermoelectric cooling element, which meant that the detector temperature could only be lowered to 230 K whereas the normal operational temperature is 215-220 K.

4.5.8 Spectral filtering;

For the initial build the wavelength dispersive prisms in Figure 4-10 were absent, and RG1000 absorption glass filters were placed in front of the detectors to block the (short wavelength) pump light but allow the (longer wavelength) downconversion to pass. Under these conditions, count rates of up to $\sim 1000 \text{ s}^{-1}$ were measured but the count level was not influenced greatly by the enhancement cavity being held on or off resonance, and it was therefore concluded that the measured counts were not due to downconversion or residual pump light.

Figure 4-17 shows how the measured photon count rate changed upon varying the 532 nm pump power level to the Ti-sapphire laser. The levelling of the measured count rate near the threshold of the Ti-sapphire laser is consistent with the expected behaviour of Ti-sapphire fluorescence that would occur due to gain saturation. Characteristic Ti-sapphire fluorescence extends out to 1050 nm and would be transmitted through the RG1000 absorption filters. The placement of the two prisms before the enhancement cavity, as shown in Figure 4-10 eliminated the fluorescence to a negligible level.

4. Pump enhanced source of correlated photons in the telecoms band

30 nm bandpass (BP) filters centred at 1584 nm were procured to replace the RG filters in order that any detected counts above the noise could be reasonably attributed to degenerate downconversion.

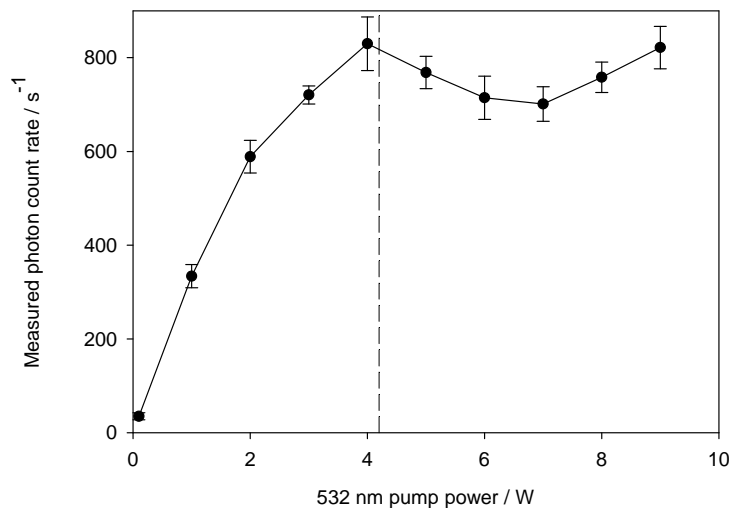


Figure 4-17 Detection of Ti-sapphire fluorescence photons with the InGaAs/InP APDs. The broken vertical line at ~ 4.2 W pumping corresponds to the lasing threshold of the Ti-sapphire laser. For subsequent experiments a twin prism arrangement was used to remove the fluorescence.

4.5.9 Coincidence counter setup

Because the single photon counters were operated in gated mode, in order to monitor the coincident photon arrivals between the two detectors the biasing pulses for the two units were triggered simultaneously by a pulse generator (Thandar TG105). The maximum possible frequency output of the function generator (6 MHz) was used to maximize the effective detection efficiency. The coincidence counter (PicoQuant HydraHarp 400 Time-Correlated Single Photon Counting Module) had two input channels and a coincidence was registered when pulses were received at both input channel within 30 ns of one another. A 2 ps resolution time stamp was allocated to each coincidence event that indicated the arrival time difference between the two pulses. Using the time stamp information a coincidence histogram was compiled, Figure 4-18 corresponds to the histogram measured from the correlated photon pair setup in Figure 4-10. It is interesting to compare the histogram with that shown in figure 2-10 which corresponds to the measurement of coincidence events due to correlated photons pairs using two non-gated detectors. For that histogram in addition to a narrow peak due to the correlated photons there was a low level of coincidences recorded across a wide range of relative arrival times due to uncorrelated photons. In

4. Pump enhanced source of correlated photons in the telecoms band

contrast, for the gated detector coincidence histogram, *all* of the coincidence events are localised within a ~ 1 ns time frame which corresponds to the detector gate time. Therefore the possibility for ‘accidental’ coincidence events due to uncorrelated photon is greatly reduced in the gated scheme because such events can only occur within a small time window, compared to a much larger time window for the un-gated detector scheme.

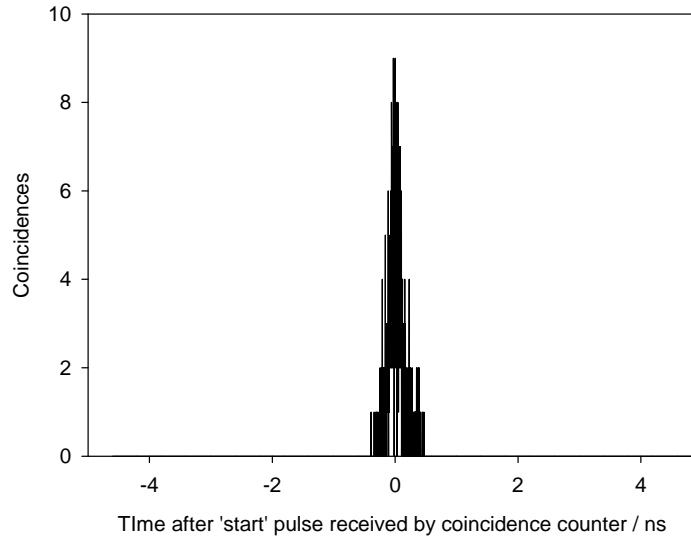


Figure 4-18 Coincidence histogram of correlated photon pair arrivals at two detectors for the setup shown in Figure 4-10. The data was collected over 10 minutes and the total number of coincidences was 617.

4.6 Characterisation of pump enhanced pair photon source

4.6.1 Measurement of downconversion spatial profile

The collimation and collection of the downconverted light into the single mode fibres was as described in section 4.5.5. The downconverted light was filtered to a ~ 30 nm band pass centred about the degenerate wavelength 1584 nm. Detectors D_1 and D_2 were mounted on manual $x-y$ (horizontal-vertical) translation stages that were adjusted to optimise the photon single count rates. The D_1 $x-y$ translation could also be moved through computer controlled stepper motors allowing for spatial profiling of the downconverted light at D_1 , and the spatial profiling at D_1 of the two-photon coincidence rate with D_2 . For this, a 1 mm aperture was placed on D_1 . The downconversion was observed to form a ~ 5 mm diameter

4. Pump enhanced source of correlated photons in the telecoms band

spot at D_1 while the spatial extent at D_1 of the coincident photon arrival rate with D_2 was just $\sim 2\text{-}3$ mm. Assuming that the spatial profile of the downconversion coupled into D_2 had the same diameter as that coupled into D_1 , then it would be expected that the spatial extent at D_1 of the coincidence rate with D_2 would be at least 5 mm. The lower measured value was probably due to the low number of events making up the coincidence profile plot, resulting from the aperture on D_1 that limited the measured coincidence counting rate to a maximum of just $\sim 0.5\text{ s}^{-1}$. Therefore the measured 2-3 mm coincidence spot diameter could be just the ‘tip’ of a much larger profile.

The maxima of the single photon and coincidence profiles coincide and this is indicative of D_2 being optimally positioned in the conjugate beam, assuming that the region of maximum single photon counts corresponds to the maximum in the filter transmission profile. Also note that the spatial profile of the downconversion is spot-like as was calculated for the degenerate output in PPKTP [Figure 4-1 (d)] as opposed to ring-like as was calculated for the degenerate output in BBO [Figure 4-1 (a)].

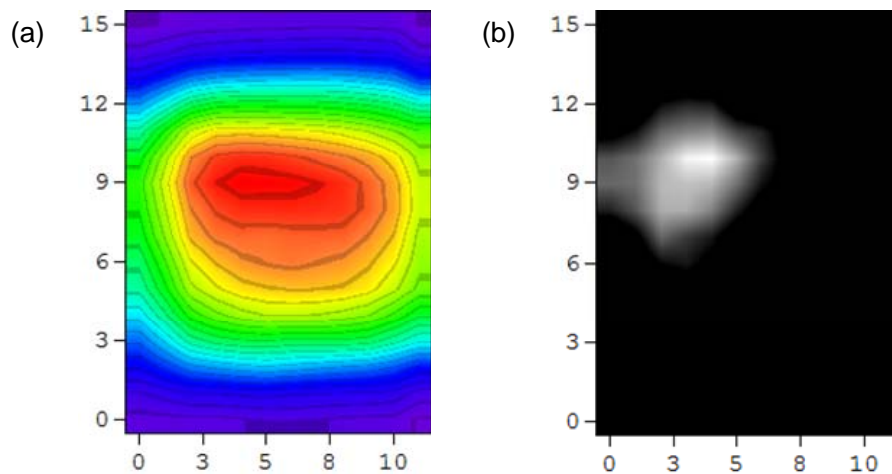


Figure 4-19 (a) Spatial profile of the downconverted light at D_1 (b) The measured coincidence profile at D_1 . A 1 mm aperture was mounted onto D_1 and the count rates were measured across the x - y grid with increments of 1 mm. No aperture was mounted onto D_2 . The duration of each measurement was 60s. The scales on the horizontal and vertical axes are in mm.

The x - y mapping setup was also used to study how the coincidence counting rate spatial profile measured at D_1 was effected by translation of D_2 , see Figure 4-20. As expected from

4. Pump enhanced source of correlated photons in the telecoms band

phase matching considerations the coincidence profile measured at D_1 moved in the opposite direction to the D_2 translation. The distance moved by the D_1 coincidence spot was approximately equal to the D_2 movement which is consistent with the photons at D_2 in Figure 4-20 (b) and (c) remaining close to the degenerate wavelength, ensured through the narrow pass filtering. The intensity of the coincidence spot at D_1 was found to decrease as D_2 was moved away from the optimal position which was partly due to a decrease in singles counts at D_2 , and partly due to fewer singles counts at D_1 in the spatial region where correlations with D_2 were found. The drop in the single photon count rates at D_1 and D_2 could be due to a change in the collected emission wavelength resulting in reduced transmission through the band pass filters.

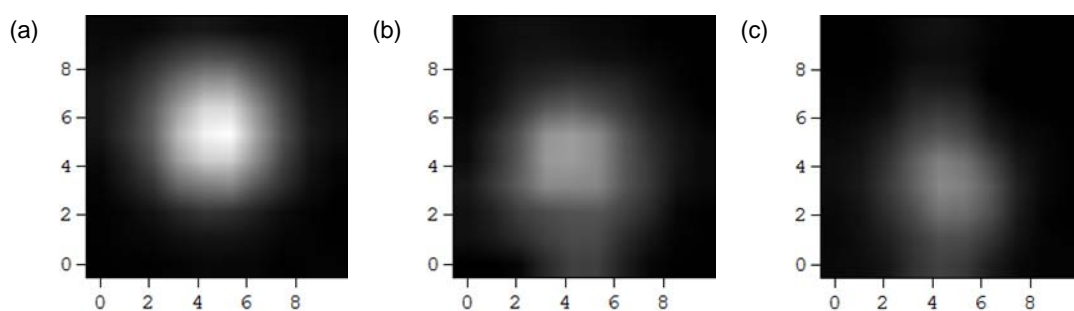


Figure 4-20 Spatial profile of the coincidence rate measured at D_1 for (a) positioning of D_2 giving optimum count rate (b) when detector D_2 was moved 1 mm ‘upwards’ relative to the position for (a), (c) when D_2 was moved 2 mm ‘upwards’ relative to the position for (a). The count rates were measured across the x-y grid with a spacing of 1 mm. No apertures were mounted on D_1 or D_2 .

4.6.2 Single photon and two photon coincidence rates

Table 4-2 shows the measured single photon counting rates at D_1 and D_2 (see Figure 4-10 for setup), in the absence ($N_{D1,nonPE}$ and $N_{D2,nonPE}$ respectively) and presence ($N_{D1,PE}$ and $N_{D2,PE}$ respectively) of the enhancement cavity, locked on resonance. Also shown are the coincidence counting rates with and without the resonant cavity ($N_{c,PE}$ and $N_{c,nonPE}$ respectively) and estimations for the dark count rates on D_1 and D_2 ($N_{D1,DC}$ and $N_{D2,DC}$ respectively). All of the singles count rates shown in Table 4-2, including the dark count measurements were taken from the mean count rate (s^{-1}) over a ten second measurement period. The coincidence counting rates were calculated from the total number of coincidences recorded over a ten minute time period.

4. Pump enhanced source of correlated photons in the telecoms band

The uncertainties on the single count rate measurements were given by the standard deviation about the mean of the associated measurement dataset. The uncertainties on the dark counts were 13 % on D_1 and 22 % on D_2 , a factor of 3-4 times larger than the ' \sqrt{N} ' uncertainty that would be expected if the dark counts were due to 'true' photon detection events. The higher dark count noise level on D_2 was probably associated with the corrosion damage of the detector thermo electric cooling element. The uncertainties on $N_{D1,nonPE}$ and $N_{D2,nonPE}$ were 8.4 % and 10 % respectively which was between 2-3 times larger than the \sqrt{N} uncertainty; the major uncertainty contributor was the dark count rate noise, while there was also further contribution due to fluctuations in the pump power. Similarly the uncertainties on $N_{D1,PE}$ and $N_{D2,PE}$ were 3.0 % and 2.0 % respectively which is also 2-3 times larger than the \sqrt{N} uncertainty; since $N_{D1,PE}$ and $N_{D2,PE}$ were much larger than $N_{D1,DC}$ and $N_{D2,DC}$ the uncertainty contribution on $N_{D1,PE}$ and $N_{D2,PE}$ from dark count noise was small, and it is likely that the uncertainty was dominated by the fluctuations in the pump power.

Table 4-2 shows the measured pump enhancement factor EF_{pump} , which is estimated from the reflectivity of the output coupler R_{M_2} , the input power through M_1 (P_{in}) and the measured output power through M_2 (P_{out,M_2}) by:

$$EF_{pump} = \frac{P_{out,M_2}}{P_{in}(1 - R_{M_2})} \quad (4.6.1)$$

From the single photon and coincidence counting rate data, the single photon and coincidence rate enhancement factors due to the resonant cavity were calculated respectively from:

$$EF_{singles} = \frac{N_{s,PE}}{N_{s,nonPE}} \quad (4.6.2)$$

$$EF_{coinc} = \frac{N_{c,PE}}{N_{c,nonPE}} \quad (4.6.3)$$

where the single photon count rates in the absence and presence of the resonant pump enhancement cavity ($N_{s,nonPE}$ and $N_{s,PE}$ respectively) are corrected for dark counts. The calculated enhancement factors (4.6.1)-(4.6.3) agree within the estimated uncertainties. The uncertainty on $EF_{singles}$ was calculated using equation (4.6.4).

4. Pump enhanced source of correlated photons in the telecoms band

	No pump enhancement	Pump enhanced
<i>Pump beam measurement</i>		
Power into cavity	130.3±1.3	130.3 ± 1.3
Power transmitted through M ₂	-	25.25 ± 0.3
Enhancement factor	-	9.69 ± 0.14
<i>Downconversion single photon count rates / s⁻¹</i>		
D ₁ count rates	78.7	444.1
D ₁ Dark counts	29.5	29.5
D ₁ dark count corrected rate	49.3	414.7
Enhancement factor	-	8.40 ± 1.8
D ₂ count rates	121.4	906.4
D ₂ Dark counts	38.1	38.1
D ₂ dark count corrected rate	83.4	868.4
Enhancement factor	-	10.42 ± 1.5
<i>Downconversion coincidence count rates / s⁻¹</i>		
Measured coincidence rate	0.22	2.01
Enhancement factor	-	9.14 ± 0.8

Table 4-2 Comparison of the measured enhancement factors with respect to the pump beam, single photon count rates at D₁, D₂, and coincidence rate between D₁ and D₂. The units of pump beam power are mWs and the count rate units are s⁻¹.

4. Pump enhanced source of correlated photons in the telecoms band

$$u_{EF_{\text{singles}}} = EF_{\text{singles}} \left[\frac{\sigma_{N_{s,PE}}^2}{N_{s,PE}^2} + \frac{\sigma_{N_{s,nonPE}}^2}{N_{s,nonPE}^2} \right]^{1/2} \quad (4.6.4)$$

where $\sigma_{N_{s,nonPE}}$ and $\sigma_{N_{s,PE}}$ are the standards deviations about the mean measured non pump enhanced and pump enhanced single photon count rates (s^{-1}) respectively. Coincidence events were not recorded with a time stamp denoting when the event had occurred and therefore the standard deviation about the mean coincidence count rate per second was not known (only the total number of coincidences measured over a much longer period of time) and a similar expression to equation (4.6.4) for the uncertainty on EF_{coinc} was not possible. $u_{EF_{\text{coinc}}}$ was instead calculated from the \sqrt{N} uncertainties. This is reasonable because the Poissonian uncertainty on the $N_{c,PE}$ and $N_{c,nonPE}$ measurements were 8.7% and 2.9% respectively, which both exceed the likely contribution of the pump power fluctuations on the uncertainty, and the coincidence rate will not be significantly influenced by the detector dark count noise.

Because of the short detector gate opening time it was not possible for both detectors to trigger from two photons separated by $> 1\text{ns}$ apart and this greatly limited the possibility for the measurement of accidental coincidences due to uncorrelated photons (see Figure 4-18) and therefore the contributions to the coincidence rate from accidental coincidences were ignored. It is interesting to calculate the expected coincidence rate due to the detector dark counts (which are uncorrelated):

$$acc_{\text{dark}} = \frac{N_{D1,DC} \cdot N_{D2,DC}}{\nu_{\text{gate}}} \quad (4.6.5)$$

where ν_{gate} is the biasing frequency of the detectors. Evaluating equation (4.6.5) for the data in Table 4-2 gives $acc_{\text{dark}} \approx 1.9 \times 10^{-4} s^{-1}$ which is much less than the typically measured coincidence counting rate.

The reason for the reduced count rates measured at D_1 relative to D_2 was the lower quantum efficiency of D_1 . The difference in magnitude between the measured single photon and the coincidence counting rates can be largely explained through considering all of the losses associated with one of the two optical paths of the system in Figure 4-10 (collimating lens to D_1 or D_2).

4. Pump enhanced source of correlated photons in the telecoms band

Table 4-3 summarizes the measured losses of the horizontally polarized photons through the system to D_1 . The loss associated with components for which there was no supplier data was estimated using a 1550 nm laser diode source (Avanex A1905 LMI) in combination with a power meter (Melles Griot Universal power meter, Germanium head). The measured coincidence rate was divided by the measured losses through the system to D_1 to give an estimate of the number of singles counts expected at D_2 assuming perfect correlation between the beams to D_1 and D_2 (see Table 4-3). The measured singles count rate at D_2 was slightly higher than the expected singles rate derived from the measured coincidence rate and system losses to D_1 . Equivalently, given the observed singles count rate at D_2 and the system losses to D_1 , the measured coincidence rate was lower than expected. This is a common observation in SPDC experiments and occurs because in general the photons within the solid cone angle in one detection channel are correlated to photons defined by a larger cone angle in the second channel (see section 2.5). The lost coincidences could also be due to imperfect placement of the detectors, although the x - y mapping investigations in section 4.6.1 indicate this is not likely to be the case.

4. Pump enhanced source of correlated photons in the telecoms band

Pump enhanced setup	
Measured coincidence rate / s ⁻¹	2.01 ± 0.06
<i>Loss factors in photon path to D₁</i>	
Collimating lens transmittance	0.730 ± 0.015
Spectral Filtering	0.62 ± 0.005
Beam steering mirror (× 2) reflectance	0.840 ± 0.016
PBS H-pol transmittance	0.982 ± 0.005
D ₁ Fibre coupling lens transmittance	0.702 ± 0.010
D ₁ Fibre loss	0.297 ± 0.001
D ₁ Quantum efficiency	0.049 ± 0.0025
Expected singles counts at D ₂ / s ⁻¹	(5.29 ± 0.36) × 10 ²
Measured singles counts at D ₂ / s ⁻¹	(8.68 ± 0.30) × 10 ²

Table 4-3 Measured coincidence rate and losses from the collimated lens to D₁. From the measured coincidence rate and losses, a prediction for the singles count rate at D₂ is made. The estimated loss due to the enhancement cavity mirrors (<0.1%) was ignored.

By extending the analysis shown in Table 4-3 to account for the losses associated with both optical paths of the system, an estimate for the photon pair generation rate within a single fibre optic spatial mode was made. The analysis is shown in Table 4-4 together with an equivalent analysis for an experiment published in the literature where the same downconversion crystal and phasematching interaction was studied [59]. In that experiment the pump enhancement cavity was absent, and the reported value for the estimated pair generation rate per mW pump was comparable to the corresponding estimated value for the non pump enhanced setup studied here.

Taking the collection angle of the system [θ_1 in figure Figure 4-13] to be 0.21°, corresponding to those photons occupying a Gaussian beam with $M^2 = 1.5$, the model described in section 4.3 predicts a pair generation rate of $6.07 \times 10^4 / \text{s}^{-1} \text{ mW}^{-1}$ pump for the pump enhanced system, which is close to the estimated generation rate shown in Table 4-4.

4. Pump enhanced source of correlated photons in the telecoms band

		<i>No pump enhancement</i>	<i>Pump enhanced</i>
<i>A) This work</i>			
Measured coincidence rate / s ⁻¹		0.22 ± 0.019	2.01 ± 0.06
<i>Loss factors</i>			
Collimating lens transmittance	(0.730 ± 0.015) ²		
Spectral Filtering	(0.62 ± 0.005) ²		
Beam steering mirror (× 2) reflectance	(0.840 ± 0.016) ²		
PBS H-pol transmittance	0.982 ± 0.005		
D ₁ Fibre coupling lens transmittance	0.702 ± 0.010		
D ₁ Fibre loss	0.297 ± 0.001		
D ₁ Quantum efficiency	0.049 ± 0.0025		
PBS V-pol reflectance	0.995 ± 0.005		
D ₂ Fibre coupling lens transmittance	0.826 ± 0.010		
D ₂ Fibre loss	0.285 ± 0.001		
D ₂ Quantum efficiency	0.120 ± 0.0025		
Detector duty cycle	(6.18 ± 0.006) × 10 ⁻³		
Estimated pair generation rate / s ⁻¹		(8.91 ± 1.0) × 10 ⁵	(8.14 ± 0.7) × 10 ⁶
Total pump power / mW	130.3 ± 1.3		
Estimated pair generation rate / s ⁻¹ mW ⁻¹ pump		(6.83 ± 0.83) × 10 ³	(6.24 ± 0.55) × 10 ⁴
<i>B) Work of Kuzucu [59],[85]</i>			
Measured coincidence rate		1	-
<i>Loss factors</i>			
D ₁ Quantum efficiency	0.16		
D ₂ Quantum efficiency	0.24		
Detector duty cycle	0.001		
Recombining Beam splitter	0.5		
Interferometer loss	0.65 ²		
Fibre coupling efficiency	0.3 ²		
Pre-fibre losses	0.65 ²		
Estimated pair generation rate / s ⁻¹		3.24 × 10 ⁶	-
Total pump power / mW	350		
Estimated pair generation rate / s ⁻¹ mW ⁻¹ pump		9.26 × 10 ³	-

Table 4-4 Measured coincidence rates with and without pump enhancement together with a breakdown of losses within the system. Also shown is a similar analysis that was carried out on the available data from the experiment of Kuzucu.

4. Pump enhanced source of correlated photons in the telecoms band

4.7 Further source characterisation; Hong-Ou-Mandel interference

4.7.1 Experimental setup

A Hong-Ou-Mandel interference experiment was carried out to assess the indistinguishability of the photon pairs. A schematic of the setup is shown in Figure 4-21.

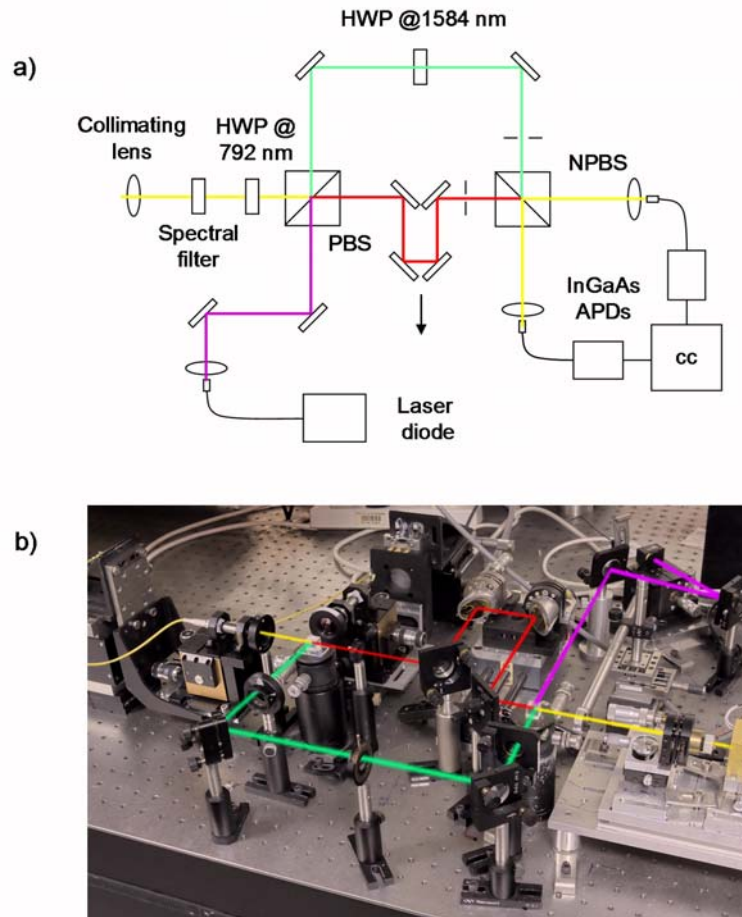


Figure 4-21 (a) Schematic of the Hong-Ou-Mandel experiment carried out on the generated photon pairs. The red and green paths represent the two arms of the interferometer, the yellow lines denote the entry and exit paths of the correlated photon pairs from the interferometer and the purple line denotes the input path of the laser diode to the interferometer, (b) photograph of the setup in (a).

The polarising beam splitter separates the orthogonal photons of each pair into separate paths of the interferometer. In one arm of the interferometer a half wave plate at the downconversion wavelength was positioned for polarisation control, in the other arm of the interferometer a roof-mirror mounted on a stepper motor translation stage formed the interferometer optical delay mechanism. The two beams were recombined at a non-polarising

4. Pump enhanced source of correlated photons in the telecoms band

beam splitter before distribution to the single photon and coincidence counting setups. A laser diode source could be coupled into the interferometer and was used to balance the two optical paths of the interferometer. Sections 4.7.2-4.7.4 detail the interferometer alignment and optimisation processes.

4.7.2 Interferometer optical path alignment and balancing procedure

The collinear geometry of the phasematching meant that the pump beam could be used to aid alignment. Since the pump was horizontally polarized and the first beam splitter of the interferometer was polarizing at 792 nm, a half wave plate at 22.5° to the horizontal was placed after the collimating lens to give even illumination of the two interferometer paths. The two beams were aligned on the recombiner such that a single interference fringe was observed on a viewing card at one of the interferometer output ports. The beam alignment was marked by aperture pairs in each arm of the interferometer.

The required interferometer optical path balancing was achieved by illuminating the interferometer with short coherence length light as described in section 2.6.4. The source was a laser diode at 800 nm (Limo laser diode array), coupled into the interferometer through the remaining ‘free’ port of the polarizing beam cube. Steering the laser diode light through the aperture pairs positioned in each interferometer arm ensured that the path of the diode light matched the aligned HOM interferometer. A silicon head power meter was positioned at an output port of the interferometer and the output monitored on an oscilloscope. As the optical delay was moved to within ~500 μm of the zero path length difference (ZPD) position, intensity interference fringes were observed as a modulation of the detected power, see Figure 4-22. Due to the large 10 μm step size of the optical delay translation stage and the absence of a method to measure the stage position to a higher accuracy than the step resolution, the figure shows the measured intensity modulation with time as the stage position was moved continuously through the fringes.

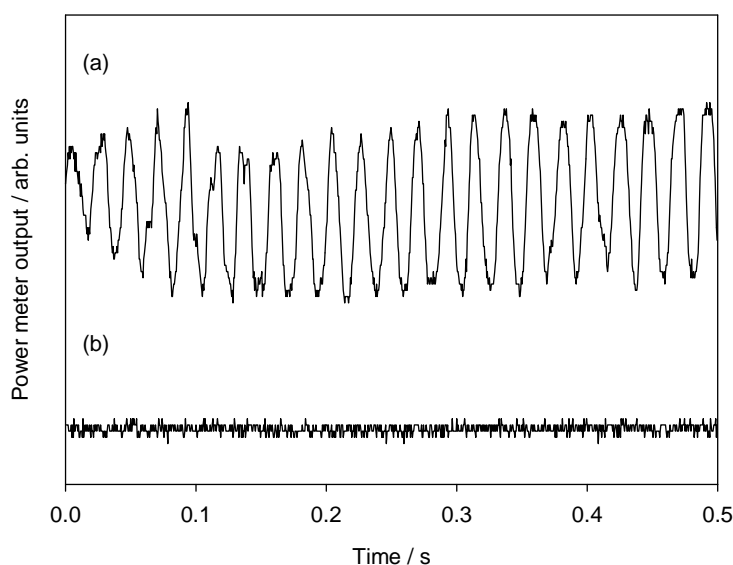


Figure 4-22 Measured output from the laser diode sourced two beam interferometer formed by the HOM framework (a) near and (b) far from the zero path difference point of the interferometer. The two traces are vertically offset from one another for clarity, but the vertical scales are the same.

4.7.3 Optimisation of photon polarisation for HOM interference

Once the alignment and path balancing was completed, the downconversion was focused in to the detector fibre using an 11 mm focal length lens. The pump half wave plate after the collimating lens was replaced with a narrow band interference filter (30 nm centred at 1584 nm) in order to block the pump beam.

The photons produced have orthogonal polarisations and since the photons are required to be indistinguishable for HOM interference, a half wave plate at 45° to the horizontal was required to rotate one of the photon polarizations. The half wave plate orientation was optimized by adjusting the path delay to be near the ZPD point through the laser diode interference procedure outlined in the previous section, and then minimizing the number of coincidences observed over a fixed time period, see Figure 4-23.

4. Pump enhanced source of correlated photons in the telecoms band

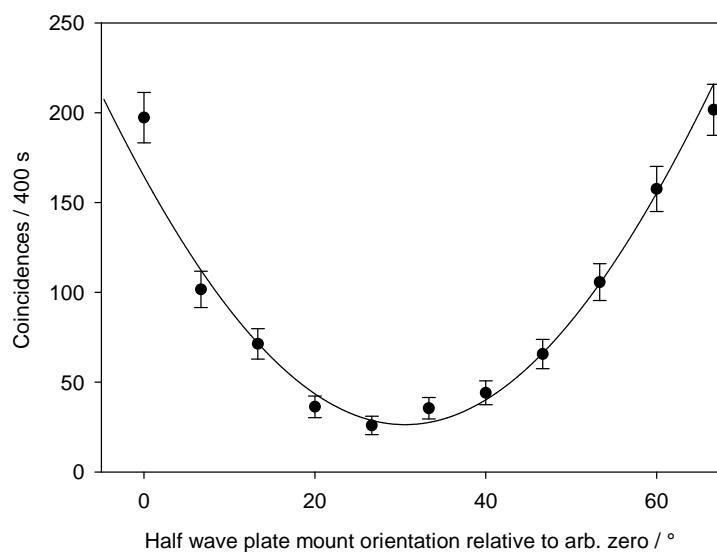


Figure 4-23 Measured coincidence rate as a function of half wave plate rotation mount angle relative to the arbitrary un-optimized position at 0°. The solid line is a Malus' law least squares fit to the data and gives a minimum in the coincidence rate at an angle of 23.4° for the mount. (corresponding to angle of 45° between the HWP and the pair photon polarisation basis).

4.7.4 Optimisation of crystal temperature for HOM interference

In addition to polarisation sensitivity, the HOM interference feature is also sensitive to spectral differences between the interfering photons and it was therefore necessary to ensure that the photons illuminating the two interferometer paths were degenerate. The phase matching for the generation process is slightly temperature dependent through the KTP refractive indices, therefore adjusting the crystal oven temperature afforded a simple means for wavelength adjustment of the emitted pairs emitted collinearly to the pump.

Figure 4-24 shows that there was a steady increase in the dip-visibility on going from a crystal temperature of 52.5°C to 21.5°C. It is not clear from the measurements whether further temperature decrease would have resulted in further visibility gain. Assuming that at a crystal temperature of 21.5 °C the degenerate photons were collinear with the pump and therefore input to the interferometer, through energy and exact phasematching considerations it was calculated that a 31°C temperature rise would lead to non-degenerate collinear signal and idler emission at 1580.8 nm and 1587.2 nm respectively, explaining the reduction HOM dip visibility at higher temperatures.

4. Pump enhanced source of correlated photons in the telecoms band

Also note from Figure 4-24 that the coincidence counting rate away from the dip is approximately constant over the tested temperatures, this can be explained in terms of (i) the flatness of downconversion spectral density in bulk crystals, see equation (4.3.2) and (ii) the ‘pair’ transmittance through the band-pass filter, defined as the product of the individual signal and idler transmittances. The pair transmittance is only 2.5% higher for degenerate pairs compared to when the signal and idler wavelengths take their calculated values at 52.5 °C.

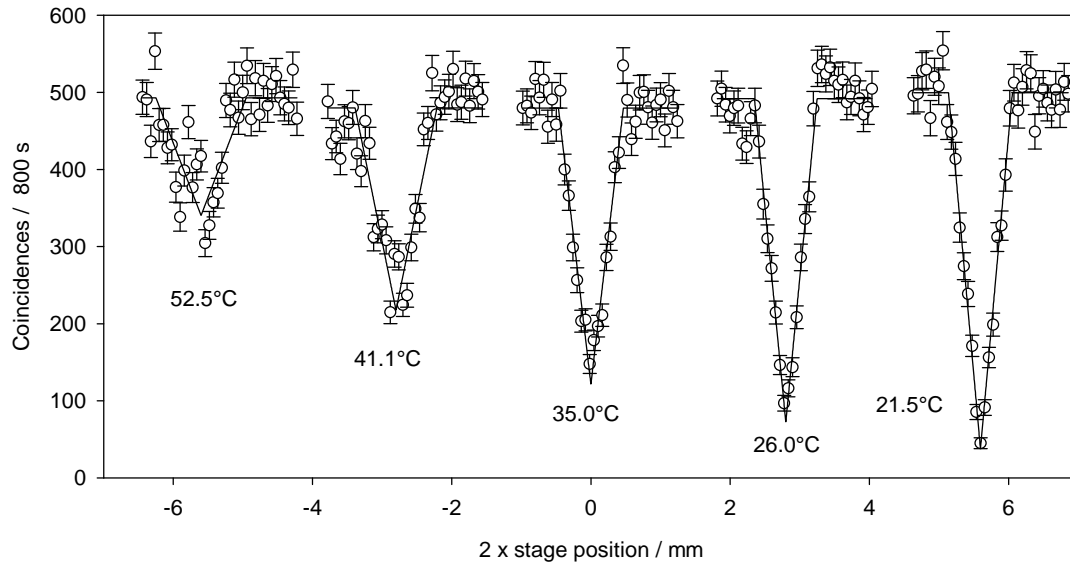


Figure 4-24 Measurement of HOM interferograms for various PPKTP oven temperatures, 26.0°C represents the coolest setting of the oven and 21.5 °C corresponds to the oven being switched off and was the average laboratory temperature. The interferograms have been displaced from one another along the position axis for clarity. The solid lines are numerical fits to the data (see section 4.7.5) The pump power was 115mW.

4.7.5 HOM interferogram characterisation

HOM interferograms were taken with both the enhancement cavity present and absent under otherwise identical temperature and downconversion polarisation conditions, see Figure 4-25. The solid lines shown in Figure 4-25 were least squares fits of a triangular function which is the predicted form of the HOM dip measured from pair photons generated through type-II phase matching [86].

The goodness of fit of the triangular function to the data was between 0.95-1.05 indicating an excellent fit in consideration of the data point uncertainties, which were taken to be the

4. Pump enhanced source of correlated photons in the telecoms band

\sqrt{N} statistical noise. This is reasonable as the \sqrt{N} uncertainty will dominate over other uncertainty contributions which were lower.

The data in Figure 4-25 verifies that the enhancement cavity did not have a significant effect on the measured interferogram other than to increase the overall coincidence count rate by \sim the cavity enhancement factor. The visibility of the pump enhanced and non pump enhanced interferograms were measured to be 0.941 ± 0.012 and 0.951 ± 0.012 respectively. The high visibility of the interferograms was due to the removal of spatial distinguishing information associated with photons through the process of coupling into single mode fibres. The small level of ‘missing’ visibility was probably due to imperfect optimisation of the downconversion HWP and crystal temperature.

The base to base width of the triangular fit is the biphoton coherence length, l_c which for the data in Figure 4-25 (a) was $936 \pm 19.8 \mu\text{m}$. The biphoton coherence time τ_c is given by $l_c/2c$ which in turn gives the phasematching bandwidth Ω_f through π/τ_c . The measured l_c corresponds to a phasematching bandwidth of $2.68 \pm 0.06 \text{ nm}$. Similarly the phasematching bandwidth measured from the data in Figure 4-25 (b) was $2.66 \pm 0.06 \text{ nm}$

Assuming a monochromatic pump it has been shown by Taylor expansion of the phase mismatch that Ω_f for an extended phase matching process is given by [87]:

$$\Omega_f = \frac{4\pi}{L|2\gamma_i|} \quad (4.7.1)$$

where L is the crystal length and:

$$\gamma_i = \frac{\partial k_p(\omega_p)}{\partial \omega_p} - \frac{\partial k_i(\omega_p/2)}{\partial \omega_p} \quad (4.7.2)$$

Evaluating equation (4.7.1) though the Sellmeier equations for KTP predicts $\Omega_f = 2.85 \text{ nm}$ for the studied interaction which is in reasonable agreement with the measured value.

4. Pump enhanced source of correlated photons in the telecoms band

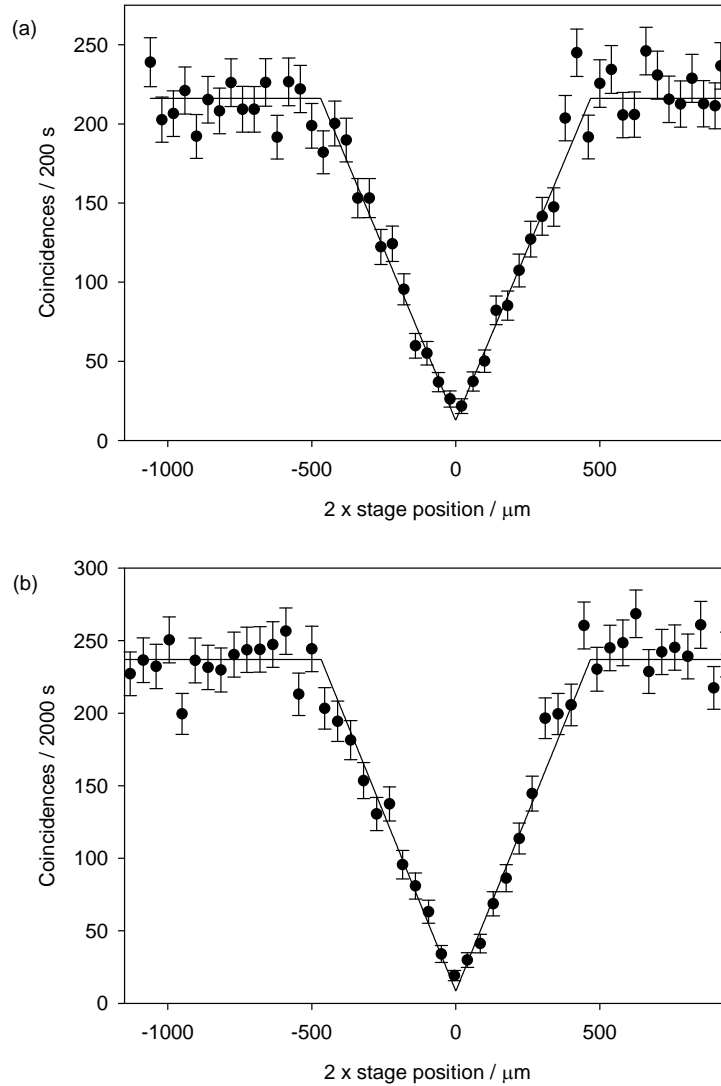


Figure 4-25 Hong-Ou-Mandel interferograms (a) with and (b) without the enhancement cavity present. The solid lines are numerical fits to the data. The pump power was 200 mW.

4.8 Conclusions

An SPDC-based source of pair photons in the telecoms band was designed and built. PPKTP was chosen as the source crystal due to the relatively high non-linear coefficient compared to crystals requiring birefringent phasematching, and also the fact that PPKTP satisfies the extended phasematching condition for degenerate downconversion into the telecoms band which means that degenerate photons are produced for a wide range of pump wavelengths. Such a crystal would therefore be suitable for future quantum optics experiments

4. Pump enhanced source of correlated photons in the telecoms band

incorporating a pulsed pump where there is greater control over when the pump photons are downconverted.

In order to increase the brightness of the source, the relative merits of placing a bulk downconversion crystal inside an optical cavity resonant for the pump beam and using a waveguide conformation non-linear crystal were compared and contrasted. A pump-enhanced bulk downconversion process was chosen for the source design because although the predicted pair generation rate was lower than the waveguide for low pump powers, the larger mode size of the pump allows a far more powerful pump beam to be used without damaging the non-linear medium, bringing higher generation rates. In addition, if the waveguide cross-section is damaged the crystal becomes unusable, but similar damage to a bulk crystal would be tolerable due to the large aperture. Also bulk crystals are still more widely available and cheaper than waveguided downconverters.

The design process of the enhancement cavity was presented; the mirror reflectivities were chosen to give a modest pump enhancement and impedance matching was avoided to ensure that some of the input beam was back reflected from the input coupler, as this was a requirement for the polarisation entangled photon pair source presented in the next chapter for which the correlated photon pair source is a component. A stable resonant mode with a large diameter was chosen to minimise diffraction losses of the generated downconversion and also to minimise the possibility for optical damage. The mode matching process of the pump beam into the optical cavity mode was presented.

Details were given for source components such as the Pound-Drever-Hall feedback mechanism used to hold the cavity on resonance, the detectors and coincidence counters, downconversion collection optics and spectral filtration elements, together with their characterisation and optimisation procedures.

The results from experimental investigations of the source were presented; a pump enhancement factor of around ten was measured, and this translated to the single photon and coincidence counting rates measured from the source. From the measured coincidence counting rate and analysis of losses throughout the system, it was estimated that the source produced $6.24 \times 10^4 \text{ s}^{-1} \text{ mW}^{-1}$ pump in a single spatial fibre optic mode, which is an order of magnitude greater than was reported for a pair source in the literature incorporating the same downconversion process but without the enhancement cavity.

4. Pump enhanced source of correlated photons in the telecoms band

A Hong-Ou-Mandel interferometer was setup to verify that the pump enhancement had no negative influence over the indistinguishability of the pair photons. Details of the interferometer configuration are given together the necessary optimisations procedures such as polarisation matching of the photon pairs and optical path balancing of the two beam interferometer.

Both in the absence and presence of pump enhancement, HOM-dip interferograms with visibilities ~ 0.95 were measured. The optimal dip-visibility was measured at crystal temperatures of $\sim 21^\circ\text{C}$. The reduced dip visibility measured at higher crystal temperatures was attributed to the change in phasematching causing increased non-degeneracy of the photons coupled into the interferometer. The bandwidth of the HOM dip, was not observed to change significantly between the non pump enhanced and pump enhanced cases, nor with change of crystal temperature.

4. Pump enhanced source of correlated photons in the telecoms band

5 Pump enhanced source of polarisation entangled photon pairs in the telecoms band

5.1 Introduction

Entangled photon pairs are an important resource for many applications in quantum optical information processes such as quantum teleportation [88], quantum key distribution [10] and implementations of quantum logic gates [89-90]. There has been much interest in the development of polarisation entangled photon pair sources based on parametric downconverters due to their simplicity and high brightness. Frequently, the states of interest are the four maximally entangled Bell states:

$$|\psi^\pm\rangle = [|H_1V_2\rangle \pm |V_1H_2\rangle] / \sqrt{2} \quad (5.1.1)$$

$$|\phi^\pm\rangle = [|H_1H_2\rangle \pm |V_1V_2\rangle] / \sqrt{2} \quad (5.1.2)$$

Each ket term corresponds to the outcome of a simultaneous measurement of the polarization state (H or V) of two photons at positions 1 and 2. High quality polarisation entangled states are characterized by ket terms that are indistinguishable with respect to all variables except polarisation. Since $\chi^{(2)}$ entangled photon pair sources capable of producing all four Bell states invariably require type-II phasematching, dispersion between the downconverted photons within the non-linear medium often leads to temporal differences between the ket terms and loss of entanglement. In earlier schemes, such temporal distinguishability was removed by positioning one or two crystals after the downconverter such that dispersive effects from the additional crystals cancelled out those associated with the downconverter [13, 91]. In order to preserve the spatial and frequency indistinguishability of the ket terms many early schemes only utilized photons from a small part of the emission cone, substantially reducing count rates. Later schemes for polarization entangled photon pair production incorporated an effective way of suppressing temporal, spatial and frequency distinguishability information without compensating crystals or spatial filters [14]. In such schemes the individual ket terms of the entangled state were formed by the downconversion

5. Pump enhanced source of polarisation entangled photon pairs in the telecoms band

pairs associated with one of two identical counter-propagating pump beams through the same downconversion medium.

In separate investigations, a method for increasing the brightness of an SPDC pair source was to enhance the pump field within the downconversion medium by placing it in an optically resonant cavity [92-93]. Since a resonant beam will naturally counter-propagate within an enhancement cavity, a pump enhanced source of downconverted photons is suitable for a single crystal source of polarization entanglement, and is the focus of this work. The pump enhanced pair sources presented in refs [92-93] would not be suited to this application due to the asymmetric resonant mode of the pump beam which would make the forward and backwardly propagating downconversion emission cones distinguishable. The enhancement cavity of the downconversion pair source discussed in the previous chapter does have a symmetric resonant mode and was incorporated into the design of the entangled photon pair source.

Most previous work on polarisation entangled photon pair sources was carried out at visible wavelengths, partly because of mature photon detection technology. In addition, a low interaction of visible photons with the atmosphere makes them suitable for free-space technologies such as some QKD implementations, where successful communication over 144 km has been demonstrated [94]. There has been relatively little investigation of polarisation entangled photons in the telecoms band, despite the fact that such technology would lend itself to distributed quantum communication protocols built upon existing long-distance fibre networks.

The two main difficulties associated with long distance fibre quantum networks based on polarization entangled states are (i) depolarisation of the entangled state due to polarisation mode dispersion within the fibre material and (ii) poor detection technology at telecoms wavelength. Recently the depolarisation concern has been shown to be less significant in modern fibres than had been previously feared; in that work the correlations between photon pairs after travelling through 100 km of optical fibre were sufficient for secure QKD [95]. In addition, InGaAs/InP APD detector technology is improving in parallel with the development of promising new detector technologies such as those based on parametric up conversion [96], superconducting transition edge sensors [97] and superconducting nanowires [98]. Therefore the prospects for distributed fibre network applications incorporating polarisation entangled photon pairs are improving.

5. Pump enhanced source of polarisation entangled photon pairs in the telecoms band

This chapter describes the operational theory and experimental demonstration of a novel source for polarisation entangled photon pairs in the telecoms band. The setup was shown to generate the two maximally entangled Bell states $|\psi^\pm\rangle$, the production of the $|\phi^\pm\rangle$ states would be possible by adding another wave plate to the setup. Quantum interference visibilities in excess of 0.95 were measured indicating high quality polarisation entanglement. Further analysis of the entangled state was performed by testing for violation of the Clauser-Horner-Shimony-Holt (CHSH) form of Bell's inequality; it was found that CHSH 'S-parameter' was 2.73 ± 0.12 , which corresponds to a violation of the classical maximum by about six standard deviations. The first build of the source was undertaken at the University of St. Andrews, where the majority of the experimental measurements presented in this chapter were made. Subsequently the experiment was transferred to the National Physical laboratory, and details of the setup at NPL are presented.

5.2 Theory of source design

The essential components of the scheme are shown in Figure 5-1. The pump beam is coupled into an optical cavity defined by mirrors M_1 and M_2 through a dichroic mirror DM that transmits at the pump wavelength and reflects the downconversion. The downconversion medium is positioned within the optical cavity that is resonant for the pump, and transmitting for the downconversion such that downconversion pairs emerge from both M_1 and M_2 . The mirrors M_3 and DM steer the downconversion towards a polarizing beam splitter, which transmits (reflects) the horizontally (vertically) polarized photons from each pair to separate detectors D_1 and D_2 .

The general expression for the entangled state described by equation (5.1.1) is:

$$|\psi\rangle = |H_1V_2\rangle + e^{i\phi}|V_1H_2\rangle \quad (5.2.1)$$

The two ket terms in equation (5.2.1) can be associated with the measurement of coincident photon arrivals at D_1 and D_2 arising from two distinct events; one due to the coincident detection of 'forwardly' propagating downconversion photons, generated by a pump photon travelling from M_1 to M_2 [Figure 5-1(a)], and another due to 'backwardly' propagating downconversion photons generated by a pump photon travelling from M_2 to M_1 [Figure 5-1(b)].

5. Pump enhanced source of polarisation entangled photon pairs in the telecom band

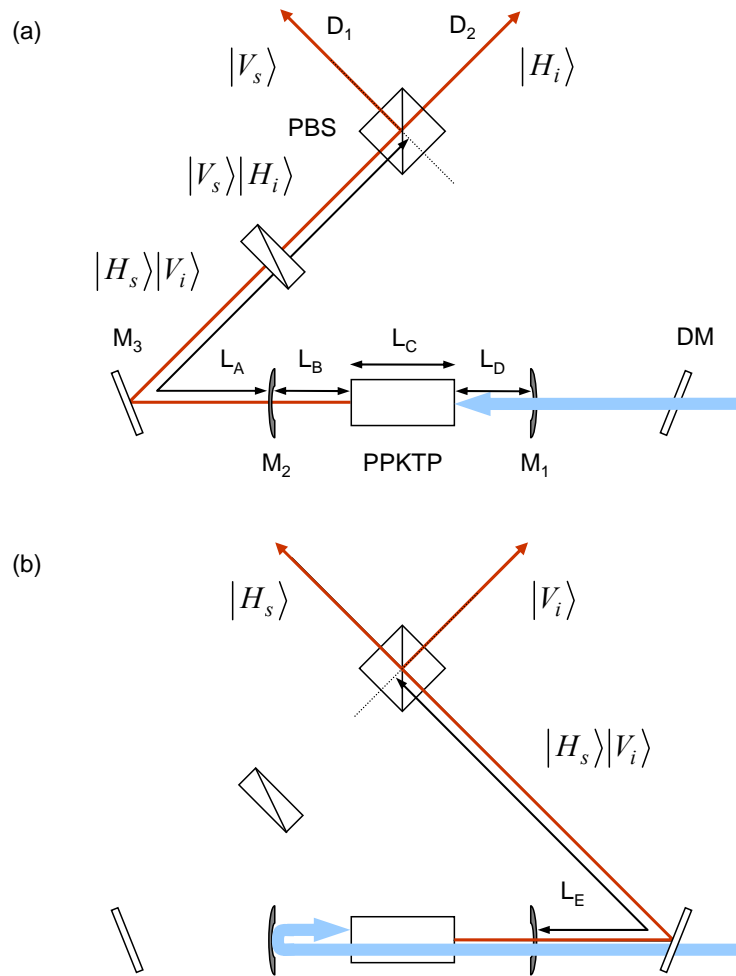


Figure 5-1 Scheme for producing the two superposition components of the entangled state in equation (5.2.1). The ket terms are either associated with downconversion photons that are produced while the pump beam is travelling from (a) right to left (forwards) or (b) left to right (backwards).

In order to form an entangled state, the component ket terms are required to be indistinguishable with respect to wavelength. Defining the signal photons to be horizontally polarised, if the downconversion polarizations are unmodified along the optical path to PBS, the PBS directs the signal photon to either D_1 or D_2 depending on the generation direction through the crystal, similarly for the idler photon. Therefore unless the signal and idler photons are perfectly degenerate then there will be ‘which-path’ information that could be used to distinguish the ket terms of equation (5.2.1) and therefore destroy entanglement. Despite the choice of phasematching for degeneracy there will always be a degree of wavelength distinguishability between the signal and idler due to the inherently wavelength anti-correlated nature of the downconversion process. Therefore a half wave plate was positioned in one of the downconverted beam paths at 45° to the polarization axes, exchanging the signal and idler polarizations in that path. The polarization exchange ensures

5. Pump enhanced source of polarisation entangled photon pairs in the telecoms band

that both ket terms of the state correspond to a signal photon received at D₁ and an idler photon at D₂, removing the ‘which-path’ information.

The $|\psi^+\rangle$ state is produced from equation (5.2.1) when $\phi = n\pi$, where n is zero or an even integer, while $|\psi^-\rangle$ is produced when n is an odd integer. Other values of ϕ will produce non-maximally entangled states that resemble an intermediate of the maximally entangled $|\psi^\pm\rangle$ states.

Non-maximally entangled states will also be created if coincidence events associated with one ket are recorded more frequently than those associated with the other ket term, i.e. the ket terms have different amplitudes. This may result from different generation rates and/or losses associated with each term. The following discussion seeks to analyse the phases and amplitudes of the $|H_1V_2\rangle$ and $|V_1H_2\rangle$ terms associated with the source design of Figure 5-1. The analysis shows that the design results in a coherent entangled state and secondly it gives an insight on how the entangled state may be changed and optimised. First, rewrite equation (5.2.1) as:

$$|\psi\rangle = \sqrt{\eta_{FW}} e^{i\phi_{FW}} |V_1H_2\rangle + \sqrt{\eta_{BW}} e^{i\phi_{BW}} |H_1V_2\rangle \quad (5.2.2)$$

where η_{FW} and η_{BW} are the classical arrival rates at D₁ and D₂ of paired photons generated in the forward and backward directions through the crystal respectively. ϕ_{FW} and ϕ_{BW} are the summed phases of the parent pump photon and the daughter pair photons up to the PBS for the forward and backward generation cases respectively. The phases associated with the optical paths from PBS to D₁ and D₂ are common between the ket terms and so are ignored. Since the pump photon can circulate around the cavity any number of times before the downconversion event occurs, the components of the two phase terms ϕ_{FW} and ϕ_{BW} associated with the enhancement cavity are given respectively by:

$$\phi_{FW_{EC}} = k_p [L_D + n_y L_C] + [k_s + k_i] L_B + \sum_{N_{even}} N [\{L_B + n_y L_C + L_D\} k_p + \pi] \quad (5.2.3)$$

$$\phi_{BW_{EC}} = k_p [L_B + n_y L_C] + [k_s + k_i] L_D + \sum_{N_{odd}} N [\{L_B + n_y L_C + L_D\} k_p + \pi] \quad (5.2.4)$$

5. Pump enhanced source of polarisation entangled photon pairs in the telecoms band

where the ‘start’ point for the phase accumulation was taken to be after the pump photon first passes through M_1 . N is the number of complete pump excursions across the cavity before creating a photon pair. n_y is the refractive index of the pump beam in the PPKTP. k_p, k_s and k_i are the pump, signal and idler wavevectors in vacuum respectively. The π term is due to reflections of the pump beam at the cavity mirrors. Equations (5.2.3)-(5.2.4) assume that the pair photons are generated as the pump beam emerges from L_C ; this is an arbitrary choice because the conversion could happen at any point along L_C , and since phase matching dictates that $k'_p = k'_s + k'_i$ where the k' are the crystal wavevectors, the phase accumulated within the crystal is independent of the downconversion event position. Since the enhancement cavity is held on resonance:

$$\left[L_B + n_y L_C + L_D \right] k_p = q k_p \frac{\lambda_p}{2} = q\pi \quad (5.2.5)$$

Therefore the pump accumulates a net phase of π or 2π for each excursion across the cavity depending on the mode order q . Inserting equation (5.2.5) into (5.2.3) and (5.2.4) and removing common terms gives:

$$\phi_{FW_{EC}} = k_p L_D + [k_s + k_i] L_B + \sum_{N_{even}} N [q\pi + \pi] \quad (5.2.6)$$

$$\phi_{BW_{EC}} = k_p L_B + [k_s + k_i] L_D + \sum_{N_{odd}} N [q\pi + \pi] \quad (5.2.7)$$

Equation (5.2.6) indicates that the summation terms of $\phi_{FW_{EC}}$ differ in phase only by integer numbers of 2π , similarly for $\phi_{BW_{EC}}$ in equation (5.2.7). This allows for the summations to be considered as a single coherent phase.

There are also phase contributions to ϕ_{FW} and ϕ_{BW} associated with the optical paths external to the enhancement cavity, i.e. the optical paths from M_2 / M_1 to PBS:

$$\phi_{FW_{EXT}} = [k_s + k_i] L_A + \phi_{M_2(s,i)} + \phi_{HWP(s,i)} + 3\pi \quad (5.2.8)$$

$$\phi_{BW_{EXT}} = [k_s + k_i] L_E + \phi_{M_1(s,i)} + 3\pi \quad (5.2.9)$$

5. Pump enhanced source of polarisation entangled photon pairs in the telecoms band

$\phi_{M_1(s,i)}$ is the collective phase acquired by the signal and idler photons when the beam passes through M_1 . Similarly $\phi_{M_2(s,i)}$ and $\phi_{HWP(s,i)}$ are the collective signal and idler phases acquired through M_2 and the half wave plate respectively. The 3π terms are due to the reflection of both downconverted photons at the beam steering mirrors (M_1 or DM) and the reflection of one photon at the polarizing beam splitter. The total phase ϕ_{FW} in equation (5.2.2) is given by the sum of $\phi_{FW_{EC}}$ and $\phi_{FW_{EXT}}$, ϕ_{BW} is given by summing $\phi_{BW_{EC}}$ and $\phi_{BW_{EXT}}$.

The factors η_{FW} and η_{BW} in equation (5.2.2) are proportional to pump field intensity through the downconversion medium in the forward and backward travelling directions respectively. The pump intensities are given by a summation over N , for a lossless system:

$$\eta_{FW} = \sum_r I_p (R_2 R_1)^r = \frac{I_p}{1 - R_2 R_1} \quad (5.2.10)$$

$$\eta_{BW} = \sum_r I_p R_2 (R_2 R_1)^r = \frac{I_p R_2}{1 - R_2 R_1} \quad (5.2.11)$$

where r is an integer and I_p is the input pump power to the cavity while R_1 and R_2 are the pump reflectivities of mirrors M_1 and M_2 respectively. It follows from equations (5.2.6)-(5.2.11) that the full expression for the produced state outlined in equation (5.2.2) is given by:

$$|\psi\rangle = \sqrt{\frac{I_p}{1 - R_2 R_1}} |V_1 H_2\rangle + \sqrt{\frac{I_p R_2}{1 - R_2 R_1}} e^{[k_s + k_i][L_D + L_E - L_A - L_B] + k_p[L_B - L_D] - \phi_{M_2(s,i)} + \phi_{M_1(s,i)} - \phi_{HWP(s,i)}} |H_1 V_2\rangle \quad (5.2.12)$$

The phase contributions due to the enhancement cavity mirrors and the half wave plate are fixed, also the optical paths L_B, L_C and L_D are fixed by the cavity resonance condition. Therefore in order to form a stable output state, only $L_E - L_A$ needs to be actively fixed. $L_E - L_A$ also needs to be variable in order to switch between the $|\psi^+\rangle$ and $|\psi^-\rangle$ states. When the system is optimised for $|\psi^+\rangle$, the $|\phi^+\rangle$ state, could be produced by positioning a half wave plate for the downconversion at either output port of PBS, and oriented at 45° to the H/V basis such that H and V are exchanged. Similarly the half waveplate could be used to switch $|\psi^-\rangle \rightarrow |\phi^-\rangle$.

5. Pump enhanced source of polarisation entangled photon pairs in the telecoms band

Section 5.3 explains the experimental mechanism used to keep the phase of the output state stable in order that a coherent entangled state was formed. Also described are the arrangements used to vary $L_E - L_A$, and to equalize η_{FW} and η_{BW} in order to maximize the entanglement.

5.3 Experimental setup

5.3.1 Overview of complete system

A schematic of the setup is shown in Figure 5-2 (a) and a photograph of the setup is shown in Figure 5-2 (b).

The Verdi and Ti-Sapphire pump lasers, in addition to the isolator and wavelength dispersive prisms (WDP) are the same as those described in section 4.5.2. The design of the PPKTP crystal was discussed in section 4.2 while the design of the resonant cavity mirrors M_1 and M_2 was described in section 4.4. The pump focussing lens L_1 , mode matching lens L_2 and electronics associated with the Pound-Drever-Hall locking servo are identical to those employed in the previous chapter.

The dichroic mirrors DM_1 and DM_2 used were specified by the manufacturer to transmit 86% of the pump light and be highly reflecting (HR) at the downconversion wavelength. Lenses L_3 and L_4 were used for collimation of the downconversion: these had 160 mm focal lengths and were positioned along the downconversion optical path at a distance from the centre of the PPKTP crystal equal to their focal length.

In order to stabilise the phase term ϕ of the entangled state, the position of a piezo-ceramic mounted gold mirror M_3 was actively adjusted to lock the relative optical path between M_2 and PBS [in the clockwise direction in Figure 5-2 (a)] with that from M_1 to PBS [anticlockwise direction in Figure 5-2 (a)]. The necessary movement of M_3 was accomplished using the side of fringe locking technique where the error signal was generated using the intensity interference fringes from the two beam interferometer defined by the optical paths that require locking, see section 5.3.2. The gold mirror pairs M_4 were used for beam steering, as was M_5 . In order to adjust the phase term of the entangled state a pair of counter-rotatable glass plates were placed in the optical path of the downconversion generated

5. Pump enhanced source of polarisation entangled photon pairs in the telecoms band

in the direction from M_1 to M_2 , see section 5.3.3. The wavelength indistinguishability of the $|H_1V_2\rangle$ and $|V_1H_2\rangle$ kets was ensured by a positioning a half wave plate in one arm of the interferometer, see section 5.2.

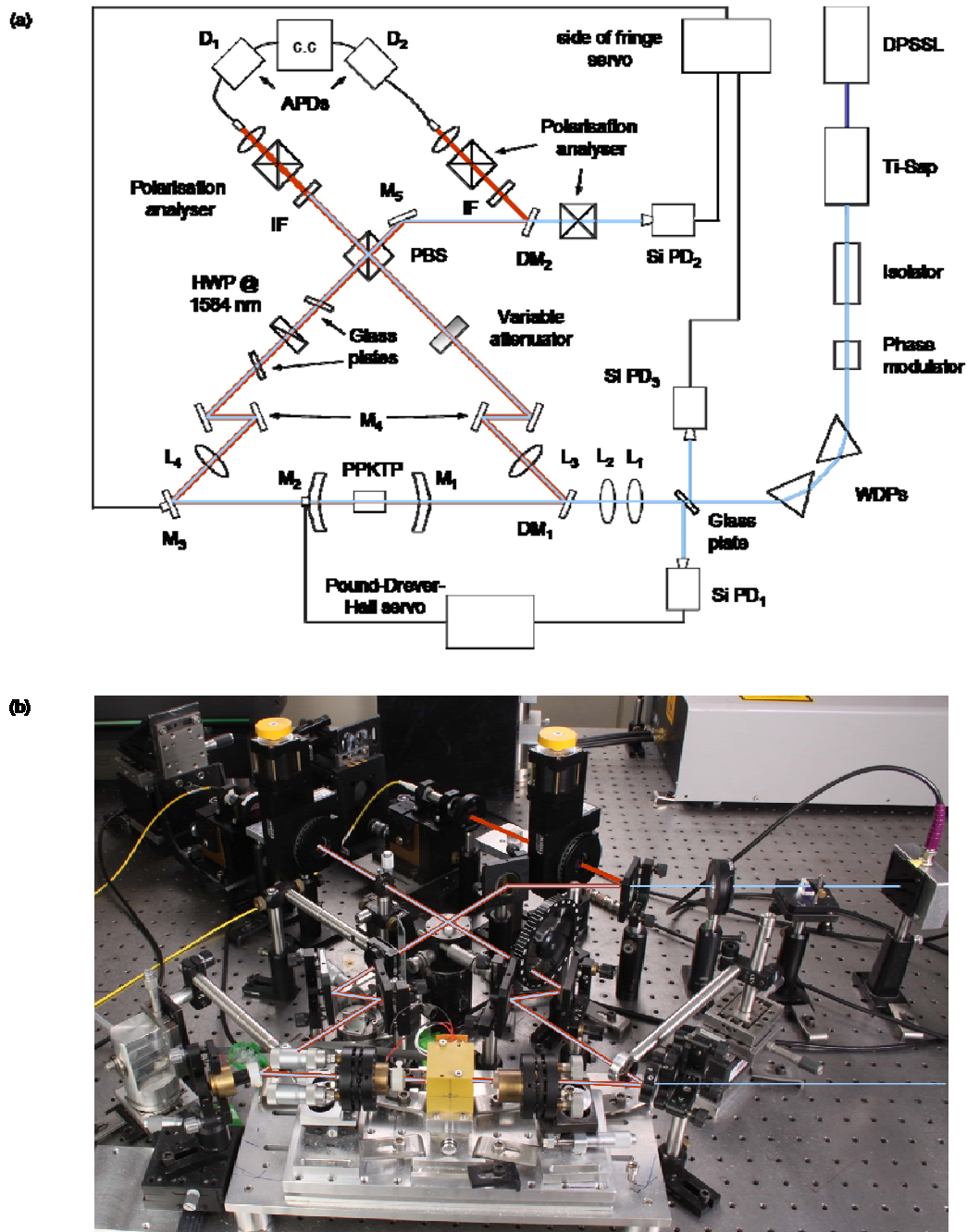


Figure 5-2 (a) Schematic for source of polarisation entangled photon pairs in the telecoms band. The blue and red lines denote 792 nm pump light and downconversion respectively, while the black lines are electrical connections. In the text the downconversion generated by a pump photon travelling from M_1 to M_2 is described as ‘forwardly’ propagating, downconversion generated in the opposite direction is referred to as ‘backwardly’ propagating. (b) Photograph of the setup in (a), the components before and including L_2 are omitted for clarity.

Because the reflectivity of M_2 , $R_{M_2} = 0.98$, the downconversion field generated from the backward passes of the pump is 2 % less bright than the field generated from the forward passes of the pump [see equations (5.2.10)-(5.2.11)]. However since $R_{DM_1} > R_{M_3}$ at the downconversion wavelength and since there are Fresnel losses at the uncoated glass plates in the forward pass arm of the interferometer, the downconversion generated from the forward passing pump is less bright at photon counting detectors D_1 and D_2 than the downconversion generated from the backwardly passing pump, i.e. $\eta_{BW} > \eta_{FW}$. Therefore in order for the entanglement to be maximal, η_{FW} and η_{BW} were equalized through attenuation of the backwardly propagating downconversion to the required level using a variable neutral density filter, see section 5.3.4.

Interference filters IF, centred at 1584 nm and having 30 nm bandwidths were positioned in front of D_1 and D_2 to block the pump wavelength. The polarisation analyzers positioned in front of D_1 and D_2 comprised a zero-order half waveplate at 1584 nm and a polarising beam splitter. The detector collection optics, photon counting detectors and the coincidence counter (c.c) were the same as those described in the previous chapter.

5.3.2 Side of fringe system for phase locking of entangled state

In order to form a stable entangled state, it was necessary to lock the relative accumulated phases of the forward and backward propagating downconversion pairs at the PBS, and this was achieved using a side-of-fringe lock system. The signal used for feedback was the intensity interference fringes formed by the recombination at PBS of 792 nm pump light transmitted through M_2 with the pump light back reflected from M_1 . The recombiner was also polarising at the pump wavelength which was nominally horizontally polarized, therefore the emergence of pump components at a single output port of PBS from each arm of the interferometer relied on at least one beam having a slight vertical polarisation component. This requirement influenced the choice of half wave plate used for exchanging the signal and idler polarisations; a zero order half wave plate for the downconversion wavelength was specified by the supplier 'II-VI infrared' to be a 1.055 wave plate for the pump wavelength, whereas a multi-order half wave plate for the downconversion was specified to be a 11.6 wave plate for the pump. Therefore the zero order wave plate would leave the pump polarisation relatively unaffected where as the multi-order wave plate gave the pump

5. Pump enhanced source of polarisation entangled photon pairs in the telecoms band

polarisation a favourable elliptical characteristic. Therefore a multi-order waveplate was chosen to perform the exchange of signal and idler polarisations.

At a single output port of the recombiner, the two pump beam components originating from different interferometer arms have orthogonal polarisations and therefore do not interfere [99]. Passing the orthogonal beams through a polarization analyzer at 45° to each polarisation transmits only those components of the electric field from each beam that are parallel, and these components do interfere. The polarization analyzer was a half wave plate and polarizing beam splitter combination.

The side-of-fringe feedback works on the principle that a change in the relative optical path between the forward and backwardly travelling pump beam through the interferometer will change the detected intensity of the spot formed by the recombined beams at a silicon photodiode (SiPD₂). This changes the output voltage from SiPD₂ relative to a chosen reference defining the locking position. The intensity change per unit optical path change is greatest at the side of an interference fringe therefore the reference voltage is chosen at the side-of-fringe in order to maximize position sensitivity. Depending on the side of fringe chosen as the reference, the intensity change will either be in phase or antiphase with the relative optical path change. An error signal was generated from the difference between the output voltage at SiPD₂ and the reference voltage. The error signal was sent to PID feedback electronics in order to generate a voltage that was amplified (Piezomechanik SVR 500/3 voltage amplifier) before application to the piezo-active mirror M₃ that moves to ensure the spot intensity measured at SiPD₂ creates an output voltage that equals the reference level.

By applying a sawtooth ramp voltage to M₃ the two beam interference intensity modulation was measured at Si PD₂, see Figure 5-3. Under the pump powers used for the entanglement measurements, the intensity modulation corresponded detector output voltages of between 0.5-1.0V, accompanied by a DC offset between 1.0-2.0 V due to the amplitude disparity between in the interfering field components. It was observed that the DC component of the detector output voltage appeared to undergo small (<5% of the fringe modulation) fluctuations over the time scale of a few seconds. Such fluctuations could affect the performance of the system since they would cause the reference voltage to correspond to different fringe positions with time, and this would mean that the phase of the entangled state would change with time. The DC fluctuations at SiPD₂ were observed to be synchronized with intensity fluctuations of the 792 nm pump light, therefore a further silicon photodiode Si PD₃ was positioned as shown in Figure 5-2 in order to monitor the intensity of the pump beam, and the side-of-fringe electronics were modified such that the reference voltage

5. Pump enhanced source of polarisation entangled photon pairs in the telecoms band

changed with the voltage fluctuation output from Si PD₃. The modification ensured that the reference voltage corresponded to the same part of the fringe modulation for upwards of 30 minutes which was much more than the period of time required for the individual measurements comprising the characterisation of the entangled state.

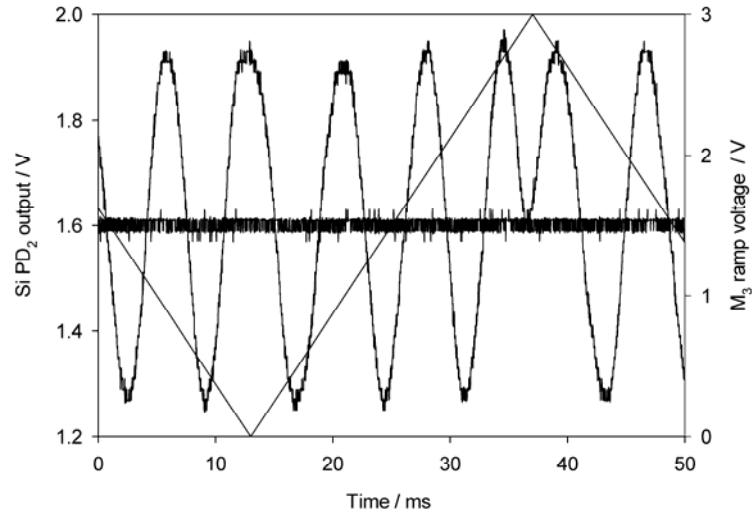


Figure 5-3 The saw-tooth function is the voltage ramp applied to the active mirror M_3 . The sinusoidal function represents the resulting interference measured at SiPD₂ between two 792 nm pump beams recombined at PBS. The horizontal trace is the reference voltage for the side of fringe system that is adjusted to correspond to the steepest part of the modulation. The reference voltage also adjusts to real-time fluctuations in the pump power measured at SiPD₃.

From equation (5.2.12), the relative phase between the entangled state ket terms is dictated by the difference between the optical paths from each side of the enhancement cavity to PBS. The side of fringe system therefore ensures the phase stability of the entangled state, but in principal could also offer a means for tuning the phase of the output state; a different reference ‘locking’ voltage corresponds to a change in the relative interferometer paths and therefore a different entangled state phase. However the side of fringe technique is most effective when the reference voltage corresponds to the steepest part of the intensity modulation curve, and tuning the reference voltage could move it unfavourably close to a peak or trough of the modulation. Therefore it was decided not to use the side of fringe system for tuning the output state but instead seek an optical tuning method, resulting in the rotatable double glass plate arrangement discussed in the following section.

5. Pump enhanced source of polarisation entangled photon pairs in the telecoms band

5.3.3 Double glass plate for tuning phase of entangled state

The wavelength dependence of the refractive index in silica glass is given by:

$$n^2(\lambda) = 1 + \frac{B_1\lambda^2}{\lambda^2 - C_1} + \frac{B_2\lambda^2}{\lambda^2 - C_2} + \frac{B_3\lambda^2}{\lambda^2 - C_3} \quad (5.3.1)$$

where $B_1 = 0.696$, $B_2 = 0.408$, $B_3 = 0.897$, $C_1 = 4.68 \times 10^{-3}$, $C_2 = 1.35 \times 10^{-2}$ and $C_3 = 97.9$. Evaluating expression (5.3.1) for the pump and signal wavelengths gives $n_p = 1.45$ and $n_s = 1.44$ respectively. Therefore for an optical path comprising free space and silica components, changing the proportion of path length occupied by silica and free space changes the relative phase between the downconversion photon pair (given by summing the signal and idler phases) and the pump photon at the end of the path.

Consider again the two beam interferometer formed by the shortest optical paths from M_2 to PBS and from M_1 to PBS; changing the silica:free space path length ratio from M_2 to PBS changes the optical path in that arm. Under such a change, the side of fringe scheme adjusts the position of M_3 to compensate for the optical path change experienced by the pump. However the optical path change experienced by the downconversion will be different, and therefore will not be compensated for by the side of fringe system. Therefore changing the silica:free space path length ratio from M_2 to PBS varies the relative phase at PBS between the forward and backwardly propagating downconversion pair photons through the interferometer, which is equivalent to changing the relative phase between the $|H_1V_2\rangle$ and $|V_1H_2\rangle$ ket terms.

The simplest mechanism for implementing this tuning concept is by rotation of a glass slide in one of the interferometer arms, see Figure 5-4. The pump and signal beams are incident at an angle θ_{silica} to the normal of the glass plate. The optical path travelled by the pump beam from the first air-glass interface s_1 to the broken vertical line after the second air-surface interface s_2 is given by equation (5.3.2) whereas the optical path travelled by a downconversion photon is given by equation (5.3.3):

$$L_{p,silica} = n_p A + C \quad (5.3.2)$$

$$L_{s,silica} = n_s B \quad (5.3.3)$$

5. Pump enhanced source of polarisation entangled photon pairs in the telecoms band

$$\text{where; } A = \frac{L}{\cos \theta_{r,\lambda_p}}, \quad B = \frac{L}{\cos \theta_{r,\lambda_s}}, \quad C = \frac{B}{\sin \theta_B} \cdot \sin(\theta_{r,\lambda_s} - \theta_{r,\lambda_p}) \cdot \sin \theta_{silica}$$

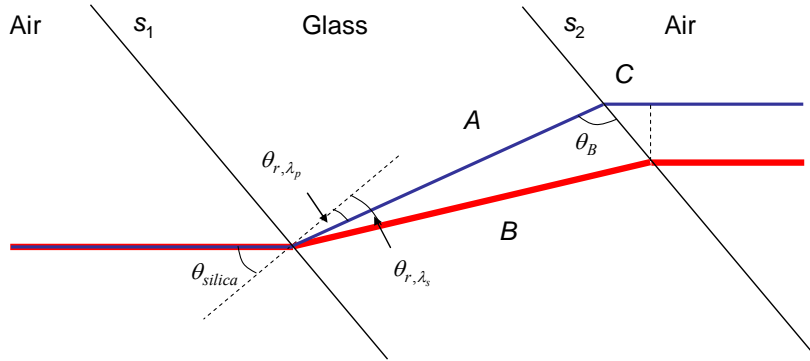


Figure 5-4 Mechanism for phase tuning of the entangled state. Changing θ_{silica} changes the optical path of the pump (blue) beam and downconversion pair (red) beam by different amounts due to wavelength dispersion. The spatial walk-off between the pump and downconversion is reversed by passing the beams through an identical silica slide with normal $-\theta_{silica}$ to the beams. The resulting interferometer phase change for the pump is compensated for by the side-of-fringe lock system, but the phase change of the downconversion interferometer is not compensated.

At the broken vertical line following s_2 the pump and signal beams are displaced from one another which would cause problems for system alignment, therefore a second identical glass slide was positioned such that the beams make an angle $-\theta_{silica}$ to the slide normal. Assuming that for all θ_{silica} the side of fringe system maintains the $\theta_{silica} = 0$ phase difference between the pump beams recombined at PBS, the phase difference between the downconversion beams recombined at PBS as a function of θ_{silica} is given by:

$$\Delta\phi_{s+i}(\theta_{silica}) = 2 \left[k_p (n_p A + C) - 2n_s k_s B \right] - \phi_{offset} \quad (5.3.4)$$

where ϕ_{offset} is due to other wavelength dispersive optical elements through the interferometer; it has been assumed that $\lambda_s = \lambda_i$.

In order to determine suitable θ_{silica} values for tuning, consider $d\Delta\phi_{s+i}/d\theta_{silica}$, the sensitivity of the phase delay with respect to θ_{silica} , for a range of θ_{silica} ; see Figure 5-5. Changes in θ_{silica} about $\theta_{silica} = 0^\circ$ result in little change of $\Delta\phi_{s+i}$ due to the small refraction angles at the

5. Pump enhanced source of polarisation entangled photon pairs in the telecoms band

air-surface interfaces. $d\Delta\phi_{s+i}/d\theta_{silica}$ increases approximately linearly with θ_{silica} upto ~ 1 rad per degree of rotation at $\theta_{silica} = 45^\circ$.

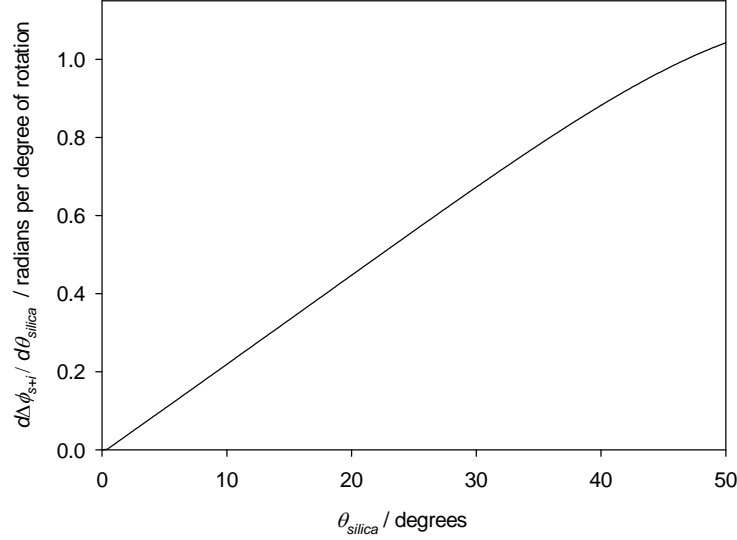


Figure 5-5 Relationship of phase tuning sensitivity with incidence angle of interferometer beam with two silica slide system. Each slide is 1 mm thick.

Since the microscope slides used were uncoated, another factor influencing suitable θ_{silica} are the Fresnel reflections of the downconversion at each interface which serve to limit the transmission of each polarisation and therefore the flux of the entanglement source. Given the type-II phasematching, the photons of each pair have orthogonal (s and p) polarisations. The Fresnel reflections for s and p polarised photons are given by equations (5.3.5) and (5.3.6) respectively.

$$R_s = \left[\frac{n_1 \cos \theta_{silica} - n_2 \sqrt{1 - \left(\frac{n_1 \sin \theta_{silica}}{n_2} \right)^2}}{n_1 \cos \theta_{silica} + n_2 \sqrt{1 - \left(\frac{n_1 \sin \theta_{silica}}{n_2} \right)^2}} \right]^2 \quad (5.3.5)$$

$$R_p = \left[\frac{n_1 \sqrt{1 - \left(\frac{n_1 \sin \theta_{silica}}{n_2} \right)^2} - n_2 \cos \theta_{silica}}{n_1 \sqrt{1 - \left(\frac{n_1 \sin \theta_{silica}}{n_2} \right)^2} + n_2 \cos \theta_{silica}} \right]^2 \quad (5.3.6)$$

5. Pump enhanced source of polarisation entangled photon pairs in the telecoms band

n_1 and n_2 are the refractive indices of the downconverted photons in the medium before and after the interface respectively. Figure 5-6 plots the transmission of s and p polarised photons at the degenerate downconversion wavelength through the two glass plate system for various θ_{silica} . For $\theta_{silica} > 10^\circ$ the transmission of the p polarisation exceeds that for the s polarisation, but since the polarisation entanglement measurements are made in coincidence, the entanglement flux is proportional to the product of the s and p transmittances, which persists at around ~ 0.76 for increasing θ_{silica} upto $\theta_{silica} \sim 40^\circ$ beyond which the pair flux diminishes rapidly. On the basis of Fresnel reflection and $d\Delta\phi_{s+i}/d\theta_{silica}$ arguments, the nominal value of θ_{silica} was chosen to be 30° ; at this value the pair photon transmission through the two slides is high and $d\Delta\phi_{s+i}/d\theta_{silica} = 0.68$, which should allow for tuning between the 0 and π entangled states with a relatively small rotation of the glass slides of around 4.6° .

Notice in Figure 5-2 (a) that the half waveplate for switching the signal and idler polarisations has been placed in between the two glass slides in order that the signal and idler photons are transmitted equally; this does not improve the overall entanglement flux through the two slides but is a helpful feature during alignment. This is because the expected signal flux associated with η_{FW} at the PBS is equal to the idler flux, the same is true for the signal and idler associated with η_{BW} and therefore if the system is well aligned, the ratio of detected counts between D_1 and D_2 when the forwardly propagating downconversion is blocked should equal the ratio of detected counts when the backwardly propagating downconversion is blocked.

The two-slide phase delay device consisted of two rotation stages each acting as a platform for one glass slide. The two rotation stages could be rotated by equal and opposite angles through turning a micrometer screw that simultaneously pushed two pins that were located on each of the rotation stages. A spring stretched across two further pins located on each stage ensured that the reverse movement could be achieved by retracting the micrometer screw. The micrometer screw allowed for precise rotations of $\sim 0.03^\circ$.

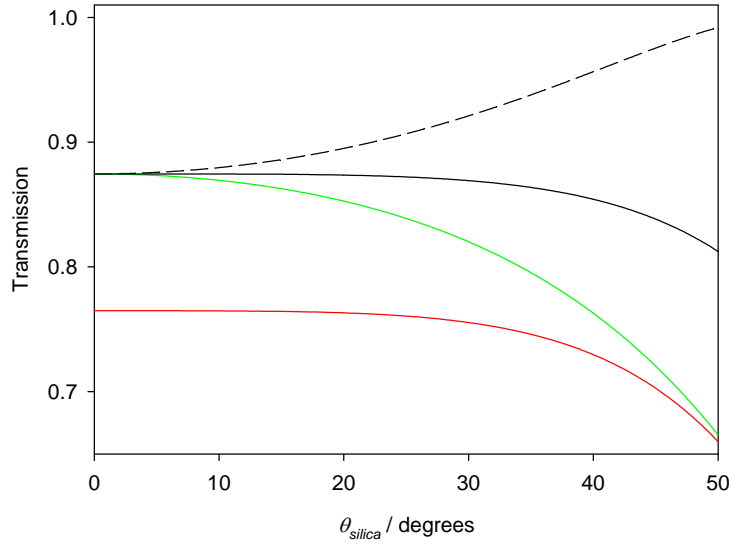


Figure 5-6 Shown are the transmission of p (--) and s (—) polarised single photons through the two slide system. Also plotted is the transmission of one photon through the system when the polarisation is rotated by 90° after the first slide (—) and the transmission of a photon pair through the two slide system (—).

5.3.4 Balancing the magnitudes of $|V_1H_2\rangle$ and $|H_1V_2\rangle$ probability amplitudes

In order to form the maximally entangled $|\psi^\pm\rangle$ states, in addition to the downconversion pairs corresponding to $|V_1H_2\rangle$ and $|H_1V_2\rangle$ requiring the correct relative phase the downconversion emission corresponding to ket each must have the equal intensity. The coefficients η_{FW} and η_{BW} described by equations (5.2.10) and (5.2.11) respectively revealed that the emission corresponding to $|V_1H_2\rangle$ emerges from the enhancement cavity $\sim 2\%$ brighter than the pair corresponding to $|H_1V_2\rangle$.

In practice η_{FW} and η_{BW} are reduced by optical losses through the system. The $|H_1V_2\rangle$ beam is deflected by DM_1 which is HR at the downconversion wavelength where as the $|V_1H_2\rangle$ beam is steered by a gold mirror M_3 , with reflectance $R_{M_3} \sim 0.92$. Collimating lenses L_3 and L_4 contribute losses to the $|H_1V_2\rangle$ and $|V_1H_2\rangle$ beams respectively, where the single photon transmittances were $T_{L_3} \approx T_{L_4} \approx 0.73$, as measured in the previous chapter. Similarly each interferometer beam is steered by gold mirrors pairs M_4 , which were measured in the previous

5. Pump enhanced source of polarisation entangled photon pairs in the telecoms band

chapter to have a combined single photon reflectance ~ 0.84 . The $|V_1H_2\rangle$ beam suffers a loss through the two glass slide phase delay mechanism; the single photon transmission is estimated to be $T_{\phi_{delay}} \sim 0.87$ from Figure 5-6. The HWP in the $|V_1H_2\rangle$ beam is HR at the downconversion wavelength. Combining the two photon generation and optical transmission properties yields the estimate $\eta_{FW} \approx 0.65 \times \eta_{BW}$. Therefore a variable attenuator was positioned in the $|H_1V_2\rangle$ beam in order to compensate for the additional losses associated with the $|V_1H_2\rangle$ beam.

5.4 Experimental results

The characterisation of the device involved the measurement of the coincident photon arrival rate at D_1 and D_2 for various polarisation analyzer angles θ_1 and θ_2 on D_1 and D_2 respectively. The two main groups of measurement were (i) those where θ_1 was oriented along either H or V and (ii) where θ_1 was oriented along the A/D (45°) basis. The first group of measurements enabled characterisation of the classical properties of the device such as single photon and coincidence counting rates while the second group of measurements relate to the characterisation of quantum entangled states.

5.4.1 Coincidence measurements in the H/V basis

Shown in Figure 5-7 are the measured number of coincident detections between D_1 and D_2 over a fixed time period as a function of the D_2 analyser angle θ_2 for $\theta_1 = 0^\circ$ and for $\theta_1 = 90^\circ$ where θ_1 is the analyzer angle on D_1 . When $\theta_1 = 0^\circ$, only horizontally polarised photons are transmitted to D_1 , and therefore only projections of the $|H_1V_2\rangle$ state component are measurable, this is confirmed by a minimum in the coincidence number about $\theta_2 = 0^\circ$ when only H polarized photons are transmitted to D_2 , and a maximum in the coincidence number at $\theta_2 = 90^\circ$. Using similar arguments, it can be seen that when $\theta_1 = 90^\circ$, only projections of the $|V_1H_2\rangle$ state component can be measured. Curves based on a \sin^2 model were fitted to the experimental data using a least squares procedure. The

5. Pump enhanced source of polarisation entangled photon pairs in the telecoms band

modulation visibilities for the fitted $\theta_1 = 0, 90^\circ$ curves were 0.971 ± 0.043 and 0.972 ± 0.036 respectively.

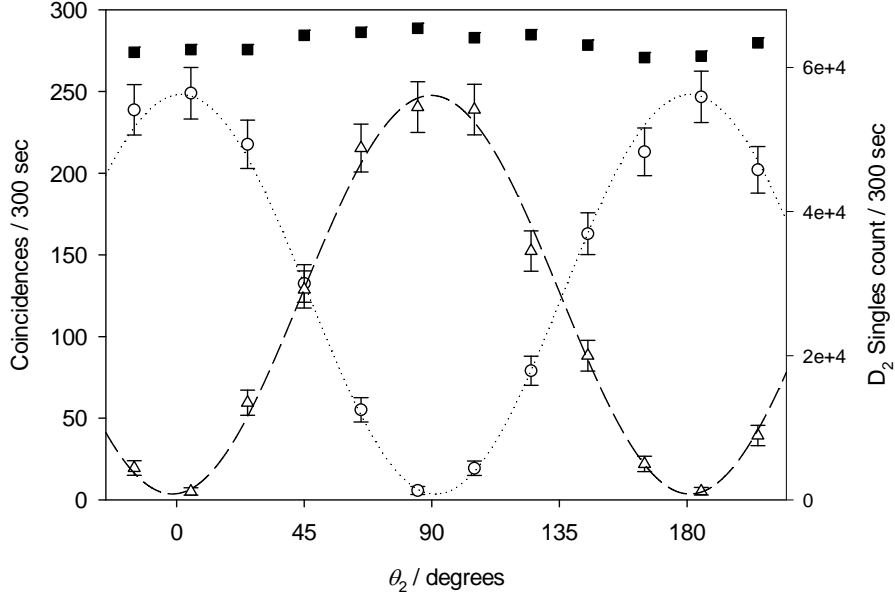


Figure 5-7 Measurements of the number of coincidences over a 300 s time period as a function of θ_2 for $\theta_1 = 0^\circ$ (triangles) and $\theta_1 = 90^\circ$ (circles). The dotted and broken lines are least squares fitted curves to the experimental data. The square data points are the measured singles counts at D_2 over the same time period as a function of θ_2 . The pump power into the enhancement cavity was 50 mW.

The single photon attenuation of the $|H_1V_2\rangle$ beam required to equalize the maxima of the $\theta_1 = 0, 90^\circ$ modulation curves in Figure 5-7 was measured to be 0.81, inferring without attenuation that $\eta_{FW_{inferred}} \approx 0.66 \times \eta_{BW_{inferred}}$, which is close to the value predicted in section 5.3.4 from the system losses.

Figure 5-7 also shows that the number of singles counts measured at D_2 is reasonably independent of θ_2 , similarly the singles counts measured at D_1 was also shown to be independent of θ_1 ; both observations are indicative of good system alignment.

The maximum of the $\theta_1 = 90^\circ$ curve, $N_{c,max}(\theta_2, \theta_1 = 90^\circ)$ gives a measure for the coincidence counting rate due to the photon pairs emerging through mirror M_2 of the enhancement cavity. In section 4.6.2, the same quantity (defined here as $N_{c,pump-enhanced}$) was measured for the setup shown in figure 4-10, incorporating the same cavity-enhanced downconversion process. In that setup, the photon pairs emerged from the enhancement cavity before reflection at two

5. Pump enhanced source of polarisation entangled photon pairs in the telecoms band

gold mirrors and were then split at a polarising beam cube to D₁ and D₂. For the $N_{c,\max}(\theta_2, \theta_1 = 90^\circ)$ measurement both photons are reflected at three gold mirrors and transmitted through two silica plates before being split at PBS, and then one of the photons undergoes a further reflection at a gold mirror before the photons are received at D₁ and D₂. Ignoring common optics and detectors between the systems, taking $R = 0.92$ for each gold mirror (see table 4-3) and the estimated Fresnel loss due to the glass slides (see Figure 5-6); per unit of pump power $N_{c,\max}(\theta_2, \theta_1 = 90^\circ)$ should equal $0.59 \times N_{c,pump-enhanced}$. The actual measured relationship was $N_{c,\max}(\theta_2, \theta_1 = 90^\circ) = 1.09 \times N_{c,pump-enhanced}$. The difference can be accounted for by the fact that for the $N_{c,pump-enhanced}$ measurement, corrosion damage to the thermo-electric cooling element of D₁ meant that the measured quantum efficiency of D₁ was low, see section 4.5.7. At the time of the $N_{c,\max}(\theta_2, \theta_1 = 90^\circ)$ measurement the problem had been repaired but due to time constraints the exact quantum efficiency of D₁ after the repair was not established. Assuming that the ‘repaired’ quantum efficiency of D₁ was equal to the previously measured well-functioning detector D₂ quantum efficiency, and that the D₂ detector quantum efficiency had not changed between the $N_{c,\max}(\theta_2, \theta_1 = 90^\circ)$ and $N_{c,pump-enhanced}$ measurements, then for the same source photons the coincidence counting rate would be 2.45 time greater after the repair of D₁. This could explain why the measured $N_{c,\max}(\theta_2, \theta_1 = 90^\circ)/N_{c,pump-enhanced}$ ratio was higher than predicted from the loss analysis by a factor of $1.09/0.59 = 1.84$.

5.4.2 Coincidence measurements in the A/D basis

The measurement outcomes $|H_1V_2\rangle$ and $|V_1H_2\rangle$ are associated with the probability amplitudes $A_{H_1V_2}$ and $A_{V_1H_2}$ respectively:

$$A_{H_1V_2} = e^{i\phi} \cos \theta_1 \sin \theta_2 \quad (5.4.1)$$

$$A_{V_1H_2} = \sin \theta_1 \cos \theta_2 \quad (5.4.2)$$

When $\theta_1 = \pm 45^\circ$ for a classical ensemble of $|H_1V_2\rangle$ and $|V_1H_2\rangle$ states, D₁ accepts around half of the vertically polarised photons from the $|V_1H_2\rangle$ beam and receives a similar flux of horizontally polarised photons from the $|H_1V_2\rangle$ beam. It follows that the measured

5. Pump enhanced source of polarisation entangled photon pairs in the telecoms band

coincidence rate will be independent of θ_2 . This can be shown using Feynman's approach [68] for determining the classical expectation value of the coincidence counting rate, i.e. by adding the sum of the squares of the probability amplitudes:

$$N_{classical, \theta_1=45^\circ}(\theta_2) = |A_{H_1V_2}|^2 + |A_{V_1H_2}|^2 = \frac{1}{2}[\sin^2 \theta_2 + \cos^2 \theta_2] \quad (5.4.3)$$

Equation (5.4.3) is a constant with θ_2 . If the $|H_1V_2\rangle$ and $|V_1H_2\rangle$ outcomes form the entangled state shown by equation (5.2.1), Feynman's approach dictates that the coincidence counting rate is given by squaring the sum of the probability amplitudes:

$$N_{entangled, \theta_1=45^\circ}(\theta_2) = |A_{H_1V_2} + A_{V_1H_2}|^2 = \left| e^{i\phi} \frac{1}{\sqrt{2}} \sin \theta_2 + \frac{1}{\sqrt{2}} \cos \theta_2 \right|^2 \quad (5.4.4)$$

Equation (5.4.4) modulates with θ_2 . The entanglement between $|H_1V_2\rangle$ and $|V_1H_2\rangle$ can be quantified from the modulation of the coincidence counting rate between D₁ and D₂ with θ_2 . The relevant metric for entanglement is the quantum interference visibility:

$$V_{\theta_1=45^\circ} = \frac{N_{\max} - N_{\min}}{N_{\max} + N_{\min}} \quad (5.4.5)$$

where N_{\max} and N_{\min} are the maximum and minimum of the coincidence rate modulation with θ_2 respectively. When $\theta_1 = 45^\circ$, for the $\phi = 0$ maximally entangled state equation (5.4.4) predicts a minimum in the measured coincidence rate at $\theta_2 = 135^\circ$. Therefore in order to tune the device to $\phi = 0$, θ_2 was set to 135° , the relative phase of the pump beams recombined at PBS was locked using the side-of-fringe system; θ_{silica} was then adjusted such that the coincidence counting rate was minimized. Under the resulting conditions, Figure 5-8 shows the measured coincidence rate as a function of θ_2 which is in excellent agreement with the modulation predicted by equation (5.4.4). A least squares procedure was used to fit a sinusoidal curve to the data from which $V_{\theta_1=45^\circ}$ was evaluated to be 0.974 ± 0.040 , indicative of a highly entangled state.

When $\theta_1 = 45^\circ$ for the $\phi = \pi$ entangled state, equation (5.4.4) predicts a minimum in the coincidence counting rate at $\theta_2 = 45^\circ$, which was found by varying θ_{silica} with the side of

5. Pump enhanced source of polarisation entangled photon pairs in the telecoms band

fringe system activated. The resulting measured coincidence counting rate as a function of θ_2 is shown in Figure 5-8, and is in excellent agreement with the form of the modulation predicted by equation (5.4.4). From the fitted curve to the data $V_{\theta_1=45^\circ}$ was found to be 0.932 ± 0.036 , the slightly lower $V_{\theta_1=45^\circ}$ value relative to that for the $\phi = 0$ state was likely due to slight error in optimizing θ_{silica} for the $\phi = \pi$ state.

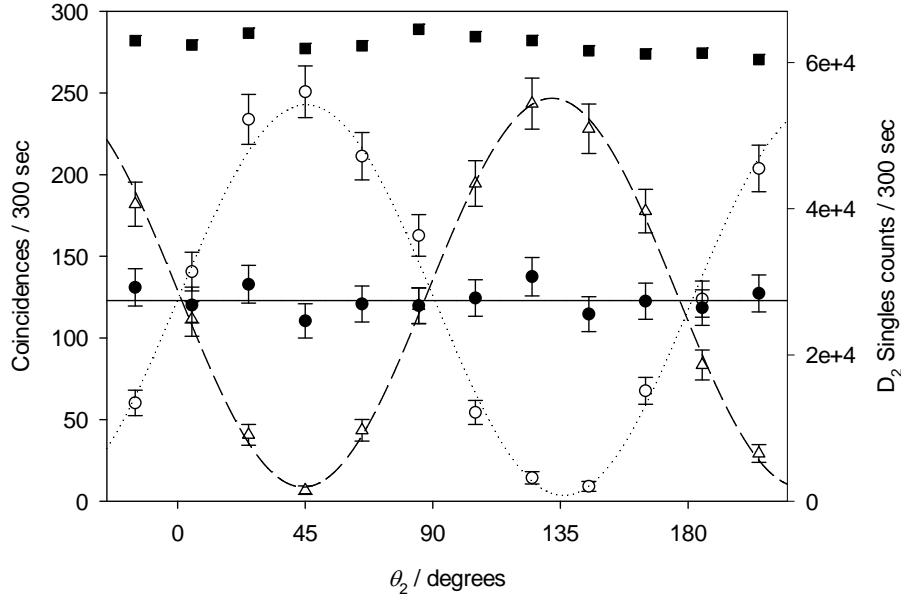


Figure 5-8 Measurements of the number of coincidences over a 300 s time period as a function of θ_2 with fixed $\theta_1 = 45^\circ$. Data sets correspond to $\theta_{silica} = 30.0^\circ$ ($\phi = 0$ state, hollow circles), $\theta_{silica} = 32.1^\circ$ ($\phi = \pi/2$ state, filled circles) and $\theta_{silica} = 34.4^\circ$ ($\phi = \pi$ state, triangles). The lines are least squares fit to the experimental data. The pump power into the enhancement cavity was 50 mW

Finally, equation (5.4.4) shows that the $\phi = \pi/2$ entangled state mimics the behaviour of the classical ensemble, i.e. the coincidence counting rate is independent of θ_2 . The optimum θ_{silica} for the $\phi = \pi/2$ state was found by setting θ_{silica} and θ_2 to coincide with a $\phi = 0, \pi$ entangled state maximum in $N_{\theta_1=45^\circ}(\theta_2)$ and then adjusting θ_{silica} such that the coincidence rate was approximately half the maximum value of $N_{\theta_1=45^\circ}(\theta_2)$. The resulting data points are closely scattered about a horizontal line, following the prediction of equation (5.4.4), and demonstrates the good stability of the system.

5. Pump enhanced source of polarisation entangled photon pairs in the telecoms band

Note that the 4.4° difference between the θ_{silica} values corresponding to the $\phi = 0$ and $\phi = \pi$ states corresponds well to the predicted value of 4.6° from the ϕ - tuning model presented in section 5.3.3.

5.4.3 Measurement of the CHSH S-Parameter

In addition to the visibility of the coincidence counting rate modulation with θ_2 for $\theta_1 = 45^\circ$, a further method of entanglement characterisation is testing for violation of a Bell inequality in the form of the Clauser-Horne-Shimony-Holt (CHSH) parameter [100]. The CHSH S -parameter is given by a linear combination of four expectation values:

$$S = |E(\theta_1, \theta_2) + E(\theta_1, \theta'_2) - E(\theta'_1, \theta_2) + E(\theta'_1, \theta'_2)| \quad (5.4.6)$$

where:

$$E(\theta_1, \theta_2) = \frac{N_{++} - N_{+-} - N_{-+} + N_{--}}{N_{++} + N_{+-} + N_{-+} + N_{--}} \quad (5.4.7)$$

The N s are measured coincidence counting rates, the first N subscript character relates to the analyzer setting of θ_1 ; if the character is '+' then $\theta_1 = \theta_1$, if the character is '-', then $\theta_1 = \theta_1 + \pi/2$. Similarly, the second character of the N subscript relates to the second analyzer setting.

The set $\{\theta_1, \theta_2, \theta'_1, \theta'_2\}$ are chosen to maximize S . There are many equally optimal sets possible, and the chosen set was $\theta_1 = -\pi/4$, $\theta_2 = 0$, $\theta'_1 = 5\pi/8$ and $\theta'_2 = 7\pi/8$. Given an optimal set of analyzer settings, for a classical state $S \leq 2$, while for an ideal entangled state $S = 2\sqrt{2}$. Therefore $S > 2$ denotes non-classical behaviour and higher values denote greater entanglement.

From equations (5.4.6) and (5.4.7), the full characterisation of the S parameter required 16 coincidence rate measurements in total, each were averaged values over a 100 second measurement time. When θ_{silica} was adjusted to give the $\phi = 0$ entangled state, the measured expectation values were; $E(-\pi/4, 0) = -0.869 \pm 0.068$, $E(-\pi/4, 7\pi/8) = -0.546 \pm 0.056$, $E(5\pi/8, 0) = 0.503 \pm 0.055$ and $E(5\pi/8, 7\pi/8) = -0.813 \pm 0.064$. Therefore $S = 2.73 \pm 0.12$, and represents a violation of the Bell inequality by around 6 standard deviations. The S -

5. Pump enhanced source of polarisation entangled photon pairs in the telecoms band

parameter uncertainty is quite large because of the low number of coincidence counts involved in the measurement.

5.5 Rebuild of experiment at the NPL

The measurements presented in sections 5.4 were made on the experimental setup built at the University of St. Andrews. NPL required that the polarisation entangled photon source be reconstructed on-site at Teddington. Some components of the St. Andrews build were NPL property, however some components were property of St. Andrews and therefore solutions had to be found so that the setup could be used by the NPL long term. Where components could not be procured for NPL within a short time scale, the items were borrowed on a short loan basis from St. Andrews. Table 5-1 summarizes the components that could be shipped directly from St. Andrews to the NPL and those components for which new or loan solutions were required.

<i>NPL components returned or purchased from St Andrews</i>	<i>New solutions required</i>	<i>Components to be loaned to the NPL from St. Andrews</i>
DPSSL	Beam steering mirrors for 532 nm laser radiation	Ti-sapphire laser
PDH and Side-of-fringe lock systems.	Beam steering mirrors for 792 nm laser radiation	1584 nm interference filters
DM ₁ , DM ₂ , M ₁ , M ₂ , M ₃	Isolator	Adaptors for fitting M ₂ , M ₃ to piezo ceramics
PPKTP	Wavelength dispersive prisms	Piezo ceramics for M ₂ , M ₃
HWP @ 1584 nm	L ₁ , L ₃ , L ₄	Adaptor for fitting M ₁ , to mount
PBS recombiner	Variable attenuator	
1584 nm pol. analyzers	ϕ tuning mechanism	
	792 nm pol. analyzer	

Table 5-1 Table showing sources for components required for rebuilding the polarisation entangled photon pair source at the NPL. See Figure 5-2 for key to component symbols.

Although the system built at the NPL was largely the same as the one shown in Figure 5-2, a notable change was that the optical path from the Ti-sapphire aperture to the mirror M₁ was

5. Pump enhanced source of polarisation entangled photon pairs in the telecoms band

shortened by approximately 1 m by removing lens L_1 altogether and replacing the mode matching lens L_2 (see section 4.4.3) with a 500 mm focal length lens positioned ~ 600 mm from M_1 . A photograph of the experimental setup at NPL is shown in Figure 5-9 and experimental data taken from the setup is shown in Figure 5-10.

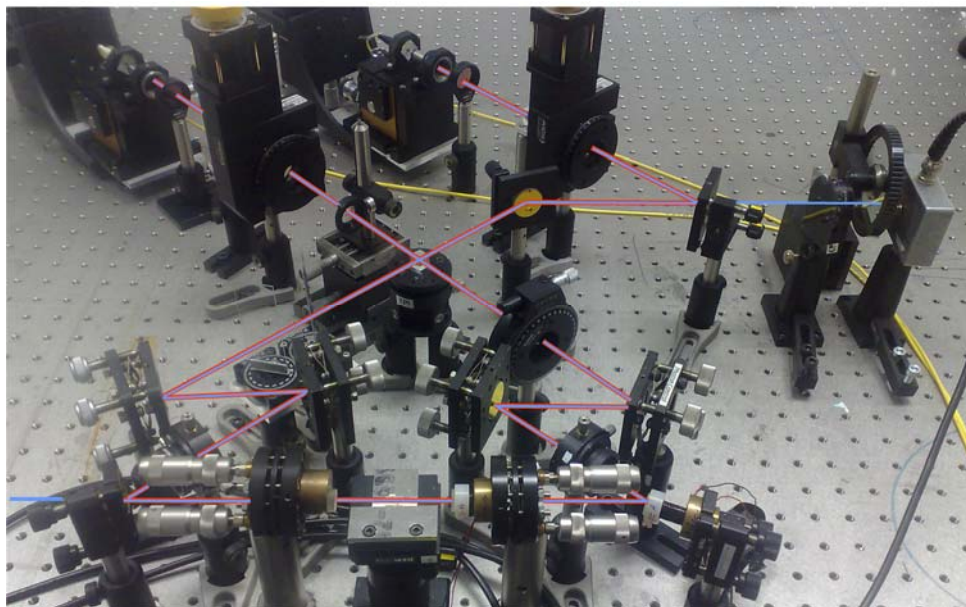


Figure 5-9 Photograph of the polarisation entangled photon pair setup at NPL. The blue and red lines represent the optical paths of 792 nm pump light and downconversion respectively.

The data in Figure 5-10 (a) shows the measured number of coincidences in a fixed time for a range of θ_{silica} when both θ_1 and $\theta_2 = 45^\circ$. The minimum in the coincidence rate corresponds to the formation of the $\phi = \pi$ state, [for which the measured coincidence rate as a function of θ_2 is shown in Figure 5-10 (b)], while the mid-point and maximum in the coincidence rate corresponds to the $\phi = \pi/2$ and $\phi = 0$ states respectively. The $\sim 4^\circ$ difference between θ_{silica} corresponding to the $\phi = 0, \pi$ states is consistent with the operation of the St. Andrews device.

From the least squares fit to the data in Figure 5-10 (b), $V_{\theta_1=45^\circ}$ was found to be 0.945 ± 0.028 , which is comparable to the visibilities achieved on the St. Andrew setup. No variable attenuator was available to put in the $|H_1V_2\rangle$ beam in order to balance the $|H_1V_2\rangle$ and $|V_1H_2\rangle$ amplitudes; instead the balancing was achieved by making an incremental change of the $|H_1V_2\rangle$ beam trajectory in order to reduce the coupling efficiency into D_1 and D_2 relative to $|V_1H_2\rangle$. For 30 mW pump power, 503 coincidences were measured when

5. Pump enhanced source of polarisation entangled photon pairs in the telecoms band

$\theta_1 = 90^\circ$ and $\theta_2 = 0^\circ$, and this corresponds to the measured coincidence counting rate due to the pairs out through mirror M_2 of the enhancement cavity. Per unit of pump power this corresponds to a coincidence counting rate that is 3.33 time greater than was measured on the equivalent St. Andrews setup. This can be largely accounted for by the replacement of lens L_3 , D_1 and D_2 focusing optics ($T = 0.73$, $T = 0.702$ and $T = 0.826$ respectively) with HT lenses; the removal of the associated losses predicts an improvement in the coincidence counting rate of 3.24 for the NPL setup, which is close to the measured improvement.

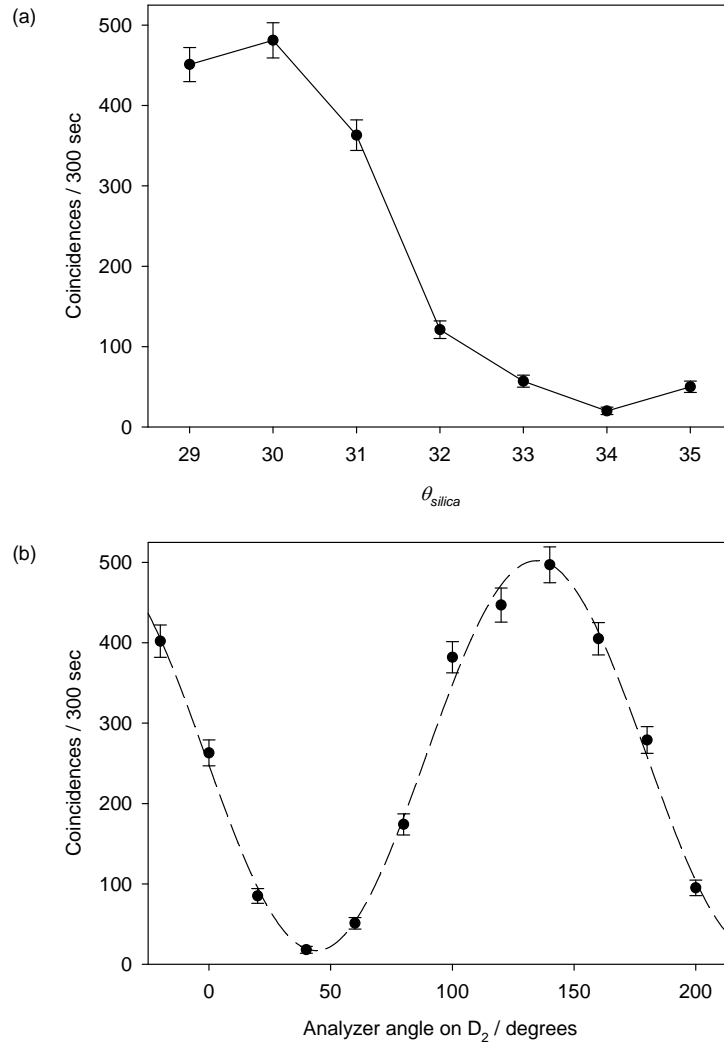


Figure 5-10 (a) Measurements of the number of coincidences over a 300 s time period as a function of θ_{silica} with $\theta_1 = \theta_2 = 45^\circ$. (b) Measurements of the number of coincidences over a 300 s time period as a function of θ_2 with $\theta_1 = 45^\circ$ and $\theta_{silica} = 34.0^\circ$ ($\phi = \pi$ state). The pump power into the enhancement cavity was 30 mW.

5.6 Conclusions

The design and implementation of a novel source of degenerate polarisation entangled photon pairs in the telecoms band based on a cavity enhanced parametric downconversion process was presented. The design of the system allowed for the production of two of the four maximally entangled Bell states, with the remaining two obtainable through the addition of a further half wave plate into the setup. The relative phase between the two kets of each entangled state was locked by using a side of fringe locking system to fix the optical path difference of a two beam interferometer formed by the 792 nm pump light reflected from and transmitted through the enhancement cavity. A two rotatable glass-slide system in combination with the side-of-fringe locked interferometer was used to vary the relative phase between the ket states to allow for tuning between maximally entangled states. Analysis of the coincidence rate between two detectors in the A/D basis revealed the production of highly entangled states, resulting in quantum interference visibilities ~ 0.95 . The entangled states produced were found to break a Bell inequality by around 6 standard deviations. The coincidence counting rates per unit pump power were higher than those expected considering the coincidence counting rate measured from the same cavity enhanced down conversion process in the previous chapter, and the optical losses associated with each measurement. This was attributed to the fact the quantum efficiency of one photon counter was low when making the measurements for the previous chapter due to damage, whereas the detector had been repaired for the measurements in this chapter.

The experiment was rebuilt at the NPL. The interference visibilities measured on that setup were comparable to those measured on the St. Andrews setup, but the count rates per mW pump power were higher on the NPL setup due to the replacement of non-ideally coated optics with HT optics for the downconverted wavelengths.

6 Design of a wavelength tuneable device for the absolute measurement of detector quantum efficiency.

6.1 Introduction

From the first demonstration of time correlation between pair photons from spontaneous parametric downconversion, it was suggested that the emission could be incorporated into a technique for the absolute measurement of detector quantum efficiency (QE) [101]. The technique is interesting because unlike current methods, it allows for absolute calibration in terms of photon number. The basic method shown in Figure 6-1, requires that two parametrically generated photons of a pair follow different optical paths to separate detectors. One detector is permanently incorporated into the setup and is known as the trigger, while the second detector is the one to be calibrated, commonly known as the detector under test (DUT). Due to the simultaneity of photon pair creation in SPDC, the detection of a photon at the trigger detector means that a photon must also be also present at the DUT; if the DUT does not register a photon, it must be as a result of either i) transmission losses in the DUT channel, η_{DUT} or ii) non unity quantum efficiency of the DUT, QE_{DUT} therefore:

$$QE_{DUT}\eta_{DUT} = \frac{N_c}{N_{trigger}} \quad (6.1.1)$$

where $N_{trigger}$ is the dark-count corrected count rate at the trigger detector and N_c is the accidental corrected coincidence counting rate between the two detectors.

Equation (6.1.1) is only true provided that the DUT receives all photons (other than those photons that are lost due to the measured transmission losses η_{DUT}) that are correlated to those photons detected by the trigger. As discussed in section 2.5, the downconversion photons occupying a given collection angle in one of two channels will have correlations with those photons occupying a larger collection angle in the second channel, therefore in order to ensure all photons received by the trigger have their conjugate received by the DUT it is necessary that $\Delta\theta_{DUT,lab} \gg \Delta\theta_{trig,lab}$, where $\Delta\theta_{DUT,lab}$ and $\Delta\theta_{trig,lab}$ are the photon collection

angles for the DUT and trigger detectors respectively. In addition, spectral filters are normally mounted on both detectors where the acceptance bandwidth through the DUT channel exceeds that through the trigger channel.

There have been studies of the technique at national metrology institutes (NMIs) [47, 102-103] that have focussed on methods for quantifying the DUT channel transmission losses and their associated uncertainties, since they represent the largest contribution to the overall uncertainty on the quantum efficiency measurement. In these investigations spectral filters limit the bandwidth over which the quantum efficiency is defined, and there is no capability to perform the measurement over multiple wavelength ranges. In principle, other spectral filters could be used to test other wavelengths but this would be costly and greatly increase the characterisation measurements required.

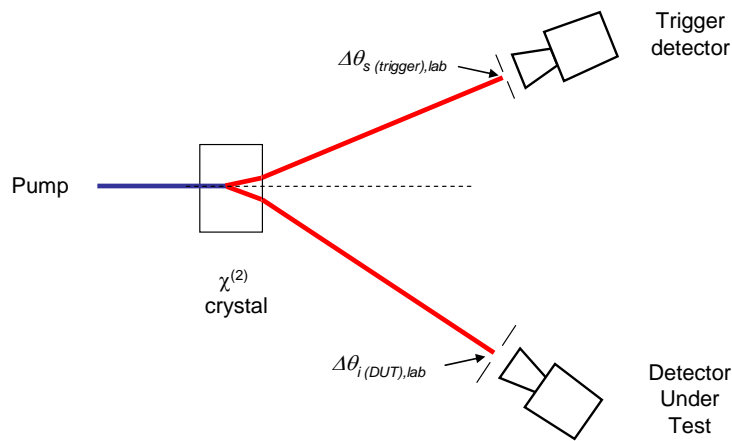


Figure 6-1 Setup for absolute calibration of photon counting detectors. The blue and red lines denote pump and downconversion beam paths respectively. Since η_{DUT} , N_c and $N_{trigger}$ are measurable, QE_{DUT} can be calculated.

The aim of this chapter is to present a framework to facilitate the design of a device that would allow measurements of detector quantum efficiency over a number of spectral windows without spectral filters, i.e. a frequency scanning quantum efficiency measurement (FSQEM) device. The device is based on a broad band parametric downconverter and the design work concerns the analysis of the spatial and spectral properties of the downconversion emission, and how these change with respect to various tuning mechanisms.

Such a device could be established as part of a measurement service at an NMI where the DUT detector belonging to an external customer would be sent for characterisation.

Alternatively for customers requiring detector calibration in larger numbers, the device could be located off-site with periodic re-calibrations at an NMI.

The chapter starts by outlining the calculation method that was used to study the spectral and spatial emission properties of photons from parametric downconversion processes. The framework for the FSQEM device design is presented with reference to a BBO downconverter system designed to measure detector quantum efficiencies in the visible/near IR region. With calculations based upon the presented theory, design parameters such as choice of travelling/stationary detectors, temperature/angle wavelength tuning of the QE measurement wavelength, detector collection angles, pump beam diameter and downconversion crystal length are investigated and discussed. Possible improvements to the modelling are also discussed.

6.2 Modelling theory and calculation method

For most other phasematching calculations within this portfolio only the interactions with exact phasematching i.e. $\Delta k = 0$ are considered, which in many cases allows for a simple analytical solutions to problems. For the device studied here it is important to know properties such as the spectral bandwidth of photons at the DUT whose conjugate is received by the trigger and whether all photons received by the trigger have their conjugate received by the DUT. Therefore it was necessary to gain a more detailed insight of the spatial and spectral properties of the downconversion through studying the interactions with $\Delta k \neq 0$. The following section details an approach.

The quantum state of photon pairs from a parametric downconversion process is given by [104]:

$$|\psi\rangle = |0\rangle + \int d\mathbf{k}_{\text{trig}} \int d\mathbf{k}_{\text{DUT}} S(\mathbf{k}_{\text{trig}}, \mathbf{k}_{\text{DUT}}) \hat{a}^\dagger(\mathbf{k}_{\text{trig}}) \hat{a}^\dagger(\mathbf{k}_{\text{DUT}}) |0\rangle \quad (6.2.1)$$

Where \mathbf{k}_{trig} and \mathbf{k}_{DUT} are the ‘trigger’ and ‘DUT’ photon crystal wavevectors respectively, and the $\hat{a}^\dagger(\mathbf{k})$ is the creation operator for a photon with wavevector \mathbf{k} . $S(\mathbf{k}_{\text{trig}}, \mathbf{k}_{\text{DUT}})$ is the

function that carries the phasematching and energy conservation conditions. The probability that a photon pair is created in modes \mathbf{k}_{trig} and \mathbf{k}_{DUT} is given by $|S(\mathbf{k}_{\text{trig}}, \mathbf{k}_{\text{DUT}})|^2$:

$$|S(\mathbf{k}_{\text{trig}}, \mathbf{k}_{\text{DUT}})|^2 = \left(\frac{d_{\text{eff}}}{2}\right)^2 \delta(\omega_{\text{trig}} + \omega_{\text{DUT}} - \omega_p) s_{\perp}(\Delta k_x, \Delta k_y) s_z(\Delta k_z) \quad (6.2.2)$$

$$s_{\perp}(\Delta k_x, \Delta k_y) = \exp\left(-\frac{1}{2} w^2 [\Delta k_x^2 + \Delta k_y^2]\right) \quad (6.2.3)$$

$$s_z(L\Delta k_z) = \text{sinc}^2\left(\frac{1}{2} L\Delta k_z\right) \quad (6.2.4)$$

d_{eff} is the effective non-linear coefficient for the interaction, Δk_x , Δk_y and Δk_z are the x , y and z components of Δk respectively, w is the pump beam diameter and the δ function conveys the energy conservation relationship. $S(\mathbf{k}_{\text{trig}}, \mathbf{k}_{\text{DUT}})$ is often referred to as the biphoton probability amplitude and can be expressed as:

$$S(\mathbf{k}_{\text{trig}}, \mathbf{k}_{\text{DUT}}) = \langle 0 | \hat{a}(\mathbf{k}_{\text{DUT}}) \hat{a}(\mathbf{k}_{\text{trig}}) | \psi \rangle \quad (6.2.5)$$

For slow detectors, the coincidence counting rate for the generated signal and idler photons is proportional to the second order Glauber correlation function [63]:

$$G^{(2)} = \int d\mathbf{k}_{\text{trig}} \int d\mathbf{k}_{\text{DUT}} \left| \langle 0 | \hat{a}(\mathbf{k}_{\text{DUT}}) \hat{a}(\mathbf{k}_{\text{trig}}) | \psi \rangle \right|^2 = \int d\mathbf{k}_{\text{trig}} \int d\mathbf{k}_{\text{DUT}} |S(\mathbf{k}_{\text{trig}}, \mathbf{k}_{\text{DUT}})|^2 \quad (6.2.6)$$

In order to describe equation (6.2.6) in terms of bounded laboratory co-ordinates, such that it defines the coincidence rate of photons through two solid angles defined by aperture pairs, consider a narrow pump beam propagating along the z direction in a thin non-linear medium with wavevector \mathbf{k}_p . \mathbf{k}_p downconverts according to the phasematching relation $\mathbf{k}_p \rightarrow \mathbf{k}_{\text{trig}} + \mathbf{k}_{\text{DUT}}$, see Figure 6-2. The magnitude of the wavevectors, \mathbf{k}_j ($j=\text{trig}, \text{DUT}, p$) are given by $n_j \omega_j / c$, where c is the speed of light in vacuum, while n_j and ω_j are the associated refractive indices and angular frequencies respectively.

The direction of the crystal wavevectors for the downconversion are described by polar angles θ_{trig} , θ_{DUT} measured from the z axis, and azimuthal angles ϕ_{trig} , ϕ_{DUT} measured from the x

axis in the $x-y$ plane, therefore wavevector mismatches associated with the two directions perpendicular to the pump propagation are given by [105]:

$$\Delta k_x = |\mathbf{k}_{DUT}| \sin \theta_{DUT} \cos \phi_{DUT} + |\mathbf{k}_{trig}| \sin \theta_{trig} \cos \phi_{trig} \quad (6.2.7)$$

$$\Delta k_y = |\mathbf{k}_{DUT}| \sin \theta_{DUT} \sin \phi_{DUT} + |\mathbf{k}_{trig}| \sin \theta_{trig} \sin \phi_{trig} \quad (6.2.8)$$

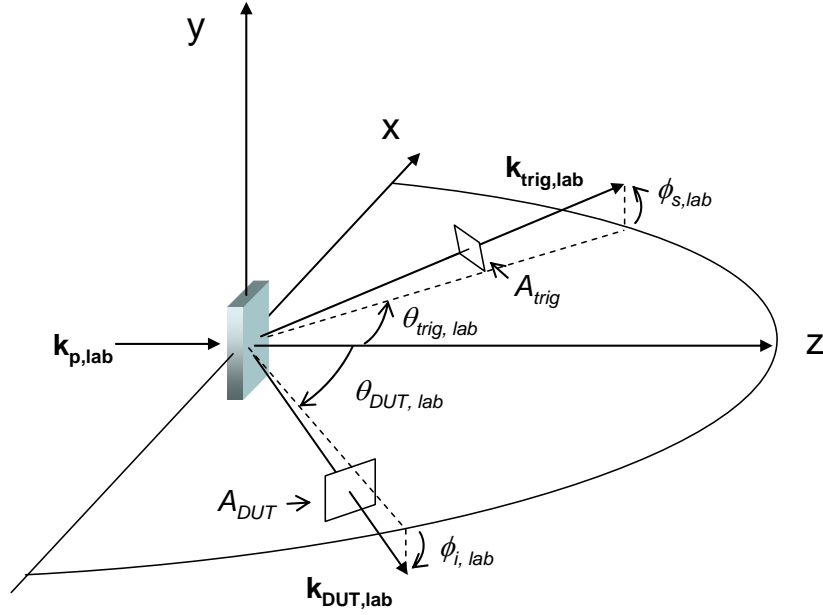


Figure 6-2 Geometry of SPDC generation and collection considering a thin crystal and a narrow pump beam. One photon of the pair with laboratory wavevector $\mathbf{k}_{trig,lab}$ is sent to the trigger detector defined by an aperture A_{trig} with a collection angle $\Delta\theta_{trig,lab} \times \Delta\phi_{trig,lab}$ centred at $\theta_{trig,lab}^0$ and $\phi_{trig,lab}^0$. The conjugate photon with wave-vector $\mathbf{k}_{DUT,lab}$ is emitted to the DUT defined by aperture A_{DUT} with a collection angle $\Delta\theta_{DUT,lab} \times \Delta\phi_{DUT,lab}$ centred at $\theta_{DUT,lab}^0$ and $\phi_{DUT,lab}^0$. $\mathbf{k}_{p,lab}$, $\mathbf{k}_{trig,lab}$ and $\mathbf{k}_{DUT,lab}$ are associated with the crystal wavevectors \mathbf{k}_p , \mathbf{k}_{trig} and \mathbf{k}_{DUT} respectively.

The total transverse wavevector mismatch is then given by $\Delta k_{\perp} = \sqrt{\Delta k_x^2 + \Delta k_y^2}$. The contribution to the phase mismatch along the pump propagation direction is given by [105]:

$$\Delta k_z = |\mathbf{k}_{DUT}| \cos \theta_{DUT} + |\mathbf{k}_{trig}| \cos \theta_{trig} - |\mathbf{k}_p| \pm \frac{2\pi}{\Lambda} \quad (6.2.9)$$

Where Λ is for a grating vector and is therefore included only in the case of periodically poled crystals. In order to quantify the phase mismatch terms, it is necessary to evaluate the

refractive indices of each photon. For the general case of a biaxial crystal, the refractive indices are given by the Fresnel equation of wave normals [106-107]:

$$\frac{s_x^2}{\frac{1}{n^2(\hat{s})} - \frac{1}{n_x^2}} + \frac{s_y^2}{\frac{1}{n^2(\hat{s})} - \frac{1}{n_y^2}} + \frac{s_z^2}{\frac{1}{n^2(\hat{s})} - \frac{1}{n_z^2}} = 0 \quad (6.2.10)$$

n_x , n_y and n_z are the principal refractive indices at a specified wavelength. For uniaxial crystals $n_x = n_y = n_o$ and $n_z = n_e$, where n_o and n_e are the ordinary and extraordinary refractive indices respectively. \hat{s} is the propagation vector, the propagation vector for the pump \hat{s}_p is defined by angles θ_p , ϕ_p relative to the crystal axes [106]:

$$\hat{s}_p = \begin{pmatrix} s_{p,x} \\ s_{p,y} \\ s_{p,z} \end{pmatrix} = \begin{pmatrix} \sin \theta_p \cos \phi_p \\ \sin \theta_p \sin \phi_p \\ \cos \theta_p \end{pmatrix} \quad (6.2.11)$$

The signal and idler propagation vectors (\hat{s}_{trig} and \hat{s}_{DUT} respectively) were defined in Figure 6-2 by angles relative to the pump wavevector, therefore a coordinate transform is required to express \hat{s}_{trig} and \hat{s}_{DUT} relative to the crystal axis [106]:

$$\hat{s}_{trig} = \begin{pmatrix} \cos \theta_p \cos \phi_p \sin \theta_{trig} \cos \phi_{trig} - \sin \phi_p \sin \theta_{trig} \sin \phi_{trig} + \sin \theta_p \cos \phi_p \cos \theta_{trig} \\ \cos \theta_p \sin \phi_p \sin \theta_{trig} \cos \phi_{trig} + \cos \phi_p \sin \theta_{trig} \sin \phi_{trig} + \sin \theta_p \sin \phi_p \cos \theta_{trig} \\ \cos \theta_p \cos \theta_{trig} - \sin \theta_p \sin \theta_{trig} \cos \phi_{trig} \end{pmatrix} \quad (6.2.12)$$

\hat{s}_{DUT} is given by exchanging θ_{trig} and ϕ_{trig} in equation (6.2.12) with θ_{DUT} and ϕ_{DUT} respectively. Substituting $1/n^2(\hat{s})$ in equation (6.2.10) for x and rearranging gives a quadratic equation in x which has two solutions that are associated with the refractive indices for different polarisation modes;

$$n = \sqrt{\frac{2}{P \pm \sqrt{P^2 - 4Q}}} \quad (6.2.13)$$

where:

$$P = \left[s_x^2 \left(\frac{1}{n_y^2} + \frac{1}{n_z^2} \right) + s_y^2 \left(\frac{1}{n_x^2} + \frac{1}{n_z^2} \right) + s_z^2 \left(\frac{1}{n_x^2} + \frac{1}{n_y^2} \right) \right] \quad (6.2.14)$$

$$Q = \left[\frac{s_x^2}{n_y^2 \cdot n_z^2} + \frac{s_y^2}{n_x^2 \cdot n_z^2} + \frac{s_z^2}{n_x^2 \cdot n_y^2} \right] \quad (6.2.15)$$

n_p , n_{trig} and n_{DUT} can then be determined by choosing the solution of equation (6.2.13) that corresponds to the polarisation mode of the photon concerned. By inserting the refractive indices into equations (6.2.7)-(6.2.9), Δk_{\perp} and Δk_z can be calculated for the downconversion interaction. Therefore the photon pair coincidence counting rate associated with the entire two photon field may be re-written as [105]:

$$\begin{aligned} G^{(2)} = & \int d\mathbf{k}_{\text{trig}} \int d\mathbf{k}_{\text{DUT}} |S(k_{\text{trig}}, k_{\text{DUT}})|^2 = \int_0^{\pi} d\theta_{\text{DUT}} \int_0^{2\pi} d\phi_{\text{DUT}} \int_0^{\infty} d\omega_{\text{DUT}} \int_0^{\pi} d\theta_{\text{trig}} \int_0^{2\pi} d\phi_{\text{trig}} \int_0^{\infty} d\omega_{\text{trig}} \\ & \times N \exp \left(-\frac{1}{2} w^2 \left[\frac{n_{\text{DUT}}^2 \omega_{\text{DUT}}^2}{c^2} \sin^2 \theta_{\text{DUT}} + \frac{n_{\text{trig}}^2 \omega_{\text{trig}}^2}{c^2} \sin^2 \theta_{\text{trig}} \right] \right) \\ & \times \exp \left(w^2 \left[\frac{n_{\text{DUT}} \omega_{\text{DUT}}}{c} \frac{n_{\text{trig}} \omega_{\text{trig}}}{c} \sin \theta_{\text{DUT}} \sin \theta_{\text{trig}} \cos(\phi_{\text{DUT}} - \phi_{\text{trig}} - \pi) \right] \right) \\ & \times \text{sinc}^2 \left(\frac{1}{2L} \left[\frac{n_{\text{DUT}} \omega_{\text{DUT}}}{c} \cos \theta_{\text{DUT}} + \frac{n_{\text{trig}} \omega_{\text{trig}}}{c} \cos \theta_{\text{trig}} - \frac{n_p \omega_p}{c} \right] \right) \cdot \delta(\omega_{\text{trig}} + \omega_{\text{DUT}} - \omega_p) \end{aligned} \quad (6.2.16)$$

Where the Jacobean required for the $d\mathbf{k}_j \rightarrow d\phi_j d\theta_j d\omega_j$ transformation is assumed to be slowly varying and is therefore included within the normalization constant N along with the effective nonlinearity. Evaluating the delta function and setting the limits of the $d\phi_j d\theta_j$ integrands such that $G^{(2)}$ corresponds to coincidence detection rate through apertures A_{trig} and A_{DUT} :

$$\begin{aligned} G_{\text{trig}+\text{DUT}}^{(2)} = & \int_{\omega_s, \min}^{\omega_s, \max} \int_{\Delta\phi_{\text{trig}, \text{lab}}} \int_{\Delta\theta_{\text{trig}, \text{lab}}} \int_{\Delta\phi_{\text{DUT}, \text{lab}}} \int_{\Delta\theta_{\text{DUT}, \text{lab}}} d\theta_{\text{DUT}} d\phi_{\text{DUT}} d\theta_{\text{trig}} d\phi_{\text{trig}} d\omega_{\text{trig}} \\ & \times N \exp \left(-\frac{1}{2} w^2 \left[\frac{n_{\text{trig}}^2 \{\omega_p - \omega_{\text{trig}}\}^2}{c^2} \sin^2 \theta_{\text{DUT}} + \frac{n_{\text{trig}}^2 \omega_{\text{trig}}^2}{c^2} \sin^2 \theta_{\text{trig}} \right] \right) \\ & \times N \exp \left(w^2 \left[\frac{n_{\text{DUT}} \{\omega_p - \omega_{\text{trig}}\}}{c} \frac{n_{\text{trig}} \omega_{\text{trig}}}{c} \sin \theta_{\text{DUT}} \sin \theta_{\text{trig}} \cos(\phi_{\text{DUT}} - \phi_{\text{trig}} - \pi) \right] \right) \end{aligned}$$

$$\times \text{sinc}^2 \left(\frac{1}{2L} \left[\frac{n_{DUT} \{ \omega_p - \omega_{trig} \}}{c} \cos \theta_{DUT} + \frac{n_{trig} \omega_{trig}}{c} \cos \theta_{trig} - \frac{n_p \omega_p}{c} \right] \right) \cdot \delta(\omega_{trig} + \omega_{DUT} - \omega_p) \quad (6.2.17)$$

In order to evaluate equation (6.2.17) numerically the integrations were replaced with summations:

$$\sum_{\omega_{trig}} \sum_{\Delta \phi_{trig,lab}} \sum_{\Delta \theta_{trig,lab}} \sum_{\Delta \phi_{DUT,lab}} \sum_{\Delta \theta_{DUT,lab}} \delta \theta_{DUT} \delta \phi_{DUT} \delta \theta_{trig} \delta \phi_{trig} \delta \omega_{trig} \quad (6.2.18)$$

The computation time scales with the product of all N_x ($x = \theta_{DUT}, \phi_{DUT}, \theta_{trig}, \phi_{trig}, \omega_{trig}$) where N_x is the number of intervals δx within the limits of the summation over x . A desktop PC (with limited power) was used for the calculations, therefore the apertures were assumed to be thin such that $\phi_{DUT} = \phi_{trig} + \pi$ and the summations over $\delta \phi_{DUT}$ and $\delta \phi_{trig}$ could be ignored, i.e.:

$$G_{trig+DUT}^{(2)} = \sum_{\Delta \omega_{trig}} \sum_{\Delta \theta_{trig,lab}} \sum_{\Delta \theta_{DUT,lab}} |S(\theta_{DUT}, \theta_{trig}, \omega_{trig})|^2 \delta \theta_{DUT} \delta \theta_{trig} \delta \omega_{trig} \quad (6.2.19)$$

θ_{DUT} and θ_{trig} define directions within the crystal where as $\Delta \theta_{DUT,lab}$ and $\Delta \theta_{trig,lab}$ that define the summation limits are laboratory angles, therefore Snell's law is required for $\theta_{trig} \rightarrow \theta_{trig,lab}$ and $\theta_{DUT} \rightarrow \theta_{DUT,lab}$. By calculating the analytically derived phase matching curves plotting $\theta_{trig,lab}$ against ω_{trig} , and then determining the ω_{trig} ordinates where the phase matching curves intersect the $\theta_{trig,lab}$ summation limits, it is possible to accurately estimate the ω_{trig} limits and therefore minimise $N_{\omega_{trig}}$.

Equation (6.2.19) is proportional to the correlated photon pair collection rate through the trigger and DUT detector apertures and forms the basis of much of the following analysis which relates to the design characteristics of a FSQEM system for the measurement of detector QEs at visible/near IR wavelengths.

6.3 Modelling of FSQEM system based on noncollinear

351.1 nm (e) → 702.2 (o) + 702.2 (o) process in BBO

Photon counting in the visible regime is a relatively mature technology, perhaps the most popular commercially available photon counting module is the Perkin Elmer SPDC-AQR series device based on silicon avalanche photodiode technology. These detectors are relatively cheap, have low dark counts, and short dead times. The detectors also have quantum efficiencies $> 10\%$ at 450 nm and 1 μm , with maximum quantum efficiencies of upto 75% at around 700 nm. Due to the high performance and ubiquity of the device, it would be the obvious choice for incorporation into the first demonstration of a FSQEM device.

BBO has excellent transmittance at the UV pump wavelengths that would be required to generate photon pairs in the operating wavelength region of silicon avalanche photodiodes. Also from the experiments of chapter 2 and 3 in this portfolio, it known that the non-collinear 351.1 nm (e) → 702.2 nm (o) + 702.2 nm (o) process is efficient, and therefore this interaction will be basis for the investigations here.

This section explores numerous parameters of the FSQEM device using the outlined theory, and presents a framework for designing other FSQEM devices that perhaps utilise other downconversion crystals and are associated with different measurement wavelengths

Firstly, properties of the system that can be determined from an exact phasematching analysis are studied. In section 6.3.1, factors such as the choice of non-collinear emission angle are discussed together with the properties that the system must have in order for the device to be frequency tuneable. A major requirement is seen to be the ability to change the centre lines defining the detector collection angles. If it is desirable to lock the position of one detector while frequency tuning, the ability to change the phasematching interaction is also necessary. The two possible mechanisms for changing the phasematching conditions are: (i) temperature dependency of both the n_e and n_o BBO refractive indices and; (ii) the dependency of the pump photon refractive index on the angle between the pump wavevector and the crystal optic axis. The two phase tuning methods are compared and contrasted in sections 6.3.2 - 6.3.3.

The limitations of the exact phase matching studies are discussed in 6.3.4, and the following analyses are based on the full (non-exact) phase matching approach presented in section 6.2.

Section 6.3.5 studies the importance of $\Delta\theta_{DUT,lab}$ choice on the device operation while section 6.3.6 discusses the parameters that affect the measurement resolution of the FSQEM device. Finally the properties of the system are discussed as the quantum efficiency measurement wavelength is tuned (section 6.3.6).

6.3.1 Choice of phase matching angle and mode of device operation

In chapter 2 where the $351\text{nm}(e) \rightarrow 702\text{nm}(o) + 702\text{nm}(o)$ interaction in BBO was used to source a HOM interferometer, a phase matching angle θ_{pm} of 35.5° was chosen over smaller θ_{pm} because smaller θ_{pm} corresponds to smaller emission angles and fitting the HOM interferometer components about the source would have been difficult.

The $\theta_{pm}=35.5^\circ$ phasematching curve plotting photon emission angle against wavelength features a trough at around 600 nm, see Figure 2-4(a). For the FSQEM device this poses a problem; placing the trigger aperture at a laboratory angle within the trough corresponds to a large spectral bandwidth of photons collected, defining a large bandwidth of conjugate photons (~ 850 nm) collected at the DUT, and resulting in a quantum efficiency measurement with poor wavelength resolution. In addition, the small angular separation of the two downconverted beams would not allow for the possibility of a compact device. The use of mirrors to separate the two beams would not be favourable for the FSQEM device because their reflectance properties would need to be characterised and such characterisation measurements would add contributions to the uncertainty budget of the quantum efficiency measurement.

At larger θ_{pm} the photon emission angle increases, allowing for the trigger and DUT to be placed closer to the source while the trough in the phasematching curve gets pushed back to shorter wavelengths, no trough is apparent at $\theta_{pm}=40^\circ$. Note however from equation (2.3.6) that d_{eff} is $\sim 7\%$ smaller at $\theta_{pm}=40^\circ$ than at $\theta_{pm}=35.5^\circ$. Also note that the larger emission angles at larger θ_{pm} may cause a reduction in the effective length of the crystal. The effective phase-matching interaction length or non-collinear length L_{eff} is defined by:

$$L_{eff} = \frac{w}{\tan \theta} \quad (6.3.1)$$

Where w is the pump beam diameter and θ is taken to be the largest collinear emission angle of the interaction.

It can be seen from the phasematching curves in Figure 2-4(a) that for a given θ_{pm} , emission occurs over all wavelengths within the required calibration regime. Therefore by moving the angular positions of the trigger and DUT detectors to points along the phasematching curve such that they collect conjugate pairs, it would be possible to quantify the DUT quantum efficiency across all wavelengths using only one phasematching condition. However since the DUT is not a permanent component of the system, it would be convenient for this detector to be stationary. Figure 6-3 shows the basic principle of a mode of operation for a FSQEM device that allows for the DUT to be held stationary. The plot shows two phase matching conditions for BBO, under both conditions the DUT is positioned to collect photons along $\theta_{DUT,lab}=12^\circ$. Also shown are the angular positions for the trigger that ensure collection of the photons paired to those received by the DUT. Therefore between the two phasematching conditions it can be seen that the quantum efficiency measurement wavelength changes between 550nm and 610 nm, while $\theta_{DUT,lab}$ remains fixed. Sections 6.3.2-6.3.3 study two possible phasematching tuning mechanisms that could be incorporating into a ‘fixed-DUT’ FSQEM device.

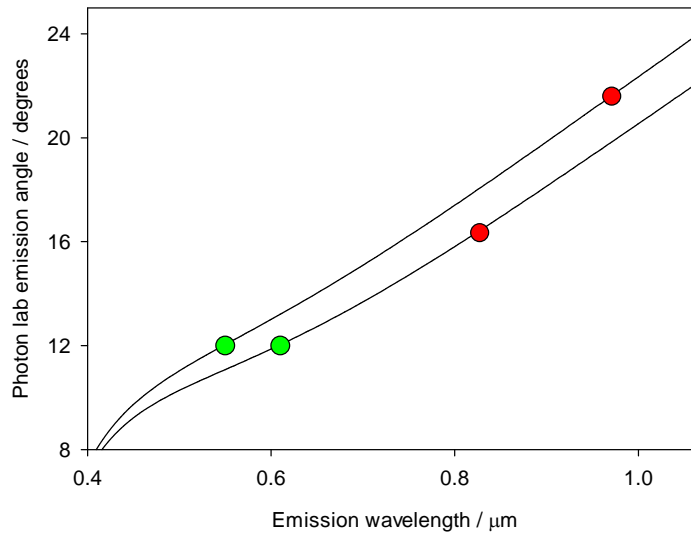


Figure 6-3 The two lines show distinct phase matching configurations. In each case the DUT collects photons travelling along $\theta_{DUT,lab}=12^\circ$ (green circles), for the lower curve, this corresponds to longer wavelengths at the DUT. By energy conservation, the photons paired to those received by the DUT pass along either $\theta_{trig,lab}=16.3^\circ$ for the lower curve or 21.6° for the upper curve (red circles).

6.3.2 Temperature tuning in BBO

The wavelength and temperature dependent refractive indices for BBO are given by [42]:

$$n_e(T) = n_e(1 - 9.3 \times 10^{-6} dT), n_e = \sqrt{2.3730 + \frac{0.0128}{\lambda^2 - 0.0156} - 0.0044\lambda^2} \quad (6.3.2)$$

$$n_o(T) = n_o(1 - 16.6 \times 10^{-6} dT), n_o = \sqrt{2.7405 + \frac{0.0184}{\lambda^2 - 0.0179} - 0.0155\lambda^2} \quad (6.3.3)$$

Where $dT = T - 20$. Figure 6-4 shows exact phasematching curves of the laboratory emission angle with wavelength at different temperatures calculated using the analytical expression (2.3.4). The DUT is positioned to collect photons along $\theta_{DUT,lab} = 10^\circ$. As the temperature is increased from 25°C through to 325°C, the phasematched wavelength received by the DUT increases from 525 nm to 820 nm while the correlated wavelength to the movable trigger detector decreases from 1.06 μm to 615 nm. Quantum efficiency measurements at shorter wavelengths would be problematic due to the diminishing quantum efficiency of the trigger detector at the longer conjugate wavelengths (if silicon technology is used). Clearly if a large tuning range for the quantum efficiency measurements is required (e.g. covering the sensitivity bandwidth of silicon technology) then a large range of crystal temperatures $> 300^\circ\text{C}$ must be accessible. Although the non-linear properties of the material should hold over such a large temperature range (BBO undergoes a phase change at 900°C [42]), there may be engineering problems to overcome such as those due to the thermal expansion of the material and the possibility of crystal damage due to the temperature gradient at the crystal-air interface.

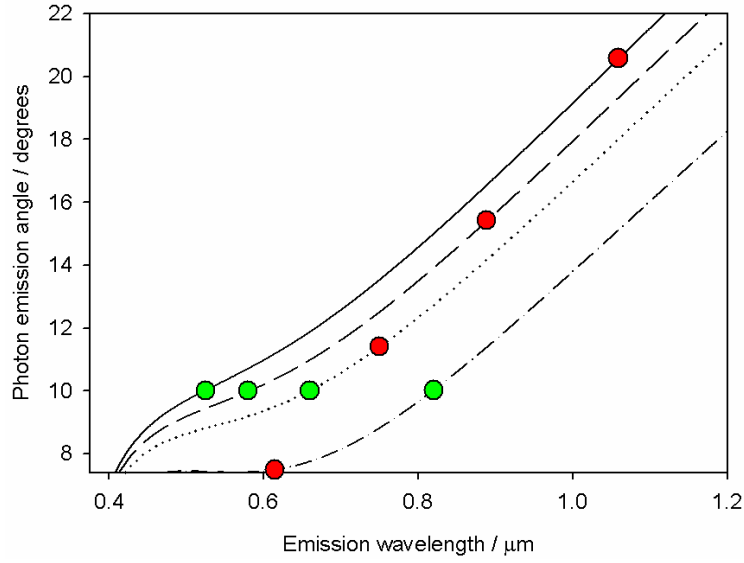


Figure 6-4 Phase matching curves for BBO with $\theta_{pm} = 40^\circ$ and $T = 25^\circ\text{C}$ (solid line), 125°C (broken line), 225°C (dotted line), 325°C (dot-dash line). The green and red circles denote collection angles / wavelengths of the DUT and trigger photons respectively, obeying energy conservation.

6.3.3 Angle tuning in BBO

As the pump refractive index depends on the angle made by the pump beam with the crystal optic axis θ_{pm} , the phasematching can be tuned with θ_{pm} . The pump and downconversion beam propagation geometries within the tilting crystal are shown in Figure 6-5, and it can be seen that:

$$\theta_{pm} = \theta_{p, \text{tilt}=0^\circ} - \theta_r \quad (6.3.4)$$

$$\theta_{\text{trig}, \text{lab}} = \arcsin\left(n_{\text{trig}} \sin\left[\theta_{\text{trig}} + \theta_r\right]\right) - \theta_{\text{tilt}} \quad (6.3.5)$$

$$\theta_{\text{DUT}, \text{lab}} = \arcsin\left(n_{\text{DUT}} \sin\left[\theta_{\text{DUT}} - \theta_r\right]\right) + \theta_{\text{tilt}} \quad (6.3.6)$$

where θ_{tilt} is the crystal tilt angle, θ_{trig} and θ_{DUT} are the crystal signal and idler emission angles from the pump; θ_r is the refraction angle of the pump beam to the crystal interface normal and $\theta_{p, \text{tilt}} = 0^\circ$ is the angle of the crystal optic axis to the crystal normal.

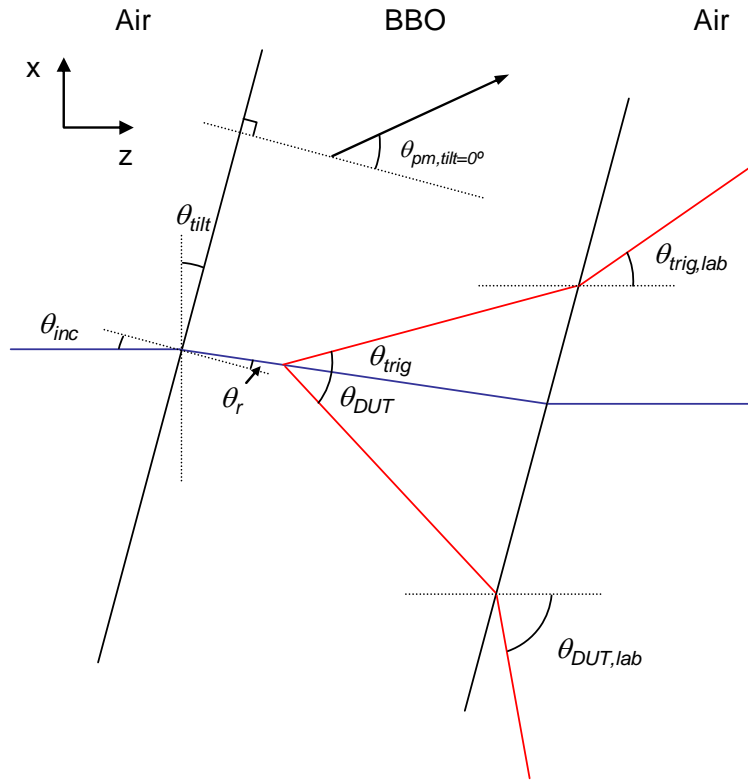


Figure 6-5 Geometry of pump (blue line) and non-collinearly emitted downconversion beams (red lines) when the crystal normal is at an angle θ_{ilt} to the pump beam.

The phase matching curves plotting photon emission angle vs. wavelength from $\theta_{ilt} = -2^\circ$ to 5.6° are shown in Figure 6-6. When the DUT is positioned to collect photons along $\theta_{DUT,lab} = 10^\circ$, from $\theta_{ilt} = -2^\circ$ to 5.6° the photon wavelength received by the DUT changes from 485 nm to 785 nm. The tuning range of photon wavelengths at the DUT could be extended by choosing other θ_{ilt} values, which is easy to implement.

A complication that occurs for non-zero θ_{ilt} is a change in the transverse spatial profile of the downconversion due the change in x co-ordinate of the pump beam with propagation through the crystal. Because the photons with emission angles $\theta_{trig}, \theta_{DUT}$ are created at all points along the crystal length, for zero θ_{ilt} the trigger and DUT photons are spread at the output face of the crystal to $L \tan \theta_{trig}$ and $L \tan \theta_{DUT}$ respectively. For non zero tilt, the trigger and DUT photon spot sizes change to $\sim L(\tan \theta_{trig} + \tan[\theta_{ilt} - \theta_r])$ and $L(\tan \theta_{DUT} - \tan[\theta_{ilt} - \theta_r])$ respectively. Taking $\theta_{DUT} = 5^\circ$ for example, the change in spread becomes significant i.e. $\tan \theta_{trig} \approx \tan[\theta_{ilt} - \theta_r]$ when $\theta_{ilt} \approx 13^\circ$.

There are clear advantages and disadvantages for both the angle tuned and temperature tuned FSQEM devices; the temperature tuning mechanism may be costly in terms of equipment and the need to solve the problems associated with high crystal temperatures, but there are no additional complications to the emission profile as a result of tilting the crystal, as in the angle tuning method. The angle tuning method however would be simple and cheap to implement. The ‘preferred’ tuning method would depend on project-specific factors such as the required tuning range and budget. The motivation of this chapter is to outline the framework for studying FSQEM systems, a thin crystal and narrow pump beam is assumed for the collection geometry (Figure 6-2) and therefore the downconversion ‘spot-size’ at the output facet of the crystal due to finite crystal length is not considered; the angle tuned system will be used for illustration of the framework, but the temperature tuned system would be equally well suited for the purpose.

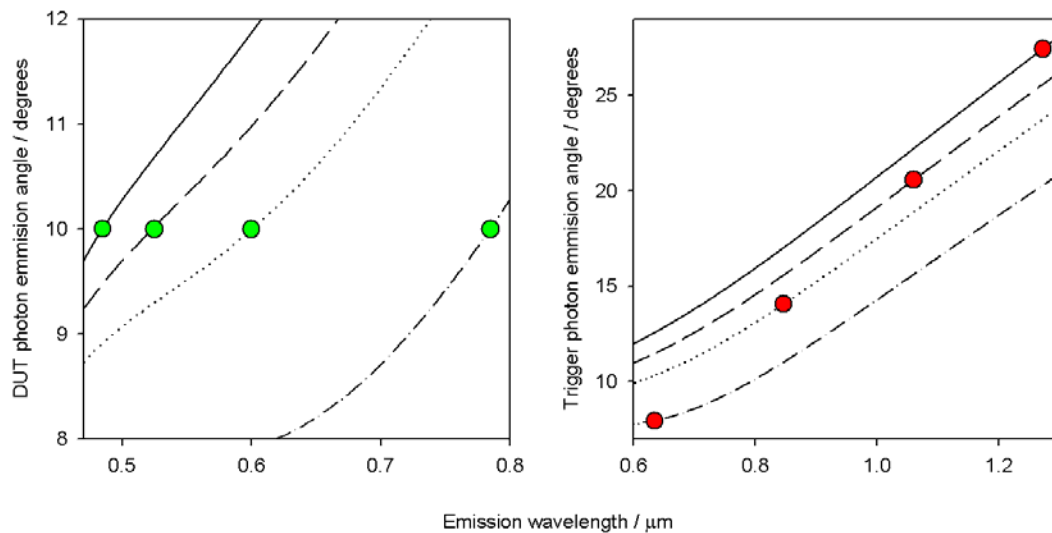


Figure 6-6 Phase-matching curves for BBO at $T = 25^{\circ}\text{C}$ $\theta_{\text{ilt}} = -2^{\circ}$ (solid line), 0° (broken line), 2° (dotted line) and 5.6° (dot-dash line). The curves in the left and right boxes correspond to the DUT and trigger photons respectively. The green and red circles denote co-ordinates of DUT/trigger photon pairs obeying energy conservation

6.3.4 The limitations of exact phase matching design calculations.

The design arguments presented in section 6.3.1-6.3.3 were made on the basis of exact phase matching calculations. The calculations were useful for studying the suitability of phase-matched interactions in non-linear crystals for application in a FSQEM device. The

calculations were also useful for understanding the suitability of different phasematching tuning mechanisms for frequency tuning the FSQEM device. However the pump beam has finite diameter and the crystal has finite length, meaning those downconversion processes that aren't precisely phasematched have finite efficiency. Therefore the $\Delta k = 0$ analytically derived phasematching curves give no accurate measure of the spectrum describing the photons received by the DUT whose conjugate is received by the trigger, and therefore no indication of the wavelength resolution of the device. In addition, the $\Delta k = 0$ analysis gives no indication of the relative DUT and trigger detector collection angles required to ensure that the conjugates of all photons received by the trigger are received by the DUT. Such questions can be answered using the numerical approach outlined in section 6.2 for investigating parametric emission solutions with $\Delta k \neq 0$. The results are presented in the following sections. Sections 6.3.5-6.3.6 discusses important device design parameters and their optimisation at a single QE measurement wavelength. Section 6.3.7 discusses the device properties as the QE measurement wavelength is tuned.

6.3.5 Calculation of the optimum $\Delta\theta_{\text{trig,lab}}$ for the FSQEM device

The $G^{(2)}$ correlation function when the angular integrals cover all space [see equation (6.2.16)] can be considered the sum of four contributions:

$$G^{(2)} = G^{(2)}_{\text{trig}+DUT} + G^{(2)}_{\text{trig only}} + G^{(2)}_{DUT \text{ only}} + G^{(2)}_{\text{neither}} \quad (6.3.7)$$

where $G^{(2)}_{\text{trig}+DUT}$ is proportional to the pair photon coincidence rate through A_{trig} and A_{DUT} , shown in equation (6.2.18). $G^{(2)}_{DUT \text{ only}}$ is proportional to the generation rate of those photon pairs where one photon is received within the aperture A_{DUT} but the second photon lies outside A_{trig} ; such events contribute to background singles counts at the DUT and should be minimized. $G^{(2)}_{\text{trig only}}$ is proportional to the generation rate of photon pairs whereby one photon is received by A_{trig} but the second photon lies outside A_{DUT} . Non-zero $G^{(2)}_{\text{trig only}}$ means that when a photon is received by the trigger, the conjugate photon is not always received by the DUT; such events invalidate equation (6.1.1) and therefore should be excluded. The $G^{(2)}_{\text{neither}}$ term corresponds to when neither photon is received by the respective detectors, and can be ignored.

6. A tuneable device for the absolute measurement of detector quantum efficiency

It is possible to evaluate all four terms in equation (6.3.7) separately. The calculation of $G^{(2)}_{DUT\ only}$ requires much computation power because the limits over the $\theta_{trig,lab}$ and ω_{trig} summations need to be extended to allow for all phase matching possibilities, and because A_{DUT} is normally large, the limits of the $\theta_{DUT,lab}$ summation are large. (For $G^{(2)}_{neither}$, the $\theta_{DUT,lab}$ limits need to be expanded even further to capture all phasematching possibilities extending calculation time again). By comparison $G^{(2)}_{trig\ only}$ is quick to evaluate as A_{trig} is normally small and therefore the $\theta_{trig,lab}$ and ω_{trig} summation limits can be tightly defined. Similarly, $G^{(2)}_{trig+DUT}$ is quick to compute due to the possibility of tightly constraining the summation limits.

The $G^{(2)}_{trig+DUT}$ and $G^{(2)}_{trig\ only}$ contributions were calculated as a function of $\Delta\theta_{DUT,lab}$, while keeping $\Delta\theta_{trig,lab}$ along with all other parameters fixed, see Figure 6-7. The calculations show that as $\Delta\theta_{DUT,lab}$ approaches zero, the conjugate photons along the path to the DUT become cut-off and as a result the number of unpaired photons received at the trigger goes up, i.e. $G^{(2)}_{trig\ only}$ increases. In addition, as $\Delta\theta_{DUT,lab}$ decreases the coincidence rate between the trigger and DUT goes to zero. The maximum calculated coincidence rate between the two detectors and zero ‘unpaired’ photons received by the trigger occurs when $\Delta\theta_{DUT,lab}$ is $\sim 4.5 \times \Delta\theta_{trig,lab}$; and corresponds to the optimum value of $\Delta\theta_{DUT,lab}$, $\Delta\theta_{DUT,opt}$. $\Delta\theta_{DUT,opt}$ is a critical design parameter of the FSQEM system, and may change as the system is tuned. $\Delta\theta_{DUT,opt}$ defines the minimum DUT collection angle that ensures the collection of all photons conjugate to those received by the trigger, a larger $\Delta\theta_{DUT,lab}$ would not yield any further improvement in the trigger-DUT pair collection efficiency but would result in a greater number of ‘unpaired’ photons to be received by the DUT, therefore increasing the background single photon count rate.

Note that $G^{(2)}_{trig+DUT}$ and $G^{(2)}_{trig\ only}$ in Figure 6-7 are individually normalized with respect to the trigger and their sum is equal to one for all $\Delta\theta_{DUT,lab}$ as expected, and is good check on the accuracy of the calculation.

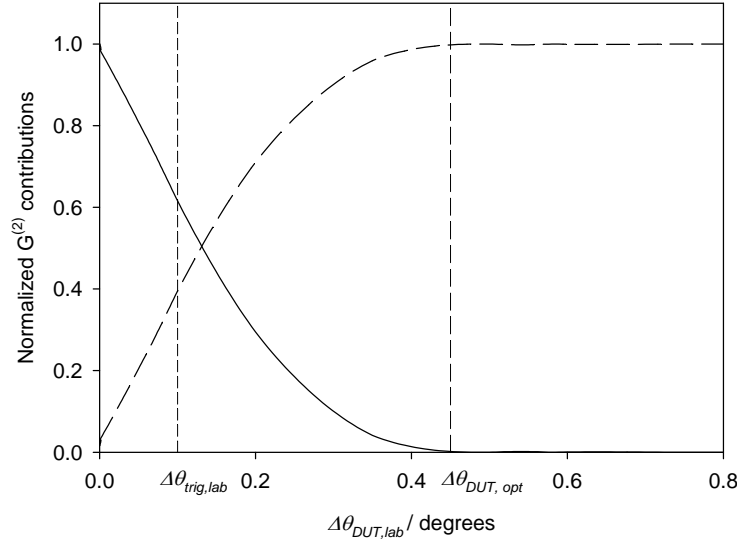


Figure 6-7 Normalized $G^{(2)}$ contributions as a function of $\Delta\theta_{DUT,lab}$; $G^{(2)}_{trig+DUT}$ (broken line), $G^{(2)}_{trig\ only}$ (solid line). The other calculation conditions are $\theta_{tilt} = 0^\circ$, $\theta_{trig,lab}^0 = 14.4^\circ$, $\theta_{DUT,lab}^0 = 11.4^\circ$ and $T = 25^\circ C$, corresponding to a QE measurement wavelength centred at 630 nm. Also $L=5$ mm and $w=1$ mm.

6.3.6 Dependency of the QE measurement bandwidth on L , w and $\Delta\theta_{trig,lab}$

The bandwidth of the $G^{(2)}_{trig+DUT}$ function with respect to λ_{DUT} , $\Delta\lambda_{DUT}$ is important because it determines the wavelength resolution of the quantum efficiency measurement in the FSQEM device. Using the model described in section 6.2, it was found that the crystal length, pump beam diameter and trigger detector collection angle all influenced $\Delta\lambda_{DUT}$.

$G^{(2)}_{trig+DUT}$ was calculated for a range of λ_{DUT} , and the bandwidth $\Delta\lambda_{DUT}$ was estimated from the FWHM of the resulting profiles. The calculation was repeated for other pump beam diameter values but otherwise identical experimental conditions, see Figure 6-8. It was found that when the beam diameter was small, the $G^{(2)}_{trig+DUT}$ bandwidth increased dramatically. Inspection of equation (6.2.3) reveals that the increase was due to the transverse components of the phase mismatch becoming significant at the smaller pump beam diameters. This is confirmed by the Gaussian-like $G^{(2)}_{trig+DUT}$ spectral profile for small pump beam diameters which tends towards a sinc^2 profile for larger beam diameters where interactions with

transverse phase-mismatched components become less efficiently generated. For the remainder of the example calculations in this chapter, a beam diameter of 1 mm was used since this corresponds to a minimum $G_{trig+DUT}^{(2)}$ bandwidth. Any further increase in the beam diameter will not improve the measurement resolution.

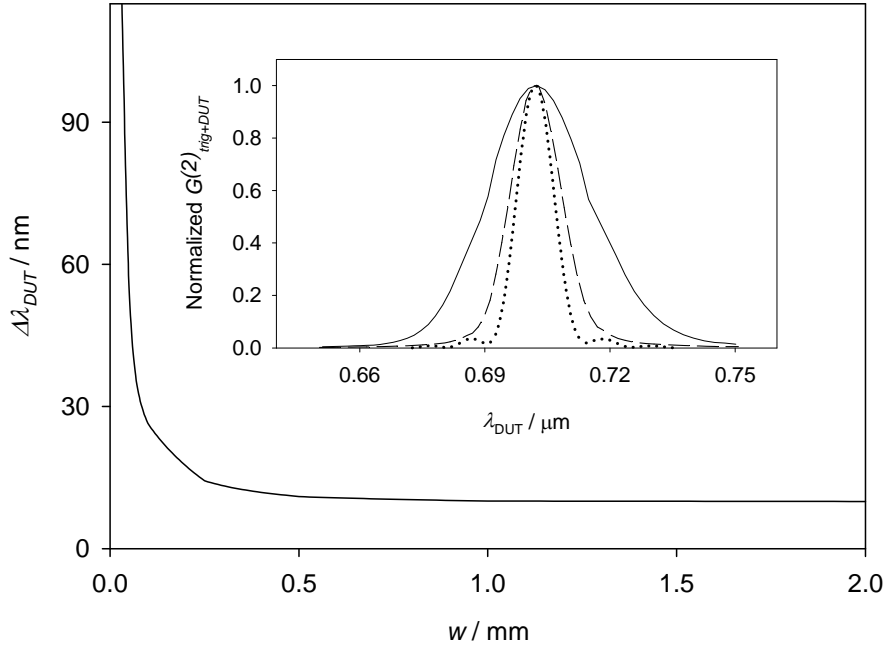


Figure 6-8 Calculated bandwidth of $G_{trig+DUT}^{(2)}(\lambda_{DUT})$ as a function of w . The inset presents the form of $G_{trig+DUT}^{(2)}(\lambda_{DUT})$ when $w = 1$ mm, 0.25 mm and 0.1 mm, shown by dotted, broken and solid lines respectively. The other parameters were $\theta_{trig,lab}^0 = \theta_{trig,DUT}^0 = 12.6^\circ$, $T = 25^\circ\text{C}$, $\theta_{ilt} = 0^\circ$, $\Delta\theta_{trig,lab} = 0.1^\circ$ and $\Delta\theta_{DUT,lab} = \Delta\theta_{DUT,opt}$.

The calculated $G_{trig+DUT}^{(2)}$ as a function of λ_{DUT} is shown in Figure 6-9 for different L , the sinc^2 profile is apparent due to the choice of beam width and narrower bandwidths are associated with longer crystal lengths. Beyond $L = 5$ mm however there is limited further reduction of the emission bandwidth.

The photon flux increases with L , however using the method described in section 2.4 the photon flux into $\Delta\theta_{trig,lab} = 0.1^\circ$ was estimated to be $3 \times 10^3 \text{ s}^{-1} \text{ mw}^{-1}$ pump when $L = 5$ mm, and the other parameters are those shown in Figure 6-9. Therefore with these parameters it should be possible to perform quantum efficiency measurements with low uncertainties at

relatively low pump powers. For the above reasons, a crystal length of 5 mm was used for the remaining calculations.

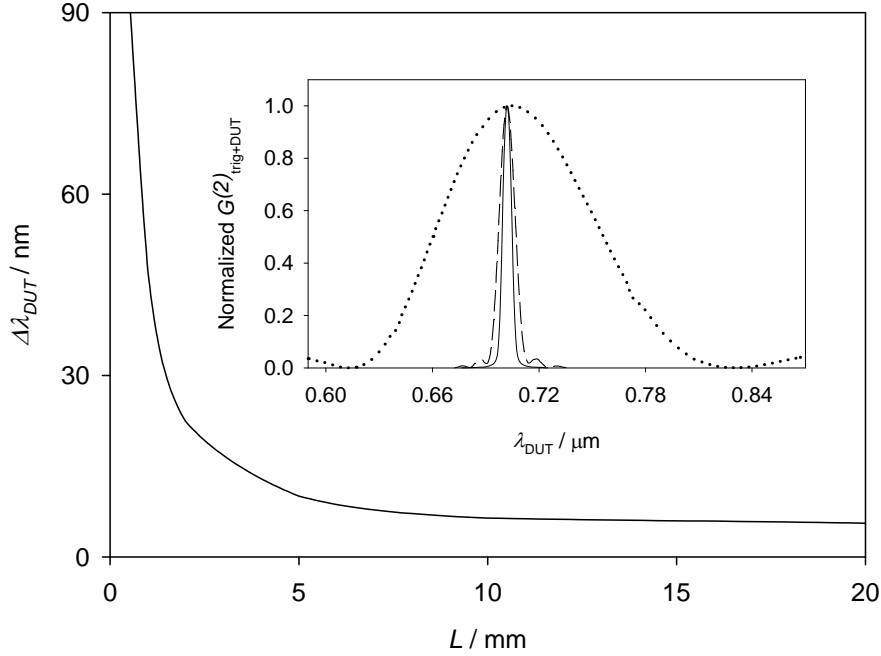


Figure 6-9 Calculated bandwidth of $G^{(2)}_{trig+DUT}(\lambda_{DUT})$ as a function of L . The inset presents the form of $G^{(2)}_{trig+DUT}(\lambda_{DUT})$ when $L = 0.5$ mm, 5 mm and 20 mm, shown by dotted, broken and solid lines respectively. The other parameters were $\theta^0_{trig,lab} = \theta^0_{trig,DUT} = 12.6^\circ$, $T = 25^\circ\text{C}$, $\Delta\theta_{trig,lab} = 0.1^\circ$ and $\Delta\theta_{DUT,lab} = \Delta\theta_{DUT,opt}$.

In addition to w and L , the absolute value of the $\Delta\theta_{trig,lab}$ influences the bandwidth of $G^{(2)}_{trig+DUT}$. $G^{(2)}_{trig+DUT}$ was calculated for a range of $\Delta\theta_{trig,lab}$, shown in Figure 6-10. The calculations show that $\Delta\lambda_{DUT}$ increases with $\Delta\theta_{trig,lab}$, and this is due to the increasing bandwidth of photons received by the trigger. At large collection angles the emission profile is spectrally flat, as has been reported in previous theoretical and practical investigations of parametric downconversion [108].

Another commonly observed feature of parametric downconversion is that the spectral bandwidth tends to a minimum value for small collection angles, as shown by the calculations of Figure 6-10 which show no significant change in $\Delta\lambda_{DUT}$ for $\Delta\theta_{trig,lab}$ between 0.01° and 0.1° . Over the same increase in $\Delta\theta_{trig,lab}$ the total area under the $G^{(2)}_{trig+DUT}$ curve which is proportional pair generation rate, increases by approximately a factor of ten. Therefore a

value of $\Delta\theta_{\text{trig},\text{lab}} \sim 0.1^\circ$ (with the other conditions of Figure 6-10), appears to give a good balance between signal level and wavelength resolution for the quantum efficiency measurement.

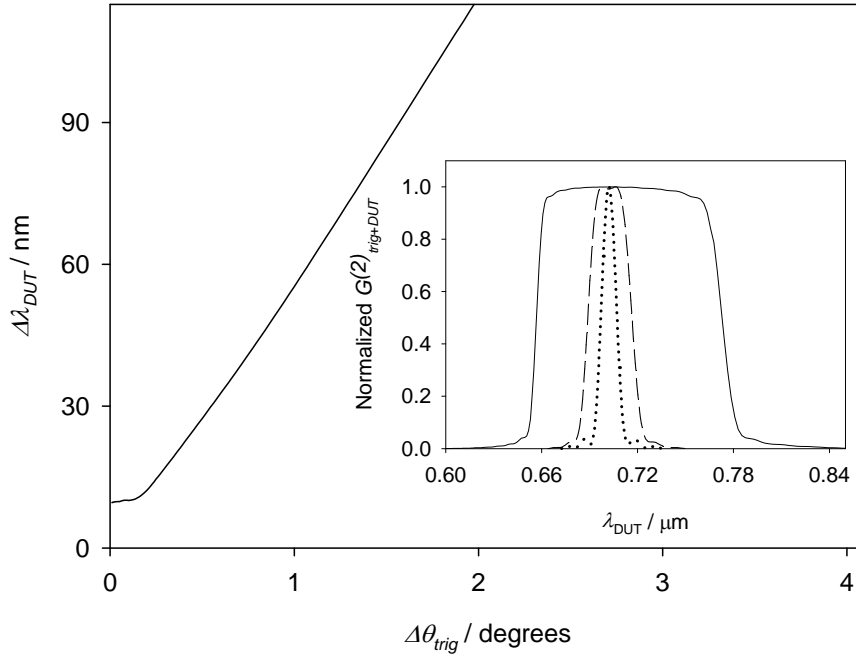


Figure 6-10 Calculated bandwidth of $G^{(2)}_{\text{trig}+DUT}(\lambda_{DUT})$ as a function of $\Delta\theta_{\text{trig},\text{lab}}$. The inset presents the form of $G^{(2)}_{\text{trig}+DUT}(\lambda_{DUT})$ when $\Delta\theta_{\text{trig},\text{lab}} = 0.01^\circ, 0.5^\circ$ and 2° , shown by dotted, broken and solid lines respectively. The other parameters were $\theta_{\text{pm}} = 40^\circ, \theta_{\text{tilt}} = 0^\circ, \theta_{\text{trig},\text{lab}}^0 = \theta_{\text{trig},DUT}^0 = 12.6^\circ, T = 25^\circ\text{C}$ and $\Delta\theta_{DUT,\text{lab}} = \Delta\theta_{DUT,\text{opt}}$.

Note that $\Delta\theta_{DUT,\text{opt}}$ increases with $\Delta\theta_{\text{trig},\text{lab}}$; it was found that the ratio $\Delta\theta_{DUT,\text{opt}}/\Delta\theta_{\text{trig},\text{lab}}$ decreases from 64 to 1.4 with increasing $\Delta\theta_{\text{trig},\text{lab}}$ across the range of $\Delta\theta_{\text{trig}}$ in Figure 6-10, but $\Delta\theta_{DUT,\text{opt}} - \Delta\theta_{\text{trig},\text{lab}}$ remained approximately constant at 0.65° . This is because changing $\Delta\theta_{\text{trig},\text{lab}}$ does not change the conversion efficiency associated with a particular phasematching interaction. $\Delta\theta_{DUT,\text{opt}} - \Delta\theta_{\text{trig},\text{lab}}$ was sensitive to changes in L due to the influence of L on the conversion efficiency of non-perfectly phase matched interactions [see equation (6.2.4)]. For example, taking $\Delta\theta_{\text{trig},\text{lab}} = 0.1^\circ$, and the other experimental parameters of Figure 6-10, $\Delta\theta_{DUT,\text{opt}} - \Delta\theta_{\text{trig},\text{lab}}$ changes from 6.4° when $L = 0.5$ mm to 0.15° when $L = 20$ mm. Due to the influence of w on the conversion efficiency of non-perfectly phase matched interactions [see equation (6.2.3)], $\Delta\theta_{DUT,\text{opt}} - \Delta\theta_{\text{trig},\text{lab}}$ was also

sensitive to w , for example when $\Delta\theta_{trig,lab}$ and the other experimental parameters are those given in Figure 6-10, $\Delta\theta_{DUT,opt} - \Delta\theta_{trig,lab}$ decreases from 0.64° to 0.59° when w is changed from $100\ \mu\text{m}$ up to $5\ \text{mm}$.

For the above analysis and that of the following section, the collection geometry (Figure 6-2) assumes a thin crystal and a narrow pump beam. The QE measurement bandwidth and $\Delta\theta_{DUT,opt}$ will also be effected by the influence on the collection problem due to finite beam diameters and crystal lengths, this is discussed further in section 6.4.

6.3.7 Investigation of device properties with tuning

In order to measure the quantum efficiency of the DUT at $\lambda_{c,DUT}$ (the centre wavelength of the $G_{trig+DUT}^{(2)}$ vs. λ_{DUT} profile), it is important to select the correct phasematching condition through θ_{ill} and also to select the correct angular position of the trigger (assuming the DUT angular position is to be kept constant). These questions can be answered from the exact phase matching and energy conservation arguments presented in 6.3.1.

It is also important to know the measurement bandwidth $\Delta\lambda_{DUT}$ to which the quantum efficiency measurement applies, and this may change as the device is tuned to other $\lambda_{c,DUT}$; similarly $\Delta\theta_{DUT,opt}$ may change with $\lambda_{c,DUT}$. Both of these possibilities can be studied by ensuring that each term of the $G_{trig+DUT}^{(2)}$ summation in equation (6.2.19) are attributed λ_{DUT} and $\theta_{DUT,lab}$ labels such that it is possible to plot $G_{trig+DUT}^{(2)}$ versus any one or more of these variables.

Figure 6-11 shows a series of 2D density plots showing the relationships of $G_{trig+DUT}^{(2)}$ with λ_{DUT} and $\theta_{DUT,lab}$ for different phasematching conditions. At each condition, the DUT angular orientation (centred at $\theta_{DUT,lab}^0 = 11.4^\circ$) was fixed at such that the collected wavelengths changed with θ_{ill} . Figure 6-11 shows that as θ_{ill} is changed from -4.8° to 5.6° , $\lambda_{c,DUT}$ is scanned from 500 to $850\ \text{nm}$ which represents nearly 60% of the useful detection bandwidth of common silicon detection technology. If the trigger detector is also based on silicon technology then $\sim 530\ \text{nm}$ would in practice be the minimum measurement wavelength

6. A tuneable device for the absolute measurement of detector quantum efficiency

due to the low response beyond $\sim 1 \mu\text{m}$. Beyond $\lambda_{c,DUT} = 800 \text{ nm}$, $\Delta\lambda_{DUT}$ increases dramatically, which would be problematic for a FSQEM device because it corresponds to a high measurement resolution bandwidth. From the spread of the density plots along the $\theta_{DUT,lab}$ axis it is clear that $\Delta\theta_{DUT,opt}$ also increases markedly as the system is tuned to longer $\lambda_{c,DUT}$, and therefore the aperture size of the DUT should be varied as the system is tuned in order to maximize $G_{trig+DUT}^{(2)}$ while zeroing $G_{trig\ only}^{(2)}$.

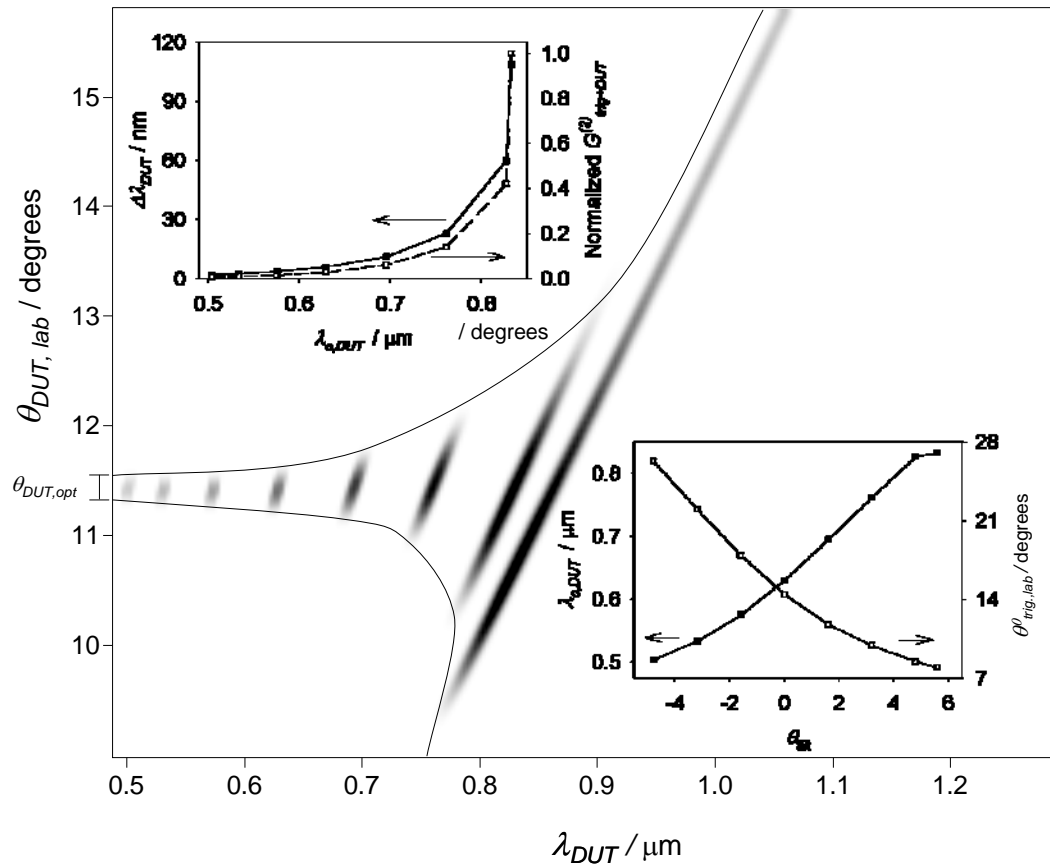


Figure 6-11 A series of $G_{trig+DUT}^{(2)}$ density plots with respect to wavelength and propagation direction of the photons received by the DUT. Each density plot in the series corresponds to different angle tuning conditions of the BBO ($\theta_{pm,tilt=0^\circ} = 40^\circ$), and different trigger detector collection angles. The wavelength centres of each density plot ($\lambda_{c,DUT}$) and the centre trigger collection angles ($\theta_{trig,lab}^0$) for each tuning configuration are shown in the bottom right inset. The top left inset shows the $G_{trig+DUT}^{(2)}$ bandwidth with respect to λ_{DUT} and total $G_{trig+DUT}^{(2)}$ at each configuration. The other system parameters are $L = 5 \text{ mm}$, $w = 1 \text{ mm}$, $\Delta\theta_{trig,lab} = 0.1^\circ$ and $T = 25 \text{ }^\circ\text{C}$.

It is interesting to note that all of the experimental parameters required for operating the FSQEM device over a wide tuning range are shown within Figure 6-11; firstly the measurement wavelength is chosen, and the required θ_{ilt} is read from the $\lambda_{c,DUT}$ plot in the bottom right inset. Then, the vertical line defining the θ_{ilt} position intersects the $\theta^0_{trig,lab}$ plot of the bottom right inset to give the required angular position for the trigger detector. The optimum DUT aperture size at the measurement wavelength is given by the associated width of the envelope function covering the combined density plots across the range of λ_{DUT} .

The growing $G^{(2)}_{trig+DUT}$ bandwidth with wavelength can be explained through studying the $\Delta k=0$ phase matching curves in Figure 6-12. When $\theta_{ilt} = -4.8^\circ$, where $\lambda_{DUT} = 504$ nm it can be seen that the trigger aperture is at a relatively steep part of the curve, indicating a narrow collected spectral bandwidth and this translates to a narrow spectral bandwidth of $G^{(2)}_{trig+DUT}$. When $\theta_{ilt} = 5.6^\circ$, where $\lambda_{DUT} = 831$ nm the trigger aperture is at a flat part of the phasematching curve, implying a large collection wavelength bandwidth and therefore a large bandwidth for $G^{(2)}_{trig+DUT}$.

The total value of $G^{(2)}_{trig+DUT}$ for a given tuning state of the device, given by summing all contributions to the associated density plot, increases with λ_{DUT} as a result of the larger number of phasematching interactions when the trigger selection bandwidth is higher [see top left inset, Figure 6-11]. Closer inspection shows that the spectral density of $G^{(2)}_{trig+DUT}$ increases by a factor of two on going from the shortest to the longest shown QE measurement wavelength, and this occurs for two reasons. One reason is an increase in the number of phasematched interactions per unit wavelength when the system is tuned for higher λ_{DUT} . In order to illustrate this point, first define the conversion efficiency Φ as the product $s_\perp s_z$, see equations (6.2.3)-(6.2.4). Then, calculating $G^{(2)}_{trig+DUT}$ from (6.2.19) using intervals of $\delta\theta_{DUT} = \delta\theta_{trig} = 2.5 \times 10^{-3}^\circ$ $\delta\lambda_{DUT} = 0.1$ nm and setting $\theta_{ilt} = 5.6^\circ$, within a 1 nm bandwidth about 830 nm, 1.6×10^4 separate interactions with $\Phi > 0.01$ were found, the interactions had an averaged Φ of 0.39. By comparison, using the same calculation intervals and setting $\theta_{ilt} = -4.8^\circ$ there were just 9.4×10^3 separate interactions with $\Phi > 0.01$ in the one nm bandwidth about 504 nm. These interactions also had an averaged Φ of 0.39.

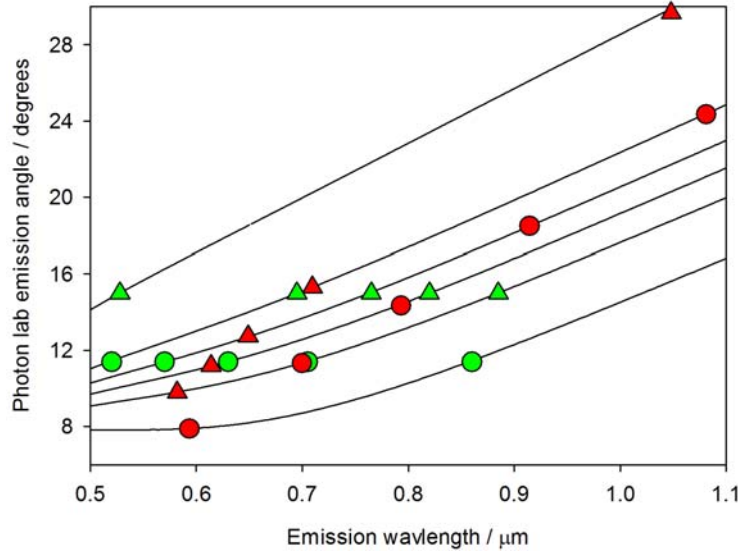


Figure 6-12 The black lines from top to bottom are phase matching curves corresponding to $\theta_{\text{tilt}} = -9^\circ, -4.8^\circ, -2^\circ, 0^\circ, 2^\circ$ and 5.6° respectively, at $T = 25^\circ\text{C}$. The green circles represent the DUT angular position $\theta_{\text{DUT,lab}}^0 = 11.4^\circ$ and define the QE measurement wavelength at each phase matching condition, the red circles indicate the trigger angular positions required to collect the conjugate photons. For $\theta_{\text{DUT,lab}}^0 = 15^\circ$ the DUT and trigger angular positions for each angle tuning condition are shown by green and red triangles respectively. For clarity the difference between $\theta_{\text{DUT,lab}}$ and $\theta_{\text{trig,lab}}$ at a given wavelength described by equations (6.3.5) and (6.3.6) has been ignored.

In addition to the number of efficient phase matching interactions, the $G_{\text{trig}+\text{DUT}}^{(2)}$ spectral density is greater when the FSQEM is tuned to a higher λ_{DUT} due to the associated change in θ_{pm} , leading to a increased d_{eff} through equation (2.3.6). For example, when the system was tuned to $\lambda_{\text{c,DUT}} = 504 \text{ nm}$, the calculated d_{eff} was 1.12 pm/V where as when the system was tuned to $\lambda_{\text{c,DUT}} = 830 \text{ nm}$, d_{eff} was 1.24 pm/V .

The problem of large $\Delta\lambda_{\text{DUT}}$ at longer λ_{DUT} can be overcome by choosing a combination of larger θ_{pm} and larger $\theta_{\text{DUT,lab}}^0$. Figure 6-12 shows that when choosing larger $\theta_{\text{DUT,lab}}^0$, $\lambda_{\text{DUT}} > 800 \text{ nm}$ can be accessed with higher- θ_{pm} phasematching curves (corresponding to more –ve tilt in Figure 6-12) that are less flat about the angular position required for the trigger (i.e. when $\lambda_{\text{trig}} < 650 \text{ nm}$), and therefore the spectral bandwidth of photons to the trigger (and therefore $\Delta\lambda_{\text{DUT}}$) will be reduced.

6. A tuneable device for the absolute measurement of detector quantum efficiency

Choosing $\theta_{DUT,lab}^0 = 15^\circ$ and $\theta_{pm,tilt=0^\circ} = 43^\circ$, Figure 6-13 shows $G_{trig+DUT}^{(2)}$ density plots against $\theta_{DUT,lab}$ and λ_{DUT} for different θ_{tilt} . The range of λ_{DUT} covered by this system is approximately the same as for the system in Figure 6-11. Although $\Delta\lambda_{DUT}$ does increase when the system is tuned to higher λ_{DUT} , the increase is less marked than for the system in Figure 6-11, and therefore the wavelength resolution of the quantum efficiency measurements is enhanced. It is also clear that the spread of the density plots along the $\theta_{DUT,lab}$ axis is less than in the previous system, although $\Delta\theta_{DUT,opt}$ still changes as the system is tuned through λ_{DUT} .

The spectral density of the $G_{trig+DUT}^{(2)}$ plots in Figure 6-13 are slightly lower than the $G_{trig+DUT}^{(2)}$ plots at similar wavelengths in Figure 6-11; this can be explained by the lower d_{eff} at higher θ_{pm} ; taking the $\theta_{tilt} = -9.6^\circ$ [$\theta_{pm,tilt=0^\circ} = 43^\circ$] phase matching solution corresponding to $\lambda_{c,DUT} = 522$ nm, the calculated d_{eff} was 0.99 pm/V (c.f. 1.12 pm/V at $\lambda_{c,DUT} = 504$ nm in the $\theta_{pm} = 40^\circ$ system) while for the $\theta_{tilt} = 4.8^\circ$ [$\theta_{pm,tilt=0^\circ} = 43^\circ$] phase matching solution corresponding to $\lambda_{c,DUT} = 821$ nm, d_{eff} was 1.19 pm/V (c.f. 1.24 pm/V at $\lambda_{c,DUT} = 830$ nm in the $\theta_{pm} = 40^\circ$ system).

The number of phase matched interactions with $\Phi > 0.01$ at any given wavelength was similar between the $\theta_{pm} = 43^\circ$ and $\theta_{pm} = 40^\circ$ systems. For example with $\theta_{tilt} = -9.6^\circ$ [$\theta_{pm,tilt=0^\circ} = 43^\circ$], the number of efficient phase matching interactions associated with the 1 nm bandwidth about $\lambda_{c,DUT} = 522$ nm was 9.8×10^3 with an average Φ of 0.39, (c.f. 9.4×10^3 interactions in 1 nm bandwidth about $\lambda_{c,DUT} = 504$ nm with average $\Phi = 0.39$ when $\theta_{tilt} = -4.8^\circ$ in the $\theta_{pm} = 40^\circ$ system) and when $\theta_{tilt} = 4.8^\circ$ [$\theta_{pm,tilt=0^\circ} = 43^\circ$] the number interactions was 1.5×10^4 with an average Φ of 0.39 in the 1 nm bandwidth about $\lambda_{c,DUT} = 821$ nm – (c.f. 1.6×10^4 interactions with average $\Phi = 0.39$ in the 1 nm bandwidth about $\lambda_{c,DUT} = 830$ nm when $\theta_{tilt} = 5.6^\circ$ in the $\theta_{pm} = 40^\circ$ system)

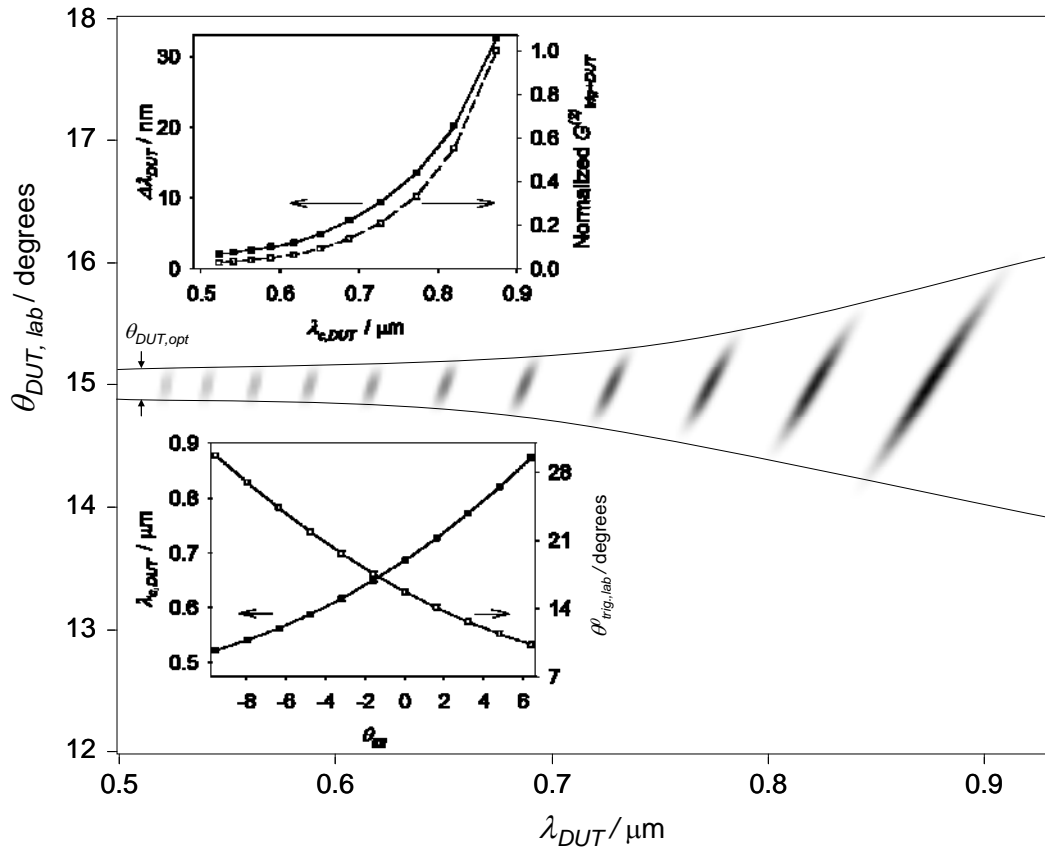


Figure 6-13 $G_{\text{trig}+DUT}^{(2)}$ density plots with respect to wavelength and propagation direction of the photons received by the DUT. Each density plot in the series corresponds to different angle tuning conditions of the BBO ($\theta_{\text{pm,tilt}=0^\circ} = 43^\circ$), with different trigger photon collection angles. The wavelength centres of each density plot and the trigger collection angles for each tuning configuration are shown in the bottom inset. The top inset shows the $G_{\text{trig}+DUT}^{(2)}$ bandwidth with respect to λ_{DUT} and total $G_{\text{trig}+DUT}^{(2)}$ at each configuration. The other system parameters are $L = 5\text{ mm}$, $w = 1\text{ mm}$, $\Delta\theta_{\text{trig,lab}} = 0.1^\circ$ and $T = 25^\circ\text{C}$.

6.4 Conclusions

Theoretical modelling was employed to investigate a device to perform wavelength tuneable quantum efficiency measurements of a single photon detector based upon the spontaneous parametric downconversion photon pair technique.

Only non-collinear systems were considered as a setup incorporating collinearly emitted pairs would require a beam splitting optic to separate and direct the photons to either the trigger or DUT, and the optic would require characterisation over a wide range of wavelengths.

It was decided to investigate a BBO based system whereby both of the generated photons were between 500 nm and 1 μm where it would be possible to incorporate high performance and low cost silicon avalanche photodiode detectors into future practical experiments. The system studied was a non-collinear device incorporating BBO with angle tuned phasematching for the downconversion of 351.1 nm (e-polarisation), into o-polarised photon pairs.

Because the DUT would not be a permanent fixture of the device, it was decided that the position of this detector should be fixed as the measurement wavelength is tuned. Using exact phasematching arguments, it was found that it was possible to tune the measurement wavelength while keeping the DUT stationary by simultaneously adjusting the phasematching condition and the angular position of the trigger detector about the pump beam. (Similar arguments can be applied to the reverse case where the trigger is kept fixed and the DUT is moved.) For the required phasematching adjustment, temperature tuning and angle tuning were studied as possible mechanisms.

For more detailed modelling of the system, an expression was formulated for the second order correlation function for the device, $G^{(2)}$, which is proportional to the generation rate of the parametrically generated photons. The expression for $G^{(2)}$ considered non-exact phasematching and the non-linear coefficient for the downconversion interaction. By evaluating $G^{(2)}$ over the trigger and DUT collection angles, it was possible to determine the effect of the BBO crystal length, pump beam width and trigger detector collection angle on the quantum efficiency measurement resolution. In addition the model was also able to determine the smallest collection angle defined by the DUT such that all photon collected by the trigger have their conjugates received by the DUT. Investigations were then carried out to determine how the system properties changed as the quantum efficiency measurement wavelength was changed through angle tuning of the phasematching. When $\theta_{pm,tilt=0^\circ} = 40^\circ$ and the angular position of the DUT was fixed at 11.4° to the pump beam, it was found that as the system was tuned for longer quantum efficiency measurement wavelengths, the spectral bandwidth associated with the measurement increased dramatically. This was attributed to the phase matching condition at longer measurement wavelengths causing a large spectral

bandwidth to be received by the trigger aperture, which in turn implies a large bandwidth of conjugate photons at the DUT. It was found that the measurement resolution at longer wavelengths could be improved at the expense of slightly lower downconversion efficiencies by a combination of increasing the angular position of the DUT relative to the pump beam and increasing θ_{pm} .

The presented model and subsequent analysis of the BBO FSQEM device carries with it a framework for the investigation of other FSQEM devices based upon other non-linear materials. Other materials such as KDP may possess more favourable properties for a visible – near IR system in that the spectral measurement resolution may not decrease so dramatically with increasing wavelength, for example.

Another FSQEM system for possible investigation would be one where the trigger detector receives a visible photon and the DUT receives a telecoms band wavelength photon. This would be interesting as it would allow for wavelength tuneable, absolute measurements of quantum efficiency for telecoms photon counters (for which there are many new technologies emerging) where the (permanent) trigger could be a high performance silicon avalanche photodiode. A possible downconversion crystal for this setup would be PPLN, a 532 nm \rightarrow 810 nm + 1550 nm process has been demonstrated previously in the literature [53].

In chapter 2 of this portfolio, it was described how focussing of the pump beam had a favourable influence on the pair collection efficiency of the generated photons. An extension of the model discussed here could be to investigate how different pump focussing conditions affect the device properties.

For the modelling a monochromatic pump beam was assumed whereas a real pump beam would have a finite spectral width. A model accounting for the finiteness of the pump spectral width would require another summation term in expression (6.2.18) (for the pump frequency ω_p), therefore increasing calculation time. A further assumption that was made is that the trigger and DUT apertures were thin rectangles in order that the azimuthal angles of the trigger and DUT photons about the pump beam could be ignored, vastly speeding up computation time. For small apertures, it is unlikely that the calculated BBO device properties would change much when incorporating the azimuthal angles. For the problem of collecting the downconversion emission through the detector apertures (Figure 6-2) the model assumed a narrow pump beam and a thin crystal; the downconversion is assumed to spread

from the point of creation into a cone towards the collection apertures. In reality there exists a spreading of the emission cone at the detector aperture due to finite pump beam diameter w and crystal length L , this spreading can be approximated by $w + L \tan \theta$. For downconversion emitted at 5° to a narrow pump beam, and occupying a cone with divergence angle 0.2° originating from a point within a thin crystal, the downconversion forms a ~ 3.5 mm spot size 1 m after the point of emission. However when $L = 5$ mm and $w = 1$ mm, the spot size at the same point in space spreads to $\sim 3.5 + 1.4 = 4.9$ mm. Such spreading (which occurs at all emission wavelengths) would have a bearing on parameters such as the quantum efficiency measurement bandwidth and $\Delta\theta_{DUT,opt}$. It would be a relatively simple matter to modify the collection model to accommodate finite pump beam diameters and crystal lengths through summing the $G^{(2)}$ contributions due to all finite elements of the pump-illuminated crystal volume. However the additional complexity would carry a considerable computing power overhead.

Many of the above suggestions above for furthering the model require significant computing power, but the calculations would be feasible with access to a computational grid. In addition performance gains could be possible through the establishment of a more efficient computation method for the modelling.

7 *Conclusions and forward look*

The portfolio of work resulted in the establishment of new capabilities at NPL which are intended to be used to help develop a national measurement infrastructure for validating nascent and future optical quantum information technologies.

A spontaneous parametric downconversion sourced Hong-Ou-Mandel interferometer was constructed and served as a test bed in the development of a procedure for measuring true photon indistinguishability. A similar procedure could be followed to characterise the indistinguishability of photons from deterministic single photon sources. Such an experiment would probably involve measuring the HOM interference between consecutive photons from a regularly spaced train of photons, therefore slight modifications to the developed procedure would be required as the procedure was based upon an interferometer where the interfering photons were generated simultaneously as pairs but randomly with time. In addition to the possibility of carrying out single photon source characterisation experiments using a modified HOM framework, the framework of the built HOM interferometer is currently being used for spectroscopic investigations.

Also as part of this portfolio of work, a source of correlated photon pairs in the telecoms band was designed and built. The source was based upon a pump-enhanced cavity downconversion process where PPKTP was chosen as the downconversion medium. The pair generation rate of the source was estimated to be $6 \times 10^4 \text{ s}^{-1} \text{mw}^{-1}$ pump which was around an order of magnitude better than was reported in the literature for a setup incorporating the same downconversion process but without pump enhancement [59]. The developed correlated photon pair source was incorporated into a novel scheme for the generation of polarisation entangled photon pairs, and the scheme was found to produce two Bell states with measured quantum interference visibilities of around 0.95. The formed entangled states were also found to break a form of Bell's inequality by around six standard deviations. The source was originally built at the University of St. Andrews and was subsequently moved to the NPL where it is currently being used for further investigations. The entanglement source could be made portable through design changes such as the replacement of the large pump lasers with a suitable compact laser diode, which are commercially available. In order to further improve the measured source brightness, and enable 'clocked' or 'gated' operation,

7. Conclusions and forward look

the possibility to convert from cw pumping to a pulse-pumping configuration could be investigated. The non-linear crystal at the heart of the source would be suitable for pulsed pumping due to the choice of extended phasematching, which should allow for the generation of degenerate indistinguishable photon pairs over the broad spectral bandwidth of the pump. Operation in the telecom band makes this source eminently suitable for investigations into how to characterize optical states and processes which may be implemented at this wavelength using fibre or waveguide networks, as well as being available for the characterisation of novel single photon detectors and coupling with other quantum systems.

Another possibility for the framework of the polarisation entanglement source is the investigation of a new scheme for the measurement of polarisation mode dispersion in materials. A previously studied method incorporating a type-II downconversion sourced HOM interferometer involved the measurement of the HOM dip temporal shift when a polarisation dispersive material (PDM) was positioned within the interferometer beam [27]. Using the method proposed here the measurement could be performed from the acquisition of a single HOM interferogram, see Figure 7-1. The polarising beam splitter of the entanglement source [PBS in Figure 5-2(a)] illuminates a HOM interferometer with both $|H_1V_2\rangle$ and $|V_1H_2\rangle$ classical states (no entangled state ‘phase-locking’ mechanism required). The PDM is positioned in arm one of the HOM interferometer, and causes the temporal delay between the H and V photons to be different for the pairs associated with the $|H_1V_2\rangle$ and $|V_1H_2\rangle$ states. Therefore by removing the distinguishing polarisation information (for example using $\pm 45^\circ$ polarisers in front of each detector D_1 and D_2) and scanning one optical path of the interferometer, it should be possible to observe *two* HOM dips in a single interferogram; one associated with each of the $|H_1V_2\rangle$ and $|V_1H_2\rangle$ type photon pairs.

The temporal separation of the dips, τ_{PMD} relates to the difference in the ‘time-of-flight’ through the dispersive medium of the H and V photons, and therefore is a measure of the material polarisation mode dispersion. The advantage of this setup over one previously referenced is that only a single (two-dip) interferogram is required for the measurement as opposed to two (single-dip) interferograms. The maximum visibility for each dip will be 0.5 because only the photons pairs corresponding to one of the $|H_1V_2\rangle$ or $|V_1H_2\rangle$ states HOM interfere for a given τ , provided τ_{PMD} is much greater than the two photon coherence time.

7. Conclusions and forward look

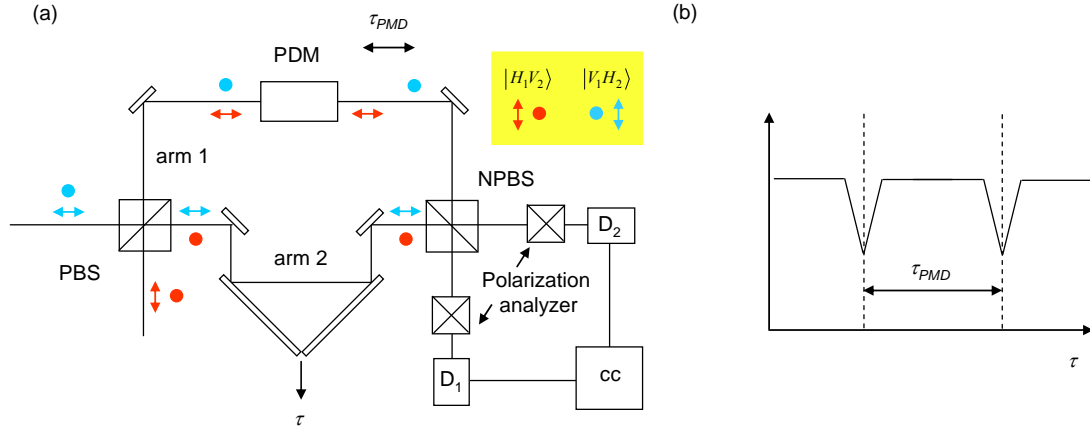


Figure 7-1 (a) Scheme for the measurement of medium polarisation dispersion using photons from the polarisation entanglement scheme framework of chapter 5. The PBS corresponds to the polarising beam splitter at the top of the ‘Christmas-tree’ arrangement shown in figure 5-2. (b) The two HOM dips associated with the $|H_1V_2\rangle$ and $|V_1H_2\rangle$ input states are separated by the polarisation mode dispersion time τ_{PMD} of the dispersing medium in arm 1 of the interferometer.

Finally, the portfolio included a study to investigate the possibility of a wavelength tuneable device for the absolute measurement of detector quantum efficiency based upon a two-detector (one permanent and one temporary test detector) and SPDC source arrangement. The study focussed on a BBO-based system for making quantum efficiency measurements at visible and near IR wavelengths. It was found that by angle tuning the phasematched downconversion process along with moving the angular position of the permanent detector about the pump beam, wavelength tune-ability could be achieved with the test detector position stationary, which is a favourable design characteristic. Other characteristics of the device such as the quantum efficiency measurement spectral bandwidth and tuning range were investigated. As a whole the study puts forward a framework for the investigation of other similar devices but incorporating other downconversion interactions and operating at other wavelengths. Suggestions for improvements to the modelling were made.

7. Conclusions and forward look

References

1. Einstein, A., B. Podolsky, and N. Rosen, *Can Quantum-Mechanical Description of Physical Reality be Considered Complete?* Physical Review. **47**(10), 777-780 (1935)
2. Bell, J.S., *On the Einstein-Podolski-Rosen Paradox* Physics. **1**, 195-200 (1964)
3. Clauser, J.F. and A. Shimony, *Bell's theorem: experimental tests and implications.* Reports on Progress in Physics. **41**(12), 1881-1927 (1978)
4. Aspect, A., P. Grainger, and G. Roger, *Experimental realization of the Einstein-Podolsky-Rosen-Bohm Gedankenexperiment: A New Violation of Bell's Inequalities.* Physical Review Letters. **49**(2), 91-94 (1982)
5. Louisell, W.H., W.H. Yariv, and A.E. Siegman, *Quantum fluctuations and noise in parametric processes.* Physical Review. **124**, 1646-1654 (1961)
6. Harris, S.E., M.K. Oshman, and R.L. Byer, *Observation of tuneable optical parametric fluorescence.* Phys. Rev. Lett. **18**, 732-734 (1967)
7. Magde, D. and H. Mahr, *Study in Ammonium Dihydrogen Phosphate of spontaneous parametric interaction tuneable from 4400 to 16000 Angstroms.* Physical Review Letters. **18**(21), 905-907 (1967)
8. Hong, C.K., Z.Y. Ou, and L. Mandel, *Measurement of subpicosecond time intervals between 2 photons by interference.* Physical Review Letters. **59**(18), 2044-2046 (1987)
9. Bouwmeester, D., J.-W. Pan, K. Mattle, M. Eibl, H. Weinfurter, and A. Zeilinger, *Experimenal quantum teleportation.* Nature. **390**, 575-579 (1997)
10. Ekert, A.K., *Quantum cryptography and Bell theorem.* Quantum Measurements in Optics. **282**, 413-418 (1992)
11. Boto, A.N., P. Kok, D.S. Abrams, S.L. Braunstein, C.P. Williams, and J.P. Dowling, *Quantum interferometric optical lithography: Exploiting entanglement to beat the diffraction limit.* Physical Review Letters. **85**(13), 2733-2736 (2000)
12. Shih, Y.H. and C.O. Alley, *New Type of Einstein-Podolsky-Rosen-Bohm Experiment Using Pairs of Light Quanta Produced by Optical Parametric Down Conversion.* Physical Review Letters. **61**(26), 2921-2924 (1988)

References

13. Kwiat, P.G., K. Mattle, H. Weinfurter, A. Zeilinger, A.V. Sergienko, and Y.H. Shih, *New high-intensity source of polarization-entangled photon pairs*. Physical Review Letters. **75**(24), 4337-4341 (1995)
14. Fiorentino, M., G. Messin, C.E. Kuklewicz, F.N.C. Wong, and J.H. Shapiro, *Generation of ultrabright tunable polarization entanglement without spatial, spectral, or temporal constraints*. Physical Review A. **69**(4), 1-4 (2004)
15. Takesue, H. and K. Inoue, *Generation of 1.5 mm band time-bin entanglement using spontaneous fiber four-wave mixing and planar light-wave circuit interferometers*. Phys. Rev. A. **72**, 041804-1-4 (2005)
16. ID quantique website; <http://www.idquantique.com>, Accessed 14th April 2010.
17. Zhirnov, V.V., R.K. Cavin, J.A. Hutchby, and G.I. Bourianoff, *Limits to Binary Logic Switch Scaling—A Gedanken Model*. Proc. IEEE. **91**(11), 1934-1939 (2003)
18. Oxborrow, M. and A.G. Sinclair, *Single-photon sources*. Contemporary Physics. **46**(3), 173-206 (2005)
19. Thew, R.T., N. Curtz, P. Eraerds, N. Walenta, J.-D. Gautier, and E. Koller, *Approaches to single photon detection*. Nuclear Instruments and Methods in Physics Research A. **610**, 16-19 (2009)
20. Cheung, J.Y., C.J. Chunnillall, E.R. Wooliams, N.P. Fox, J.R. Mountford, J. Wang, and P.J. Thomas, *The quantum candela: a re-definition of the standard units for optical radiation*. Journal of Modern Optics. **54**(2-3), 373-396 (2007)
21. Kwiat, P.G., A.M. Steinberg, and R.Y. Chiao, *Observation of a Quantum Eraser - A Revival of Coherence in a 2-Photon Interference Experiment* Physical Review A. **45**(11), 7729-7739 (1992)
22. Pittman, T.B., D.V. Strekalov, A. Migdall, M.H. Rubin, A.V. Sergienko, and Y.H. Shih, *Can Two-Photon Interference be considered the Interference of Two Photons*. Physical Review Letters. **77**(10), 1917-1920 (1996)
23. Kim, Y.-H., S.P. Kulik, M.V. Chekhova, W.P. Grice, and Y.H. Shih, *Experimental entanglement concentration and universal Bell-state synthesizer*. Physical Review A. **67**, 010301-1-4 (2003)
24. Sagioro, M.A., C. Olindo, C.H. Monken, and S. Pádua, *Time control of two-photon interference*. Physical Review A. **69**, 053817-1-5 (2004)
25. Pan, J.-W., D. Bouwmeester, H. Weinfurter, and A. Zeilinger, *Experimental Entanglement Swapping: Entangling Photons That Never Interacted*. Phys. Rev. Lett. **80**, 3891-3894 (1998)
26. Galvez, E.J., C.H. Holbrow, M.J. Pysher, J.W. Martin, N. Courtemanche, L. Heilig, and J. Spencer, *Interference with correlated photons: Five quantum mechanics experiments for undergraduates*. American Journal of Physics. **73**(2), 127-140 (2005)

References

27. Dauler, E., G. Jaeger, A. Muller, A. Migdall, and A. Sergienko, *Tests of a two-photon technique for measuring polarization mode dispersion with subfemtosecond precision*. Journal of Research of the National Institute of Standards and Technology. **104**(1), 1-10 (1999)
28. Abouraddy, A.F., M.B. Nasr, B.E.A. Saleh, A.V. Sergienko, and M.C. Teich, *Quantum-optical coherence tomography with dispersion cancellation*. Physical Review A. **65**(5), 053817-1-6 (2002)
29. Knill, E., R. Laflamme, and G.J. Milburn, *A scheme for efficient quantum computation with linear optics*. Nature. **409**(6816), 46-52 (2001)
30. Yuan, Z.L., B.E. Kardynal, R.M. Stevenson, A.J. Shields, C.J. Lobo, K. Cooper, N.S. Beattie, D.A. Ritchie, and M. Pepper, *Electrically driven single-photon source*. Science. **295**(5552), 102-105 (2002)
31. Kiraz, A., M. Atatüre, and A. Imamoglu, *Quantum-dot single-photon sources: Prospects for applications in linear optics quantum-information processing*. Physical Review A. **69**(3), 032305-1-10 (2004)
32. Yamamoto, Y., C. Santori, G. Solomon, J. Vuckovic, D. Fattal, E. Waks, and E. Diamanti, *Single photons for quantum information systems*. Prog. in Inf. **1**, 5-37 (2005)
33. Bödefeld, C., J. Ebbecke, J. Toivonen, M. Söpanen, H. Lipsanen, and A. Wixforth, *Experimental investigation towards a periodically pumped single-photon source*. Physical Review B. **74**, 035407-1-5 (2006)
34. Pittman, T.B., J.D. Franson, and B.C. Jacobs, *Investigation of a single-photon source based on quantum interference*. New Journal of Physics. **9**, 1-7 (2007)
35. Hijlkema, M., B. Weber, H.P. Specht, S.C. Webster, A. Kuhn, and G. Rempe, *A single-photon server with just one atom*. Nature Physics. **3**(4), 253-255 (2007)
36. Santori, C., D. Fattal, J. Vuckovic, G.S. Solomon, and Y. Yamamoto, *Indistinguishable photons from a single-photon device*. Nature. **419**(6907), 594-597 (2002)
37. Legero, T., T. Wilk, A. Kuhn, and G. Rempe, *Characterization of single photons using two-photon interference*. Adv. At. Mol. Opt. Phys. **53**, 253-289 (2006)
38. Brida, G., M. Genovesse, and C. Novero, *On the measurement of photon flux in parametric down-conversion*. Eur. Phys. J. D. **8**, 273-275 (2000)
39. Rarity, J.G. and P.R. Tapster, *Fourth-order interference in parametric downconversion*. J. Opt. Soc. Am. B. **6**(6), 1221-1226 (1989)
40. Jhans, H., J.M. Honig, and C.N.R. Rao, *Optical properties of reduced LiNbO₃*. J. Phys. C Solid State Phys. **19**, 3649-3658 (1986)

References

41. Bierlein, J.D. and H. Vanherzeele, *Potassium titanyl phosphate: properties and new applications*. J. Opt. Soc. Am. B. **6**(4), 622-633 (1989)
42. Eimerl, D., L. Davis, S. Velsko, E.K. Graham, and A. Zalkin, *Optical, mechanical, and thermal properties of barium borate*. J. Appl. Phys. . **62**(5), 1968-1983 (1987)
43. Kato, K., *Second-harmonic generation to 2048 Å in β -BaB₂O₄*. IEEE J.QE. **22**(7), 1013-1014 (1986)
44. Barnes, N.P., J. Gettemy, and R.S. Adhav, *Variation of the refractive index with temperature and the tuning range for KDP isomorphs*. J. Opt. Soc. Am. **72**(7), 895-898 (1982)
45. Dmitriev, V.G., G.G. Gurzadyan, and D.N. Nikogosyan, *Handbook of Nonlinear Optical Crystals*. Springer Series in Optical Sciences, ed. A.E. Siegman. 1999, ISBN No:3-540-65394-5
46. Cheung, E.C., K. Koch, and G.T. Moore, *Measurements of second-order nonlinear optical coefficients from the spectral brightness of parametric fluorescence*. Optics Letters. **19**(3), 168-170 (1994)
47. Cheung, J.Y., C.J. Chunnillall, and J. Wang, *Radiometric applications of correlated photon metrology*. SPIE. **5551**, 220-230 (2004)
48. Monken, C.H., P.H. Souto Ribeiro, and S. Pádua, *Optimizing the photon pair collection efficiency: A step toward a loophole-free Bell's inequalities experiment*. Physical Review A. **57**(4), R2267-2269 (1998)
49. Pittman, T.B., D.V. Strekalov, D.N. Klysko, M.H. Rubin, A.V. Sergienko, and Y.H. Shih, *Two-photon geometric optics*. Physical Review A. **53**(4), 2804–2815 (1996)
50. Fox, N.P., *Trap detectors and their properties*. Metrologia. **28**(3), 197-202 (1991)
51. Kim, Y.H., *Quantum interference with beamlike type-II spontaneous parametric down-conversion*. Physical Review A. **68**, 013804-1-4 (2003)
52. Spence, A.E., D.C. Stoudt, N.L. Swanson, A.D. Parks, and F.E. Peterkin, *A method for balance the paths of a two-photon interferometer*. Review of Scientific Instruments. **71**(1), 23-26 (2000)
53. de Chatellis, H.G., A.V. Sergienko, B.E.A. Saleh, and M.C. Teich, *Non-collinear and non-degenerate polarization-entangled photon generation via concurrent type-I parametric downconversion in PPLN*. Optics Express. **14**(21), 10060-10072 (2006)
54. Resch, K.J., J.S. Lundeen, and A.M. Steinberg, *Experimental observation of nonclassical effects on single-photon detection rates*. Phys. Rev. A. **63**, 020102-1-4 (2001)
55. Strauf, S., N.G. Stoltz, M.T. Rakher, L.A. Coldren, P.M. Petroff, and D. Bouwmeester, *High-frequency single-photon source with polarization control*. Nature Photonics. **1**, 704-708 (2007)

References

56. Rohde, P.P. and T.C. Ralph, *Frequency and temporal effects in linear optical quantum computing*. Phys. Rev. A. **71**, 032320-1-10 (2005)
57. *Guide to the Expression of Uncertainty in Measurement, GUM*. 1995: ISO, International Organization for Standardization
58. de Riedmatten, H., I. Marcikic, W. Tittel, H. Zbinden, and N. Gisin, *Quantum interference with photon pairs created in spatially separated sources*. Physical Review A. **67**(2), 022301-1-5 (2003)
59. Kuzucu, O., M. Fiorentino, M.A. Albota, F.N.C. Wong, and F.X. Kartner, *Two-photon coincident-frequency entanglement via extended phase matching* Physical Review Letters. **94**(16), 083601-1-5 (2005)
60. Fujii, G., N. Namekata, M. Motoya, S. Kurimura, and S. Inoue, *Bright narrowband source of photon pairs at optical telecommunication wavelengths using a type-II periodically poled lithium niobate waveguide*. Optics Express. **15**, 12769-12776 (2007)
61. Albota, M.A. and E. Dauler, *Single photon detection of degenerate photon pairs at 1.55 μ m from a periodically poled lithium niobate parametric downconverter*. Journal of Modern Optics. **51**(9-10), 1417-1432 (2004)
62. Wolberg, J., *Data Analysis Using the Method of Least Squares: Extracting the Most Information from Experiments*. 2005: Springer, ISBN No:3540256741
63. Glauber, R.J., *The Quantum Theory of Optical Coherence*. Phys. Rev. **130**, 2529-2539 (1963)
64. Rarity, J.G. and P.R. Tapster, *Two-color photons and nonlocality in fourth-order interference*. Physical Review A. **41**(9), 5139-5146 (1990)
65. Kim, Y.-H., *Measurement of one-photon and two-photon wavepackets in spontaneous parametric downconversion*. J. Opt. Soc. A. **20**(9), 1959-1966 (2003)
66. Burlakov, A.V., M.V. Chekhova, O.A. Karabutova, and S.P. Kulik, *Collinear two-photon state with spectral properties of type-I and polarization properties of type-II spontaneous parametric down-conversion: Preparation and testing*. Physical Review A. **64**(4), 041803-1-4 (2001)
67. Luo, H., X. Fang, and B. Ertas, *Hilbert Transform and Its Engineering Applications*. AAIA Journal. **47**(4), 923-932 (2009)
68. Feynman, R.P., R.B. Leighton, and M. Sands, *The Feynman Lectures on Physics*. Vol. 3. 1970: Addison-Wesley, ISBN No:0-201-02115-3
69. Mishina, H. and T. Asakura, *2 Gaussian-Beam Interference*. Nouvelle Revue D Optique. **5**(2), 101-107 (1974)
70. Mandel, L., *Coherence and Indistinguishability*. Optics Letters. **16**(23), 1882-1883 (1991)

References

71. Cheung, J., J.L. Gardner, A. Migdall, S. Polyakov, and M. Ware, *High accuracy dual lens transmittance measurements*. Applied Optics. **46**(22), 5396-5403 (2007)
72. Migdall, A.L., R.U. Datla, A. Sergienko, J.S. Orszak, and Y.H. Shih, *Absolute detector quantum-efficiency measurements using correlated photons*. Metrologia. **32**, 479-483 (1995)
73. Toptica Photonics website; <http://www.toptica.com>, Accessed 9th June 2009 2009.
74. Raicol crystals website; <http://www.raicol.com>, Accessed 12th May 2010.
75. HC photonics website; <http://www.hcphotonics.com>, Accessed 12th May 2010.
76. ADVR website; <http://www.advr-inc.com>, Accessed 12th May 2010.
77. Fiorentino, M., S.M. Spillane, R.G. Beausoleil, T.D. Roberts, P. Battle, and M.W. Munro, *Spontaneous parametric down-conversion in periodically poled KTP waveguides and bulk crystals*. Optics Express. **15**(12), 7479-7488 (2007)
78. Battle, P., *Private e-mail correspondence RE: PPKTP waveguides*. 2008, ADVR inc.
79. Alexandrovski, A., M. Fejer, and G. Mitchell, *CW gray-track formation in KTP*, in *CLEO '99*. 1999: Baltimore.
80. Grice, W.P., R.S. Bennink, Z. Zhao, K. Meyer, W. Whitten, and R. Shaw. *Spectral and spatial effects in spontaneous parametric down-conversion with a focused pump*. in *Proc. SPIE*. 2008.
81. Spurr, M. and M.H.D. Dunn, *Euclidean Light*. Optics and Photonics News, (August 2002), 40-44 (2002)
82. Chang, W.S.C., *Principles of Lasers and Optics*. 2005: Cambridge University Press
83. Website for School of Physics and Astronomy, University of St Andrews, Photonics simulation software for teaching (PSST) ; <http://www.st-andrews.ac.uk/~psst/> Accessed 12th May 2010.
84. Drever, R.W.P., *Laser and phase frequency stabilization using an optical resonator*. Applied Physics B. **31**(2), 97-105 (1983)
85. Kuzucu, O., *private e-mail communication*. 2009.
86. Rubin, M.H., D.N. Klyshko, Y.H. Shih, and A.V. Sergienko, *Theory of two-photon entanglement in type-II optical parametric downconversion*. Physical Review A. **50** (6), 5122-5133 (1994)
87. Giovannetti, V., L. Maccone, J.H. Shapiro, and F.N.C. Wong, *Extended phase-matching conditions for improved entanglement*. Physical Review A. **66**, 043813-1-9 (2002)
88. Gottesman, D. and I.L. Chuang, *Demonstrating the viability of universal quantum computation using teleportation and single-qubit operations*. Nature. **402**, 390-393 (1999)

References

89. Ralph, T.C., A.G. White, W.J. Munro, and G.J. Milburn, *Simple scheme for efficient linear optics quantum gates*. Physical Review A. **65**, 012314-1-6 (2001)
90. Pittman, T.B., B.C. Jacobs, and J.D. Franson, *Probabilistic quantum logic operations using polarizing beam splitters*. Physical Review A. **64**, 062311-1-9 (2001)
91. Kuklewicz, C.E., M. Fiorentino, G. Messin, and J.H. Shapiro, *High-flux source of polarization-entangled photons from a periodically poled KTiOPO₄ parametric down-converter*. Physical Review A. **69**, 013807-1-5 (2004)
92. Oberparleiter, M. and H. Weinfurter, *Cavity-enhanced generation of polarisation-entangled photon pairs*. Optics Communications. **183**, 133-137 (2000)
93. Volz, J., C. Kurtseifer, and H. Weinfurter, *Compact all-solid-state source of polarization entangled photon pairs*. Applied Physics Letters. **79**(6), 869-871 (2001)
94. Ursin, R., F. Tiefenbacher, B. Blauensteiner, T. Jennewein, J. Perdigues, P. Trojek, B. Omer, M. Furst, M. Meyenburg, J. Rarity, A. Sodnik, C. Barbieri, W. H., and A. Zeilinger, *Entanglement-based quantum communication over 144-km*. Nature Physics. **2**, 481-486 (2007)
95. Hübel, H., M.R. Vanner, T. Lederer, B. Blauensteiner, T. Lorünser, A. Poppe, and A. Zeilinger, *High-Fidelity transmission of polarization encoded qubits from an entangled source over 100 km of fiber*. Optics Express. **15**(12), 7853-7862 (2007)
96. Takesue, H., E. Diamanti, C. Langrock, M.M. Fejer, and Y. Yamamoto, *1.5 mm single photon counting using polarization-independent up-conversion detector*. Optics Express. **14**(26), 13067-13072 (2006)
97. Miller, A.J., S.W. Nam, J.M. Martinis, and A.V. Segienko, *Demonstration of a low-noise near-infrared photon counter with multiphoton discrimination* Applied Physics Letters. **83**(4), 791-792 (2003)
98. Gol'tsman, G.N., O. Okunev, G. Chulkova, A. Lipatov, A. Semenov, K. Smirnov, B. Voronov, and A. Dzardanov, *Picosecond superconducting single-photon optical detector*. Applied Physics Letters. **79**(6), 705-707 (2001)
99. Hariharan, P., *Optical Interferometry*. 2nd ed. 2003: Academic Press, ISBN No:0123116309
100. Clauser, J.F., M.A. Horne, A. Shimony, and R.A. Holt, *Proposed Experiment to Test Local Hidden-Variable Theories*. Physical Review Letters. **23**, 880-884 (1969)
101. Burnham, D.C. and D.L. Weinberg, *Observation of simultaneity in parametric production of optical photon pairs* Physical Review Letters. **25**(2), 84-87 (1970)
102. Ware, M. and A. Migdall, *Single-photon detector characterization using correlated photons: the march from feasibility to metrology*. Journal of Modern Optics. **51**(9), 1549-1557 (2003)

References

103. Brida, G., S. Castelletto, I.P. Degiovanni, M. Genovesse, C. Novero, and M.L. Rastello, *Towards and accuracy budget in quantum efficiency measurement with parametric fluorescence*. Metrologia. **37**, 629-632 (2000)
104. Joobeur, A., B.E.A. Saleh, and M.C. Teich, *Spatiotemporal coherence properties of entangled light beams generated by parametric down-conversion*. Phys. Rev. A. **50**(4), 3349-3361 (1994)
105. Fujiwara, H., Y. Kawabe, S. Takeuchi, and K. Sasaki, *Numerical analysis of spatial propagation of parametric fluorescence photon pairs using the tuning-curve filtering method*. Phys. Rev. A. **75**, 023802-1-8 (2007)
106. Boeuf, N., D. Branning, I. Chaperot, E. Dauler, S. Guérin, G. Jaeger, A. Muller, and A. Migdall, *Calculating characteristics of noncollinear phase matching in uniaxial and biaxial crystals*. Opt. Eng. **39**, 1016 (2000)
107. Kaschke, M. and C. Koch, *Calculation of Nonlinear Optical Polarization and Phasematching in Biaxial Crystals*. Applied Physics B. **49**, 419-423 (1989)
108. Byer, R.L. and S.E. Harris, *Power and Bandwidth of Spontaneous Parametric Emission*. Physical Review. **168**(3), 1064-1068 (1968)

Appendix 1: SPDC wavefunction

The following analysis presents spontaneous parametric downconversion using the quantum theory of electromagnetic fields to study the nonlinear interaction between the pump, signal and idler photons. Consider the parametric downconversion of a pump photon with frequency ω_p , wavevector $\mathbf{k}_p(\omega_p)$ and polarisation $\hat{E}_p(\omega_p)$ into signal and idler photons described by $\{\omega_s, \mathbf{k}_s, \hat{E}_s\}$ and $\{\omega_i, \mathbf{k}_i, \hat{E}_i\}$ respectively. Quantum mechanically, the pump acts upon two vacuum modes and the Hamiltonian for the interaction \hat{H}_{int} is given by:

$$\hat{H}_{\text{int}} = \int_V d^3\mathbf{r} \chi^{(2)} \hat{E}_p^{(+)}(\mathbf{r}, t) \hat{E}_s^{(-)}(\mathbf{r}, t) \hat{E}_i^{(-)}(\mathbf{r}, t) + H.c. \quad (\text{A1.1})$$

where $\chi^{(2)}$ is the non-linear susceptibility and $H.c.$ is the Hermitian conjugate of the first term. Describing the electric fields of the signal (s) and idler (i) polarisations in terms of quantized fields:

$$\hat{E}_{s,i}^{(+)}(\mathbf{r}, t) = i \int \frac{E_{s,i}}{2\pi} \hat{a}_{s,i}(\omega_{s,i}) e^{i[\mathbf{k}_{s,i}(\omega_{s,i})\mathbf{r} - \omega_{s,i}t]} d\omega_{s,i} \quad (\text{A1.2})$$

$\hat{a}_{s,i}(\omega_{s,i})$ is the annihilation operator for the s, i polarisation modes with wavevector $\mathbf{k}_{s,i}$, $E_{\mathbf{k}_{s,i}}$ is given by:

$$E_{s,i} = \left[\frac{\hbar \omega_{s,i}}{2\varepsilon_0 n_{s,i}^2 V_Q} \right]^{1/2} \quad (\text{A1.3})$$

V_Q is the interaction, or quantization volume, n describes the refractive index of a mode with specified polarisation and wavevector, ε_0 is the permittivity of free space and $\hbar = h/2\pi$ where h is Planck's constant. The creation and annihilation operators are normalised and satisfy the commutation relationship $[\hat{a}_j(\omega_j), \hat{a}_k^\dagger(\omega'_k)] = 2\pi\delta_{jk}\delta(\omega_j - \omega'_k)$. The pump is treated as a classical plane wave and therefore:

$$E_p^{(+)}(\mathbf{r}, t) = \int_0^\infty \frac{d\omega_p}{2\pi} E_p(\omega_p) e^{i(\mathbf{k}_p \cdot \mathbf{r} - \omega_p t)} \quad (\text{A1.4})$$

Combining equations (A1.1)-(A1.4) and expanding $\int_V d^3\mathbf{r} \rightarrow \int dx \int dy \int dz$ gives:

$$\begin{aligned} \hat{H}_{\text{int}} = & \int d\omega_p \int dx \int dy \int dz \int d\omega_s \int d\omega_i \chi^{(2)} E_p(\omega_p) E_s E_i \hat{a}_s^\dagger(\omega_s) \hat{a}_i^\dagger(\omega_i) \\ & \times e^{i(\omega_s + \omega_i - \omega_p)t} e^{iz(k_{pz} - k_{sz} - k_{iz})} e^{-ix(k_{sx} + k_{ix})} e^{-iy(k_{sy} + k_{iy})} + H.c. \end{aligned} \quad (\text{A1.5})$$

The $(k_{sx} + k_{ix})$ and $(k_{sy} + k_{iy})$ terms represent the transverse phase mismatch along the x and y axes respectively, therefore assuming the requirement for perfect transverse phasematching:

$$\int_{-\infty}^\infty dx \int_{-\infty}^\infty dy e^{-ix(k_{sx} + k_{ix})} e^{-iy(k_{sy} + k_{iy})} = (2\pi)^2 \delta(k_{sx} + k_{ix}) \delta(k_{sy} + k_{iy}) \quad (\text{A1.6})$$

The integral over the crystal length gives the longitudinal phase matching function:

$$\int_{-L/2}^{L/2} dz e^{iz(k_{pz} - k_{sz} - k_{iz})} = i \text{sinc}\left(\frac{\Delta k_z L}{2}\right) \quad (\text{A1.7})$$

The time evolution of the vacuum signal and idler modes due to the interaction Hamiltonian is given by:

$$|\psi(t)\rangle \approx |0\rangle - \frac{i}{\hbar} \int_{-\infty}^t dt \hat{H}_{\text{int}}(t) |0\rangle \quad (\text{A1.8})$$

The process of single photon detections means that only the second term of equation (A1.8) is considered. The time dependent part integral of the resulting expression amounts to the conservation of energy:

$$\int_{-\infty}^t dt e^{i(\omega_s + \omega_i - \omega_p)t} = 2\pi \delta(\omega_s + \omega_i - \omega_p) \quad (\text{A1.9})$$

which means the integral over ω_p can be removed, therefore:

$$|\psi\rangle = E_p E_s E_i \frac{2\pi}{i\hbar} \int d\omega_s \int d\omega_i \chi^{(2)} \text{sinc}\left(\frac{\Delta k_z L}{2}\right) \hat{a}_s^\dagger(\omega_s) \hat{a}_i^\dagger(\omega_i) |0\rangle \quad (\text{A1.10})$$

Equation (A1.10) describes the output state of the downconversion process. The state can be used to analyse quantum optical processes incorporating a parametric downconversion source. A similar expression to (A1.10) is used in chapter 6 in the modelling of a SPDC-based device for measuring single photon detector quantum efficiencies, and in the following appendix (A1.10) is used to study a SPDC-sourced two beam (single photon) interferometer together with an SPDC-sourced Hong-Ou-Mandel (two photon) interferometer.

Appendix 2: Correlation functions for SPDC and SPDC sourced 2-beam interferometers

The following analysis uses the quantum theory of electromagnetic fields to describe the shape of SPDC sourced two beam (single photon) and HOM (two photon) interferograms. The following analysis is an expansion of that presented in reference [65]. I thank the author Y.H. Kim (Pohang University of Science and Technology) for his assistance in helping me understand the mechanics of certain parts of the analysis through private e-mail communications.

1. First order correlation function associated with SPDC signal photon

The average counting rate of an ideal photo detector is proportional to $tr[\hat{\rho}E^{(-)}(t)E^{(+)}(t)]$ where $E^{(-)}$ and $E^{(+)}$ are the negative and positive frequency components of the incident field. Because photo detectors have finite response times and are not localised at one point in space, it is necessary define a more general expression for the average counting rate, where $E^{(-)}$ and $E^{(+)}$ are evaluated at different space time. This general expression is known as the first order correlation function $G^{(1)}$. $G^{(1)}$ quantifies the correlations of the complex fields at separated points and times. The first order correlation function corresponding to the signal downconversion can be written as:

$$G_{SPDC}^{(1)}(\tau) = tr[\hat{\rho}E_s^{(-)}(t)E_s^{(+)}(t+\tau)] \quad (\text{A2.11})$$

where the field operators are given by:

$$E_s^{(-)}(t) = \int_0^\infty d\nu a_s^\dagger(\Omega + \nu)\exp(i\nu t), \quad E_s^{(+)}(t) = \int_0^\infty d\nu a_s(\Omega + \nu)\exp(-i\nu t) \quad (\text{A2.12})$$

\hat{p}_s is the signal photon density operator which is given by the partial trace of the two photon density operator:

$$\hat{p}_s = \text{tr}_i[\hat{\rho}] = \text{tr}_i[|\psi\rangle\langle\psi|] \quad (\text{A2.13})$$

$|\psi\rangle$ is the downconversion wavefunction A1.10, derived in Appendix 1:

$$|\psi\rangle = \int d\omega_s \int d\omega_i \text{sinc}\left(\frac{\Delta k_z L}{2}\right) \hat{a}_s^\dagger(\omega_s) \hat{a}_i^\dagger(\omega_i) |0\rangle \quad (\text{A2.14})$$

where the combined constants of equation A1.10 have been normalized to one. Introducing the detuning frequency $\nu = \omega_s - \Omega = \omega_i + \Omega$ where $\Omega = \omega_p/2$:

$$\begin{aligned} |\psi\rangle &= \int d\nu S(\nu) a_s^\dagger(\Omega + \nu) a_i^\dagger(\Omega - \nu) |0\rangle \\ \langle\psi| &= \int d\nu S(\nu) a_s(\Omega + \nu) a_i(\Omega - \nu) \langle 0| \end{aligned} \quad (\text{A2.15})$$

where $S(\nu)$ is the sinc term in equation (A2.14) that describes the photon spectral function, therefore:

$$\hat{p}_s = \int d\nu |S(\nu)|^2 a_s^\dagger(\Omega + \nu) |0\rangle \langle 0| a_s(\Omega + \nu) \quad (\text{A2.16})$$

Substituting (A2.12) and (A2.16) into (A2.11) gives:

$$G_{SPDC}^{(1)}(\tau) = \text{tr} \left[\int_0^\infty d\nu |S(\nu)|^2 a_s^\dagger(\Omega + \nu) |0\rangle \langle 0| a_s(\Omega + \nu) a_s^\dagger(\Omega + \nu) a_s(\Omega + \nu) \exp(-i\nu\tau) \right] \quad (\text{A2.17})$$

When taking the trace, the components can be cycled within the expression therefore:

$$G_{SPDC}^{(1)}(\tau) = \int_0^\infty d\nu |S(\nu)|^2 \langle 0| a_s(\Omega + \nu) a_s^\dagger(\Omega + \nu) a_s(\Omega + \nu) a_s^\dagger(\Omega + \nu) |0\rangle \exp(-i\nu\tau) \quad (\text{A2.18})$$

since $a_s a_s^\dagger a_s a_s^\dagger |0\rangle \rightarrow |0\rangle$, and $\langle 0|0\rangle = 1$:

$$G_{SPDC}^{(1)}(\tau) = \int_0^\infty d\nu |S(\nu)|^2 \exp(-i\nu\tau) \quad (\text{A2.19})$$

Equation (A2.19) shows that $G_{SPDC}^{(1)}(\tau)$ is given by the Fourier transform of the signal photon power spectrum.

2. First order correlation function describing the output of a SPDC signal photon sourced two beam interferometer

Consider a two beam interferometer sourced by a beam of signal (unpaired) photons from a parametric downconversion process. At the output port of the recombiner the single photon count rate is given by:

$$R_{s,TBI} = tr \left[\hat{\rho}_s E_s^{(-)}(t) E_s^{(+)}(t) \right] \quad (A2.20)$$

where $\hat{\rho}_s$ is given by equation (A2.13) and the field operators are given by:

$$\begin{aligned} E_s^{(-)}(t) &= a^\dagger(\omega) \exp(i\omega t) + a^\dagger(\omega) \exp[i\omega(t+\tau)] \\ E_s^{(+)}(t) &= a(\omega) \exp(-i\omega t) + a(\omega) \exp[-i\omega(t+\tau)] \end{aligned} \quad (A2.21)$$

The optical delay between the two interferometer arms is given by τ . Evaluating (A2.20) we have $a^\dagger a |0\rangle \rightarrow |0\rangle$, also $\langle 0|0\rangle = 1$ therefore:

$$R_{s,TBI} = \int_0^\infty d\omega |S(\omega - \Omega)|^2 [2 + 2 \cos(\omega\tau)] = 1 + \left| G_{SPDC}^{(1)}(\tau) \cos(\Omega\tau) \right| / \left| G_{SPDC}^{(1)}(0) \right| \quad (A2.22)$$

Equation (A2.22) shows that the interference fringe pattern envelope measured at the output of a τ -scanning 2-beam interferometer is given by the Fourier transform of the interfering photon power spectrum. This is an experimentally observed relationship.

3. Second order correlation function associated with the output of a SPDC photon pair sourced two-beam (HOM) interferometer

By analogy with $G^{(1)}$ which gave a measure of the single photon counting rate due to an electric field, the second order correlation function $G^{(2)}$ gives a measure of the coincidence counting rate between two detectors D_1 and D_2 due to two electric fields. Generally $G^{(2)}$ is given by:

$$\begin{aligned}
 G^{(2)}(\tau) &= R_c = \int \left| \langle 0 | E_1^{(-)}(t_2) E_2^{(-)}(t_1) E_2^{(+)}(t_2) E_1^{(+)}(t_1) | \psi \rangle \right| dt_1 dt_2 \\
 &= \int \left| \langle 0 | E_2^{(+)}(t_2) E_1^{(+)}(t_1) | \psi \rangle \right|^2 dt_1 dt_2
 \end{aligned} \tag{A2.23}$$

$E_1^{(+)}(t_1)$ and $E_2^{(+)}(t_2)$ are the quantized electric fields at detectors D₁ and D₂. For the SPDC sourced HOM interferometer, D₁ and D₂ are positioned at the output of the HOM recombiner where the quantized electric fields are:

$$E_1^{(+)}(t_1) = -\int d\nu a_s(\Omega + \nu) \exp[-i(\Omega + \nu)t_1] + i \int d\nu a_i(\Omega - \nu) \exp[-i(\Omega - \nu)(t_1 + \tau)] \tag{A2.24}$$

$$E_2^{(+)}(t_2) = -i \int d\nu a_s(\Omega + \nu) \exp[-i(\Omega + \nu)t_2] + \int d\nu a_i(\Omega - \nu) \exp[-i(\Omega - \nu)(t_2 + \tau)] \tag{A2.25}$$

where τ is the optical delay between the two interferometer paths. The field at D₁ [equation (A2.24)] comprises a component due to a signal photon transmitted through the HOM recombiner, and a component due to the idler photon reflected at the recombiner. Similarly the field at D₂ [equation (A2.25)] comprises a reflected signal photon and a transmitted idler photon. Since $a_s a_s^\dagger a_i^\dagger |0\rangle \rightarrow 0$, $a_i a_s a_s^\dagger a_i^\dagger |0\rangle \rightarrow |0\rangle$, $a_s a_i a_i^\dagger a_s^\dagger |0\rangle \rightarrow |0\rangle$ and $a_i a_i a_s^\dagger a_s^\dagger |0\rangle \rightarrow 0$:

$$\begin{aligned}
 \langle 0 | E_2^{(+)}(t_2) E_1^{(+)}(t_1) | \psi \rangle &= -\int d\nu S(\nu) \exp[-i(\Omega - \nu)(t_2 + \tau)] \exp[-i(\Omega + \nu)t_1] \\
 &\quad + \int d\nu S(\nu) \exp[-i(\Omega + \nu)t_2] \exp[-i(\Omega - \nu)(t_1 + \tau)]
 \end{aligned} \tag{A2.26}$$

Equation (A2.26) conveys the observation that only the ‘R-R’ and ‘T-T’ components need to be considered for calculating the coincidence counting rate. The conjugate of equation (A2.26) is:

$$\begin{aligned}
 &-\int d\nu' S(\nu') \exp[i(\Omega - \nu')(t_2 + \tau)] \exp[i(\Omega + \nu')t_1] \\
 &+ \int d\nu' S(\nu') \exp[-i(\Omega + \nu')t_2] \exp[i(\Omega - \nu')(t_1 + \tau)]
 \end{aligned} \tag{A2.27}$$

Therefore the coincidence counting rate at the two output ports of the HOM interferometer, $R_{c,HOM}$ is given by:

$$G_{HOM}^{(2)}(\tau) = R_{c,HOM} = \int dt_+ dt_- \int d\nu d\nu' S(\nu) S(\nu') \exp[i(\nu - \nu')\tau] \times$$

$$\begin{aligned} & [\exp(ivt_-) + \exp(-iv't_-)] + [\exp(-ivt_-) + \exp(iv't_-)] \\ & - [\exp(ivt_-) + \exp(iv't_-)] - [\exp(-ivt_-) + \exp(-iv't_-)] \end{aligned} \quad (\text{A2.28})$$

where $t_- = t_2 - t_1$ and $t_+ = t_1 + t_2$, using $\cos x = \frac{e^{-ix} + e^{+ix}}{2}$ gives:

$$\begin{aligned} G_{HOM}^{(2)}(\tau) = & \int dt_+ dt_- \int d\nu d\nu' S(\nu) S(\nu') \exp[i(\nu - \nu')\tau] \times \\ & [\cos(\nu - \nu')t_- - \cos(\nu + \nu')t_-] \end{aligned} \quad (\text{A2.29})$$

Taking the dt_+ integral over the range $0 \rightarrow T_+$ and normalizing gives $\frac{1}{T_+} \int_0^{T_+} dt_+ = 1$. For dt_- , integrating over an even function:

$$\begin{aligned} & \frac{1}{2T_-} \int_0^{T_-} dt_- [\cos(\nu - \nu')t_- - \cos(\nu + \nu')t_-] \\ & = \left[\frac{\sin(\nu - \nu')t_-}{\nu - \nu'} - \frac{\sin(\nu + \nu')t_-}{\nu + \nu'} \right]_0^{T_-} \\ & = \text{sinc}(\nu - \nu')T_- - \text{sinc}(\nu + \nu')T_- \approx \delta(\nu - \nu') - \delta(\nu + \nu') \end{aligned} \quad (\text{A2.30})$$

since $T_- \gg 1/\nu$. Therefore:

$$G_{HOM}^{(2)}(\tau) = R_{c,HOM} \approx \int_{-\infty}^{\infty} d\nu |S(\nu)|^2 - \int_{-\infty}^{\infty} d\nu |S(\nu)|^2 \exp(i2\nu\tau) \quad (\text{A2.31})$$

From equation (A2.19) $G_{SPDC}^{(1)}(\tau) = \int_0^{\infty} d\nu |S(\nu)|^2 \exp(-i\nu\tau)$, therefore equation (A2.31) can be re-written as :

$$R_{c,HOM} \approx G_{SPDC}^{(1)}(0) - G_{SPDC}^{(1)}(2\tau) = 1 - \frac{G_{SPDC}^{(1)}(2\tau)}{G_{SPDC}^{(1)}(0)} \quad (\text{A2.32})$$

Equation (A2.32) describes the shape of the dip in the coincidence rate between the two output ports of a τ -scanning HOM interferometer. Comparison of equation (A2.32) with equation (A2.22), reveals that the HOM dip shape takes the same form as the single photon intensity interference fringe pattern envelope observed at the output of a τ -scanning two beam interferometer. The only difference between the two envelopes is that the HOM dip is twice squeezed along the τ axis. Equivalently equation (A2.32) shows that the form of the HOM dip is given by the Fourier transform of the signal photon power spectrum, this is important for the curve fitting model to the HOM dip data developed in section 3.2.3.